Development of jammed microgel-based materials for embedded 3D printing, injectable cell delivery applications, and in vitro cancer cell migration studies

---

A

Dissertation

Presented to

the faculty of the School of Engineering and Applied Science

University of Virginia

---

in partial fulfillment

of the requirements for the degree

Doctor of Philosophy

by

Julia Tumbic

May 2024

This

Dissertation

is submitted in partial fulfillment of the requirements
for the degree of

Doctor of Philosophy

Author: Julia Tumbic

This Dissertation has been read and approved by the examing committee:

Advisor: Chris Highley

Advisor:

Committee Member: Don Griffin

Committee Member: Shayn Peirce-Cottler

Committee Member: Steven Caliari

Committee Member: Liheng Cai

Committee Member:

Committee Member:

Accepted for the School of Engineering and Applied Science:

Jennifer L. West, School of Engineering and Applied Science

May 2024

Table of Contents

List of Figures

Acknowledgements

First, thank you Dr. Highley for the support, kindness, and attentiveness over the years. It's been great to grow along with the lab.

Thanks to my committee, Dr. Peirce-Cottler, Dr. Griffin, Dr. Cai, and Dr. Caliari, for their valuable feedback and suggestions throughout my PhD journey. Your guidance helps us all become better scientists.

Thanks to my labmates. There'd be no fun to be had, had there not been my lab. Jack, Natasha, Greg, Emily, and Remy, I wish you all the best.

To my family, thanks for the never ending support, you guys never stop pushing me to be better.

To my friends, thanks for the memories, may there be many more.

Chapter 1:

Go with the flow: granular materials and polyelectrolytes for injectable hydrogel applications

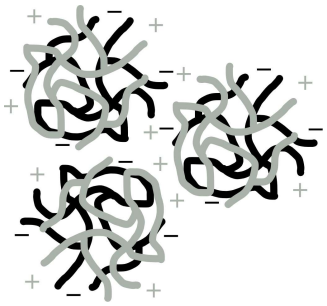

Part 1: Granular materials for injectable hydrogel applications

Granular materials are a promising platform for a wide range of biomedical applications. These are systems in which particles are packed together to form a solid-like material. However, upon application of a force, these particles can rearrange and become a fluid-like material. Due to this behavior plus properties such as micro-scale porosity, this class of materials is a promising platform for injectable hydrogel systems commonly used for 3D bioprinting of *in vitro* tissue models or for delivery of therapeutics or cells to a wound within the human body in a minimally-invasive manner. The inherent microporosity that is formed allows for sufficient oxygen and nutrient diffusion, helping to maintain high cell viabilities. These types of systems have been made using an interesting class of polymers known as polyelectrolytes, charged polymers that can be used to form responsive materials but also have inherent dynamic bonding properties. This background chapter describes factors that modulate jammed granular material properties, methods that have been used to alter granular systems to enhance stabilization and cell viability post-extrusion, and polyelectrolyte behaviors and how these behaviors have been used in injectable material design.

Granular material formation, jamming transition, and properties

Granular materials are typically composed of particles greater than 1μm in diameter[1], and are created using several techniques, with the two most used techniques being through microfluidic devices and batch emulsification. Microfluidic devices can be used, where an aqueous phase and an oil phase are pumped through separate channels into a connecting channel, formulating an aqueous particle surrounded by an oil phase. Upon crosslinking, these particles can be removed from oil. This technique

is conducive to formulating a monodisperse, or roughly equivalent size, population of particles. Through careful design of the microfluidic device, core-shell particles can be produced, with several applications in drug and cell delivery as well as 3D printing. Non-spherical particles, such as rods[2–4] and crescent moon-shaped particles[5], have been previously made using microfluidic devices. Batch emulsification, on the other hand, entails mixing of an oil phase with an aqueous hydrogel pre-cursor phase using an overhead stirrer[6] or stirbar[7,8]. This generally produces a polydisperse, or broad distribution, of particle sizes. Multiple types of crosslinking mechanisms have been used to formulate microgels with batch emulsification such as click chemistry reactions requiring UV light, or thermal transitions found commonly in materials like gelatin.

Particulate systems are considered jammed when particles are in contact with neighboring particles[9,10]. This is known as the jamming transition. This jamming transition can be reflected as an inflection point when examining viscosity as a function of particle concentration. As viscosity reaches the jamming transition, a sharp rise in viscosity with further particle concentration can be seen[11]. This is due to restricted movement of particles by neighboring contacting particles. When this jamming transition is exceeded in terms of particle concentration, a variable known as the yield stress comes into play. Yield stress is defined as the minimum stress needed for a material to yield. For particles to successfully rearrange and fluidize, a stress greater than the yield stress must be applied to break interparticle contacts[12]. As described in further detail below, these interparticle contacts as well as properties of individual particles dictate bulk rheological, mechanical, and microstructural properties. Specifically, these variables include particle size polydispersity, particle stiffness, particle size, and attractive or repulsive interactions amongst particles.

Polydispersity has been studied in jammed particle systems and found to have an effect on bulk rheological properties. In discussing jammed particle systems, polydispersity (PDI) refers to the distribution of particle sizes and is calculated as follows:

$$PDI = \left(\frac{\sigma}{2a} \right)^2$$

Where σ is the standard deviation of the particle size distribution, and α is the mean particle diameter[13]. As PDI becomes larger, the more polydisperse the particle system is. Monodisperse particles, where all particle diameters are roughly equivalent in size, can crystallize when packed as ordered lattices can be formed through events such as shearing[14,15]. These crystalline structures can alter mechanical properties such as stiffness, and potentially flow as these structures would need to be broken up to allow for particle rearrangements to occur. Polydisperse packings, on the other hand, can inhibit crystallization and higher packing densities can be achieved. Crystallization is inhibited due to the

broad range of sizes. Higher packing densities can be achieved due to smaller particles taking up pore spaces created by larger particles[14]. Thus, higher viscosities and bulk stiffnesses can be seen in polydisperse jammed particle systems.

Particles of high stiffnesses were initially studied in these systems and are referred to in the literature as hard particles. Due to the high stiffness, a maximum packing density exists, and has been calculated to be 0.64, assuming a monodisperse particle population[16,17]. This is due to the lack of deformation that the particles can undergo. However, if softer microparticles are packed together, facets can form due to the enhanced elasticity of the softer polymer network, and thus the highest packing density that can be achieved can exceed that of hard particles. The increase in facet formation increases friction between particles[18], leading to higher critical yield values regardless of particle size[19]. In a previous study, microgel stiffness was also found to play a role in energy dissipations, measured from the loss modulus curves, where higher stiffness led to lower dissipation with no trend found in microgel size. Additionally, an increase in particle stiffness has been found to lead to a general increase in bulk stiffness[19].

Generally, as soft particles continue to deform and reach high packing densities, the mechanics of these particle systems can reach those of continuous hydrogels. This can be explained by the rubber elasticity theory, explained by the following equation:

$$G = \upsilon k_B T = C\left[\frac{N_a}{M_m N}\right] k_B T$$

Where G is shear modulus, υ is the number density of chains, C is the polymer concentration, Na is Avogadro's number, M_m is monomer molecular weight, and N is the number of monomers present in the polymer between crosslinks[10,20]. In short, as polymer concentration in a hydrogel increases, shear modulus linearly increases. In several studies, the correlation of shear modulus to microgel concentration has been observed[10,21]. This can occur regardless of microgel size[10].

Particle size can play a role in rheological properties, but under specific conditions. In one study, colloidal-scale and granular-scale microgels were prepared and examined for changes in rheological properties as a function of size. Interestingly, even though colloidal-scale particles are susceptible to Brownian motion, both length scales generally lead to similar properties when subjected to low strains and frequencies. Under flow conditions, however, differences arose due to the inherent nature of the particles, where granular-scale particles are 'fuzzy' with loose polymer ends surrounding a denser core of crosslinked polymer, whereas colloidal-scale particles are instead separated by a solvent layer, leading to increased interparticle friction in packed granular-scale particles that is not present in colloidal-scale systems[10]. Another study specifically examining granular-scale particles, size played a

minor role in altering properties such as critical yield strain and energy dissipation, but this was primarily in stiff-particle-based systems[19].

Particle size can impact cell behaviors. In one study, particles comprised of poly(ethylene glycol)-vinyl sulfone were prepared and crosslinked together. In scaffolds made up of smaller microparticles, mesenchymal stromal cells had a higher density compared to that of scaffolds prepared with large particles. Interestingly, macrophages took on an inflammatory phenotype when added to small particle-based scaffolds, and a non-inflammatory phenotype in the large particle case[22]. In another study, researchers examined cell behaviors in packed spheres made up of collagen-coated polystyrene with varying sizes. It was found that at the smallest tested spheres, between 14 and 20μm in diameter, cells would often detach from the particle surfaces, whereas when particle diameters ranged from 38-85μm, cells were able to proliferate[23]. These works illustrate how particle size may need to be considered when designing microgel-based materials for *in vitro* model or injectable hydrogel development.

Lastly, interparticle interactions can play a role in bulk mechanical and rheological properties. Particle interactions can be classified as repulsive or attractive. Phase diagrams have been previously reported to illustrate changes in variables affecting this transition[24,25]. To test this, some studies have used emulsion systems, which have been shown to behave similarly to particle-based systems. In a study on attractive emulsion systems, change of interaction strengths produced different rheological properties in the bulk system, such as two-step yielding for intermediate interaction strengths, repulsive glass behavior caused by electrostatic repulsions and steric effects, and gel-like behavior when interparticle interaction strengths were high[26]. These interparticle interactions have also been shown to impact microstructural properties, where greater interparticle attractive forces can lead to the formation of clusters that can then lead to changes in pore size distributions[25,27].

Jammed granular materials have properties necessary for injectable materials applications

Jammed granular materials encompass two key requirements for injectable materials, namely shear-thinning and self-healing behaviors. Shear-thinning refers to the decrease in viscosity with shear rate, and self-healing refers to the ability of a material to reform broken bonds and retain original mechanical properties post-deformation. These behaviors are achieved in granular systems through particle rearrangements and caging dynamics. To induce flow in a packed system, as described above, a sufficient force, generally one past the yield stress, must be applied to the granular system. This force enables particle rearrangements to occur and thus for the material to flow and exhibit shear-thinning behaviors. Self-healing is achieved through the re-establishment of contacts between neighboring particles as an applied force is removed[9]. As described in the section above, these interparticle contacts are key to forming a solid-like material out of particles.

Jammed particle systems have been used previously in many 3D printing applications due to these inherent shear-thinning and self-healing behaviors. A technique known as embedded 3D printing, where an ink is printed into a support hydrogel or suspension bath, takes particular advantage in using jammed particle-based materials. As an ink, microparticles made up of materials like modified hyaluronic acid (HA)[28], gelatin[29], and poly(ethylene glycol) (PEG)[30] have been used and shown to produce good filament formation and maintain shape post-extrusion, crucial properties for 3D printed scaffolds. When using a technique like embedded 3D printing, in which an ink is printed into a support material and requires the same behaviors as for printing inks, granular materials have been successfully used. Supports comprised of gelatin fragments[31,32] and Carbopol[9] were used to print intricate or complex constructs that would otherwise be difficult to print using a traditional layer-by-layer printing technique. These could be achieved due to the shear-shinning and self-healing behaviors to allow for ink to be deposited and then encapsulated by the microparticle-based support.

In traditional continuous or bulk hydrogel systems, both shear-thinning and self-healing behaviors have been achieved in a multitude of ways and can be included as part of a jammed particle system. One commonly used method is through the incorporation of reversible or dynamic bonds. These bond types can be easily broken upon the application of a force, but due to affinities, can easily reform upon removal of this force. For example, guest-host bonds such as adamantane and beta-cyclodextrin have been added to polymers such as hyaluronic acid[8] include more detail?. Hydrazone bonding has been utilized as well, where aldehydes can interact with hydrazide or other amine-containing groups. This has been previously demonstrated in HA-based systems[33,34], as well as in xanthan-PEG hydrogels[35], poly(ethylenimine)-PEG hydrogels[36], and PEG-maleimide microgels[37]. Electrostatic interactions have been employed as well for creating dynamically-bonded systems. As the name suggests, positively-charged and negatively-charged polymers can interact and form a gel, or a charged molecule can interact with a polymer of an opposing charge. A well-known example is alginate. Alginate is derived from seaweed and can form a gel upon the addition of calcium chloride. The calcium ions form a distinct ‘egg-box’ bond between alginate groups, thus forming a hydrogel. This bonding has allowed for the use of alginate in 3D printing applications, as the polymer chains can disassociate during extrusion then reform into a network after extrusion[38,39].

These reversible bond types can be incorporated into microparticles as well to help stabilize the particles further at rest. For instance, HA-based particles made to promote hydrazone bonding between particles were formulated for vocal fold regeneration. Vocal folds are soft tissues, and thus to effectively regenerate this tissue, careful design of the injectable hydrogel system must be carried out. The design of hydrazone-bond-based particle system allowed for control over factors such as degradation and bulk mechanical properties[40]. In another study, particles made up of PEG-maleimide were formulated to

induce guest-host bonding between particles. This study also examined particle processing effects, comparing spherical microparticles to fragmented particles. The authors found that spherical particles enhanced self-healing behavior that was not observed in the fragmented granular system. This guest-host particle system showed promise in cell delivery applications, specifically for pancreatic islets as a treatment for diabetes[37].

Secondary crosslinking reactions can also be used to further stabilize particles post-printing or injection. These crosslinking reactions typically use a technique like UV crosslinking, where particle formulations are made with photoinitiators that can quickly crosslink particles together upon UV exposure. In Chapter 2, we see this play out using a dilute photo-curable HA-based solution. Other materials, such as microporous annealed particles (MAP)[41], have successfully used a technique where excess reactive groups coat the outer edge of the microparticles. These reactive groups can then be used to form covalent crosslinks between particles via UV exposure. In 3D printing, perfusable channels were printed into a support bath comprised of gelatin microgels with a continuous gelatin interstitial solution. This interstitial solution was enzymatically-crosslinkable through the addition of transglutaminase that over time post-printing would facilitate stabilization of the support bath and then enable subsequent evacuation of the printed ink to leave behind a perfusable channel[32].

Particles can be made up of cells rather than hydrogels, and similar stabilization processes described above can be used for these cell-laden particles. Particles made up of embryoid bodies were mixed with a temperature-responsive ECM solution. When kept at low temperatures, this ECM solution is in a liquid-like state, and printing of complex networks resembling vasculature could be printed. Upon heating to physiological temperature, the interstitial ECM gelled, and the ink could be evacuated, leaving behind an open, perfusable vascular-like network[42]. Similarly, pre-vascularized spheroids made up of human mesenchymal stromal cells (MSCs) were combined with fibrin and methacrylated gelatin (GelMA) to create an injectable system for bone tissue engineering[43].

Another key aspect to injectable materials and inks is shear-protection, and this can be provided via dynamic bonds. Essentially, for a cell-laden 3D printed construct or cell delivery system to be effective, viability post-extrusion is a crucial factor. To enhance shear-protection, shear-thinning materials are often used. The shear-thinning behavior allows for stresses that come from the extrusion process to be experienced by the materials, thus offloading stress from cells onto the surrounding hydrogel material. It was found that extensional flow is a key contributor to cell death immediately post-injection, as opposed to shear forces or pressure drop across the nozzle. To alleviate the damage caused by extensional flow, the researchers found that alginate hydrogels could be used as these hydrogels could possibly undergo ‘plug flow’ where the perimeter of the hydrogel experiences shear and extensional forces, but the interior maintains a gel-like state. This is commonly observed behavior amongst

hydrogels with dynamic bonds[44]. Other engineered hydrogels that have been designed and achieved high cell viabilities post-injection include double-networks[45,46], HA modified to use hydrazone bonding[33], and hydrogel-nanoparticle composites[47].

In granular systems, cell viability has been found to depend on both particle properties and interparticle interactions. In a recent study, methacrylated HA-based particles were created via covalent crosslinking with dithiothreitol. Dynamic interparticle interactions were established using guest-host chemistries of added adamantane and cyclodextrin. The end application for this particulate system was 3D bioprinting of stem cells. The researchers found via rheological testing that the yield stress of the granular system must exceed the force required to break the dynamic guest-host bonds for cell viability to be high[8]. Thus, interparticle interactions as well as particle mechanics are important considerations to designing injectable granular systems.

Part 2: Polyelectrolytes to engineer injectable materials

Polyelectrolytes are a class of polymers containing charges along the polymer backbone, and are found throughout the human body, making them extremely relevant for the development of *in vitro* tissue models. For example, hyaluronic acid, a major component of the extracellular matrix, is negatively charged and therefore can keep water within a tissue. Proteins often contain charged moieties that aid in protein conformation that is crucial to proper functioning. Thus, polyelectrolytes are a common material to use in developing hydrogels for tissue engineering applications. Due to the presence of charges along the polymer chain, polyelectrolytes are frequently used in applications where dynamic electrostatic interactions can be used.

In general, polymer chains consist of length scale units called blobs. These are generally defined as the unit of polymer within which thermal energy dominates[48]. Blobs though can take on different definitions. For example, correlation blobs are used when discussing polymers in semidilute conditions, which differs from a thermal blob. Polyelectrolytes are discussed in terms of electrostatic blobs, the size of which can be described with the following equation when the polymer is in an ideal conformation:

$$D_e \approx b\, g_e^{\frac{1}{2}}$$

Where D_e is the size of the electrostatic blob, b is segment length, and g_e is the number of monomers within the polymer chain[49]. Within an electrostatic blob, thermal energy dominates and electrostatic interactions do not play a role in polymer chain conformation at this length scale. When length scales exceed this blob size, electrostatic interactions dominate, and the electrostatic blobs are thus arranged

linearly due to electrostatic repulsion when in a salt-free environment[49,50], in contrast to non-polyelectrolyte polymers which, depending on the solvent, can take on a number of conformations from aggregates to extended chains[48]. Due to the presence of charged groups along the polymer backbone, polyelectrolyte chains take on conformations that more closely match those of non-polyelectrolyte polymers when salt concentration increases, causing charges on the polyelectrolyte to be shielded, or pH is altered towards the isoelectric point of the polyelectrolyte[49,50]. Thus, these two variables are often considered when designing polyelectrolyte-based biomaterials.

Another consideration that can factor into polyelectrolyte-based biomaterial design is the dissociating groups along the polymer backbone. These dissociating groups are categorized according to the strength of dissociation of the group or pK_a value and can have an impact on polyelectrolyte hydrogel properties. Strong cationic groups include ammonium-based groups. Weakly cationic groups can include moieties such as amines or pyridines. Weakly anionic groups are typically carboxylic acids. And strongly anionic groups would be those comprised of sulfonic acids[51,52]. The primary difference between weak and strong groups is environmental sensitivity. Strong polyelectrolytes always maintain their charged state. Weak polyelectrolytes can change their conformations and subsequent behaviors in response to stimuli such as changes in pH[51,53], and thus make this category of polyelectrolytes useful in applications requiring a stimulus response.

Polyelectrolyte processing methods

Processing and uses of polyelectrolytes, like other hydrogel materials, can be broadly fit into four categories depending on the end-application: 1) gels, 2) polymer brushes, 3) fibers, and 4) microparticles. These are discussed in further detail below.

Gels:

Similar to other hydrogels, polyelectrolytes can be modified to include crosslinking mechanisms to form a gel. Coacervates can be formed through adding a polycation and polyanion together in equivalent amounts so as to neutralize charge. Coacervate gels are thus inherently injectable, as electrostatic interactions are dynamic in nature. For example, a triblock copolymer containing pyridine groups was added to a solution with a polyanion. Without an electrophile in solution, the pyridine groups remain uncharged and the coacervate remained in a liquid-like state. When gelled in the presence of an activator, the material was demonstrated to have good injectability and self-healing behaviors. This material was also degradable *in vivo*[54]. In another study, silica nanoparticles were functionalized with

poly(ethylenimine). These particles were combined with HA, forming a composite coacervate hydrogel system. These gels were shown to be self-healing and shear-thinning. These hydrogels could be loaded with a cancer therapeutic at high loading efficiencies in the presence of the silica nanoparticles, and could subsequently be release from the hydrogel over time[55].

Naturally-occurring polyelectrolytes have also been modified to include other modes of crosslinking to form hydrogels. For instance, HA has previously been modified to include a norbornene group onto the N-acetylglucosamine group along the backbone[56]. This addition of a norbornene moiety allows for the HA chains to be covalently crosslinked in the presence of UV light with a dithiol crosslinker. This norbornene-modified HA has been used in numerous studies for tissue engineering applications, ranging from forming microgels for injectable applications[28,57] to cartilage tissue engineering[58], to forming vasculature via formation of an interpenetrating network with collagen[59].

Polyelectrolytes have been previously modified to include moieties to enhance antimicrobial activity for treating wounds or antibiotic-resistant bacteria. In one study, chitosan, a naturally occurring cationic polysaccharide, was modified to include quaternary ammonium groups that could also interact with carboxylic acid groups on gelatin. This composite hydrogel was able to prevent both gram-positive and gram-negative bacteria from proliferating, showing enhanced antibacterial properties[60]. In another study, a multifunctional injectable hydrogel for wound recovery applications was formulated to include ionic linkages to provide antibacterial properties and tissue adhesion. This was achieved through the addition of a quaternized chitosan to give antibacterial properties and the researchers showed effectiveness against methicillin-resistant staphylococcus aureus (MRSA) in a mouse model. Because tissues are generally negatively-charged, the positive charges of the hydrogel aided in tissue adhesion, facilitating wound healing in rat tail amputation models[61].

Polymer brushes:

Polyelectrolyte chains can adsorb onto oppositely-charged surfaces. This behavior can be used to form polyelectrolyte multilayer materials, where polyanions and polycations are alternatingly added to a substrate, or to form polyelectrolyte brushes. When a polyelectrolyte adsorbs onto a surface, parts of the chain adhere to the surface, while other parts of the polymer chain remain in solution in the form of loops and tails. This introduces another blob known as an adsorption blob, the size of which is described by the following equation when in a good solvent:

$$\xi_{ads} = \frac{b}{\varepsilon^{\frac{3}{2}}}$$

Where ξ_{ads} is the adsorption blob size, b is the Kuhn length, and ε is related to the number of monomers within the polymer chain[48]. Typically, when several polymer chains adsorb onto a surface, polymer concentration is highest at the surface and decreases as the length from the surface increases. This is described as by the following equation:

$$\Gamma = b^{-2}\left(\frac{b}{\xi_{ads}}\right)^{\frac{2\nu-1}{\nu}}$$

Where Γ is the concentration, b is the polymer Kuhn length, ξ_{ads} is the adsorption blob size, and v is an exponent related to solvent conditions[48].

When polymer concentration is sufficiently high, a conformation known as a brush can be formed. This occurs due to increased steric and repulsive interactions between polymer chains. For polyelectrolytes, assuming good solvent conditions, this critical grafting density is characterized by the following equation:

$$\sigma^{*} \sim b^{-2} N^{\frac{-6}{5}}$$

Where σ* is the critical grafting density, b is the Kuhn length, and N is the number of Kuhn length segments[62].

Polyelectrolyte brushes have been used in a multitude of applications. One of these applications is in mimicking synovial fluid. In one study, a zwitterionic-based polyelectrolyte brush was formed onto microgels made up of poly(N-isopropylacrylamide) (PNIPAAm) to imitate synovial fluid. Because polyelectrolytes are generally hydrophilic, these brush-architectures thus are important for creating such a surface. In addition to materials exhibiting decreased friction with the addition of the zwitterionic brush layer, cell viability amongst these particles was measured and found to be high, thus leading to additional biomedical applications[63].

Charges from polyelectrolyte brushes can be used to facilitate drug delivery via electrostatic interactions with the drug cargo. In one study, a block copolymer was synthesized with grafted poly(lactic-co-glycolic acid) (PLGA) chains. PLGA is an anionic polymer, and the inclusion of this polymer allowed for the electrostatic interaction with cationic proteins used for cancer treatments. This technology also improved stability of the protein, and in turn enhanced efficacy when tested against cancer cells[64].

Polyelectrolyte brushes can be used to form antifouling surfaces. Antifouling surfaces are important in many biomedical applications as fouling behavior often leads to problems such as a foreign body response. To create an antifouling surface, polyelectrolytes were designed to switch between cationic,

anionic, and zwitterionic states. This flexibility in charged states allowed the material to have enhanced antifouling properties[65].

Fibers:

A common method to process polymers to mimic the fibrous nature of native ECM is to create fibers. Several techniques can be used to achieve this, the most common being electrospinning. To create electrospun fibers, a polymer solution is created containing the polymer of interest plus good solvents and optionally viscosity agents. The solution is then added to a syringe and placed onto a syringe pump. An electric field is applied to the solution and to a collector to facilitate fiber formation. Fibers from the syringe then travel to the collector in a whipping fashion, drying out along the way, and deposit onto the collector[66]. If needed, crosslinking of the polymers can be achieved post-spin if the polymer is water-soluble.

An example of using polycationic fibers is for antibacterial wound dressings. In a recent study, N,N-dimethyl epoxypropyl octadecyl ammonium chloride, or QAS, was grafted onto gelatin. This molecule has antibacterial properties. The addition of QAS produces a positive charge along gelatin chains. This material was successfully electrospun into nanofibers, with transglutaminase being used to crosslink the gelatin chains together. This material was shown to have a good cytocompatibility, thus demonstrating its potential use for wound dressings[67].

Polyelectrolytes are inherently pH-sensitive, and thus can be used for applications requiring this property. To create fibers, two oppositely charged polymers, poly(allylamine hydrochloride) and poly(acrylic acid), were mixed, forming a complex. This complex solution could be successfully electrospun into nanofibers, and these fibrous membranes were then tested to assess pH sensitivity. These fibers could swell and deswell with the fluctuation of pH, thus leading to potential applications in drug delivery or tissue engineering[68].

NorHA fibers have been electrospun into nanofibers and used to formulate fibrous hydrogels. After electrospinning, NorHA fibers were segmented to create short fibrous components. Fibers could be crosslinked at different densities to form fiber-based hydrogels. These materials showed strain-stiffening behavior, thus mimicking a characteristic found in native tissues. When mesenchymal stromal cells were seeded into these constructs, the cells could contract the material macroscopically. To further understand applications in biofabrication, fiber alignment could be achieved via shear, and exhibited shear-thinning and self-healing behaviors, pointing towards future applications in bioprinting[69].

Particle-based materials:

As stated earlier, microparticles can be formed using a variety of techniques like batch emulsification or microfluidic devices. This still applies for polyelectrolyte-based microparticles. As discussed in Part 1, interparticle interactions dictate bulk rheological properties. This can be achieved in a jammed polyelectrolyte-based particulate system by simply using particles of opposing charges to induce changes in rheological or bulk mechanical properties. Because these are polyelectrolytes, the effects of salt concentration and pH on polymer conformation are still present.

Polyelectrolyte-based particles were formulated and used to study the effects of polyelectrolyte-based particles on cell viabilities and proliferation as well as to further understand the role of polyelectrolyte charges when particles are in a state known as 'near-jamming'. Particles comprised of PNIPAAm were created via precipitation polymerization. Further modification was done to create cationic, anionic, and zwitterionic particles. Rheologically, both anionic and cationic microgels scaled with traditional polyelectrolyte scaling laws when in a high salt environment, while no change in properties of the zwitterionic microgels took place at a specific salt concentration. Cell culture experiments showed good viability and proliferation in supports with anionic and zwitterionic microgels, whereas cationic microgel-based supports were considered cytotoxic[12].

Colloidal gels comprised of gelatin type A particles were created and used to study endothelial morphogenesis. As is well known in the biomaterials community, vascularization of biomaterials is a major hurdle necessitating extensive work in the development of support constructs that can facilitate vasculature formation. One way to do so is through colloidal particles that can form a gel. To tune microstructural and mechanical properties of these colloidal gels, gelatin type B particles, poly(acrylic acid) (PAA) solution, and sodium salt solution were separately added to gelatin type A particles. The interaction of oppositely charged particles lead to confined vascular networks, whereas colloidal particles with PAA produced an interconnected endothelial network[70]. A similar study using gelatin type A and type B particles to form a colloidal gel showed stress relaxation values similar to what is achieved *in vivo*[71].

Another study focused on the formulation granular-scale particles to form an injectable therapeutic system for stimulating nerve outgrowth. Chitosan and gelatin were both modified via methacrylation to facilitate crosslinking to form microparticles. Chitosan retained its cationic nature, whereas this reaction with gelatin produces a negatively-charged polymer. This synthesis thus allowed for electrostatic interactions between the two particle populations. To test drug release, nerve growth factor (NGF) concentration over time was measured and it was found that these microparticle-based materials could release NGF over time. *In vivo* studies demonstrated improved nerve outgrowth[72].

References:

1. Chen, M., Wu, G., Gan, B., Jiang, W. & Zhou, J. Physical and Compaction Properties of Granular Materials with Artificial Grading behind the Particle Size Distributions. *Adv. Mater. Sci. Eng.* **2018**, e8093571 (2018).
2. Qazi, T. H. *et al.* Anisotropic Rod-Shaped Particles Influence Injectable Granular Hydrogel Properties and Cell Invasion. *Adv. Mater.* **34**, 2109194 (2022).
3. Tunable uptake/release mechanism of protein microgel particles in biomimicking environment | Scientific Reports. https://www.nature.com/articles/s41598-017-06512-5.
4. Rommel, D. *et al.* Functionalized Microgel Rods Interlinked into Soft Macroporous Structures for 3D Cell Culture. *Adv. Sci.* **9**, 2103554 (2022).
5. Kim, S.-H., Abbaspourrad, A. & Weitz, D. A. Amphiphilic Crescent-Moon-Shaped Microparticles Formed by Selective Adsorption of Colloids. *J. Am. Chem. Soc.* **133**, 5516–5524 (2011).
6. Gelatin Microgel Incorporated Poly(ethylene glycol)-Based Bioadhesive with Enhanced Adhesive Property and Bioactivity | ACS Applied Materials & Interfaces. https://pubs.acs.org/doi/10.1021/acsami.6b01364.
7. Chan, K. M. C. *et al.* Functionalizable hydrogel microparticles of tunable size and stiffness for soft-tissue filler applications. *Acta Biomater.* **10**, 2563–2573 (2014).
8. Morley, C. D., Ding, E. A., Carvalho, E. M. & Kumar, S. A Balance between Inter- and Intra-Microgel Mechanics Governs Stem Cell Viability in Injectable Dynamic Granular Hydrogels. *Adv. Mater.* **35**, 2304212 (2023).
9. Bhattacharjee, T. *et al.* Writing in the granular gel medium. *Sci. Adv.* **1**, e1500655 (2015).
10. Menut, P., Seiffert, S., Sprakel, J. & Weitz, D. A. Does size matter? Elasticity of compressed suspensions of colloidal- and granular-scale microgels. *Soft Matter* **8**, 156–164 (2011).
11. Fernandez-Nieves, A., Wyss, H., Mattsson, J. & Weitz, D. A. *Microgel Suspensions: Fundamentals and Applications*. (John Wiley & Sons, 2011).

12. O'Bryan, C. S., Kabb, C. P., Sumerlin, B. S. & Angelini, T. E. Jammed Polyelectrolyte Microgels for 3D Cell Culture Applications: Rheological Behavior with Added Salts. *ACS Appl. Bio Mater.* (2019) doi:10.1021/acsabm.8b00784.

13. Clayton, K. N., Salameh, J. W., Wereley, S. T. & Kinzer-Ursem, T. L. Physical characterization of nanoparticle size and surface modification using particle scattering diffusometry. *Biomicrofluidics* **10**, 054107 (2016).

14. Khabaz, F., Liu, T., Cloitre, M. & Bonnecaze, R. T. Shear-induced ordering and crystallization of jammed suspensions of soft particles glasses. *Phys. Rev. Fluids* **2**, 093301 (2017).

15. Teich, E. G., Galloway, K. L., Arratia, P. E. & Bassett, D. S. Crystalline shielding mitigates structural rearrangement and localizes memory in jammed systems under oscillatory shear. *Sci. Adv.* **7**, eabe3392 (2021).

16. Ni, R., Stuart, M. A. C. & Dijkstra, M. Pushing the glass transition towards random close packing using self-propelled hard spheres. *Nat. Commun.* **4**, 2704 (2013).

17. Berryman, J. G. Random close packing of hard spheres and disks. *Phys. Rev. A* **27**, 1053–1061 (1983).

18. Seth, J. R., Cloitre, M. & Bonnecaze, R. T. Elastic properties of soft particle pastes. *J. Rheol.* **50**, 353–376 (2006).

19. Emiroglu, D. B. *et al.* Building block properties govern granular hydrogel mechanics through contact deformations. *Sci. Adv.* **8**, eadd8570 (2022).

20. Flory, P. J. *Principles of Polymer Chemistry*. (Cornell University Press, 1953).

21. Di Lorenzo, F. & Seiffert, S. Particulate and continuum mechanics of microgel pastes: effect and non-effect of compositional heterogeneity. *Colloid Polym. Sci.* **291**, 2927–2933 (2013).

22. Lowen, J. M. *et al.* Multisized Photoannealable Microgels Regulate Cell Spreading, Aggregation, and Macrophage Phenotype through Microporous Void Space. *Adv. Healthc. Mater.* **12**, 2202239 (2023).

23. Cunha, A. F. *et al.* Cell Response in Free-Packed Granular Systems. *ACS Appl. Mater. Interfaces* **14**, 40469–40480 (2022).

24. Liu, A. J. & Nagel, S. R. Jamming is not just cool any more. *Nature* **396**, 21–22 (1998).

25. Trappe, V., Prasad, V., Cipelletti, L., Segre, P. N. & Weitz, D. A. Jamming phase diagram for attractive particles. *Nature* **411**, 772–775 (2001).

26. Fuhrmann, P. L. *et al.* Rheological behaviour of attractive emulsions differing in droplet-droplet interaction strength. *J. Colloid Interface Sci.* **607**, 389–400 (2022).

27. Koeze, D. J. & Tighe, B. P. Sticky Matters: Jamming and Rigid Cluster Statistics with Attractive Particle Interactions. *Phys. Rev. Lett.* **121**, 188002 (2018).

28. Highley, C. B., Song, K. H., Daly, A. C. & Burdick, J. A. Jammed Microgel Inks for 3D Printing Applications. *Adv. Sci.* **6**, 1801076 (2019).

29. Song, K., Compaan, A. M., Chai, W. & Huang, Y. Injectable Gelatin Microgel-Based Composite Ink for 3D Bioprinting in Air. *ACS Appl. Mater. Interfaces* **12**, 22453–22466 (2020).

30. Xin, S. *et al.* Generalizing hydrogel microparticles into a new class of bioinks for extrusion bioprinting. *Sci. Adv.* **7**, eabk3087 (2021).

31. Hinton, T. J. *et al.* Three-dimensional printing of complex biological structures by freeform reversible embedding of suspended hydrogels. *Sci. Adv.* **1**, e1500758 (2015).

32. Compaan, A. M., Song, K., Chai, W. & Huang, Y. Cross-Linkable Microgel Composite Matrix Bath for Embedded Bioprinting of Perfusable Tissue Constructs and Sculpting of Solid Objects. *ACS Appl. Mater. Interfaces* **12**, 7855–7868 (2020).

33. Lou, J. *et al.* Dynamic Hyaluronan Hydrogels with Temporally Modulated High Injectability and Stability Using a Biocompatible Catalyst. *Adv. Mater.* **30**, 1705215 (2018).

34. Yang, K. *et al.* Antibacterial hyaluronic acid hydrogels with enhanced self-healing properties *via* multiple dynamic bond crosslinking. *Int. J. Biol. Macromol.* **256**, 128320 (2024).

35. Sharma, P. K., Taneja, S. & Singh, Y. Hydrazone-Linkage-Based Self-Healing and Injectable Xanthan–Poly(ethylene glycol) Hydrogels for Controlled Drug Release and 3D Cell Culture. *ACS Appl. Mater. Interfaces* **10**, 30936–30945 (2018).

36. Wang, L. L. *et al.* Injectable, Guest–Host Assembled Polyethylenimine Hydrogel for siRNA Delivery. *ACS Publications* https://pubs.acs.org/doi/full/10.1021/acs.biomac.6b01378 (2016) doi:10.1021/acs.biomac.6b01378.

37. Widener, A. E., Duraivel, S., Angelini, T. E. & Phelps, E. A. Injectable Microporous Annealed Particle Hydrogel Based on Guest–Host-Interlinked Polyethylene Glycol Maleimide Microgels. *Adv. NanoBiomed Res.* **2**, 2200030 (2022).

38. Lee, K. Y. & Mooney, D. J. Alginate: properties and biomedical applications. *Prog. Polym. Sci.* **37**, 106–126 (2012).

39. Grant, G. T., Morris, E. R., Rees, D. A., Smith, P. J. C. & Thom, D. Biological interactions between polysaccharides and divalent cations: The egg-box model. *FEBS Lett.* **32**, 195–198 (1973).

40. Jia, X. *et al.* Hyaluronic Acid-Based Microgels and Microgel Networks for Vocal Fold Regeneration. *Biomacromolecules* **7**, 3336–3344 (2006).

41. Griffin, D. R., Weaver, W. M., Scumpia, P., Di Carlo, D. & Segura, T. Accelerated wound healing by injectable microporous gel scaffolds assembled from annealed building blocks. *Nat. Mater.* **14**, 737–744 (2015).

42. Skylar-Scott, M. A. *et al.* Biomanufacturing of organ-specific tissues with high cellular density and embedded vascular channels. *Sci. Adv.* **5**, eaaw2459 (2019).

43. Fang, Y. *et al.* Engineering Highly Vascularized Bone Tissues by 3D Bioprinting of Granular Prevascularized Spheroids. *ACS Appl. Mater. Interfaces* **15**, 43492–43502 (2023).

44. Aguado, B. A., Mulyasasmita, W., Su, J., Lampe, K. J. & Heilshorn, S. C. Improving Viability of Stem Cells During Syringe Needle Flow Through the Design of Hydrogel Cell Carriers. *Tissue Eng. Part A* **18**, 806–815 (2012).

45. Cai, L., Dewi, R. E. & Heilshorn, S. C. Injectable Hydrogels with In Situ Double Network Formation Enhance Retention of Transplanted Stem Cells. *Adv. Funct. Mater.* **25**, 1344–1351 (2015).

46. Han, C., Zhang, H., Wu, Y., He, X. & Chen, X. Dual-crosslinked hyaluronan hydrogels with rapid gelation and high injectability for stem cell protection. *Sci. Rep.* **10**, 14997 (2020).

47. Non-Newtonian Polymer–Nanoparticle Hydrogels Enhance Cell Viability during Injection - Lopez Hernandez - 2019 - Macromolecular Bioscience - Wiley Online Library. https://onlinelibrary.wiley.com/doi/full/10.1002/mabi.201800275.

48. Rubinstein, M. & Colby, R. H. *Polymer Physics*. (Oxford University Press, Oxford, New York, 2003).

49. Dobrynin, A. V., Colby, R. H. & Rubinstein, M. Scaling Theory of Polyelectrolyte Solutions. *Macromolecules* **28**, 1859–1871 (1995).

50. Khokhlov, A. R. & Khachaturian, K. A. On the theory of weakly charged polyelectrolytes. *Polymer* **23**, 1742–1750 (1982).

51. Stuart, M. A. C., Vries, R. J. de & Lyklema, J. Polyelectrolytes. in *Fundamentals of Interface and Colloid Science. Vol. V : Soft Colloids* 2.1-2.84 (Elsevier, 2005).

52. Tiwari, R. & Walther, A. Strong anionic polyelectrolyte microgels. *Polym. Chem.* **6**, 5550–5554 (2015).

53. Nová, L., Uhlík, F. & Košovan, P. Local pH and effective pKA of weak polyelectrolytes – insights from computer simulations. *Phys. Chem. Chem. Phys.* **19**, 14376–14387 (2017).

54. Wu, B. *et al.* Chemical signal regulated injectable coacervate hydrogels. *Chem. Sci.* **14**, 1512–1523 (2023).

55. Newham, G., Evans, S. D. & Ong, Z. Y. Mechanically tuneable physical nanocomposite hydrogels from polyelectrolyte complex templated silica nanoparticles for anionic therapeutic delivery. *J. Colloid Interface Sci.* **617**, 224–235 (2022).

56. Gramlich, W. M., Kim, I. L. & Burdick, J. A. Synthesis and orthogonal photopatterning of hyaluronic acid hydrogels with thiol-norbornene chemistry. *Biomaterials* **34**, 9803–9811 (2013).

57. Muir, V. G. *et al.* Sticking Together: Injectable Granular Hydrogels with Increased Functionality via Dynamic Covalent Inter-Particle Crosslinking. *Small* **18**, 2201115 (2022).

58. Schwab, A. *et al.* Modulating design parameters to drive cell invasion into hydrogels for osteochondral tissue formation. *J. Orthop. Transl.* **41**, 42–53 (2023).

59. Crosby, C. O. *et al.* Phototunable interpenetrating polymer network hydrogels to stimulate the vasculogenesis of stem cell-derived endothelial progenitors. *Acta Biomater.* **122**, 133–144 (2021).

60. Bhattacharjee, B., Ghosh, S., Mukherjee, R. & Haldar, J. Quaternary Lipophilic Chitosan and Gelatin Cross-Linked Antibacterial Hydrogel Effectively Kills Multidrug-Resistant Bacteria with Minimal Toxicity toward Mammalian Cells. *Biomacromolecules* **22**, 557–571 (2021).

61. Fang, W., Yang, L., Chen, Y. & Hu, Q. Bioinspired multifunctional injectable hydrogel for hemostasis and infected wound management. *Acta Biomater.* **161**, 50–66 (2023).

62. Das, S., Banik, M., Chen, G., Sinha, S. & Mukherjee, R. Polyelectrolyte brushes: theory, modelling, synthesis and applications. *Soft Matter* **11**, 8550–8583 (2015).

63. Liu, G. *et al.* Synovial fluid-inspired biomimetic lubricating microspheres: Zwitterionic polyelectrolyte brushes-grafted microgels. *Friction* **11**, 938–948 (2023).

64. Li, X. *et al.* Poly(L-Glutamic Acid)-Based Brush Copolymers: Fabrication, Self-assembly, and Evaluation as Efficient Nanocarriers for Cationic Protein Drug Delivery. *AAPS PharmSciTech* **21**, 78 (2020).

65. Subramanian Sundaram, H., Ella-Menye, J.-R., D. Brault, N., Shao, Q. & Jiang, S. Reversibly switchable polymer with cationic/zwitterionic/anionic behavior through synergistic protonation and deprotonation. *Chem. Sci.* **5**, 200–205 (2014).

66. Electrospinning and Electrospun Nanofibers: Methods, Materials, and Applications | Chemical Reviews. https://pubs.acs.org/doi/10.1021/acs.chemrev.8b00593.

67. Yu, N. *et al.* Cationic Gelatin Cross-Linked with Transglutaminase and Its Electrospinning in Aqueous Solution. *Langmuir* **39**, 3668–3677 (2023).

68. Boas, M., Gradys, A., Vasilyev, G., Burman, M. & Zussman, E. Electrospinning polyelectrolyte complexes: pH-responsive fibers. *Soft Matter* **11**, 1739–1747 (2015).

69. Davidson, M. D. *et al.* Programmable and contractile materials through cell encapsulation in fibrous hydrogel assemblies. *Sci. Adv.* **7**, eabi8157 (2021).

70. Nair, S. K. *et al.* Colloidal Gels with Tunable Mechanomorphology Regulate Endothelial Morphogenesis. *Sci. Rep.* **9**, 1072 (2019).

71. Bertsch, P., Andrée, L., Besheli, N. H. & Leeuwenburgh, S. C. G. Colloidal hydrogels made of gelatin nanoparticles exhibit fast stress relaxation at strains relevant for cell activity. *Acta Biomater.* **138**, 124–132 (2022).

72. Hsu, R.-S. *et al.* Adaptable Microporous Hydrogels of Propagating NGF-Gradient by Injectable Building Blocks for Accelerated Axonal Outgrowth. *Adv. Sci.* **6**, 1900520 (2019).

Chapter 2:

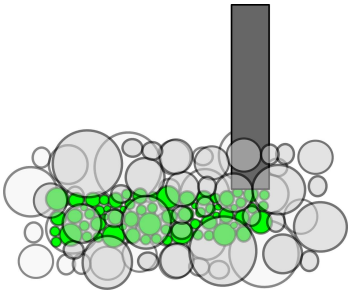

Printing particles into particles: Achieving small perfusable channels and other small features

Introduction

To mimic complex human tissues, with their finely detailed and interlocking architectures reflective of tissue functions, 3D bioprinting techniques have been in development. These techniques enable multiscale control over construct complexity, from macroscale structure to microscale composition, and spanning a large range of tissue mechanics. Some examples include bioprinting of bone tissue, where porosity can be included to form trabeculae-like structures found in native bone[1–4]. Intestinal *in vitro* models have been fabricated with villi-like and crypt-like features through careful design of hydrogel materials for layer-by-layer (LbL)[5–8] and stereolithographic printing techniques[9,10]. While the multiscale nature of 3D bioprinting has enabled the fabrication of a variety of tissue-like constructs, some challenges remain. For instance, some features like individual cell-laden droplets can be difficult to incorporate within an LbL printed construct. The ink must also be able to withstand gravity, otherwise the printed construct can collapse. This limits the materials available and requires specific mechanical properties for bioprinting inks, where softer inks are preferred for soft tissues. As a result, 3D bioprinting requires further refinement.

Embedded 3D printing (e3DP) is a spin-off of the traditional bioprinting approaches that solve some of disadvantages with LbL printing[11–13]. To achieve complex, heterogeneous structures typically difficult to print, e3DP uses a support material to, as the name suggests, support extruded ink filaments, acting as a 3D canvas. These supports vary in material choice, from synthetic polymers like UV-curable Pluronic[13] to natural materials like modified hyaluronic acid[14] and composite ECM-based materials[15] but generally have two crucial rheological properties: 1) shear-thinning behavior, and 2) self-healing behavior. As an ink moves through the support, the support must flow to accommodate the moving

printing nozzle and extruding ink, but upon removal of the nozzle, the support needs to re-solidify to encapsulate the ink. To achieve these properties, bond types can be modified. Bond types like guest-host create a permissive environment, where bonds are readily and easily broken and reformed[14], thus satisfying both support requirements.

Another subset of permissive materials is packed granular microgels[11,12,16]. Granular microgels have the rheological properties crucial for embedded 3d bioprinting when jammed i.e. packed together. In their jammed state, when particles are in contact with other particles[17,18], this material behaves like an elastic solid when at a standstill. A force is required to break the particle network and fluidize the support. Upon cessation of this force, the particle network reforms, resolidifying the support[11,18]. These are advantageous transitions for bioprinting inks and supports. Because microgels are discrete pockets of polymer network, extrusion forces on a granular ink are lower compared to their bulk hydrogel counterparts[19]. These microparticles can be stabilized through a secondary crosslinking reaction with one another[20] or through an interstitial material[21], providing a method to maintain shape fidelity of the ink and provide more structure to the support. Previous studies have demonstrated these advantages in practice, printing retrievable objects from a gelatin slurry[12], printing of perfusable channels using gelatin-based fragments[21] and organoid bodies as the support material[22], and printing fine features into a Carbopol-based support[11]. A limiting factor to be considered, however, when using granular microgels lies in resolution, where the diameter of the microgels plays a significant role[22].

By utilizing the advantages of jammed granular microgels and controlling particle diameters towards and within the single-digit micron range, we demonstrate the printing of high-resolution, complex features within a biopolymer-based support by extruding a jammed microgel ink into a jammed microgel support. Here, we use two commonly used biopolymers: gelatin and hyaluronic acid (HA). Gelatin is widely known for its thermal gelation that can be exploited for use as a removable ink. HA, found in tissues like the brain and articular cartilage to name a few, was modified with a norbornene group (NorHA) to facilitate crosslinking via UV light. Both materials were made into microgels and then jammed to form a gelatin ink and NorHA support. We show that the gelatin ink can be extruded into the NorHA support to form perfusable channels, high resolution voxel-esque depots with controllable spacings, branching structures, and depots surrounding a filament. We also illustrate that fibroblast viability can be maintained or enhanced in a thick perfusable scaffold compared to a non-perfusable construct, and that endothelial cells can be added to a perfused channel, forming a cell-lined channel.

Methods

Synthesis

NorHA was fabricated using a previously described method[23]. Briefly, sodium hyaluronate was mixed with Dowex resin for 2-3h, followed by filtration and pH correction to roughly 7 to fabricate HA-TBA. Post-lyophilization, HA-TBA modification was measured using H^1 NMR. Based off this modification, HA-TBA was then reacted with 5-norbornene-2-carboxylic acid to form NorHA through an esterification reaction with di-tert-butyl decarbonate and 4-dimethylaminopyridine. The degree of modification was calculated based on H^1 NMR spectra to be 12-15% (SI Fig. 1).

Support Medium and Granular Ink Preparation

A precursor 3 wt% NorHA solution was prepared in PBS containing 0.157 mg/mL, 0.313 mg/mL, or 0.626 mg/mL dithiothreitol (DTT, Sigma) and 6.6mM lithium phenyl-2,4,6-trimethylbenzoylphosphinate (LAP, Sigma). The alterations in the DTT concentrations lead to crosslinking densities of 2mM, 4mM, and 8mM of norbornene groups consumed in the crosslinking reaction, and the materials are referred to as NorHA-2, NorHA-4, and NorHA-8, respectively. This NorHA solution was homogenized in light mineral oil with 2% Span80 (Sigma) for 2 minutes at 3000rpm, followed by UV curing for 5min at approximately 10mW/cm^2. The microgels and oil were then stirred at 1000rpm with isopropanol to begin de-emulsification. After stirring, the mixture was filtered over a 0.22μm hydrophilic PVDF membrane (Durapore, Millipore). Microgels were washed an additional two times over the filter with isopropanol. After filtering, the microgels were left to dry then added into a 50mL conical and vortexed with 70% ethanol and placed on a rocker at least overnight. To finish processing, microgels were washed with PBS four times using centrifugation to ensure ethanol removal and equilibration in PBS. Microgels were then filtered over a 40μm cell strainer and stored at 4°C until needed.

To prepare the NorHA support, the NorHA microgels were centrifuged at 3214xg for 10 minutes, and PBS was decanted. A small volume of PBS was then added back to loosen the microgel pellet, and the microgels were then aliquoted into Eppendorf tubes, and centrifuged at 5283xg (7500rpm) for 5 minutes. Again, excess PBS was removed. A 1% NorHA solution was prepared in PBS with 0.625mg/mL of an MMP-degradable dithiol crosslinker (GCNSVPMSMRGGSNCG), previously synthesized using a peptide synthesizer (Liberty Blue), and 6.6mM LAP. This interstitial matrix was in approximate equal volume to the NorHA microgels in the Eppendorf tube. The microgels and interstitial

solution were vortexed for 20-30 minutes, then centrifuged at 5283xg (7500rpm) for 5 minutes. Excess 1% NorHA solution was removed, and centrifugation was repeated if necessary.

Gelatin microgels were prepared using a modified method. A 15% gelatin solution in PBS and a light mineral oil solution with 2% Span80 were separately heated to 80°C. The oil was then added to the gelatin solution and immediately homogenized at 9000rpm for 2 minutes. The emulsion was then stirred at 1000rpm until it reached room temperature. To prepare the gelatin-based ink, the microgels were jammed by centrifugation at 8000rpm for 2 minutes. A 1% HA (HA-500K, Lifecore) solution was prepared in PBS and then added in a volume equal to that of the gelatin microgels. All washing steps and storage conditions were the same as for the NorHA microgels.

3D printing device preparation

To create devices for printing perfusable channels, custom-designed molds and frames were designed using AutoCAD and printed using a Formlabs 2 printer. The design consists of three reservoirs in series connected by channels. After printing, the molds were processed by soaking twice in isopropanol followed by post-curing at an elevated temperature for at least an hour. The mold was glued onto a glass slide, and a frame was secured onto the glass slide using binder clips. Sylgard-184 (PDMS) was prepared according to manufacturer's instructions, where a 1:10 ratio of curing agent to base was mixed and then cast onto the mold devices and cured at 37°C overnight. After removal, PDMS casts and glass slides were adhered together via plasma treatment in air. Shortly after, these devices were placed into a solution of 1:200 v/v 3-mercaptopropyltrimethoxy silane (Sigma) to 200 proof ethanol for approximately 1 hour, then washed with ethanol and placed into 1M HCl for at least one hour prior to washing with DI water[24].

Particle Size Analysis

NorHA microgels were tagged with a thiolated Rhodamine-B peptide via UV crosslinking, and gelatin microgels were prepared with FITC-dextran (2MDa, Sigma) added to the gelatin solution prior to homogenization. A Leica DMI-8 microscope was used to image the microgels using a 20x objective. Microgels were diluted with PBS and placed onto a glass slide. A coverslip was then placed over the microgels. The fluorescent images were thresholded in ImageJ, then the watershed function was used to separate contacting particles, followed by using the particle analysis function to obtain microgel diameters. Particles that were unable to be separated using the watershed function were discarded

prior to running particle analysis. Images of the undiluted jammed support were taken as well after compressing onto a glass slide with a glass coverslip.

Rheology

Flow, frequency, and strain sweeps were carried out on both the NorHA support medium and gelatin microgel ink. A parallel plate system was used, as this provides a gap 10x the microgel diameters[25]. To prevent wall slip, a sandblasted 20mm plate with a solvent trap was used as the top geometry, and sandpaper was placed on the bottom plate. Gap size was set to 500μm, and temperature was kept at 20°C. Prior to each test, the NorHA support and gelatin ink were sheared for $150s^{-1}$ and $250s^{-1}$, respectively, to erase shear history or aging and reset the material. For flow sweeps, the shear rate was decreased from 500 s^{-1} to 0.001 s^{-1} with steady-state sensing with 5% tolerance over a 5s sampling period and a max equilibration time of 60s. The stress to strain rate relationship was fit to the Herschel-Bulkley equation:

$$\tau = \tau_0 + k\dot{\gamma}^n$$

Where τ is stress, τ_0 is the yield stress, k is a consistency index, $\dot{\gamma}$ is strain rate, and n is a constant describing shear-thinning, shear-thickening, or Newtonian fluid behavior. Frequency sweeps were carried out from 0.01 to 10Hz with an applied strain of 1%, and strain sweeps were done from 0.01% to 500% with an applied frequency of 1Hz. For the NorHA support, a UV curing step was included using a quartz bottom plate. The test was conducted at room temperature with an applied strain and frequency of 1% and 1Hz. A delay time of 2 minutes was used to obtain pre-UV exposure storage and loss moduli. The material was exposed to UV light with an intensity of $10mW/cm^2$ for 60s. After UV exposure, the test was run for an additional ten minutes.

3D Printing

To create perfusable channels via 3D printing, devices were prepared as described earlier. The connecting PDMS channels were blocked with 15% gelatin to prevent NorHA support from flowing in during printing. The NorHA support was then added to the central reservoir. A gelatin ink was prepared and loaded into a 100μL Nanofil syringe. This was placed onto either a modified Felix 3.2 printer[26], or a Felix bioprinter with custom-made clips designed in AutoCAD and printed with a Formlabs 2 printer (SI Fig. 5). Extrusion was controlled by varying the E value in the Gcode, and all prints were done using a feedrate of 50mm/min. A 26G needle was used for all prints except for the lowest flow rate tested,

where a 36G needle was employed. The NorHA support was then crosslinked via exposure to UV light at 10mW/cm^2 for 1 minute. To remove the gelatin ink, the device was placed in a humidified environment at 37°C, with one side reservoir containing PBS to create a pressure gradient and facilitate ink removal. Images were taken on a microscope with a 5x objective after printing, and after ink removal. Measurements of filament diameter, channel diameter, and perfusable diameter were made using ImageJ. Statistical analysis was done in OriginPro 8.1, with a one-way ANOVA and post-hoc Tukey test to determine statistical significance.

To print depots and other complex features, NorHA support was added to a PDMS holder, and gcodes were prepared. Gelatin inks with FITC-dextran (MW=2MDa, Sigma) or RITC-dextran (MW=70kDa, Sigma) were used for imaging purposes. After printing, images were taken on a DMI8 microscope (Leica) with a 5x objective.

Diffusion

Perfusable channels were prepared as described earlier. PBS in the reservoirs was replaced the next day and the device was allowed to sit for an additional 1h at 37°C prior to initiating the diffusion experiments. A 1µg/mL Rhodamine-B (Rho-B, Sigma) solution and a 0.112mg/mL fluorescein isothiocyanate-bovine serum albumin (FITC-BSA, Sigma) were prepared in PBS. The corresponding solutions were added in equal volumes to both side reservoirs, and either the microscope began continuous image acquisition for the Rho-B experiment, or timepoints of 1h, 3h, 6h, and 24h were taken for the FITC-BSA experiment. Both experiments were carried out at room temperature. The fluorescence gradient of the solutions diffusing out of the channel into the peripheral support was measured using ImageJ.

Material Preparation for Cell Culture Experiments

The NorHA support and gelatin ink were prepared in the same manner as described earlier but steps after rehydration in 70% ethanol were carried out in a biosafety cabinet. The 1% NorHA matrix was made with complete fibroblast media and then sterile-filtered through a 0.22µm PVDF syringe filter. A thiolated arginylglycylaspartic acid peptide (GCGYCRGDSPG, GenScript) was added to the 1% NorHA to a final concentration of 1mg/mL. The 1% HA for the gelatin ink was disinfected via UV light. PDMS devices were disinfected by soaking in 70% ethanol after treatment with silane was complete.

Proliferation and Viability in Thin Support Gels

3T3 NIH mouse fibroblasts were plated at a density of 2000 cells/cm^2. Dulbecco's modified eagle medium (DMEM) containing l-glutamine and high glucose was supplemented with 10% calf bovine serum and 1% antibiotic/antimycotic. Cells were then harvested using 0.05% trypsin in EDTA and centrifuged at 130xg for 5 minutes. Cells were resuspended to 100million cells/mL for cell culture experiments.

To assess cell viability within the NorHA support, cells were added to NorHA-4 support in ratios of 1:10, 1:20, and 1:50 volumetric ratios of the cell suspension to NorHA support, prepared as described earlier. 100µL of this cell-laden support was added to 48-wells and then cured at 10mW/cm^2 for 60s. Complete media was added to each well. Proliferation was quantified using an alamar blue assay on days 1, 3, 5, 7, and 9, with fold change calculated relative to day 1. The assay was prepared according to manufacturer's instructions, where the assay was mixed with complete medium in a 1:10 volumetric ratio. This working medium was heated to 37°C prior to addition to the thin gel samples.

Effect of perfusion on viability of 3T3 fibroblasts in thick constructs

Cells were harvested and added to NorHA-4 support as described earlier. The printing device was set up as described earlier. The cell-laden support was then added to the central reservoir of the printing device, shown in Fig. 1B. To create non-perfusable constructs, the NorHA support was polymerized using UV light, as described earlier, and complete media was added to the side reservoirs and on top of the support. Perfusable constructs were prepared by printing a filament into the cell-laden support, crosslinking the support, then the ink was evacuated upon placing the device into a 37°C incubator.

To run viability tests, the constructs were removed from the device and cut perpendicular to the channel prior to staining with calcein blue AM (Invitrogen) and ethidium-homodimer 1. The cut constructs were first washed with DPBS, then a DPBS solution containing 20µM calcein blue AM and 4µM ethidium homodimer-1 (EthD-1) was added to the samples and placed in the incubator for at least 20 minutes. After incubation, samples were washed with DPBS then imaged in an inverted widefield microscope (DMi-8, Leica). For some samples, calcein AM and EthD-1 were used to stain perfused and non-perfused constructs to obtain images in the longitudinal plane (SI Fig. 7).

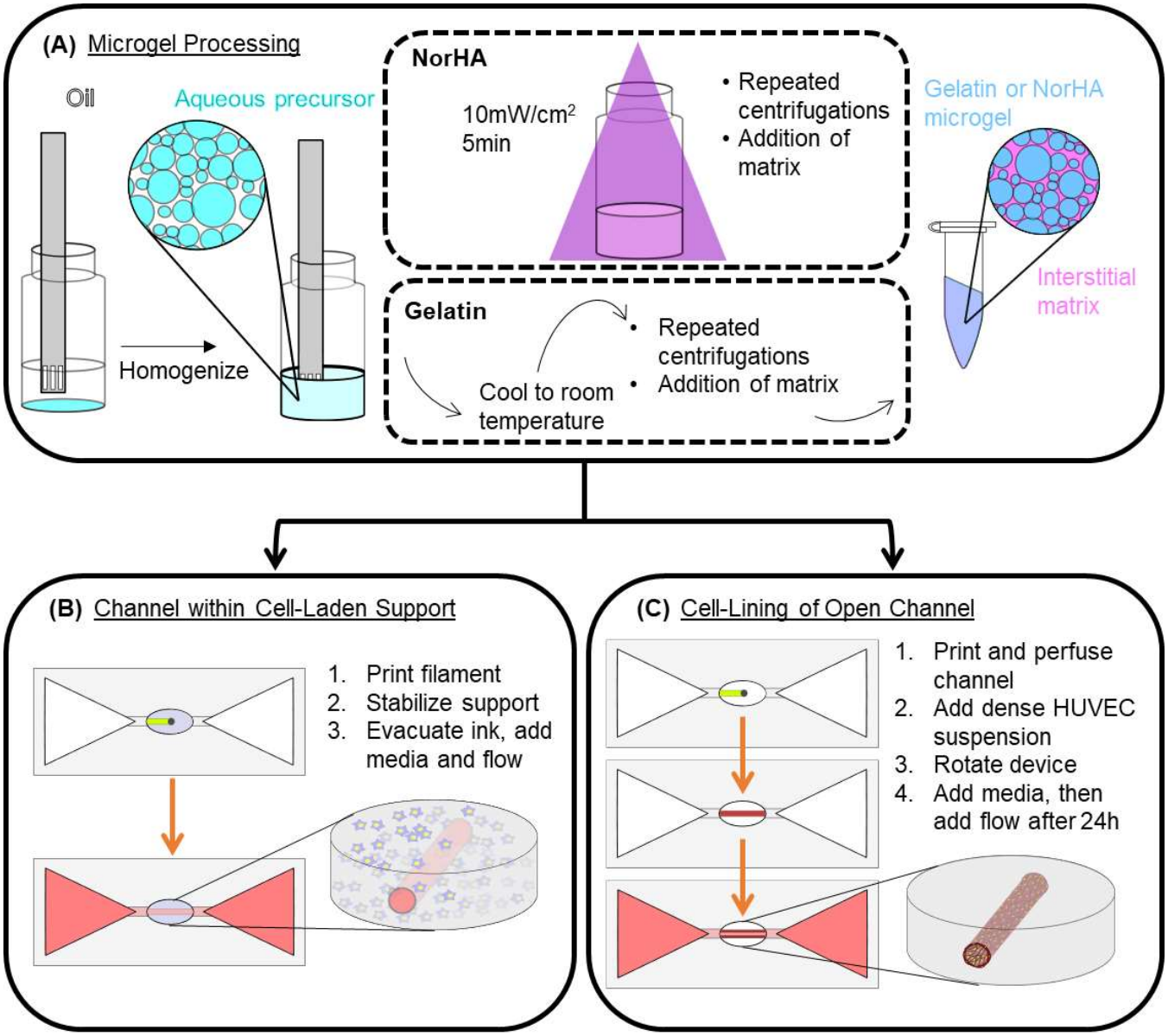

Figure 1: Schematics of the (A) NorHA and gelatin microgel processing, (B) the experimental process for creating a perfusable channel within a fibroblast-laden NorHA support, and (C) the experimental processing to creating a HUVEC-lined open channel

Lining of an open channel with human umbilical vein endothelial cells

Human umbilical vein endothelial cells (HUVECs) were cultured with the EGM-2 Bulletkit (Lonza). HUVECs were harvested at passage 5 using 0.025% trypsin in EDTA, followed by centrifugation at 200xg for 5 minutes and counted using a 1:5 dilution with trypan blue.

To line an open channel, a perfusable channel was printed into an acellular NorHA-4 support as described earlier. The interstitial 1% NorHA was prepared with thiolated RGD (GCGYCRGDSPG,

GenScript) at a final concentration of 8mg/mL. The gelatin microgel ink used for this printing was prepared using a modified procedure with a lower interstitial HA content or approximately 0.5%. After ink evacuation, HUVECs were harvested and resuspended to 30 million cells/mL. Following a previously published protocol[27], 5-10μL of the cell suspension was added to the channels, then the devices were placed in the incubator and were flipped every 30 minutes for 4 hours. This process can be seen in Fig. 1C. Media was then carefully added to the reservoirs. After approximately 24h, flow was introduced by placing the devices on an orbital rocker.

Fluorescent imaging was done by staining the HUVECs with CellTracker Deep Red (Invitrogen) on D1 and D3 post-seeding. The channels were washed with DPBS, then a roughly 5μM CellTracker Deep Red stain solution was added to each sample and the devices were incubated for 15 minutes at 37°C. This stain solution was then removed and replaced with DPBS. Channels were imaged on a widefield microscope (DMI 8, Leica) using a 10x objective.

Results and Discussion

Rheological properties can be tuned by adjusting microgel crosslinking density

Particle sizes and size distributions were altered by modifying the crosslinking density of the microgels (Fig. 2A and B). Particles were first tagged with a thiolated Rho-B peptide then imaged on an inverted widefield microscope, as described in the methods section. All particles were polydisperse, as expected given the selected processing method. Interestingly, with the increase in crosslinking density from 8mM to 4mM, the particle size distribution broadened (Fig. 2B and Table 1). With this also came an increase in average particle diameter (Table 1). Both NorHA-2 and NorHA-4 particles had nearly identical particle diameters and size distributions (Fig. 2B and Table 1). Qualitatively, crosslinking density impacted

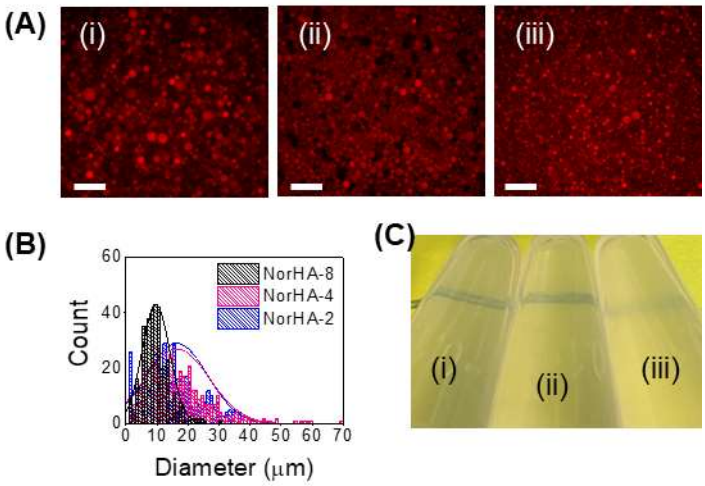

Figure 2: (A) fluorescent images of NorHA particles of different crosslinking densities of (i) 2mM, (ii) 4mM, and (iii) 8mM, where red is the Rho-B peptide (scalebar=100μm); (B) particle size distributions of each NorHA microgel group; (C) images of jammed (i) NorHA-2, (ii) NorHA-4, and (iii) NorHA-8 particles, with a line to distinguish opacities

visual appearance, where the NorHA-8 jammed particles were opaquer compared to the less crosslinked particles (Fig. 2C).

Particles that comprise a jammed system dictate the bulk rheological properties. Thus, rheological experiments were conducted on jammed particles systems comprised of NorHA-2, NorHA-4, and NorHA-8 particles (Fig. 3). Unidirectional shear data show yield stress behavior for all particle systems (Fig. 3A), illustrated by the plateau in stress at low shear rates. This yield stress is dependent on the extent of NorHA crosslinking, with lower crosslinking leading to a linear decrease in yield stress. The Herschel-Bulkley equation was fit for all materials tested, with values located in SI Table 2.

Table 1: Average particle size and CV

Material	Diameter (μm)	CV (%)	n
NorHA-8	9.63 ± 4.50	46.7	393
NorHA-4	16.44 ± 10.47	63.7	466
NorHA-2	16.45 ± 9.81	59.6	427
Gelatin Ink	4.60 ± 3.77	82.0	520

The NorHA systems exhibited typical jammed microgel systems shown in the frequency sweeps (Fig. 3B). Specifically, the storage moduli for the NorHA-4 and -8 systems are frequency-independent, while the NorHA-2 storage modulus shows a slight dependence on frequency. A clear characteristic minimum is present in the loss modulus, decreasing with decreasing crosslinking density of the particles.

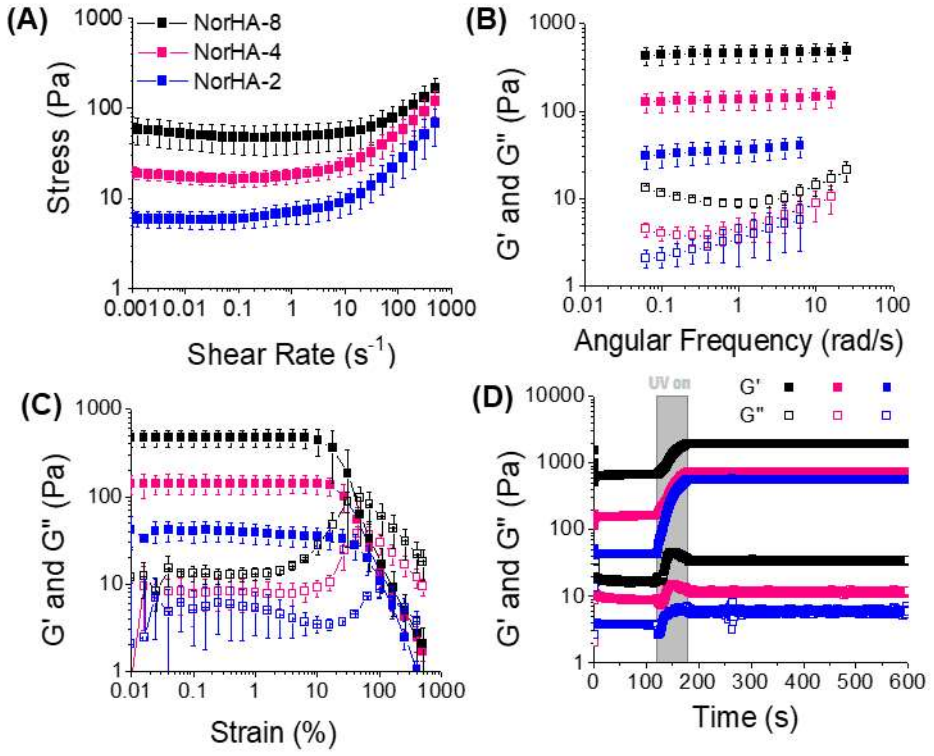

Figure 3: Rheological characterizations of jammed NorHA-2, -4, and -8 supports, with (A) flow sweeps, (B) frequency sweeps, (C) strain sweeps, and (D) UV curing tests conducted. Error bars represent standard deviation

Strain sweeps show that the storage moduli for all the NorHA systems are strain-independent at low strains (Fig. 3C). Then the material begins to yield and eventually crossover with the corresponding loss moduli. The onset of the storage modulus yield

depends on the crosslinking density of the particles. As the particle crosslinking increases, the onset of yielding increases. The G'-G" crossover follows this trend as well.

Stiffness of the crosslinked microgel systems were expectedly dependent on crosslinking density of the microgels (Fig. 3D) since bulk properties are dependent on the microgel properties. All microgel systems were measured on a quartz plate and exposed to UV light for 60s at an intensity of 10mW/cm^2. Degradable crosslinker concentrations remained the same for all samples. Final modulus values ranged from approximately 450Pa for the NorHA-2 system to roughly 1700Pa for the NorHA-8 system. The crosslinked gels were significantly higher in modulus compared to their non-crosslinked counterparts (SI Fig. 2).

Particle size analysis and melting characteristics of the gelatin ink formulation were also assessed. The gelatin microgels had an average diameter of 4.6 ± 3.77 μm with a CV of 82% (Fig. 4A and 4B, and table 1), indicating high polydispersity. The gelatin ink is shear-thinning and was easily extruded through a 25G blunt needle (4C). Similar to the NorHA microgel systems, the gelatin ink has a yield stress (SI Fig. 3), as well as frequency-dependent loss moduli with a characteristic minimum (Fig. 4D) and yielding at an oscillatory strain of 24.55% with a maximum present in the loss modulus at the G'-G" crossover in the strain sweeps (Fig. 4E and Table 3). At room temperature, this ink can hold a shape as a thick droplet, but upon heating to 40^{o}C, this droplet collapses due to gelatin particles melting (Fig. 4F).

The rheological behaviors of all tested materials are in line with other microgel-based materials[25,28]. In the unidirectional shear-testing, the tested materials have a yield stress that correlates to particle crosslinking density. The materials were predictably shear-thinning, in line with previous work on microgel rheological behavior[11]. This shear-thinning behavior is expected because as the applied stress reaches the yield stress of the material, the particles can freely rearrange and thus fluidize the bulk system.

The frequency sweeps showed relatively frequency-independent storage moduli values for all materials, and decreased with decreasing crosslinking density as expected since the particles are expected to be softer. There is a characteristic minimum found in the loss modulus curve for all tested materials. This is another key rheological signature in jammed particle systems, where at low frequencies, is due to particle rearrangements, and at high frequencies, a result of dissipation of the solvent[25]. The frequency at which this minimum occurs appears to correlate to particle crosslinking density where the lower the crosslinking density, the lower the frequency at which this minimum occurs. Since polymer crosslinking density affects viscoelastic properties, this change in frequency could be attributed to an increase in dissipative behavior of the particles, thus leading to a lower frequency when

this behavior dominates. Scaling factors correlating G" with frequency were calculated for each crosslinking density. The NorHA-4 and -8 supports had scaling factors of 0.33 and 0.34, respectively, while the NorHA-2 supports had a scaling factor of 0.27. Within a jammed microparticle system, two events can occur: 1) the particle deform due to stress, and 2) slip planes form. The scaling factor, if slip dominates, would be a scaling factor of 0.5[29]. The factors calculated here are lower and may then indicate that both slip and particle deformations are occurring in the system as frequency increases, especially in the case of the NorHA-2 supports where particles are predicted to be softer. This data also indicates that the presence of the interstitial 1% NorHA, at least at this concentration, does not appear to affect key signature rheological properties of the jammed NorHA microgel supports.

Strain sweeps likewise show typical jammed microgel behavior. At low frequencies, the storage moduli values remain strain-independent and are solid-like, indicated by the higher G' compared to G". This is followed by yielding and then the G'-G" crossover with a characteristic peak in the loss modulus at this strain. Interestingly, there is a dip in the loss modulus during yielding but before the modulus crossover for the NorHA-2 material. From a previous study[30], there is an overshoot in the low strain regime that appears to become larger as particle crosslinking density decreases. The previous study states that this could be due to contact breaking between particles, but not at a sufficient level to induce flow. This has

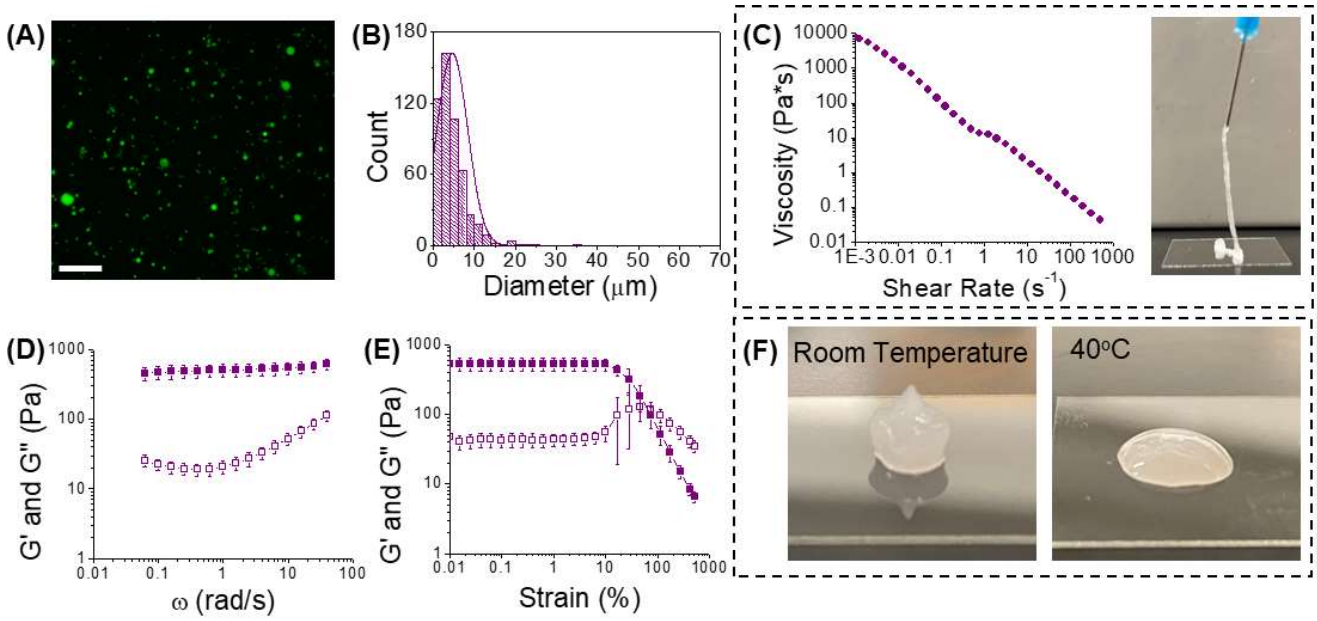

Figure 4: Characterization of gelatin microgels, with (A) fluorescent images of gelatin/FITC-dextran microgels taken (scalebar=100μm) and (B) the particle size distribution measured; rheological characterizations show (C) shear-thinning behavior, also shown by the ink flowing through a 25G needle, (D) frequency sweeps and (E) strain sweeps were conducted as well; qualitatively, (F) the ink can hold a thick droplet shape at room temperature, but upon heating to 40°C, the ink melts. Error bars denote standard deviation.

been seen in another previous study[31] where this weak overshoot at low strains also appears to be dependent on particle properties.

As the particle becomes softer, the particles become increasingly deformable as packing fraction increases. This means that the particles can create more facets with neighboring particles, which in turn increases friction between the particles and would lead to an increase in the G'-G" crossover. This has occurred in previous studies[31,32]. These results differ from the yield stress data potentially due to testing differences, where the material in the unidirectional shear test was subjected to high shear rate followed by low shear rate. In the oscillatory strain test, oscillatory strain was ramped from low to high strain, and in combination with particle softness and presence of oscillations, could lead to a higher onset and crossover with a lower crosslinking density.

UV curing of the supports show an obvious and expected increase in G' of all materials, an increase of roughly 3X-4X. The crosslinked values ranged from roughly 500 Pa for NorHA-2 to 1800Pa for NorHA-8. This is in line with the expectation that particle stiffness contributes to bulk stiffness. The range of values obtained here also show that the support is tunable. When using the following equation and an assumption of a poisson's ratio (v) of 0.5:

$$E = 2G(1+v)$$

Where E is Young's modulus, and G is shear modulus. The values obtained for the crosslinked supports here are within ranges for soft tissues like brain, lung, small intestine, and liver[33,34].

The rheological properties of gelatin ink are similar to those of the NorHA materials, as expected. The particles are small and polydisperse, with an average diameter of 4.60 ± 3.77μm. A smaller diameter was used as particle diameters would ultimately affect the final channel diameter. The ink is shear-thinning, and therefore extrudable through a needle. There is a characteristic minimum in the loss modulus of the frequency sweep, and a characteristic peak in the loss modulus in the strain sweep at the G'-G" crossover. Again, the presence of interstitial HA does not appear to affect key signatures in the rheological properties, at least in the dilute concentration regime.

Perfusable channels and complex architectures can be printed

Since 3D printing allows for easy alterations to feature sizes, filaments were printed with varying flow rates to control filament diameter. Gelatin ink with high molecular weight FITC-dextran within the particles was used for imaging purposes. Microscope images were taken directly after printing, then two

days later when the gelatin ink was evacuated at 37°C using PBS in one of the reservoirs to introduce a pressure differential. To print the smallest diameter, a 36G needle had to be used, the other three diameters were printed with a 26G needle. As shown in figure 5A, filaments varying from approximately 100μm to 700μm were successfully printed.

Flow through the channels was visualized using fluorescent microspheres through a roughly 250-300μm diameter channel. Fluorescent microspheres were added to one of the reservoirs to induce flow through the channel, then images were taken over time. As shown in Fig. 5C, while the walls of the channel are irregularly shaped, the microsphere moves in a linear pattern and does not get trapped along the walls of the channel.

A key advantage of perfusable channels is to create diffusive gradients within a material. To test the ability of small molecules and large proteins to diffuse into the surrounding support from a perfused channel, solutions of RhoB and FITC-BSA were added to the reservoirs of the devices and the fluorescence was monitored over time via microscopy. As expected, RhoB diffused quickly into the surrounding NorHA support, reaching distances of approximately 1400μm from the channel edge over a span of 40 minutes (Fig. 5D). On the other hand, FITC-BSA predictably diffused much slower, with the FITC-BSA reaching roughly the same distance over a 24h period (Fig. 5E). The trend in fluorescence here shows a nonlinear diffusion at shorter timescales, that then becomes linear after 24h (Fig. 5E).

Filaments of varying diameters were achieved by varying the flow rates. However, perfusion was limited to filament diameter. The channels that could be perfused, which were produced at the higher flow rates, appear to show a perimeter of fluorescent gelatin microgel ink. This could be due to two things. One, the gelatin particles become embedded within the interstitial 1% NorHA solution. Two, the slightly positively-charged gelatin particles are interacting electrostatically with the negatively-charged interstitial NorHA solution. However, since there is an HA solution between the gelatin particles, which would hinder the electrostatic interactions between the gelatin particles and the interstitial NorHA solution in the support, it is likely that it is case one. The other interesting observation was the decrease in diameter from post-evacuation, where the printed filament was larger compared to the diameter with the embedded ink. This was significant between all groups except the lowest flow rate tested. This has been seen previously, where the perfused channel size decreases post-ink evacuation[35] and could be attributed to the evacuation method used.

The lack of perfusion in the two smaller flow rates tested could be due to the setup used for evacuating the printed ink. Hydrostatic pressure was used to induce flow through the channel as the device and

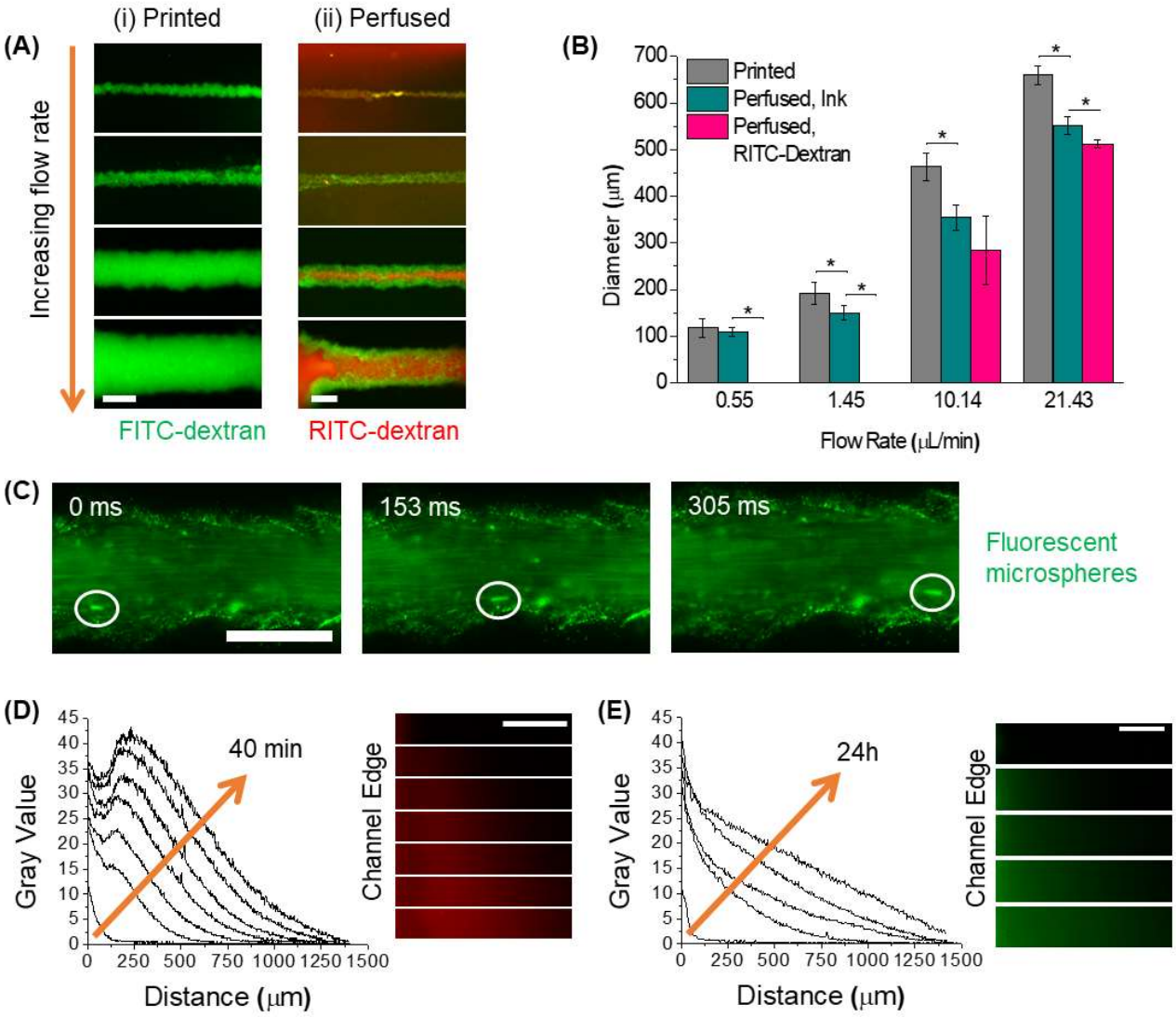

Figure 5: (A) Fluorescent images of (i) printed filaments and (ii) post-thermal treatment to 37°C to melt the ink, with green representing FITC-dextran and red representing RITC-dextran, and a scalebar indicating 400μm, (B) quantification of printed filaments compared to post-thermal treatment of the channel with ink and the perfusable area only (* indicates a significance of $p<0.05$ and error bars denote standard deviation), (C) flow of fluorescent microspheres through a perfused channel, showing laminar flow (scalebar=300μm), (D) diffusion of a Rho-B solution from a channel into the surrounding gel over time (scalebar=300μm), (E) diffusion of a FITC-BSA solution from a channel into the surrounding gel over time (scalebar=300μm).

materials were heated to 37°C. However, as the diameter of the printed filament becomes smaller, a larger pressure to move the gelatin ink out would be required. This could be achieved through pumping PBS or cell media through the channel to produce a higher pressure differential.

A potential use of these perfusable channels includes the establishment of diffusive gradients to control cell behaviors. To test this, diffusion of a small molecule, RhoB, and large protein, FITC-BSA, were added to the device with a printed perfused channel and measured over time (Figs. 5D and 5E). As expected, the small molecule diffused outwards faster compared to the larger protein. The gradient also became increasingly linear as time went on. Careful placement of channels within a tissue construct can aim to alleviate the diffusion limitation typically found in thick tissue constructs. The ability of large and small molecules, despite the perimeters containing gelatin ink, suggests the ability to include chemoattractants and growth factors to influence cell behaviors or processes such as angiogenesis.

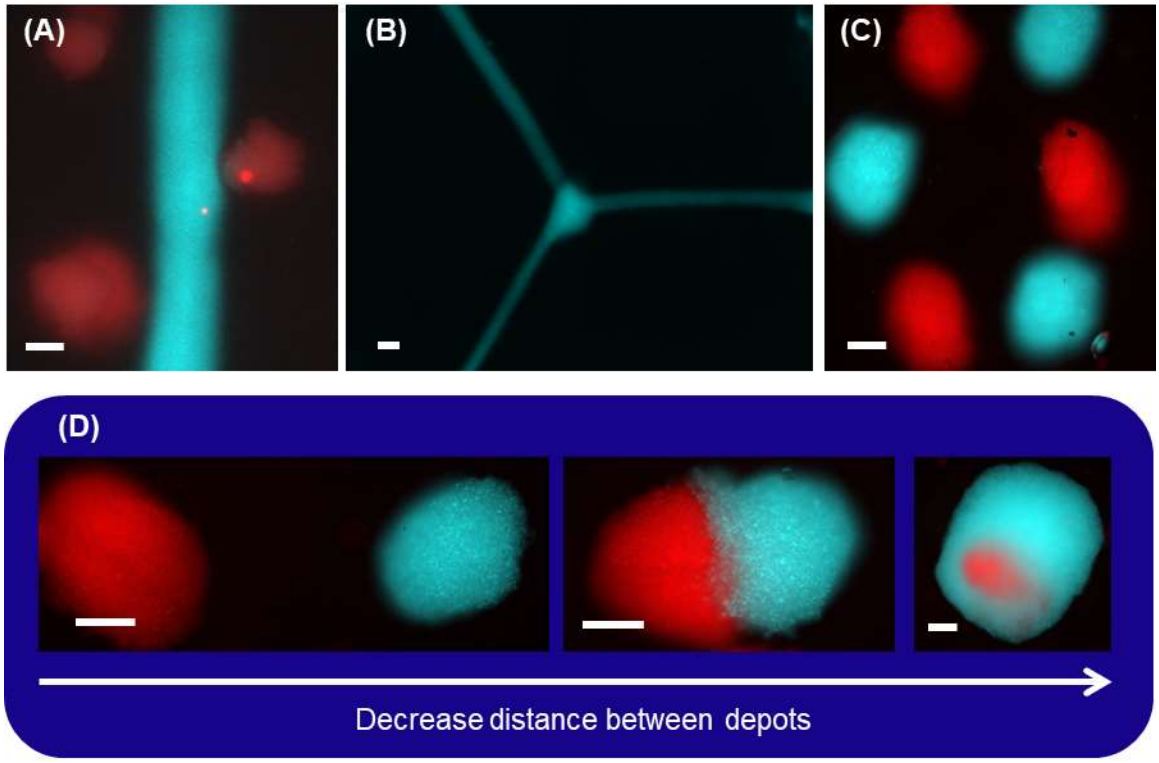

Figure 6: printing of complex features within a jammed NorHA microgel support, with (A) depots surrounding a filament, (B) a branching structure, (C) voxel-esque printing of depots, and (D) two depots printed at varying distances from one another. Scalebars represent 300μm.

To illustrate versatility in our printing system, other features were printed. Tissues naturally have specific architecture within them that enables proper functioning, and the ability to control where cells are located within an engineered construct is beneficial, either directly via 3D printing or indirectly via establishment of a chemotactic gradient. To illustrate this, fluorescent polymers were separately added to the gelatin microgels during particle fabrication, then used to represent two different printing inks. In figure 6A, a filament can be printed surrounded by depots, illustrating the potential for a perfusable channel to defuse nutrients and oxygen into surrounding cell-laden depots. Branching structures that

can mimic more complex vascular structures were also successfully printed, with filaments of roughly 200μm in diameter (Fig. 6B). Voxel-like depots of different fluorescent inks, approximately 300μm in diameter, were extruded in a circle in an alternating fashion (Fig. 6C. Additionally, placement of depots with varying proximities to one another was easily controlled, as shown in Fig. 6D, where there is a spacing of approximately 600 μm between depots, depots right next to each other, and depots printed right next to or within one another.

From Fig. 6, the ability to print multiple types of architectures or features provides a platform for several applications in tissue engineering. For example, branching structures are found in vasculature, and the diameters of the vascular bed as it goes from arteries to capillaries back to veins changes drastically. In this system here, channels of varying diameters were able to be printed, and branching structures could also be printed. Additionally, depots could be printed next to a filament. This is reminiscent of recent studies, where embryoid bodies were formed next to a microfluidic channel[36] or hepatic spheroids being placed between two channels[37]. Various types of cancer have also been shown to ablate nearby vascularized channels[38–40] and this could be recapitulated in the system shown here. Depots of different fluorescing inks could be printed in a voxel-like manner, and with controllable distances. This gives the opportunity to control where cells are located to establish native tissue architecture.

Fibroblasts can be incorporated into the support and perfused

To obtain information on cell growth within these materials given adequate nutrient and oxygen transport, fibroblasts were seeded into thin NorHA-4 microgel support gels and cultured over a nine-day period with proliferation testing every other day. Cells were added as a suspension at a density of 100 million cells/mL in a volumetric ratio based on the approximate volume of the NorHA support. Selected ratios for this experiment, in cells:support, were 1:50, 1:20, and 1:10. All samples show an initial increase in metabolic activity until day 5 (SI Fig. 5), where there is a plateau, followed by another increase in metabolic activity. The fold change values are, expectedly, dependent on cell density. The lowest cell density had a larger increase in fold change, whereas the opposite occurred for the highest cell density group.

Perfusable and non-perfusable thick constructs were compared with regards to cell viability, with the expectation that the perfusable construct would show higher viability compared to the non-perfusable construct. A dense suspension of fibroblasts was added to the support in a 1:10 volumetric ratio. This cell-laden support was then pipetted into a PDMS-based device, and subsequently stabilized via UV crosslinking. On day 1, the viability appears to be roughly equivalent in both perfusable and non-

perfusable samples based on the live/dead imaging (Fig. 7). However, a difference is present on day 4. The cell viability in the non-perfusable sample decreases compared to D1, whereas the perfusable sample has a region of higher cell viability localized to the perimeter of the open channel that extends roughly 50-100μm into the support (Fig. 7A).

When fibroblasts were embedded within the support material at roughly a 100μm thickness, proliferation was observed via alamar blue assay. At the lowest cell density, there was an over 10x increase in proliferative activity within the support. At the highest cell density, proliferation was maintained roughly throughout the testing period, but remained greater than 1 throughout the testing period. This data illustrates how the fibroblasts could maintain their viability or proliferate throughout an extended period of time given adequate nutrient and oxygen diffusion. As such, this indicates that cell death within a thicker construct would be due to oxygen and nutrient-deprivation or the printing process rather than the composition of the support material.

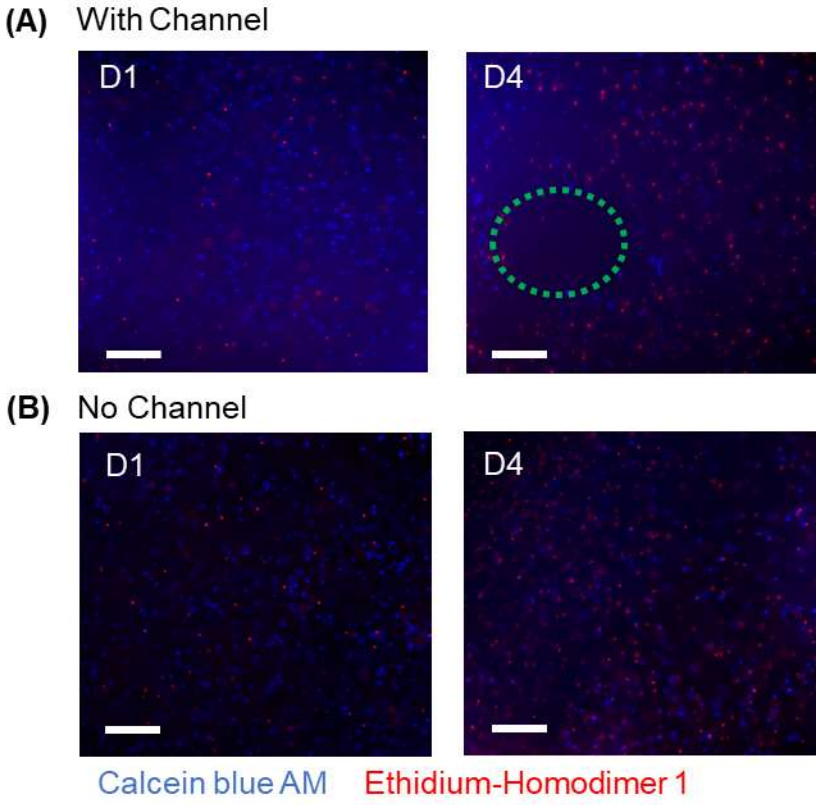

Figure 7: live/dead imaging of cross-sections of fibroblasts within (A) perfusable and (B) non-perfusable NorHA supports. The scalebars are 200μm. The green dotted circle in the right panel of (A) represents the location of the perfusable channel. The area around the perfusable channel shows higher viability compared to any region within the non-perfusable support.

In general, the printing process did not appear to affect cell viability. Both perfused and non-perfused samples had cell death over the 4-day period. However, this cell death was more prominent in the non-perfused constructs. On D1, the cell viabilities were similar within the perfusable and non-perfusable constructs. In a cross-sectional image, there is an area around the perfusable channel on D4 that shows a 50μm depth from the channel edge with high cell viability compared to the rest of the construct and the non-perfused construct (Fig. 7). This indicates that not only are cells receiving nutrients and oxygen, but that the printing process appears to not affect cell viability. This was also seen in another sample looking at the channel in the longitudinal axis. Over a 4-day period, there is an increase in cell death in the perfusable channel, but more cell death is apparent in the non-perfused sample during the

same time period. This therefore suggests that the printing process is cytocompatible and that cell death can be attributed to limited oxygen and nutrient diffusion.

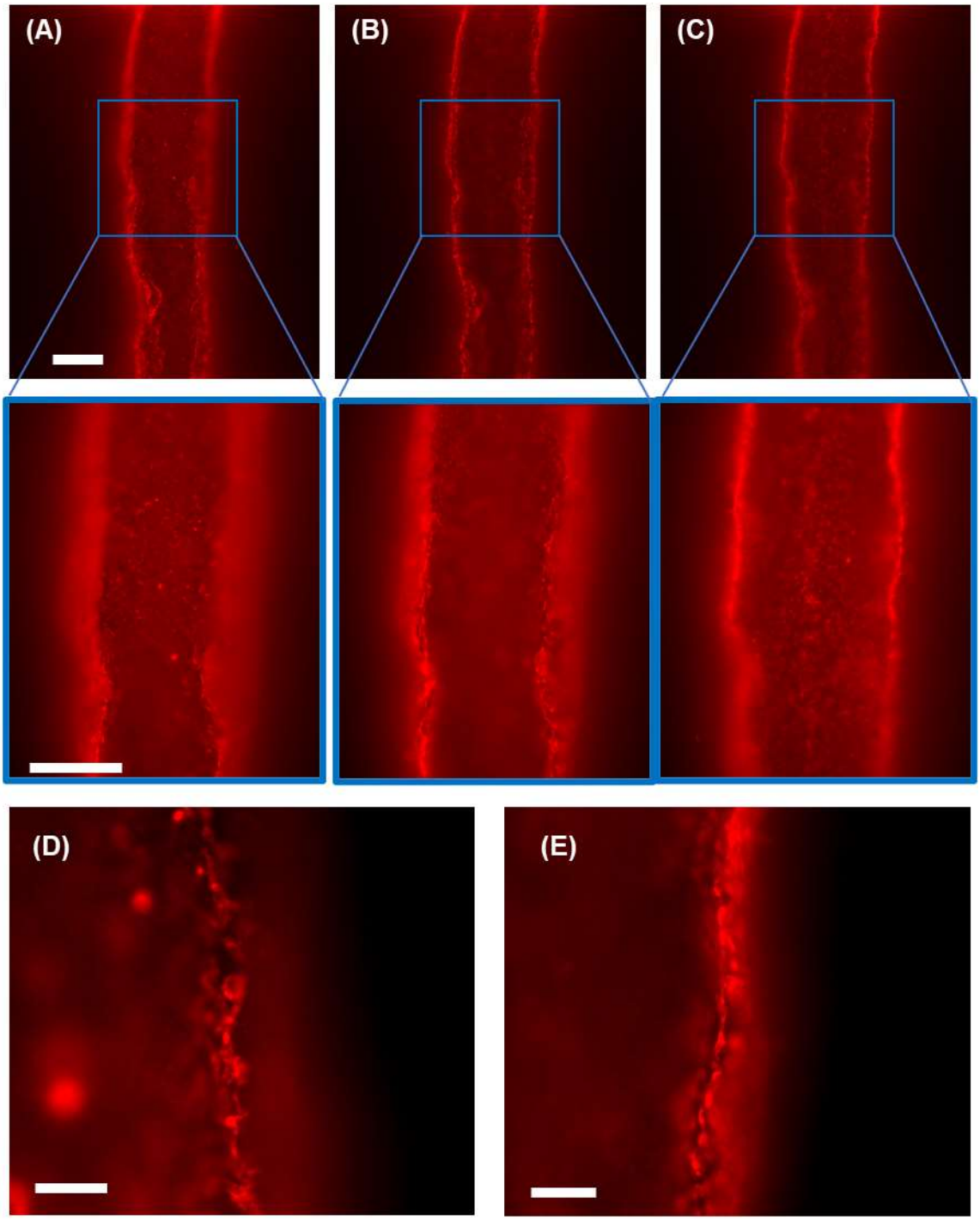

Figure 8: lining of an open channel with HUVECs labelled with CellTracker Deep Red on D3, with coverage seen in the (A) top plane, (B) mid-plane, and (C) bottom plane, with a closeup of the lining along the side of the channel on D1 (D) and D3 (E). Scalebars represent 300μm.

HUVECs can line perfused channels and persist over several days

Since these channels are reminiscent of vasculature found within the human body, HUVECs were added to perfusable channels and imaged. HUVECs were able to line the interior of perfusable channels (Fig. 8 and SI Figs. 8-10). NorHA microgels were treated with thiolated RGD prior to HUVEC addition to facilitate cell attachment. Because vasculature naturally has blood flow, which in turn plays a significant role on vasculature function, flow was introduced to the channels one day after HUVEC seeding. Images were taken on D1 and D3, with D1 being no flow and D3 with flow. Cells are seen in all planes, and this cell coverage persists over the testing period, indicating that there is no cell death and cells can remain adhered to the interior of the perfusable channels in the presence of flow. Additionally, fluorescence qualitatively changes from D1 with no flow to D3 with flow. On D1, fluorescence appears to occur more evenly across the channel, but on D3 looks more confined to the walls of the channel. This may be indicative of a change in morphology over time[27] where cells may be adopting more elongated morphologies.

Conclusions and Future Work

NorHA supports were prepared with varying intra-particle crosslinking. This led to tuning of mechanical properties, such as yield stress. A gelatin microgel-based ink was also formulated and shown to be printable within the NorHA-4 support. When printed as a filament, this ink could be removed upon heating to 37°C, leaving behind a perfusable channel. Filament diameters were tunable, from about 650μm down to roughly 100μm. Interestingly, and potentially a result of processing, channels were not perfusable below a filament diameter of about 400μm. Fibroblast viability was improved around the vicinity of a perfusable channel, indicating that several channels are needed for large constructs. Lining of a perfusable channel with HUVECs was achieved with the help of RGD, illustrating the potential of these channels to be used to form vasculature within a cell-laden hydrogel. Future work in this project entails testing barrier properties of endothelialized channels and drawing comparisons to bare channels and to values found in the literature. Other key aspects of an endothelial barrier such as VE-Cadherin expression should be measured as well. Additional experiments to examine HUVEC-lined channels under no flow conditions as well as to compare to blank control channels can also be conducted to determine parameters for future vascular channel experiments.

References

1. Celikkin, N. *et al.* In vitro and in vivo assessment of a 3D printable gelatin methacrylate hydrogel for bone regeneration applications. *J. Biomed. Mater. Res. B Appl. Biomater.* **110**, 2133–2145 (2022).
2. Yan, Y. *et al.* Vascularized 3D printed scaffolds for promoting bone regeneration. *Biomaterials* **190–191**, 97–110 (2019).
3. Zhang, M., Qian, T., Deng, Z. & Hang, F. 3D printed double-network alginate hydrogels containing polyphosphate for bioenergetics and bone regeneration. *Int. J. Biol. Macromol.* **188**, 639–648 (2021).
4. Zhang, X. *et al.* 3D printed reduced graphene oxide-GelMA hybrid hydrogel scaffolds for potential neuralized bone regeneration. *J. Mater. Chem. B* **11**, 1288–1301 (2023).
5. Han, H. *et al.* A Bioprinted Tubular Intestine Model Using a Colon-Specific Extracellular Matrix Bioink. *Adv. Healthc. Mater.* **11**, 2101768 (2022).
6. Kim, W. & Kim, G. H. An intestinal model with a finger-like villus structure fabricated using a bioprinting process and collagen/SIS-based cell-laden bioink. *Theranostics* **10**, 2495–2508 (2020).
7. Kim, W. & Kim, G. Intestinal Villi Model with Blood Capillaries Fabricated Using Collagen-Based Bioink and Dual-Cell-Printing Process. *ACS Appl. Mater. Interfaces* **10**, 41185–41196 (2018).
8. Heichel, D. L., Tumbic, J. A., Boch, M. E., Ma, A. W. K. & Burke, K. A. Silk fibroin reactive inks for 3D printing crypt-like structures. *Biomed. Mater.* **15**, 055037 (2020).
9. Torras, N. *et al.* A bioprinted 3D gut model with crypt-villus structures to mimic the intestinal epithelial-stromal microenvironment. *Biomater. Adv.* **153**, 213534 (2023).
10. Taebnia, N. *et al.* Dual-Material 3D-Printed Intestinal Model Devices with Integrated Villi-like Scaffolds. *ACS Appl. Mater. Interfaces* **13**, 58434–58446 (2021).
11. Bhattacharjee, T. *et al.* Writing in the granular gel medium. *Sci. Adv.* **1**, e1500655 (2015).
12. Hinton, T. J. *et al.* Three-dimensional printing of complex biological structures by freeform reversible embedding of suspended hydrogels. *Sci. Adv.* **1**, e1500758 (2015).
13. Wu, W., DeConinck, A. & Lewis, J. A. Omnidirectional Printing of 3D Microvascular Networks. *Adv. Mater.* **23**, H178–H183 (2011).

14. Song, K. H., Highley, C. B., Rouff, A. & Burdick, J. A. Complex 3D-Printed Microchannels within Cell-Degradable Hydrogels. *Adv. Funct. Mater.* **28**, 1801331 (2018).

15. Kajtez, J. *et al.* Embedded 3D Printing in Self-Healing Annealable Composites for Precise Patterning of Functionally Mature Human Neural Constructs. *Adv. Sci.* **9**, 2201392 (2022).

16. Bhattacharjee, T. *et al.* Liquid-like Solids Support Cells in 3D. *ACS Biomater. Sci. Eng.* **2**, 1787–1795 (2016).

17. de Gennes, P. G. Granular matter: a tentative view. *Rev. Mod. Phys.* **71**, S374–S382 (1999).

18. Liu, A. J. & Nagel, S. R. Jamming is not just cool any more. *Nature* **396**, 21–22 (1998).

19. Highley, C. B., Song, K. H., Daly, A. C. & Burdick, J. A. Jammed Microgel Inks for 3D Printing Applications. *Adv. Sci.* **6**, 1801076 (2019).

20. Griffin, D. R., Weaver, W. M., Scumpia, P., Di Carlo, D. & Segura, T. Accelerated wound healing by injectable microporous gel scaffolds assembled from annealed building blocks. *Nat. Mater.* **14**, 737–744 (2015).

21. Compaan, A. M., Song, K., Chai, W. & Huang, Y. Cross-Linkable Microgel Composite Matrix Bath for Embedded Bioprinting of Perfusable Tissue Constructs and Sculpting of Solid Objects. *ACS Appl. Mater. Interfaces* **12**, 7855–7868 (2020).

22. Skylar-Scott, M. A. *et al.* Biomanufacturing of organ-specific tissues with high cellular density and embedded vascular channels. *Sci. Adv.* **5**, eaaw2459 (2019).

23. Gramlich, W. M., Kim, I. L. & Burdick, J. A. Synthesis and orthogonal photopatterning of hyaluronic acid hydrogels with thiol-norbornene chemistry. *Biomaterials* **34**, 9803–9811 (2013).

24. Wu, J. *et al.* Inkjet-printed microelectrodes on PDMS as biosensors for functionalized microfluidic systems. *Lab. Chip* **15**, 690–695 (2015).

25. Menut, P., Seiffert, S., Sprakel, J. & Weitz, D. A. Does size matter? Elasticity of compressed suspensions of colloidal- and granular-scale microgels. *Soft Matter* **8**, 156–164 (2011).

26. Reid, J. A. *et al.* Accessible bioprinting: adaptation of a low-cost 3D-printer for precise cell placement and stem cell differentiation. *Biofabrication* **8**, 025017 (2016).

27. Kinstlinger, I. S. *et al.* Perfusion and endothelialization of engineered tissues with patterned vascular networks. *Nat. Protoc.* **16**, 3089–3113 (2021).

28. O'Bryan, C. S., Kabb, C. P., Sumerlin, B. S. & Angelini, T. E. Jammed Polyelectrolyte Microgels for 3D Cell Culture Applications: Rheological Behavior with Added Salts. *ACS Appl. Bio Mater.* (2019) doi:10.1021/acsabm.8b00784.

29. Liu, A. J., Ramaswamy, S., Mason, T. G., Gang, H. & Weitz, D. A. Anomalous Viscous Loss in Emulsions. *Phys. Rev. Lett.* **76**, 3017–3020 (1996).

30. Sridharan, S., Meinders, M. B. J., Sagis, L. M., Bitter, J. H. & Nikiforidis, C. V. Jammed Emulsions with Adhesive Pea Protein Particles for Elastoplastic Edible 3D Printed Materials. *Adv. Funct. Mater.* **31**, 2101749 (2021).

31. Hirsch, M., Charlet, A. & Amstad, E. 3D Printing of Strong and Tough Double Network Granular Hydrogels. *Adv. Funct. Mater.* **31**, 2005929 (2021).

32. Emiroglu, D. B. *et al.* Building block properties govern granular hydrogel mechanics through contact deformations. *Sci. Adv.* **8**, eadd8570 (2022).

33. Chaudhuri, O. *et al.* Hydrogels with tunable stress relaxation regulate stem cell fate and activity. *Nat. Mater.* **15**, 326–334 (2016).

34. Lou, L., Paolino, L. & Agarwal, A. Bridging the Gap in Ashby's Map for Soft Material Properties for Tissue Engineering. *ACS Appl. Mater. Interfaces* **15**, 24197–24208 (2023).

35. Seymour, A. J., Shin, S. & Heilshorn, S. C. 3D Printing of Microgel Scaffolds with Tunable Void Fraction to Promote Cell Infiltration. *Adv. Healthc. Mater.* **10**, 2100644 (2021).

36. Clark, A. T. Human embryo implantation modelled in microfluidic channels. *Nature* **573**, 350–351 (2019).

37. Bonanini, F. *et al.* In vitro grafting of hepatic spheroids and organoids on a microfluidic vascular bed. *Angiogenesis* **25**, 455–470 (2022).

38. Watkins, S. *et al.* Disruption of astrocyte–vascular coupling and the blood–brain barrier by invading glioma cells. *Nat. Commun.* **5**, 4196 (2014).

39. Silvestri, V. L. *et al.* A Tissue-Engineered 3D Microvessel Model Reveals the Dynamics of Mosaic Vessel Formation in Breast Cancer. *Cancer Res.* **80**, 4288–4301 (2020).

40. Nguyen, D.-H. T. *et al.* A biomimetic pancreatic cancer on-chip reveals endothelial ablation via ALK7 signaling. *Sci. Adv.* **5**, eaav6789 (2019).

Supplemental Information

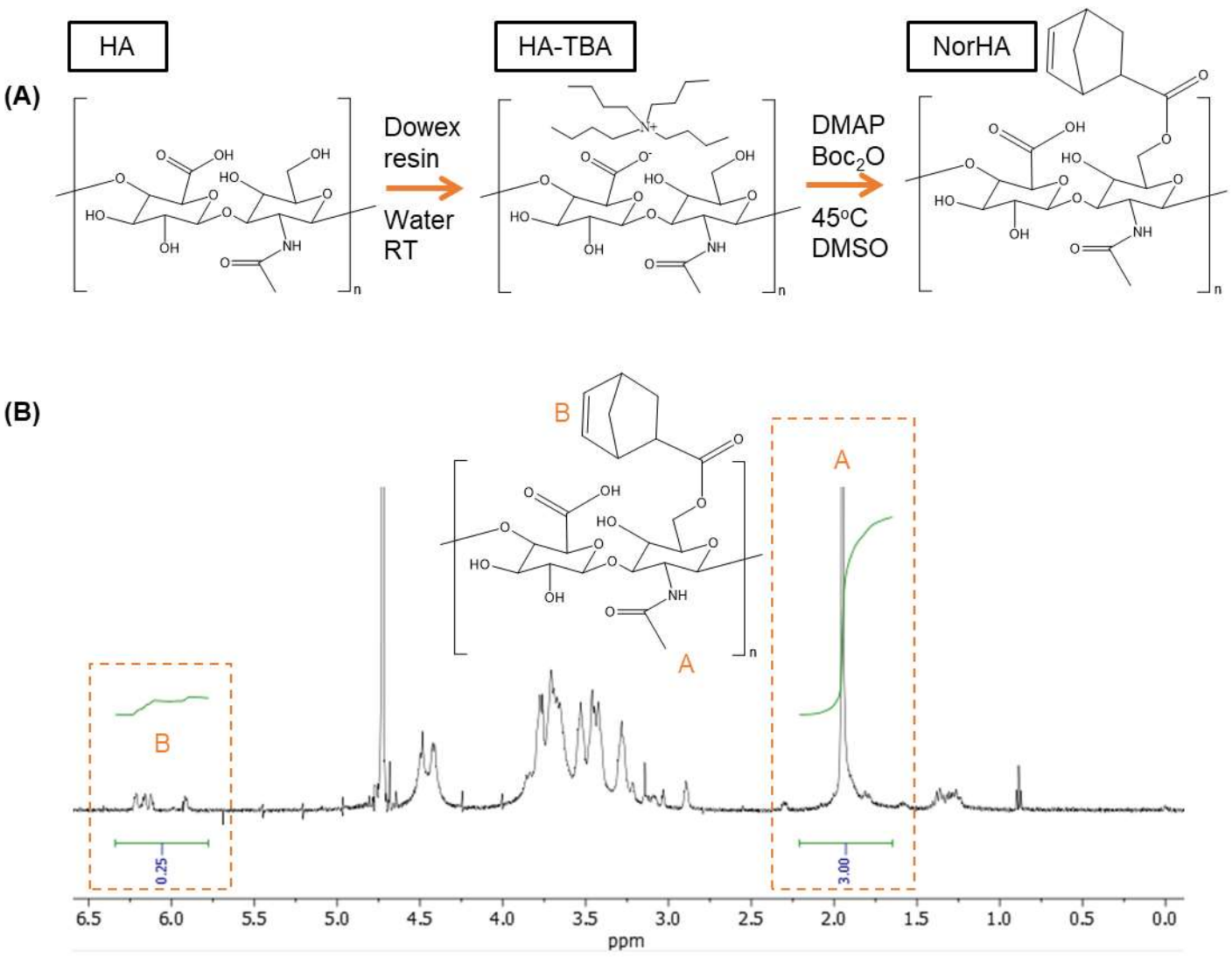

SI Fig. 1: (A) synthesis of NorHA using a multistep process, and (B) an example of NMR spectrum for NorHA, showing roughly 12.5% modification

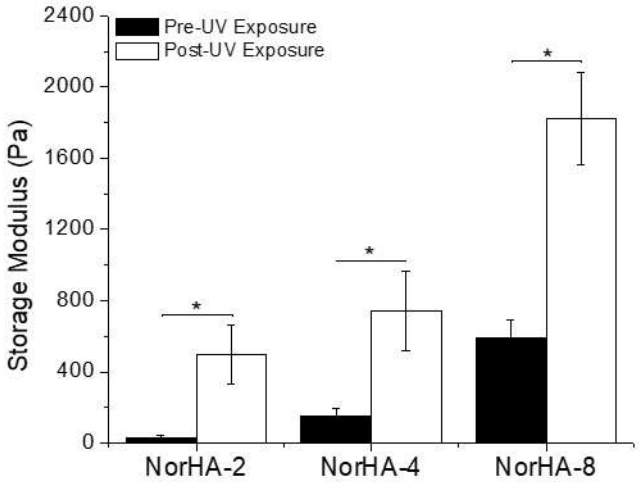

SI Fig. 2: Average storage modulus before and after crosslinking of NorHA-2, -4, and -8 microgels with interstitial NorHA. As expected, the storage modulus is significantly different post-crosslinking, and is dependent on crosslinking density of the particles themselves.

SI Table 2: Herschel-Bulkley parameters

Material	Yield Stress (Pa)	K	n
NorHA-8	50.40 ± 17.47	0.90 ± 0.57	0.81 ± 0.10
NorHA-4	16.97 ± 2.71	1.52 ± 0.72	0.69 ± 0.03
NorHA-2	5.97 ± 1.32	0.63 ± 0.30	0.74 ± 0.03
Gelatin Ink	72.73 ± 11.44	11.83 ± 8.95	0.56 ± 0.11

SI Table 3: Strain sweep onset and G'-G" crossover

Material	Onset (%)	G'-G" Crossover (%)
NorHA-8	18.94 ± 7.27	37.96 ± 12.13
NorHA-4	26.80 ± 1.61	54.27 ± 5.83
NorHA-2	51.96 ± 20.73	124.16 ± 11.37
Gelatin Ink	24.55 ± 10.76	62.53 ± 30.23

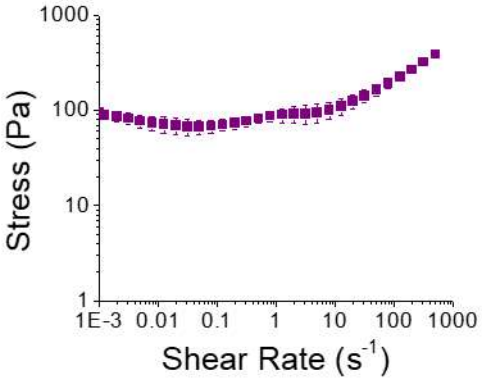

SI Fig. 3: Yield stress testing of gelatin microgel-based ink

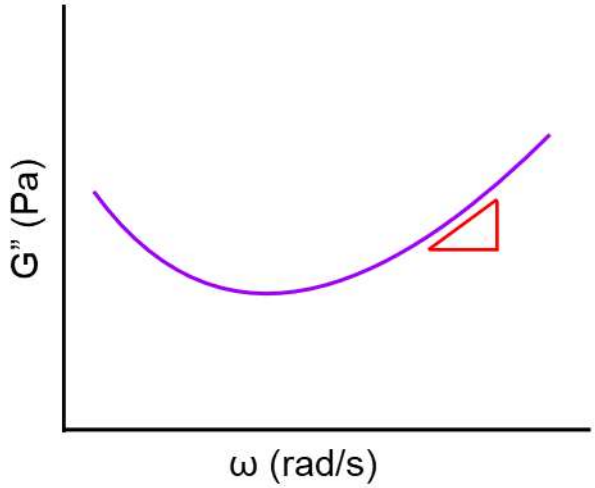

Sample	Slope
NorHA-2	0.27 +/- 0.07
NorHA-4	0.34 +/- 0.04
NorHA-8	0.33 +/- 0.08

SI Fig. 4: Schematic illustrating region in which slope of high frequency regime was calculated

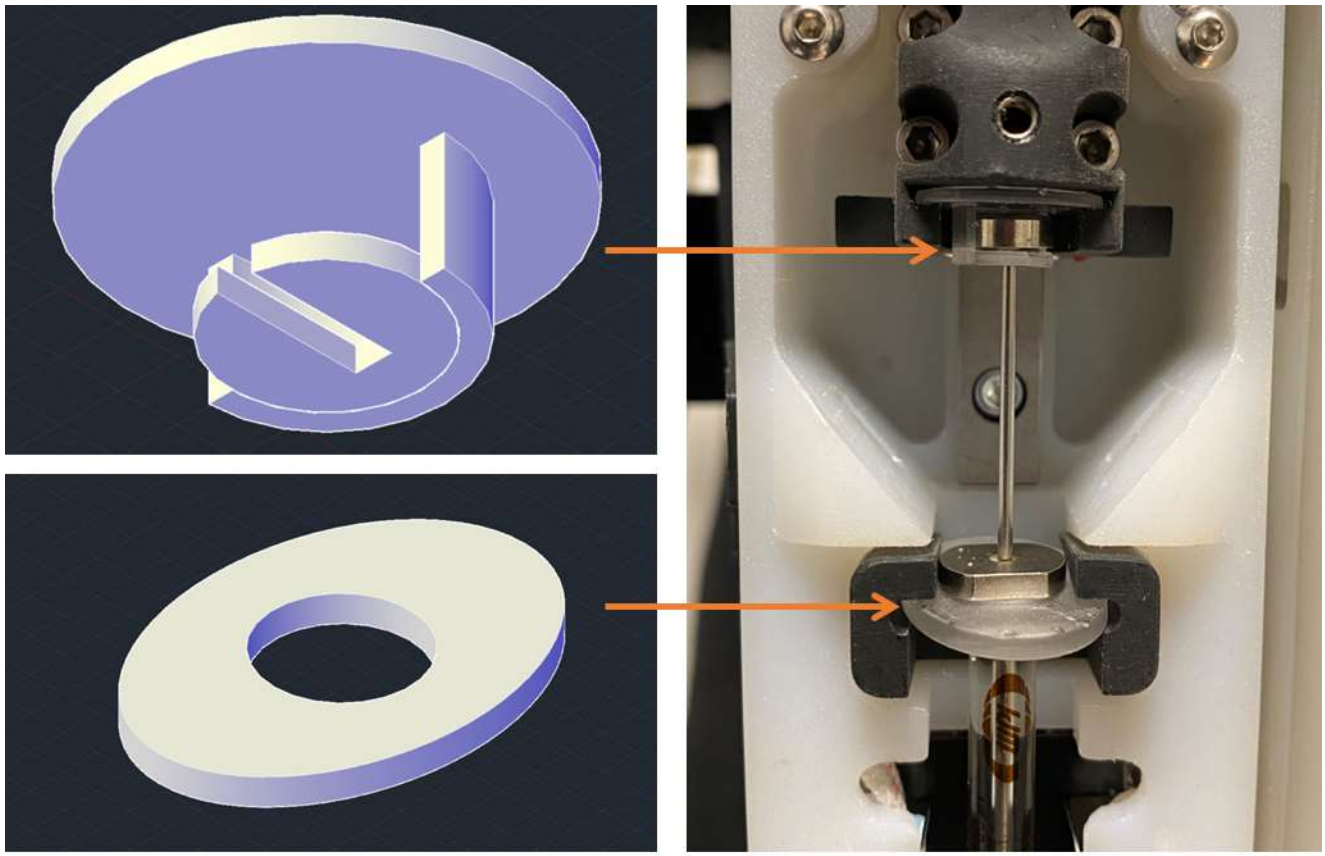

SI Fig. 5: AutoCAD design and photo of custom-designed clips enabling use of a 100uL Nanofil syringe to be used in a Felix Bioprinter

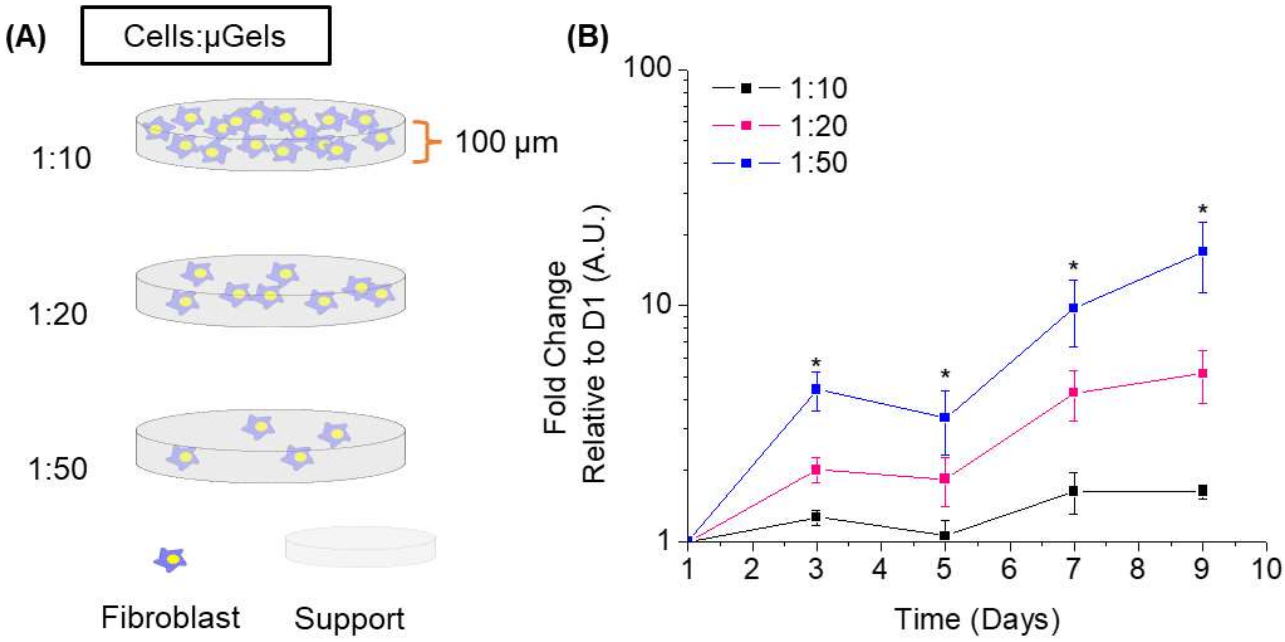

SI Fig. 6: (A) fibroblast proliferation experiment setup with varying cell densities within NorHA-4 supports, and (B) alamar blue assay results over a 9-day time period showing either maintenance of cell viability or proliferation of fibroblasts within the NorHA-4 supports.

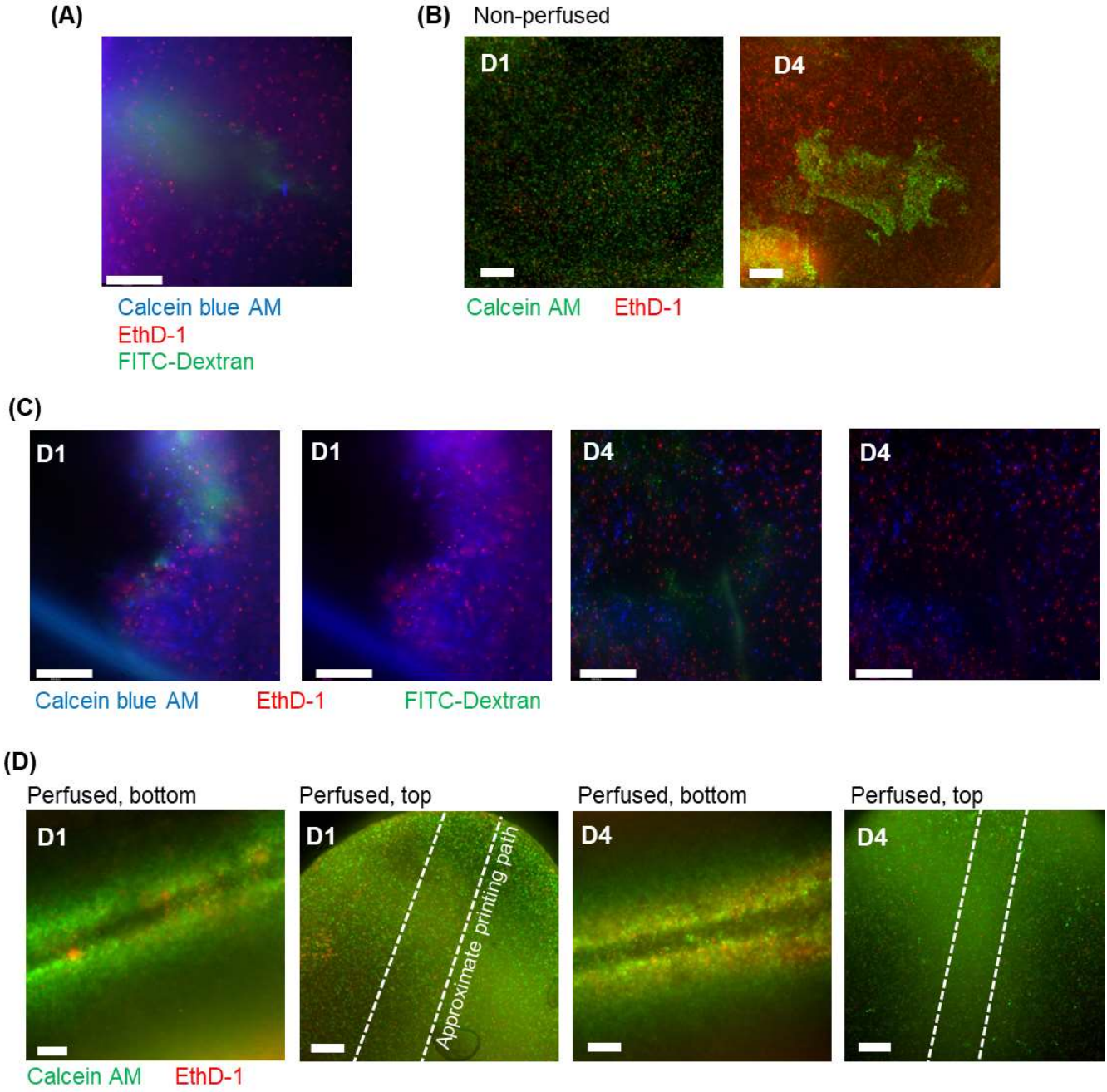

SI Fig. 7: (A) Image from Fig. 7 but with a FITC channel to show that the region highlighted is a channel, (B) another non-perfused sample illustrating low viability from D1 to D4 as expected, (C) Channel cross-section on different samples on D1 and D4, (D) longitudinal plane of channel on D1 and D4 on top and bottom of support, white lines indicate approximate printing path. Scalebars for all images are 300μm.

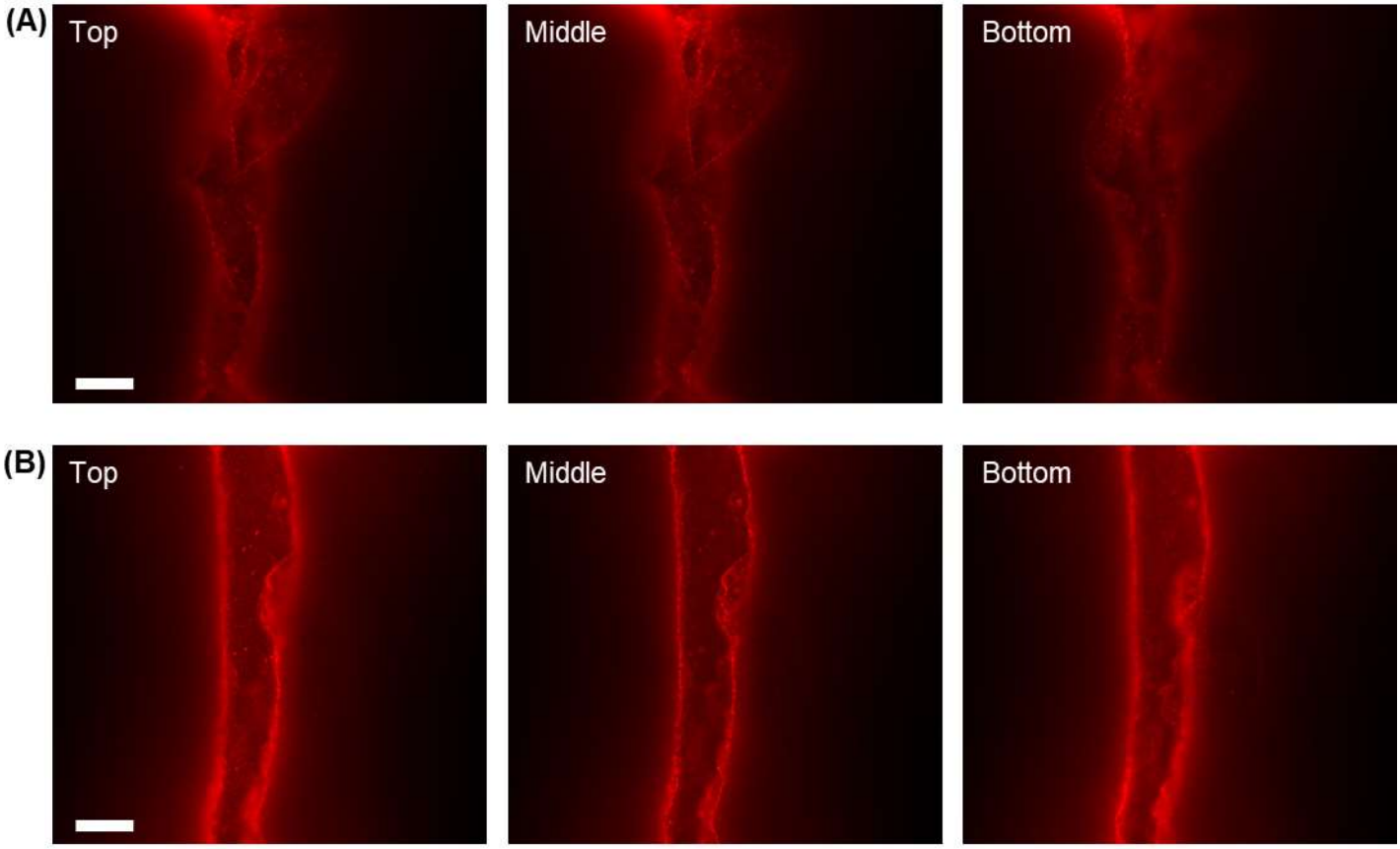

SI Fig. 8: Images from two other HUVEC-lined channels along the top, mid, and bottom planes. Scalebar=300μm

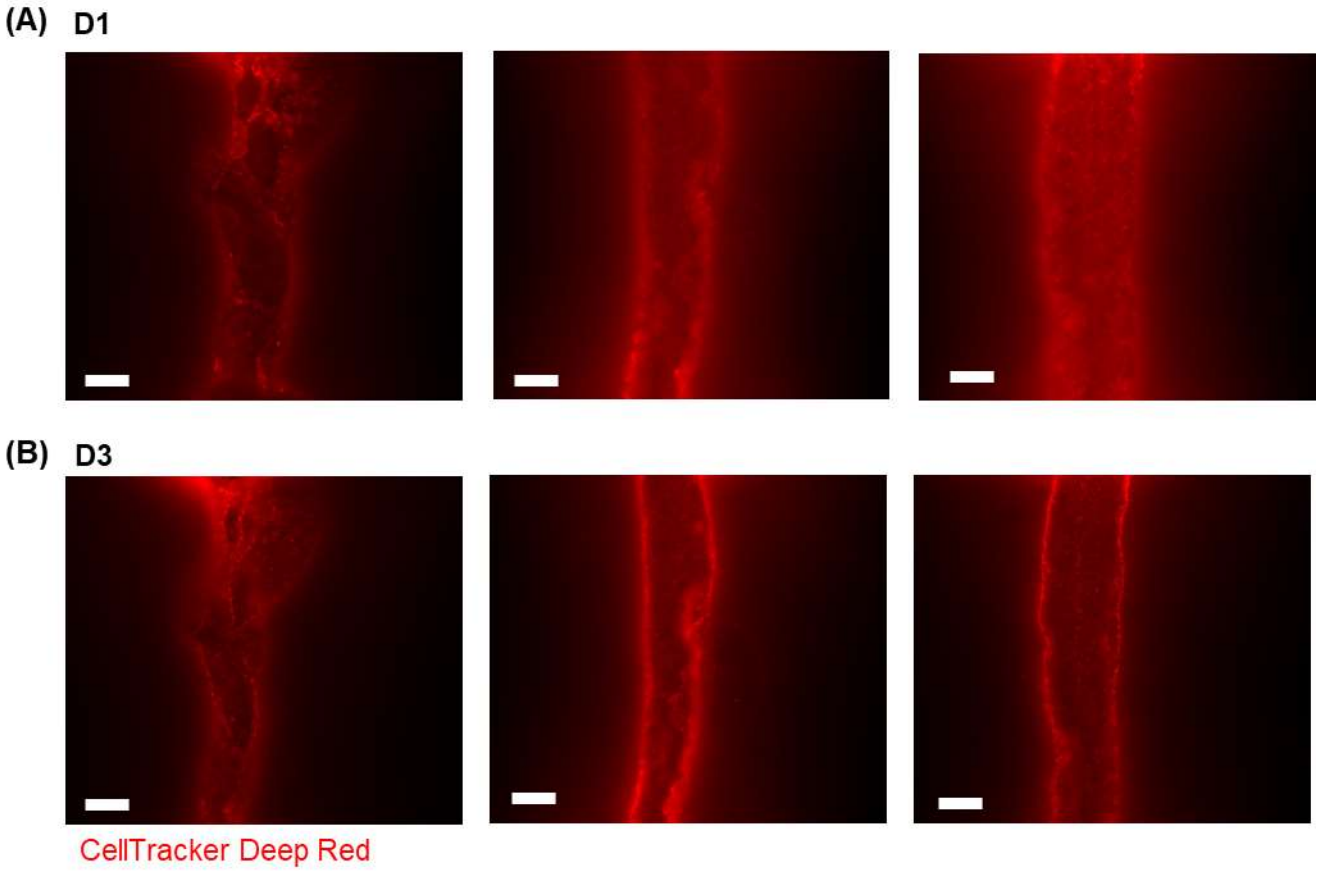

SI Fig. 9: (A) Images of three separately printed channels lined with HUVECs on D1 post-seeding, and (B) same channels imaged on D3 post-seeding. Scalebars=300μm

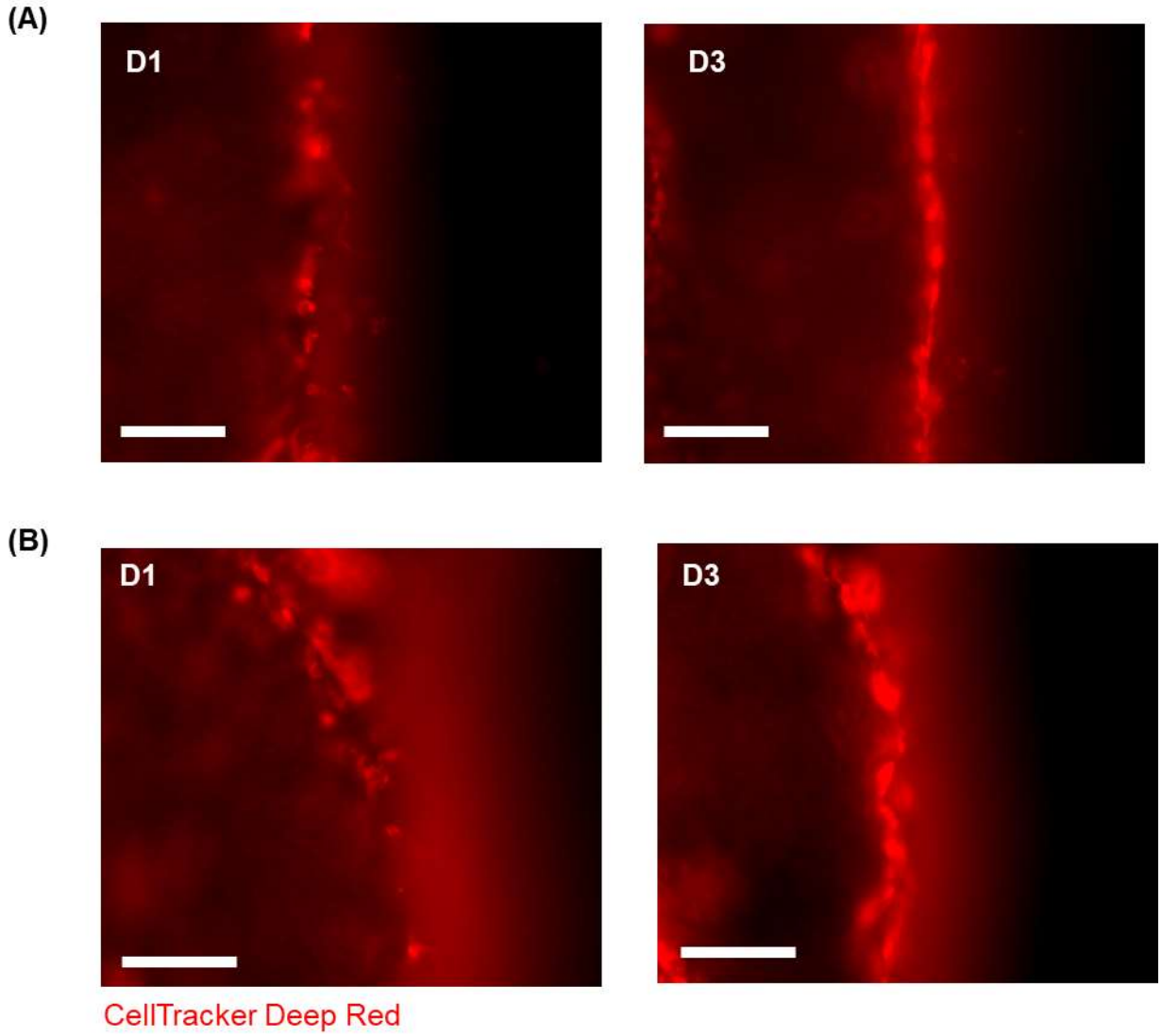

SI Fig. 10: (A) closeup of a HUVEC-lined channel edge on a separately printed sample on D1 and D3, showing possible proliferation and flattening of HUVECs, and (B) closeup on a separately printed and HUVEC-lined channels on D1 and D3 post-seeding

Chapter 3:

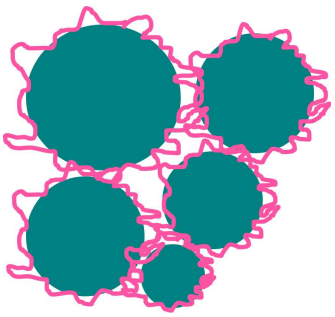

Particle tethering:

weak interactions make ‘strong’ injectable gels

Introduction

Injectable hydrogels have shown great promise in multiple areas in of biomedicine. Some of these areas include 3D printing, where inks must be deposited through nozzles to create intricate structures, and therapeutic deliveries for applications such as wound healing[1,2], cancer stem cell targeting[3], or rheumatoid arthritis treatment[4], to name a few. Two main properties are typically focused on when designing an injectable hydrogel: 1) shear-thinning behavior, and 2) self-healing behavior; and both properties require similar engineering strategies. To extrude through a needle, bonds need to be broken to allow material to flow. Self-healing is the reverse, where the structure of a material becomes disrupted and the engineered network must be designed to recover from the disruption and reform with the original mechanical properties. To achieve these properties, bonds, like hydrazone bonds[5,6], guest-host bonds[7], and electrostatic interactions[6,8,9] have been employed since these bond types are easily broken and quickly reformed upon application and removal of a force, respectively. Shear-thinning behavior can be inherent in some materials, such as hyaluronic acid[10]. Self-healing has also been achieved by designing interpenetrating networks (IPNs)[11,12], semi-IPNs[13], and embedding nanoparticles into the hydrogel, where one of the components of this multifunctional materials can aid in restoring mechanics post-damage[14,15].

Injectable hydrogels, however, require further design and engineering to properly mimic native tissue. Several biopolymers, namely collagen, fibrin, and neurofilaments, strain-stiffen in response to a force[16]. This behavior comes from polymer alignment and exists to prevent tissue damage[16]. To mimic this strain-stiffening behavior, several techniques have been employed, such as modifying charges in a bovine serum albumin-poly(ethylene glycol) based hydrogel[17], boronate-ester bonds in combination with altering polymer concentration[18], and use of hydrophobic interactions in peptide-based gels[19] and crimped and aligned fibrous components[20]. Poroelasticity is another feature that describes water

movement through a porous material. This can be found in tissues like cartilage[21] and the dermis[22] where water movement aids in energy dissipation[21,23], thus helping to protect the tissue. Alterations in poroelastic characteristics can be observed in various pathologies such as fibrosis[24,25]. Poroelasticity is often found in conjunction with viscoelasticity, a property frequently studied in biomaterials systems, known as poroviscoelasticity[26]. Thus, the incorporation of other properties must be considered when designing an injectable material meant to mimic native human tissue.

Granular materials have been extensively studied for a wide variety of applications and have become a promising platform in tissue engineering and biofabrication. In injectable applications, like cell delivery or 3D printing, granular-based materials have been a focus of development and study because due to an inherent solid-liquid transition when a force is applied. Granular systems are comprised of particles rather than a bulk gel, and thus undergo particle rearrangements when subjected to sufficiently high forces[27]. This allows for facile extrusion through small nozzles compared to a bulk network[28], which would require permanent network disruption. Granular materials are also self-healing, re-establishing the solid-like mechanical properties from the pre-extruded state. To maintain a solid-like state when injected into a tissue, a crosslinking mechanism must be established to bond particles together. This has been achieved in materials such as MAP hydrogels, which employ a covalent-crosslinking mechanism[1]. Dynamic bonds such as guest-host bonds[29], hydrazone bonds[30], and electrostatic interactions[9] can be used to modify these interparticle interactions. Granular gels, therefore, can be modified in a number of ways to achieve desired properties and are a good candidate for an injectable hydrogel system.

In this study, we sought to take advantage of electrostatic interactions to alter physical properties of a granular hydrogel system. Hyaluronic acid (HA) was modified to include a norbornene group on the backbone (NorHA) to enable UV-crosslinking to form microgels via batch emulsification. Because HA is anionic, gelatin type A was modified to form a cationic polymer that could adsorb onto the NorHA microgels via electrostatic interactions. The goal of this work was divided into three parts. First, we studied the interactions between the NorHA particles with (+) Gel, and the effects of packing fraction and (+) Gel concentration on these interactions. The addition of (+) Gel produced a granular material with poroelastic-like effects as well as strain-stiffening behavior. Second, we examined a formulation with varying (+) Gel concentrations on the potential use of this material as an injectable system. Here, (+) Gel-containing formulations facilitated filament formation even at low concentrations, and required low extrusion pressures. Third, we assessed the shear-protecting effects of this electrostatic granular system on fibroblasts after extrusion.

Methods

Syntheses

Norbornene-modified hyaluronic acid (NorHA) was prepared as described in chapter 1, using a previously established method[31]. Briefly, HA was dissolved in DI water to achieve a 2wt% solution, followed by addition of an ion exchange resin (Dowex). This reaction was then filtered over a Buchner funnel and the pH adjusted to roughly 7 prior to lyophilization. The synthesized HA-TBA was dissolved in anhydrous dimethylsulfoxide (DMSO) and reacted with 5-norbornene-2-carboxylic acid and 4-(dimethylamino)pyridine (DMAP), catalyzed with di-tert-butyl decarbonate (BOC_2O). The reaction was run overnight. The resulting material was dialyzed against DI water for three days, followed by purification via ethanol precipitation, resuspension in DI water, and further dialysis against DI water for an additional three days. This material was lyophilized and stored at -20°C until needed. The degree of modification was characterized via H^1 NMR in D_2O.

Cationic gelatin ((+) Gel) was prepared using a modified published procedure[32] by reacting gelatin Type A (300 bloom) at 2% in PBS with 1-ethyl-3-(3-dimethylaminopropyl)carbodiimide (EDC HCl, Sigma), N-hydroxyl succinimide (NHS, Sigma), and ethylene diamine (EDA, Sigma) (Fig. 1B). Per gram of gelatin, the weight ratios of reactants were 1:0.6:3.6 of EDC:NHS:EDA. The gelatin was first dissolved in PBS at 37°C, then NHS and EDA were added to the solution at room temperature. The pH was adjusted to 5.5 to 6, after which the EDC was added. The pH was then further adjusted to 4.5 to 5 and allowed to react for approximately 24h at room temperature. The (+) Gel was then dialyzed against DI water for 2-3 days at room temperature. A fluorescamine assay (Sigma) was used to evaluate the change in amine groups using a calibration curve with glycine and compared with unmodified gelatin. The assay protocol was modified from a previously published study[33], where the fluorescamine powder was first dissolved in DMSO at a concentration of 3mg/mL. Gelatin solutions were diluted to roughly 1.25mg/mLin PBS but adjusted depending on fluorescence values. Then, 30µL of assay was added and mixed with 90µL of gelatin solution. The assay and gelatin were allowed to react for 15 min prior to running fluorescence testing.

Granular system preparation

NorHA microgel fabrication

A precursor 3 wt% NorHA solution was prepared in PBS containing 0.313 mg/mL dithiothreitol (DTT, Sigma) and 6.6mM lithium phenyl-2,4,6-trimethylbenzoylphosphinate (LAP, Sigma). This NorHA

solution was homogenized in light mineral oil with 2% Span80 for 2 minutes at 3000rpm, followed by UV curing for 5min at approximately 10mW/cm^2. De-emulsification was started by adding isopropanol to the emulsion post-crosslinking. After stirring, the mixture was filtered over a 0.22μm hydrophilic PVDF membrane. Microgels were washed an additional two times over the filter with isopropanol. After filtering, the microgels were left to dry then added into a 50mL conical and vortexed with 70% ethanol and placed on a rocker for two days. To finish processing, microgels were washed with PBS four times using centrifugation to ensure ethanol removal and equilibration in PBS. Microgels were then filtered over a 40μm cell strainer and stored at 4°C until needed.

Jamming and interstitial material addition

A variable called a jamming fraction was used in this study to control packing density, and is defined here as the ratio of interstitial volume to jammed particle weight. Particles were jammed in pre-weighed eppendorf tubes at 21130xg for 5 minutes. Excess PBS or media was then removed. Particles were centrifuged again if needed to fully remove excess PBS or media. Once particles were packed, the particles were weighed out. Based on this weight, gelatin solutions were added to achieve a 0.3 jamming fraction. To achieve a 0 jamming fraction, the particles were centrifuged again at 21130xg and excess solution was removed. To achieve a 0.5 jamming fraction, additional PBS was added to the particles corresponding to the original weight of the particles.

Zeta potential measurements

All materials were prepared in filtered 0.1X PBS. For the gelatin samples, all samples were prepared at 5mg/mL. NorHA microgels were tested at 3mg/mL due to their size[34]. Zeta potentials were measured using a zetasizer (Zetasizer Ultra, Malvern) and calculated using the Smoluchowski equation. Each sample was run three times with independently-prepared samples.

Confocal imaging of interstitial space, and porosity and pore size measurements

NorHA microgel supports were prepared at different jamming fractions and (+) Gel concentrations. The interstitial gelatin contained high molecular weight FITC-dextran (2MDa) to aid in visualization during image acquisition. Images were acquired using a confocal microscope (Stellaris 5, Leica). Briefly, PDMS (Sylgard 184) holders were created and plasma bonded onto glass-bottom 6-well plates. Light

mineral oil was placed on top of samples to prevent dehydration. Z-stacks were taken with slices set to 2μm for a total depth of 25-40μm. Area fraction was calculated from three independently-prepared samples for each jamming fraction and (+) Gel concentration using FIJI. A 2D slice was thresholded then the measure function was used to obtain area fraction. For each group, three independently-prepared samples were used.

Average pore size and pore size distributions were estimated using a FIJI plug-in, BoneJ. Z-stacks obtained from confocal microscopy were first resliced to obtain isotropic pixels. The resliced stack was then thresholded using Otsu's method[35,36]. The thickness function in BoneJ[37] was used to calculate trabecular thickness, which returns the average pore size within the scaffold. The resulting thickness map that is also calculated from this function was used to obtain pore size distributions (SI Fig. 7). An n of 2-3 independently-prepared samples was used for each group.

Porosity and pore size were measured for samples compressed to 30% and 60%. To achieve these compressions, custom-made plugs with thicknesses of 1mm or 2mm were printed using a PLA printer (Prusa) that would achieve 33% and 67% compressions if the material were placed in a PDMS (Sylgard 184) holder with a depth of 3mm (SI Fig. 8). The materials were set up as described above and compressed before imaging on a confocal microscope (Stellaris 5, Leica). Z-stacks of similar dimensions were obtained and used to quantify area fraction and pore size. Measurements were done in duplicate on independently prepared samples.

As described above, formulations containing 0-3% (+) Gel with high molecular weight FITC-dextran were extruded at flow rates of 11.68mL/h and 1.17mL/h into PDMS holders plasma-bonded to glass-bottom 6-well plates. Light mineral oil was placed on top to prevent dehydration during imaging. Imaging was done to obtain z-stacks that were then used to calculate porosity and pore size using FIJI as described above. Measurements were done in triplicate with three independently-extruded samples.

Rheology

NorHA particles were jammed with 0-3% (+) Gel at different jamming fractions. Samples were prepared right before testing. An 8mm sand-blasted parallel plate was used in combination with a Peltier plate with sandpaper placed onto it to prevent wall slip. Testing was done at 20°C. For each sample, the top geometry was placed carefully onto the material to not compress the material, then the test was started. Strain sweeps were conducted in shear from 0.5% to 500% with a frequency of 0.1Hz. After a strain sweep, the material was compressed to roughly 30%. This was followed by another strain sweep. The

material was then further compressed to roughly 60% of the original sample height, and a final strain sweep was conducted. After each compression, the material was carefully trimmed prior to the start of the next strain sweep. Analysis of the change in storage modulus, critical strain (defined as departure linearity in the strain sweep), yield strain, and modulus crossover changes was carried out.

For self-healing studies, strain sweeps were conducted, oscillating rapidly between 0.5% and 500% every 60s for a total of seven cycles. Frequency was held at 0.1Hz. An 8mm sand-blasted parallel plate geometry was used, and a Peltier plate was used to control testing temperature, held at 20°C. Similar to the experiment setup described above, the top geometry was carefully placed in contact with the sample to avoid any compression of the sample.

Strain-stiffening analysis

Strain-stiffening behavior was quantified using MITLAOS software[38]. Stress and strain data were taken from the original rheology files at the highest point in G' in the strain sweep prior to yielding. To evaluate strain-stiffening behavior, the Chebyshev coefficient, e3, calculated from MITLAOS, was plotted against (+) Gel concentration without compression and as a function of compressed strain for each sample.

Extrusion testing

A syringe holder designed to hold a 1mL syringe was 3D printed using an STL printer (Formlabs) (SI Fig. 11). Microgel formulations were prepared and added into 1mL syringes with air bubbles removed via needle, stored at 4°C and tested the next day. A 100N load cell was used on an Instron machine set up for compression testing. 25G blunt needles were added to the syringes prior to testing. The syringes were compressed at a rate of 0.5mm/s, corresponding to a volumetric flow rate of approximately 27.54 mL/h. Materials were compared to extruded PBS and 30% Pluronic. The change in pressure over extruded volume was calculated and graphed.

Extruded filaments for each ink were examined visually. For each ink, 50µL was extruded at either a high flow rate of 11.68mL/h or a low flow rate of 1.17mL/h. Each extrusion was repeated five times. There was a pause of at least two minutes between extrusions. Videos were acquired using an iPhone 11, and filament lengths were measured using FIJI.

Fibroblast viability pre-and post-extrusion

NIH 3T3 fibroblasts (ATCC) were cultured in high glucose DMEM supplemented with 10% fetal bovine serum (Gibco) and 1% antibiotic/antimycotic (Gibco). Cells were harvested at passage 10 using 0.05% trypsin. For experiments, harvested fibroblasts were treated with CellTracker Green (CMFDA, Invitrogen) according to manufacturer's instructions. Briefly, 50µg of dye was dissolved in sterile DMSO, then added to serum-free medium to a final concentration of 5µM. This was added to the harvested cells and incubated for 30 min at 37°C. The cells were centrifuged afterwards then resuspended in complete media to 50 million cells/mL.

NorHA microgels were prepared aseptically after hydration in 70% EtOH, with other steps described above occurring in a biosafety cabinet. Particles were washed with DPBS followed by equilibration in complete media. (+) Gel solutions were prepared using PBS and were sterilized via UV exposure for 60min.

To prepare formulations with varying (+) Gel concentrations, NorHA microparticles were jammed via centrifugation at 21130xg. Excess media was removed and the corresponding volume of 1% or 3% (+) Gel solution or PBS was added to obtain a jamming fraction of 0.3. The interstitial solutions contained approximately 2µM ethidium homodimer-1 (EthD-1) to stain dead cells. A solution of cells that would correspond to roughly 2 million cells per mL of support. Separate samples were prepared (n=3) for the non-extruded groups. For the extruded groups, the cell-loaded formulations were placed into 1mL syringes and extruded through 25G blunt needles at a flow rate of 11.68mL/h using a syringe pump. Three separate extrusions were done for each formulation. All samples were added to PDMS holders plasma bonded to a glass-bottom 6-well plate. Fluorescent and phase contrast images were taken every 2h on an Okolab stage incubator with medical gas over an 18h period.

Viability was calculated using FIJI. Images for each dye were separately stacked via max intensity, followed by background subtraction and contrast enhancement by 0.1%. Processed images were then added together using the image calculator function to obtain an image for counting all cells within an ROI. This image was then processed again for background subtraction then blurring with a Gaussian filter to remove any background effects. The image was thresholded, watershedded, then the 'analyze particles' function was used to count cells. The same process was used to count viable cells, but the 'subtract' feature in the image calculator was used instead to remove cells that were stained with both EthD-1 and CellTracker Green. Viability was then calculated by dividing the viable cell count by the total cell count.

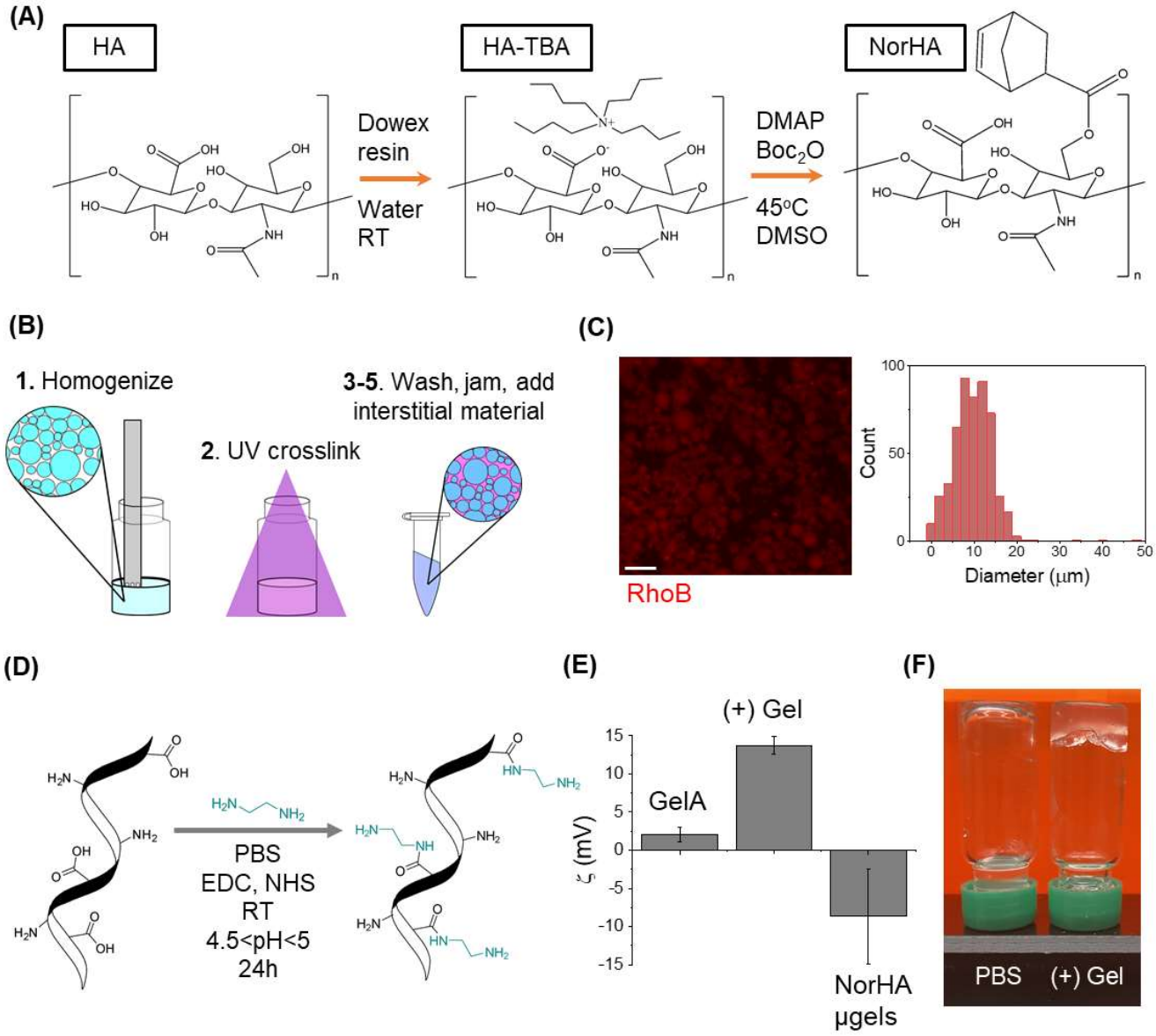

Fig. 1: (A) NorHA synthesis route, (B) NorHA microgel fabrication, (C) widefield image of NorHA microgels (scalebar=40μm) with particle size distribution (n=524), (D) (+) Gel synthesis route, (E) zeta potential of gelatin type A, (+) Gel, and NorHA microgels (n=3, * represents $p<0.05$, and error bars denote standard deviation) and (F) photo of particles at dilute packing densities with PBS or a 1% (+) Gel solution, illustrating how the (+) Gel can tether particles together to form a gel-like material.

Statistical analysis

Statistical analyses were carried out using Origin. One-way ANOVAs were used with a post-hoc Tukey test to determine statistical significance and specify differences between groups. A p-value of less than 0.05 was considered statistically significant.

Results and Discussion

Materials characterization

Norbornene-modified hyaluronic acid (NorHA) was prepared via an established reaction with Boc_2O to couple norbornene groups to the alcohol groups located on the n-acetylglucosamine group (Fig. 1A). The modification of this reaction was between 16% and 21%, calculated from H^1 NMR (SI Fig. 1). NorHA microgels were formed via batch emulsification with a homogenizer (Fig. 1B) and the resulting particle size and distribution was measured after de-emulsifying and hydrating the particles in PBS (Fig. 1C and 1D). The average particle diameter was calculated to be 9.91 ± 4.85 μm. The particle size distribution was broad, which was expected due to the batch emulsification method used to form the particles. This was confirmed by calculating the coefficient of variation, which was 48.99 %.

Cationic gelatin ((+) Gel) was prepared using EDC chemistry to couple amine groups from ethylenediamine to pre-existing carboxylic acid groups on the gelatin backbone (Fig. 1D). By doing so, the zeta potential of the gelatin increased from 2.08 ± 0.97mV to 13.76 ± 1.11 mV, a significant increase (Fig. 1E). This modification was confirmed further with a fluorescamine assay, which showed an increase from 224.65 ± 21.54 μmol NH_2 per g material to 500.08 ± 35.76 μmol NH_2 per g material (SI Fig. 3), also a significant difference. The zeta potential of the NorHA microgels was -8.64 ± 6.23 mV. When added to the particles, the (+) Gel appears to tether the NorHA particles together, keeping it in a gel-like state even at dilute packing densities compared to PBS alone, as visualized by gel inversion tests (Fig. 1F). NorHA particles with (+) Gel showed a gel-like material when the vial is inverted, characteristic of a solid-like gel, but bare particles flowed upon inversion, demonstrating liquid-like properties.

Rheology

In early rheological testing, formulations of NorHA particles with (+) Gel ejected PBS as the top geometry compressed the sample. This was indicative of poroelastic behavior[39]. To test this further, oscillatory strain sweeps were conducted at compressive strains of about 0%, 30% and 60%. A similar test was used previously and adapted for this study[39,40]. In general, poroelasticity is discussed alongside viscoelasticity. In the granular system developed here, the bulk mechanics are due to particle interactions as opposed to polymer networks, therefore, poroelasticity is discussed in conjunction with particle rearrangements rather than viscoelasticity. It was expected that as (+) Gel-based formulations were compressed, interactions between the (+) Gel that adsorbs onto the particles would become

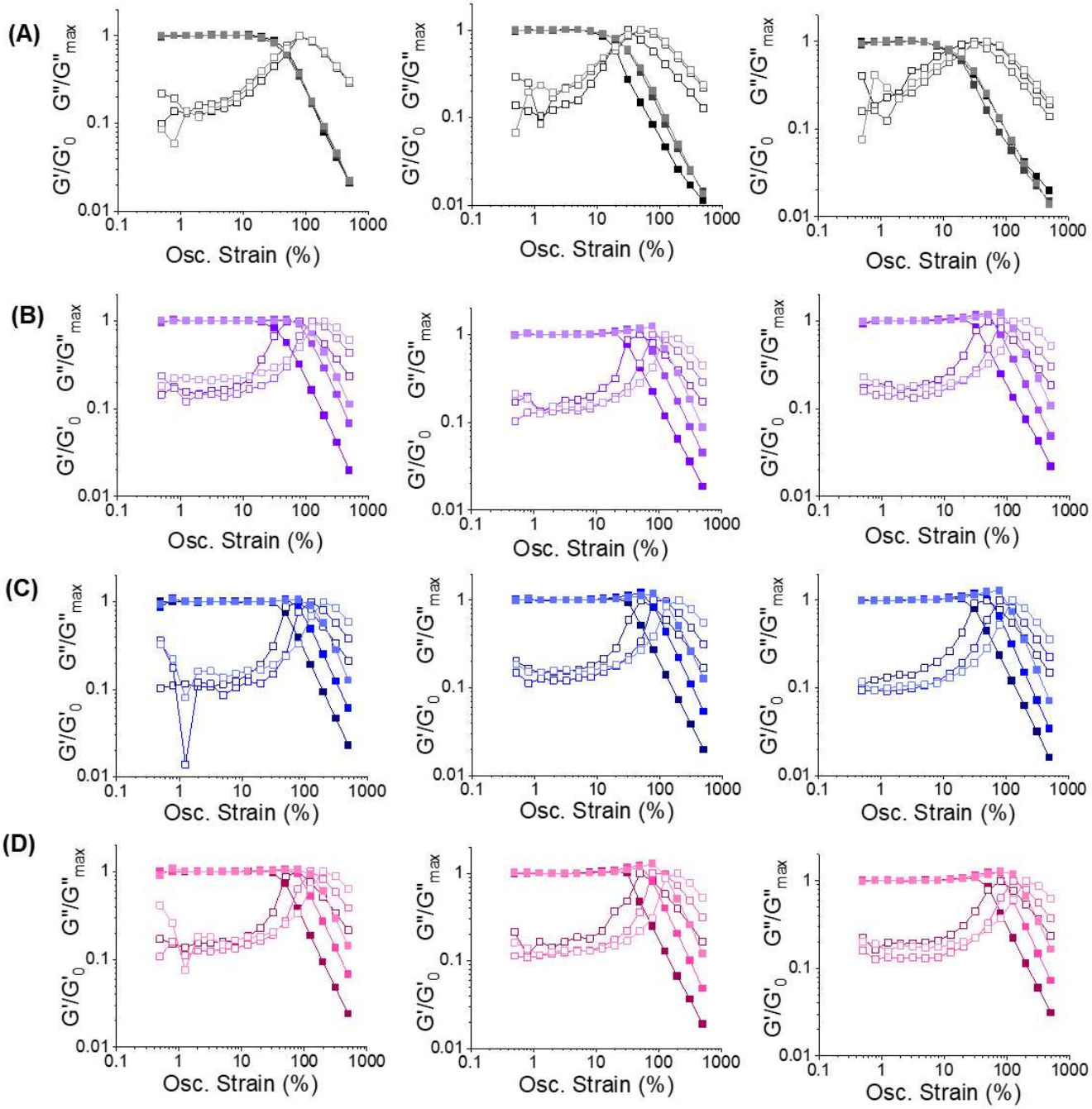

Fig. 2: normalized strain sweeps at different compressive strains (shown by color gradients where lighter denotes increased compressive strain), jamming fraction (going across row) and (+) Gel concentration (black=0 ug/mg, purple=3 ug/mg, blue=6 ug/mg (5 for 0.5 jamming fraction), and red=9 ug/mg (10 for 0.5 jamming fraction)), storage moduli are normalized to G0 from the linear viscoelastic regime, and loss moduli are normalized against the maximum value found in the original loss moduli data.

enhanced and lead to changes in, for example, yielding behavior, but that particles could still rearrange since electrostatic interactions are dynamic. Whereas in a bare particle system, we expect that the particles can freely rearrange during compression, thus leading to no changes in the rheological results with compressive strain.

Jamming fraction and (+) Gel concentration were varied to assess the influence of (+) Gel and porosity on yielding behavior of these formulations as a function of compressive strain (Fig. 2 and SI Fig. 3). For formulations containing no (+) Gel (Fig. 2A), the strain sweeps at each compressive strain were nearly identical at all tested jamming fractions. This indicates that particle rearrangements freely occur as the material is compressed, as expected, and therefore poroelastic behavior is not a feature of PBS-based supports. Once (+) Gel is introduced (3 μg/mg in Fig. 2B, 6 μg/mg in Fig. 2C, and 9 μg/mg in Fig. 2D, except as noted), critical strain, storage modulus, yielding onset, and modulus crossover values, extracted from the rheology data, generally increase as the material is compressed at any (+) Gel concentration (Fig. 3). This data suggest that (+) Gel may be restricting some particle rearrangements and may act to enhance interparticle interactions through increasing particle density as water is removed from the system. However, because electrostatic interactions are dynamic in nature, particle rearrangements could still occur. Interestingly, at all jamming fractions, storage moduli of (+) Gel-containing supports under no compressive strain were roughly equivalent, whereas PBS-based formulations generally had smaller storage moduli (SI Fig. 5). This could be due to testing via bulk rheology, where small strains and frequencies, the differences in (+) Gel concentration may not be apparent. The (+) Gel-containing formulations also displayed an abrupt decline in G' after strain-stiffening, which could be due to the force placed on the material exceeding the bond strength between the (+) Gel chains and NorHA microgels and can explain the smaller extent of strain-stiffening when compared to other biological gels[16].

To confirm the rheological measurements were due to the (+) Gel chains and the NorHA particles interacting electrostatically, rheology of these systems with varying salt concentrations and 1% and 2% Tween20 were analyzed (SI Fig. 6). An increase in salt concentration shields charges to test for electrostatic interactions, whereas the addition of Tween20 interferes with hydrophobic interactions that can be found in gelatin-based materials[41]. Strain sweeps show little to no change in the jammed systems containing either 1% or 2% Tween20, indicating that there are little to no hydrophobic interactions contributing to the bulk rheological properties (SI Fig. 6B). The addition of salt to the system, however, did cause a decrease in the storage modulus, yield onset, and modulus crossover. This confirms that electrostatic interactions play a predominant role in the bulk rheological properties (SI Fig. 6A). This can also be seen visually, where a sample containing 1% Tween20 appeared to retain the gel-like properties seen in the non-treated particulate system. In contrast, when salt is introduced, there is a clear difference where the jammed system becomes increasingly liquid-like (SI Fig. 6C).

In addition to linear increases in the onset and moduli crossover points, there was a noticeable strain-stiffening behavior in the formulations containing (+) Gel. To analyze this behavior, Lissajous curves

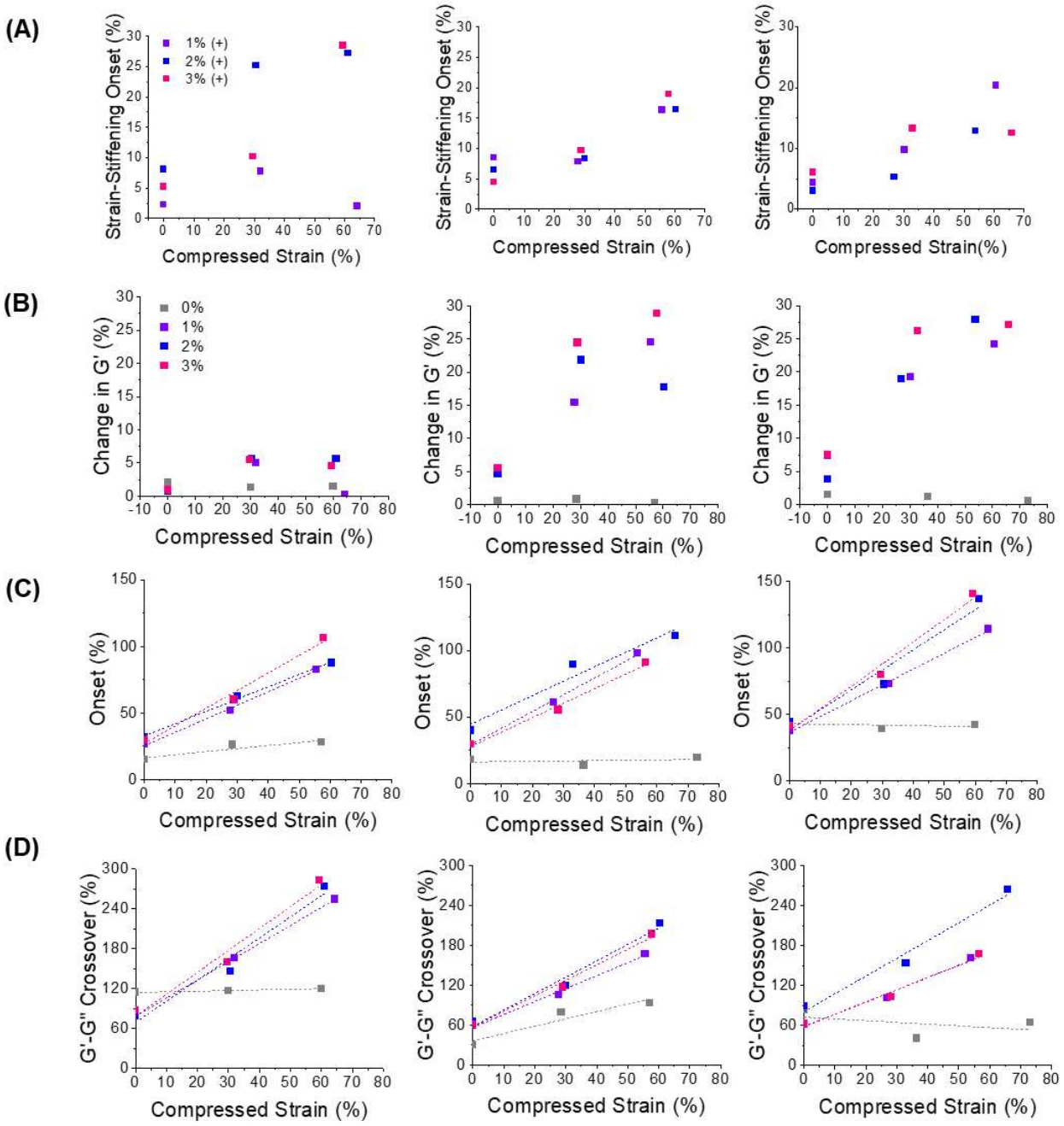

Fig. 3: Change in (A) critical strain, (B) storage modulus, (C) yielding onset, and (D) moduli crossover as a function of (+) Gel concentration and compressive strain, at (i) 0, (ii) 0.3, and (iii) 0.5 jamming fractions. For supports tested at a jamming fraction of 0.5, (+) Gel concentrations of 0% (gray), 0.6% (purple), 1% (blue) and 2% (pink)

were generated at the points of strain-stiffening as this would capture the changes in behavior with (+) Gel concentration and applied compressive strains. For comparison, the points prior to yielding in the PBS-based formulations were used (Fig. 4A). Under no compression, all materials showed primarily viscoelastic behavior, as expected, where the Lissajous curves are linear but open (Fig. 4B). As compression is introduced, a noticeable change in the shape of the Lissajous curves for (+) Gel-

containing formulations is observed. With compression, the Lissajous curves take on an inverted sigmoidal shape, indicative of strain-stiffening behavior (Fig. 5A). This was not observed in the PBS controls, as expected.

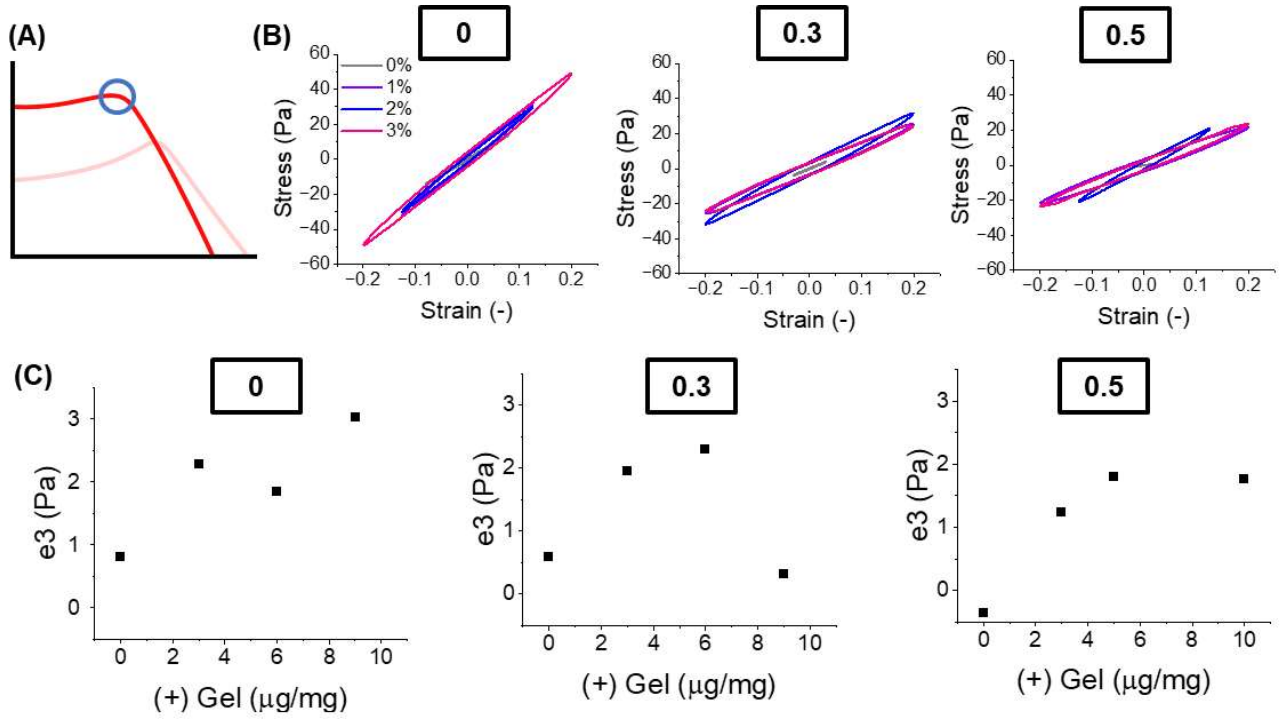

Fig. 4: (A) diagram of where point in strain sweep is being used in LAOS analysis, (B) LAOS at different (+) Gel concentrations and jamming fractions under no compression, and (C) change in the Chebyshev coefficient, e3, as a function of (+) Gel concentration and jamming fraction

Further analysis was done by examining the Chebyshev coefficient, e3, for each material as a function of (+) Gel concentration under no compression and under compressive strains. This value describes the nonlinear component of the elastic contributions found in the material and is calculated via decomposition of the Lissajous curve[42]. When e3 is greater than 0, strain-stiffening behavior is present, otherwise the material is strain-softening when e3 is negative[42]. Generally, as (+) Gel concentration increases, the e3 value also increases across all jamming fractions, suggesting that (+) Gel contributes to strain-stiffening behavior (Fig. 4C). When compression is introduced, a similar trend is seen. As formulations containing (+) Gel are compressed further, the strain-stiffening behavior is enhanced, as illustrated by the increase in e3 (Fig. 5B). This data can also suggest the presence of poroelastic-like behaviors as (+) Gel-particle interactions are enhanced under compression.

Porosity and effect of (+) Gel concentration and compression

Because (+) Gel is expected to adsorb onto the NorHA microgels, the change in particle-particle interactions may cause microstructural changes of the packed microgel supports. Thus, area fractions, average pore sizes, and pore size distributions of the packed materials were assessed using confocal microscopy. For all materials, FITC-dextran, a neutrally-charged polymer, was added to the (+) Gel or PBS solutions to visualize the interstitial space (Fig. 6A). Computational tools (FIJI) were then used to

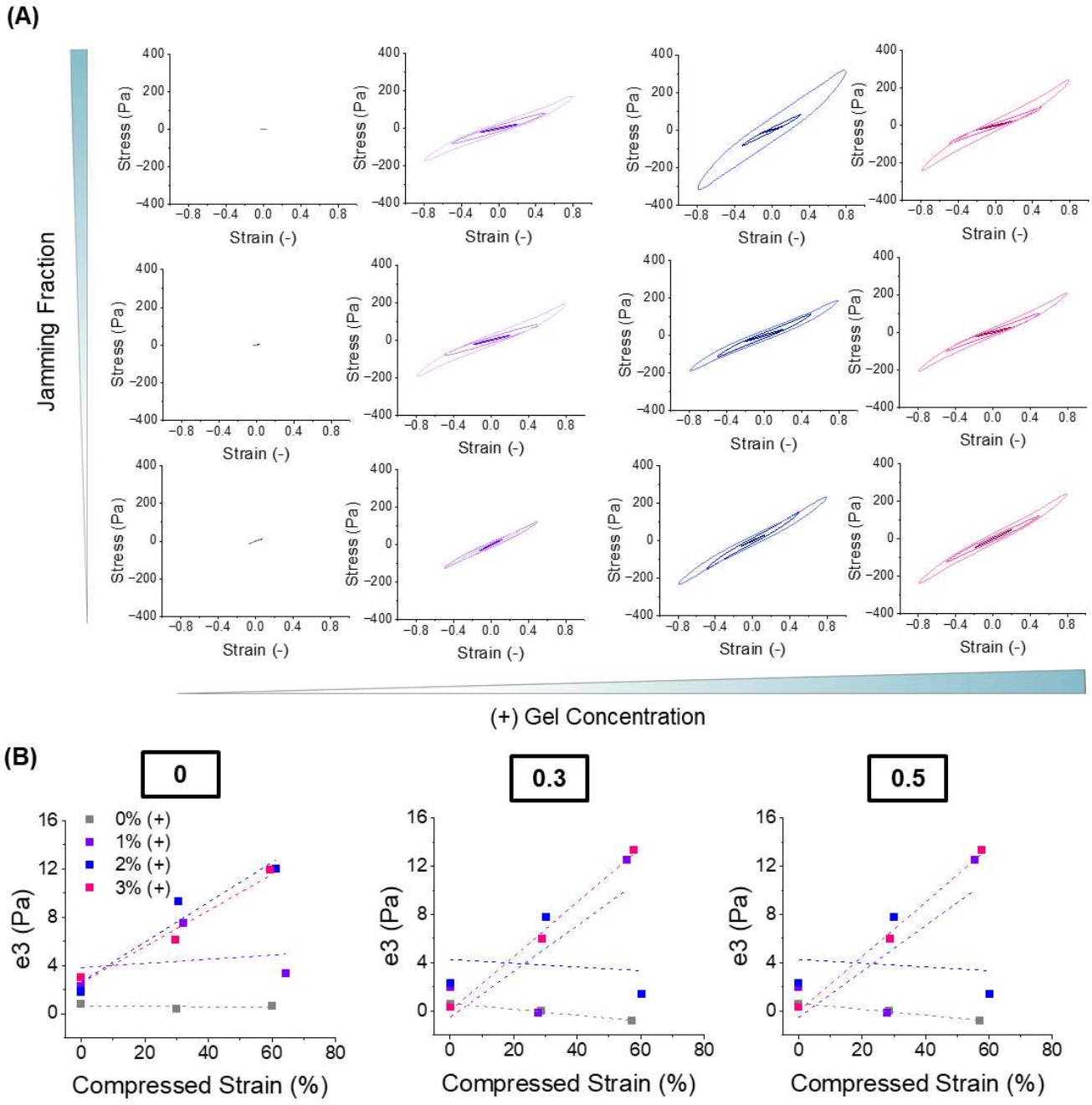

Fig. 5: (A) change in LAOS as a result of material compression and as functions of jamming fraction and (+) Gel concentration, (B) change in the Chebyshev coefficient, e3, as a function of compressive strain, (+) Gel concentration, and jamming fraction.

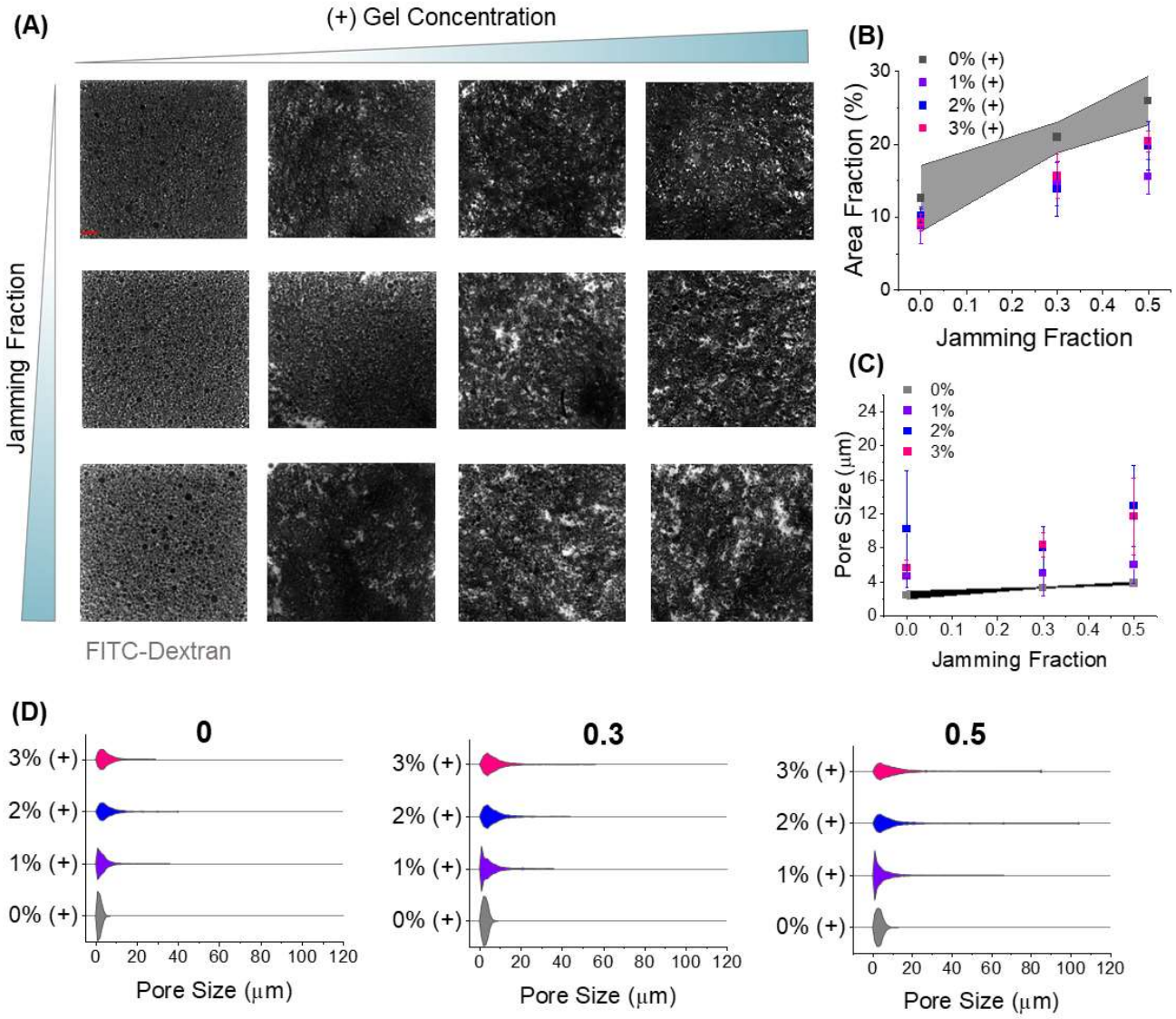

Fig. 6: (A) confocal images of particles at different jamming fractions and (+) Gel concentrations (scalebar=50μm), (B) change in area fraction as a result of jamming fraction and (+) Gel concentration, (C) change in average pore size as a result of jamming fraction (error bars represent standard deviation), and (D) pore size distributions due to changes in (+) Gel concentrations and jamming fractions.

quantify area fraction from the acquired images. As expected, area fraction increased with jamming fraction, showing that the porosity within the jammed systems is easily tunable (Fig. 6B). Average pore size and pore size distributions were measured and assessed using an ImageJ plugin, BoneJ (SI Fig. 7). Average pore sizes in the (+) Gel-containing formulations were generally greater across all jamming fractions compared to PBS-based formulations (Fig. 6C). This can be attributed to the difference in pore size distributions, where higher distributions are seen in the (+) Gel-containing formulations (Fig. 6D). This broader distribution can be attributed to the presence of aggregate-like clusters that seem to form when adding (+) Gel to the microgels. This type of structure has been seen previously in particle-based systems where attractive interparticle interactions were dominant[43,44].

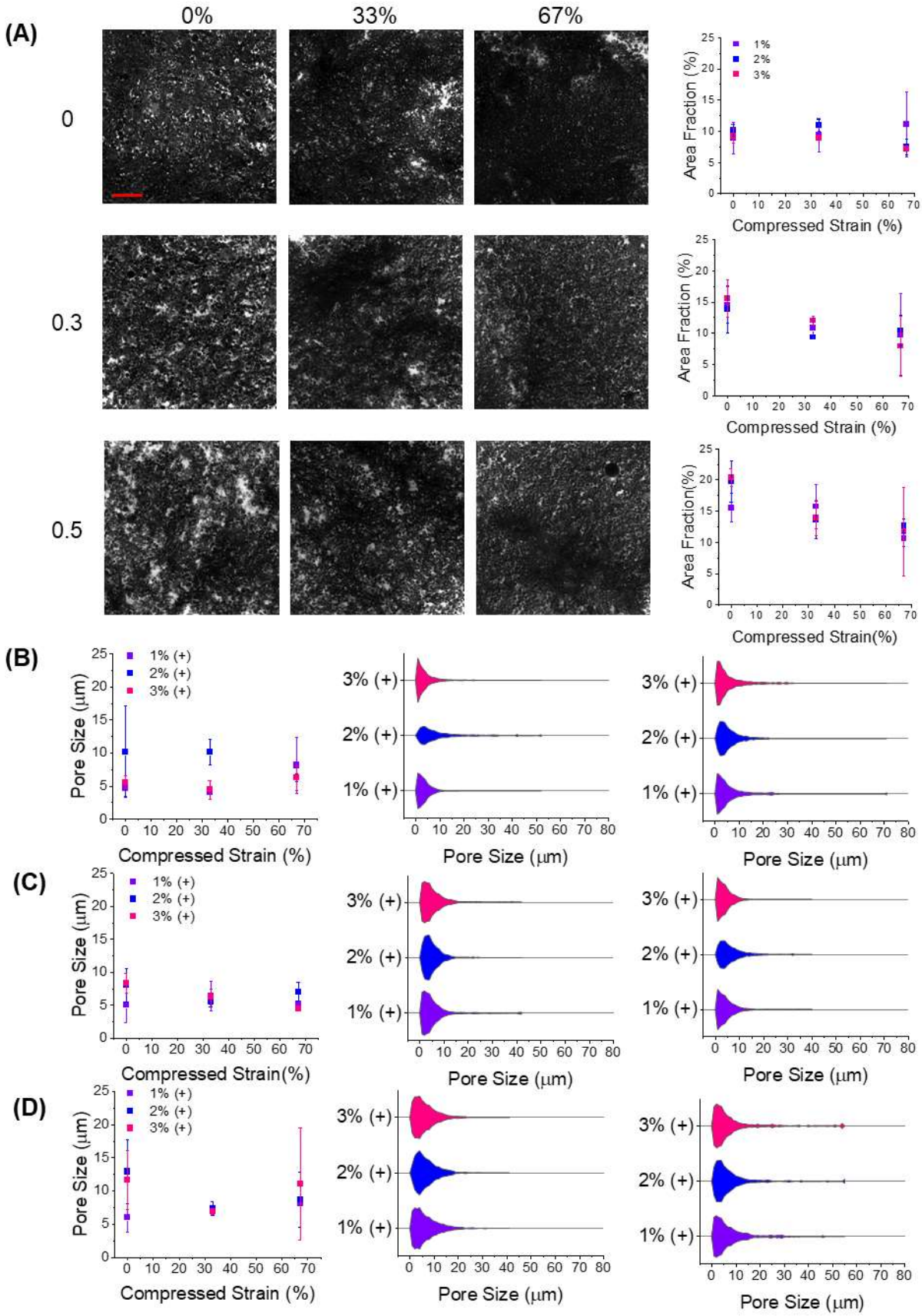

Fig. 7: (A) confocal images of 3% (+) Gel formulations compressed at 0%, 33%, and 67% strains at different jamming fractions and with the corresponding graphs showing change in area fractions (scalebar=100μm), and changes in (i) average pore sizes and (ii) pore size distributions for jamming fractions of (B) 0, (C) 0.3, and (D) 0.5. Error bars for all graphs represent standard deviation.

From the rheology data, there is a clear trend in formulations containing (+) Gel of compressive strain with respect to rheological measurements. Since this material has rheological behavior pointing to poroelastic characteristics, area fractions and pore sizes of compressed formulations containing (+) Gel were assessed. The formulations were again imaged with HMW FITC-dextran in the interstitial space (Fig. 7A and SI Fig. 9-10). Formulations were compressed to 33% or 67% using a custom-made device described in the Methods section (SI Fig. 8). Overall, a decrease in area fraction was observed as compression was increased, and this decrease appears to be dependent on jamming fraction, as formulations with high packing densities were less affected by compression (Fig. 7A). When examining pore size distributions, there is a general shift towards smaller pore sizes as compressive strain increases (Fig. 7B-D). These results combined with rheological data indicate that these materials have poroelastic characteristics and become denser under a compressive force, thus leading to enhanced electrostatic interactions and increased yielding onset and moduli crossover points.

Extrusion testing and filament measurements, and porosity calculations

Three primary measurements were made to examine the effect of (+) Gel concentration on injectability of these particle-based formulations (Fig. 8A), which were the average injection force, pressure during extrusion, and self-healing behavior. To measure the injection force, an Instron machine was used to extrude particles with 0-3% (+) Gel from a 1mL needle through a 25G needle at a vertical speed of 0.5mm/s, corresponding to a volumetric flow rate of 27.54mL/h (SI Fig. 11). The microgel-based formulations were compared to PBS and a commonly used printing ink, Pluronic (Fig. 8B). The average pressure needed for PBS was 0.18kPa, and this jumps to approximately 4kPa for 30% Pluronic. The average pressures needed to extrude the particle-based formulations ranged from 0.47kPa for bare particles to 0.91kPa for the 1% (+) Gel formulation. The 2% and 3% (+) Gel formulations were within this range at 0.84 and 0.71 kPa respectively. The decrease in force as (+) Gel increases may be due to an increase in repulsion forces as more (+) Gel chains adsorb to the particle surface. No significant differences were found amongst the (+) Gel-containing formulations. The 1% and 2% (+) Gel formulations were significantly different compared to the PBS-based formulation. While the (+) Gel-containing formulations were significantly different compared to the 0% (+) Gel formulation and PBS, these results show that formulations containing (+) Gel were closer to PBS in terms of injection force compared to 30% Pluronic, illustrating the ease of injecting these (+) Gel-based supports. Significant differences were found between Pluronic and every microgel formulation tested. These results show that while (+) Gel holds particles together, this type of bonding can be easily broken via a small extrusion force, thus facilitating processes such as injections or 3D printing.

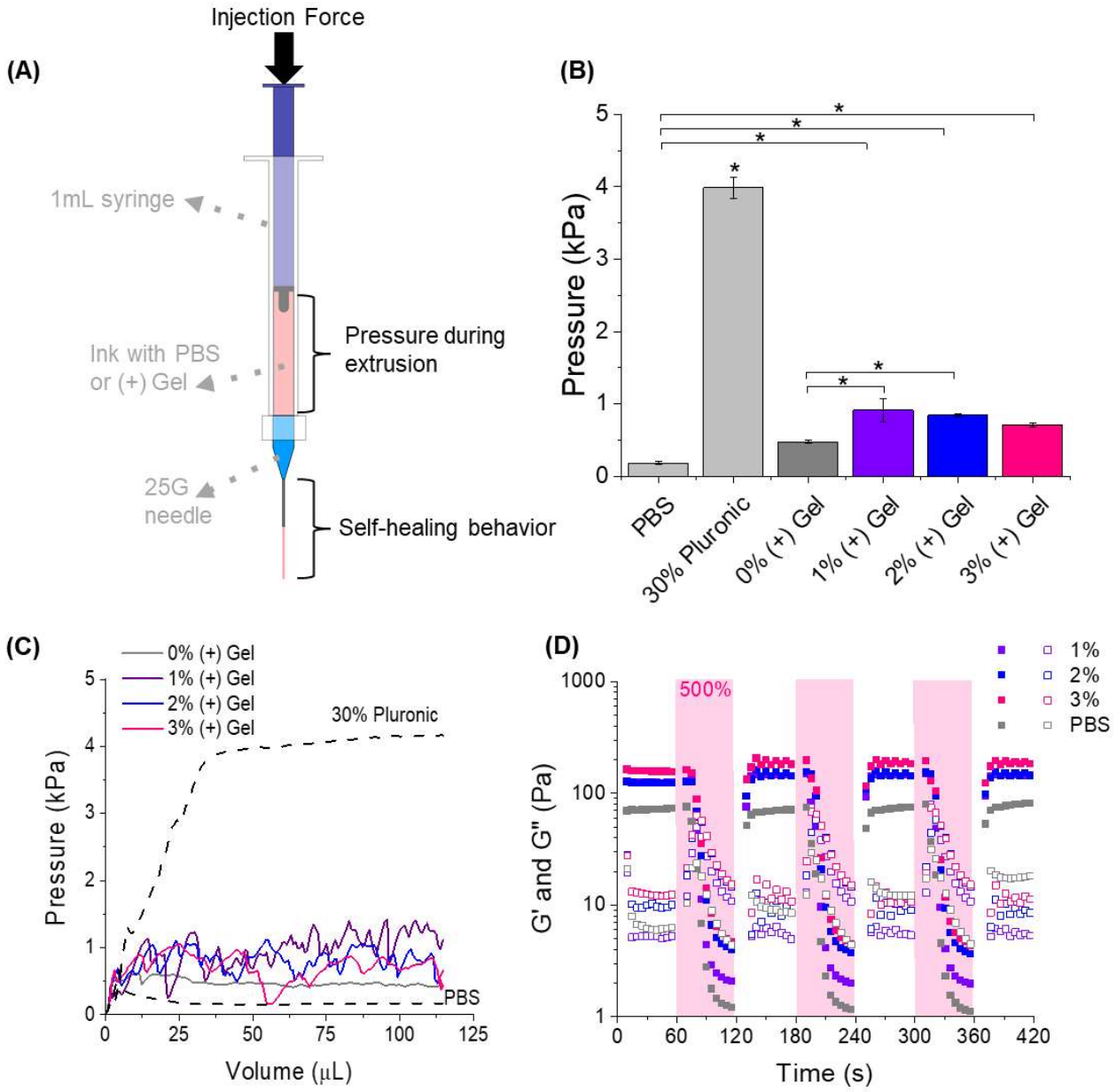

Fig. 8: (A) schematic of variables tested for assessing injectability of formulations with different (+) Gel concentrations, (B) average pressure during extrusion with Pluronic F-127 and PBS used for comparison (n=2, * denotes $p<0.05$, and error bars represent standard deviation), (C) representative data of pressure over volume of formulations as a function of (+) Gel concentrations with Pluronic and PBS used for comparison, and (D) repeated high and low strain rheology to show self-healing behavior of the materials over several 'injection' cycles as a function of (+) Gel concentration.

The pressure over volume was calculated for each formulation from the injectability tests (Fig. 8C). This data further shows how more similar the microgel-based formulations are to PBS compared to 30% Pluronic. Under the flow conditions used in testing, PBS reaches a peak pressure of approximately 0.5kPa then levels off after roughly 25μL has been extruded, maintaining an injection pressure of about 0.18kPa. Pluronic, in contrast, reaches a max pressure of about 4kPa and levels off after reaching about 40μL of ejected volume while maintaining this injection force. The 30% Pluronic, PBS, and 0%

(+) Gel formulations show smooth lines as the ejected volume increases. As (+) Gel is introduced to the microgel-based formulations, there is an increase in pressure fluctuations during ejection. This could be attributed to the presence of aggregate-like clusters, shown in confocal images (Fig. 6A) where pressure would increase with a large cluster, then upon ejection of this cluster, the pressure would decrease.

Rheology was conducted on microgel-based formulations to assess self-healing behavior as a function of (+) Gel concentration over multiple high-low strain cycles (Fig. 8D) using a commonly-used test[28]. A low strain of 1% and high strain of 500% were used and were cycled every 60s for a total of 7 cycles, rapidly inducing repeated solid-liquid transitions. All formulations transitioned from solid-like materials to liquid-like behavior as the strain increased, as expected (Fig. 8D). The formulations containing (+) Gel all exhibit self-healing behavior as well as fast recovery as the applied strain was decreased from 500% to 1%. Upon the change in strain, storage moduli values were restored to nearly the original value from the first cycle. This was not observed in the 0% (+) Gel (PBS only) formulation. As the material continued to be cycled, recovery became slower, which may be attributed to the applied variables used in the rheological testing.. These indicate that the 0% (+) Gel formulation may be restructuring upon cessation of the high strain, and that the addition of (+) Gel contributes to faster recovery.

Filament formation of each formulation was examined. This was done in air for evaluation, previously done in multiple studies[45–48], as this can be predictive of the 3D printing process but can also be indicative of use as an injectable hydrogel for non-3D printing applications. Because the material has poroelastic characteristics, extrusion at high and low flow rates was conducted using a syringe pump to assess any changes in filament formation[40]. The high flow rate was set to 11.68mL/h, the maximum the pump could achieve with the 1mL syringe. The low flow rate was set to 1.17mL/h. The formulations were extruded in 50μL increments and recorded over time. The maximum filament length prior to filament breakage was measured as a function of (+) Gel over time. The data shows that extruded filaments looked nearly identical for all formulations containing (+) Gel, where the filaments were linear with a bead at the end (Fig. 9A). The 0% (+) Gel formulation, on the other hand, had primarily short droplet-like filaments, as expected. This can be attributed to the (+) Gel tethering the particles to one another, whereas the lack of electrostatic interparticle interactions leads to shorter, more droplet-like filaments as the weight of the bead causes the filament to break at shorter lengths. The presence of the droplet at the end of the filaments occurred in all (+) Gel formulations. During extrusion, of which timestamps can be seen in Fig. 9B, the material would kink and roll on itself, followed by ejection of a filament, which did not appear to occur in the PBS-based formulations.

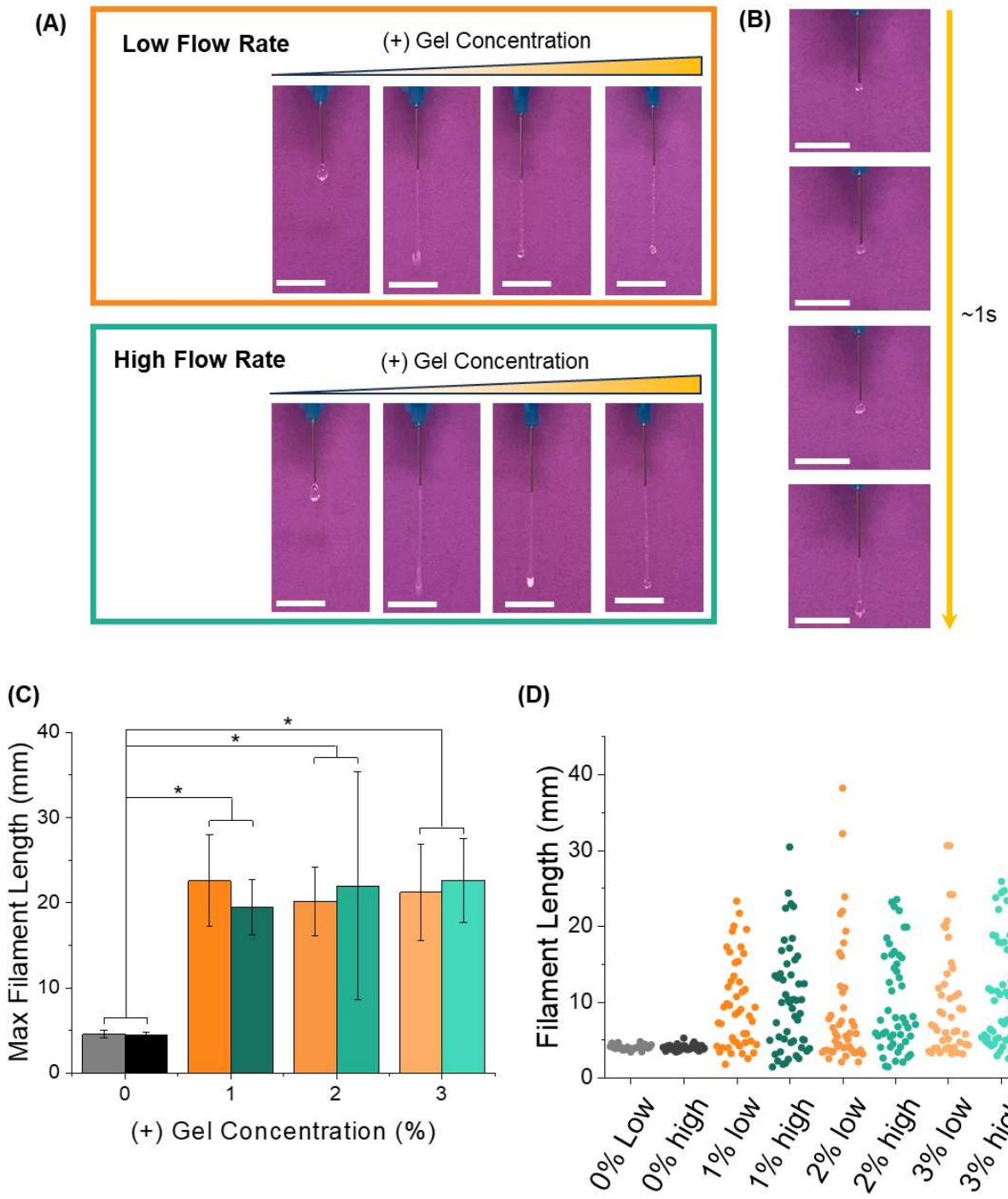

Fig. 9: (A) images of formulations containing varying concentrations of (+) Gel at low (1.17mL/h) and high (11.68mL/h) flow rates (scalebar=1cm), (B) an example of a (+) Gel containing formulation being extruded and the material balling up during the first 1s of extrusion forming the characteristic bead of material at the end of the (+) Gel containing formulations (scalebar=1cm), (C) max filament lengths achieved for each extruded formulation at high (green) and low (orange) flow rates, n=5, error bars indicate standard deviation and * represents a p-value less than 0.05, (D) distribution of filament lengths for each formulation at high (green) and low (orange) flow rates

Max filament length was measured immediately prior to filament breakage (Fig. 9C). Without (+) Gel, average max filament length was approximately 5mm at both high and low flow rates. Upon the addition of (+) Gel, the max filament length increased to roughly 23mm regardless of (+) Gel concentration. This was also independent of flow rate, as both values for high and low flow rate for each formulation were not statistically significant. To further understand the effect of (+) Gel concentration on ejection of these formulations, all filament lengths were measured and compared (Fig. 9D). The PBS-only formulation had a small distribution of filament lengths. In comparison, the distributions became much larger as (+) Gel was added and did not appear to be dependent on concentration.

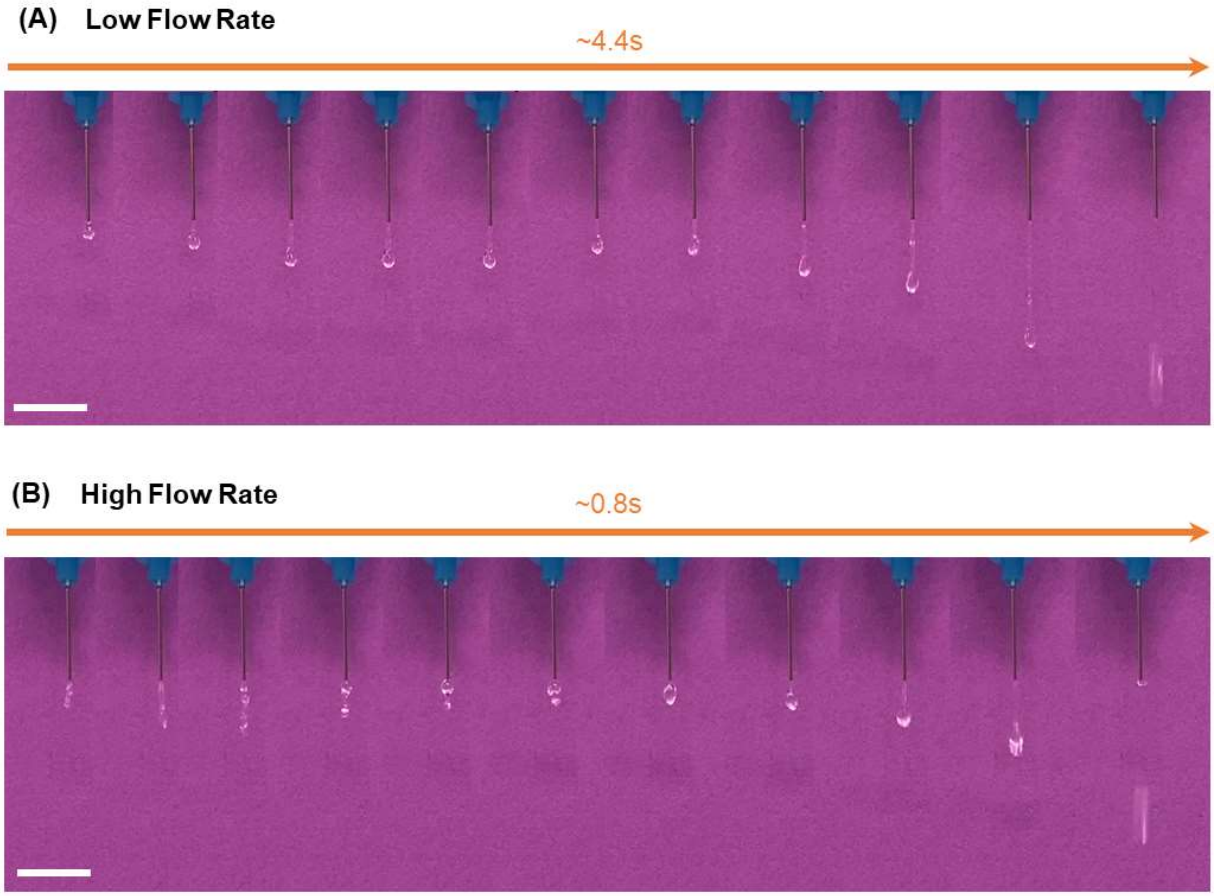

Fig. 10: time-lapse images of 1% (+) Gel formulations extruded at (A) low and (B) high flow rates, scalebar=1 cm

An interesting phenomenon occurred during extrusion for the (+) Gel formulations. At both high and low flow rates, the filament would increase in length as expected, but would then retract followed by lengthening then breakage. This can be seen in Fig. 10, where 1% (+) Gel formulations are used as an example. This retraction would sometimes include conglomeration of the existing filament with extruding filament, forming a bead at the end. This could be attributed to possible relaxation processes within the filament during extrusion. During extrusion, the filament becomes extended upon exiting the

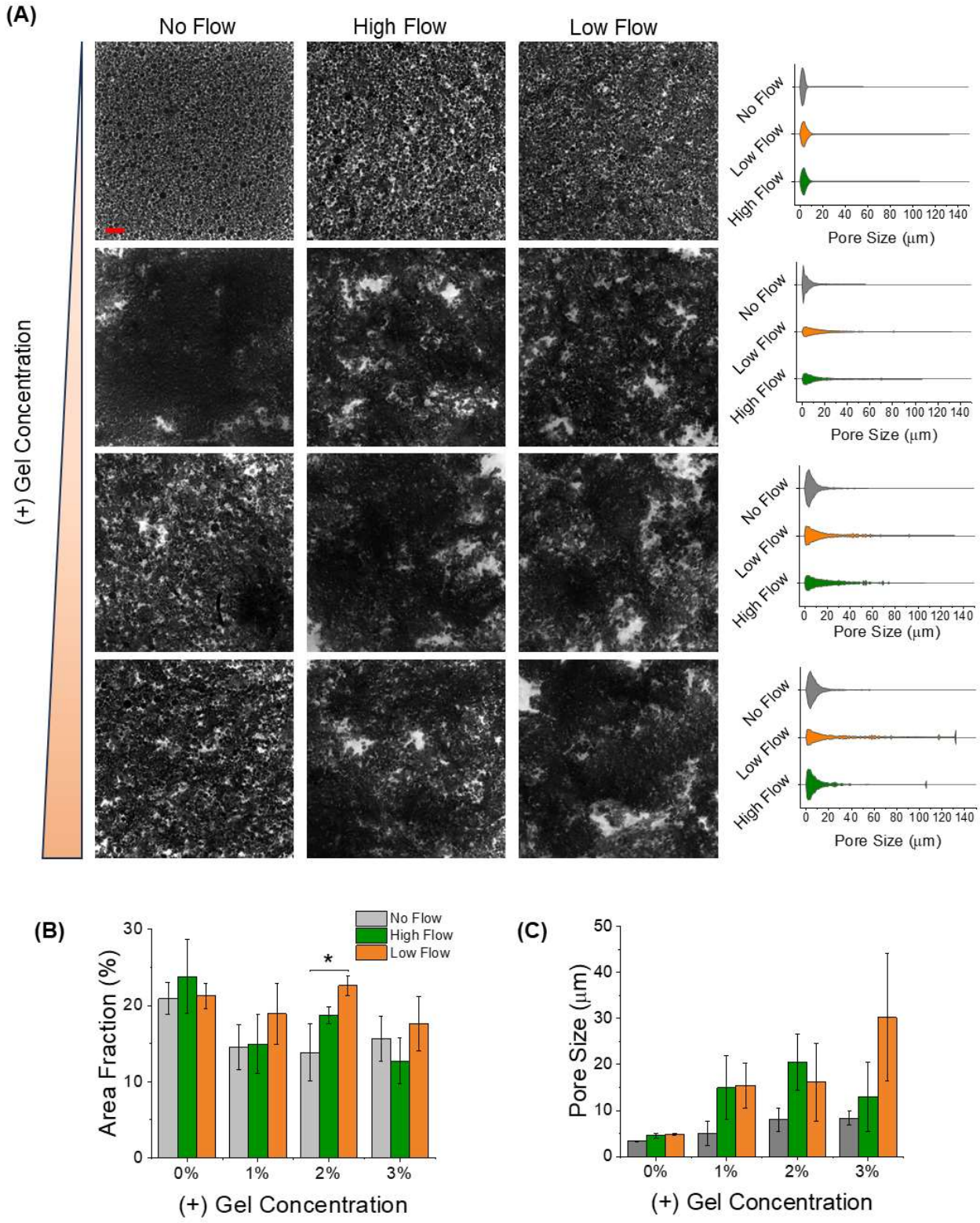

Fig. 11: (A) confocal images of formulations with different (+) Gel concentrations under no flow, high flow, and low flow conditions with corresponding pore size distributions (scalebar=50μm), (B) change in area fraction as a function of flow rate and (+) Gel concentrations (n=3, * represents $p<0.05$, and error bars denote standard deviation), and (C) change in average pore size as a result of flow for each (+) Gel concentration (n=3, * represents $p<0.05$, and error bars denote standard deviation)

nozzle, and the electrostatic interactions may relax during this stage, causing the filament to shorten. While this may not impact the material for injectable-based applications, this may impact 3D printed construct shape fidelity.

Because the material compresses during extrusion from a syringe barrel through a needle, confocal images were obtained to assess the change in area fraction and pore size with respect to flow rates (Fig. 11A). As shown in Fig. 11B, area fraction did not change with respect to flow rate or have a trend with (+) Gel concentration. The only statistically significant difference was between the low flow rate and no flow rate groups in the 2% (+) Gel formulation, which showed an increase in area fraction. Pore sizes showed an increase with both high and low flow rates in formulations with (+) Gel. As seen in the confocal images, the microstructural appearance changed pre- and post-extrusion of (+) Gel-containing formulations, where there appears to be larger pores present. This can be seen in the pore size distributions and average pore size as well (Fig. 11A and 11C), where there is generally an increase in range to include larger pore sizes post-extrusion. This may have implications in cell behaviors post-extrusion, where pore size plays a role in cell behaviors like migration and proliferation, and potentially in 3D printing applications to create a customized construct.

Cell viability with and without extrusion

To assess shear-protecting capabilities of this system as a function of (+) Gel concentration, 3T3 fibroblasts were dispersed into the supports at approximately 2 million cells per uL of support, and then extruded at high flow rates into PDMS holders through a 25G needle. Comparisons were made to cell-laden supports that had not been extruded and were instead gently mixed using a wide-bore pipette tip. Cell-tracker green dye was used instead of calcein AM due to dye longevity, transport through the support, and fragility of the supports to handling that would be needed for multiple staining procedures. Results show that there is an improvement in viability with (+) Gel concentration in both extruded and non-extruded groups, seen visually in Fig. 12A and quantitatively in Figs. 12B and 12C. Additionally, there is a trend of decreasing viability over time for all groups, but viability stabilizes after about 6h. Taken together, the viability results suggest two things. One, the low cell viabilities in the non-extruded groups indicate that more (+) Gel may be required to improve fibroblast viability specifically, or that a component of the system is introducing cytotoxicity. Two, it appears that (+) Gel may provide some shear-protecting effect, but additional work into enhancing shear-protection is required.

The morphology of the fibroblasts also changed over time. In further experimentation, the cells were almost exclusively adopting a rounded morphology at the 1h timepoint for all (+) Gel concentrations

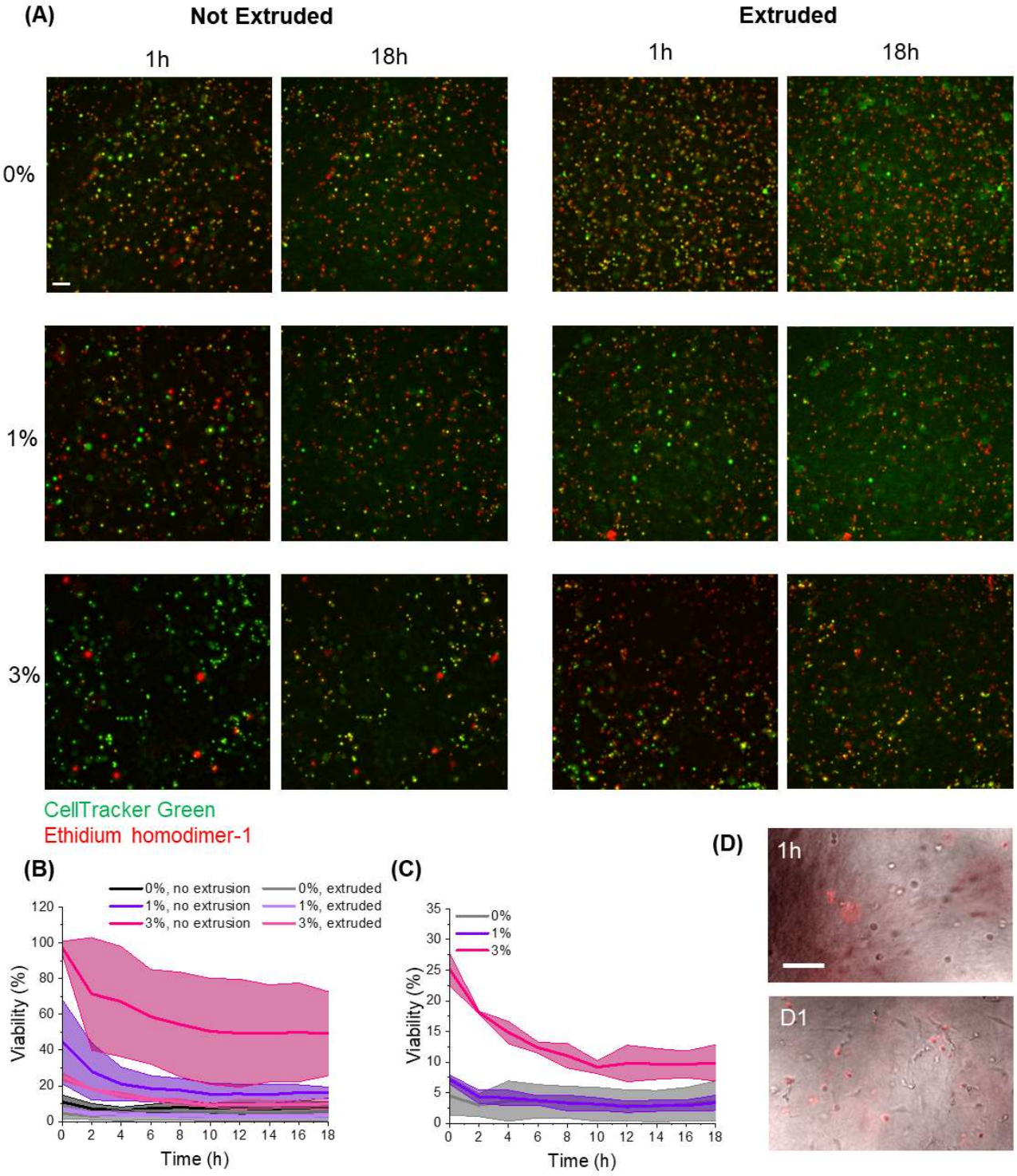

Fig. 12: (A) non-extruded and extruded groups of fibroblasts within microgel supports at a jamming fraction of 0.3 and varying (+) Gel concentrations (scalebar=100μm), (B) viability of all groups over an 18h time period (shaded regions indicate standard deviation), (C) closeup of (B) showing only extruded groups, and (D) change in morphology of live fibroblasts at 1h post-extrusion and one day post-extrusion in a support with 3% (+) Gel (scalebar= 100μm).

tested. This was expected as the cells would require more time to form adhesions with the surrounding material. At the D1 timepoint, live cells became more elongated. This occurred in all samples regardless of (+) Gel concentration and if the material was extruded (SI Fig. 13).

Conclusions and Future Work

This study evaluated the rheological characteristics and injectability of jammed NorHA microgels with adsorbed (+) Gel chains. This work sets the stage for several applications, such as those in injectable wound healing applications and in 3D printing. The addition of (+) Gel to anionic NorHA particles produces a porous scaffold with strain-stiffening and self-healing behaviors, pre-requisites of an injectable hydrogel system that can mimic native tissue. Microstructurally, these materials are easily tunable, and densify under compression leading to poroelastic-like behaviors as well. Extrusion of the supports was easily achievable, requiring pressures on the scale of neat PBS, and filament formation was observed regardless of (+) Gel concentration. Due to this plus the self-healing behavior examined rheologically, this material could be used in applications like 3D printing. Lastly, cell experiments with fibroblasts indicate that additional work is required to obtain high cell viabilities. A positive trend in (+) Gel concentration was seen, as cell viabilities in those supports were higher. However, low viability was still observed in the non-extruded groups. Thus, additional work is needed to enhance the shear-protecting capabilities of this system for future applications in injectable systems. F

uture work for this project includes additional material characterization in addition to addressing the low cell viabilities. For instance, alignment of (+) Gel chains could be assessed using a technique such as confocal microscopy with fluorescently-tagged (+) Gel chains. A similar experiment to the one conducted in this chapter could be used to further test these samples under both compressive and shear strains. To address low cell viabilities, determining the source of low cell viabilities and enhancing the shear-protecting capabilities, possibly through the inclusion of other well-known shear-protecting gels and solutions, are crucial. Material interactions may need to first be considered, and testing cytocompatibility could be achieved through methods such as LDH assays. Particle sizes may also need to be reconsidered, as this may impact cell viabilities when mixing together with the microgel-based medium. Other future work may include assessing the formulations for 3D printing with and without cells.

References

1. Griffin, D. R., Weaver, W. M., Scumpia, P., Di Carlo, D. & Segura, T. Accelerated wound healing by injectable microporous gel scaffolds assembled from annealed building blocks. *Nat. Mater.* **14**, 737–744 (2015).
2. Lin, X. *et al.* An injectable and light curable hyaluronic acid composite gel with anti-biofilm, anti-inflammatory and pro-healing characteristics for accelerating infected wound healing. *Int. J. Biol. Macromol.* **253**, 127190 (2023).
3. Wang, T. *et al.* Photothermal hyaluronic acid composite hydrogel targeting cancer stem cells for inhibiting recurrence and metastasis of breast cancer. *Int. J. Biol. Macromol.* **252**, 126358 (2023).
4. Kumar, A. *et al.* Highly Biocompatible Smart Injectable Hydrogel for the Management of Rheumatoid Arthritis. *ACS Biomater. Sci. Eng.* **9**, 5312–5321 (2023).
5. Sharma, P. K., Taneja, S. & Singh, Y. Hydrazone-Linkage-Based Self-Healing and Injectable Xanthan–Poly(ethylene glycol) Hydrogels for Controlled Drug Release and 3D Cell Culture. *ACS Appl. Mater. Interfaces* **10**, 30936–30945 (2018).
6. Yang, K. *et al.* Antibacterial hyaluronic acid hydrogels with enhanced self-healing properties *via* multiple dynamic bond crosslinking. *Int. J. Biol. Macromol.* **256**, 128320 (2024).
7. Wang, L. L. *et al.* Injectable, Guest–Host Assembled Polyethylenimine Hydrogel for siRNA Delivery. *ACS Publications* https://pubs.acs.org/doi/full/10.1021/acs.biomac.6b01378 (2016) doi:10.1021/acs.biomac.6b01378.
8. Zhang, J. *et al.* Highly transparent, self-healing, injectable and self-adhesive chitosan/polyzwitterion-based double network hydrogel for potential 3D printing wearable strain sensor. *Mater. Sci. Eng. C* **117**, 111298 (2020).
9. Hsu, R.-S. *et al.* Adaptable Microporous Hydrogels of Propagating NGF-Gradient by Injectable Building Blocks for Accelerated Axonal Outgrowth. *Adv. Sci.* **6**, 1900520 (2019).
10. Chernos, M. *et al.* Rheological study of hyaluronic acid derivatives. *Biomed. Eng. Lett.* **7**, 17–24 (2017).

11. Wang, Y. *et al.* An Injectable Interpenetrating Polymer Network Hydrogel with Tunable Mechanical Properties and Self-Healing Abilities. *Macromol. Chem. Phys.* **218**, 1700348 (2017).

12. Hafezi, M., Khorasani, S. N., Khalili, S. & Neisiany, R. E. Self-healing interpenetrating network hydrogel based on GelMA/alginate/nano-clay. *Int. J. Biol. Macromol.* **242**, 124962 (2023).

13. Liu, Y., Hsu, Y.-H., Huang, A. P.-H. & Hsu, S. Semi-Interpenetrating Polymer Network of Hyaluronan and Chitosan Self-Healing Hydrogels for Central Nervous System Repair. *ACS Appl. Mater. Interfaces* **12**, 40108–40120 (2020).

14. Appel, E. A. *et al.* Self-assembled hydrogels utilizing polymer–nanoparticle interactions. *Nat. Commun.* **6**, 6295 (2015).

15. Shao, C. *et al.* Mimicking Dynamic Adhesiveness and Strain-Stiffening Behavior of Biological Tissues in Tough and Self-Healable Cellulose Nanocomposite Hydrogels. *ACS Appl. Mater. Interfaces* **11**, 5885–5895 (2019).

16. Storm, C., Pastore, J. J., MacKintosh, F. C., Lubensky, T. C. & Janmey, P. A. Nonlinear elasticity in biological gels. *Nature* **435**, 191–194 (2005).

17. Gu, J. *et al.* Tuning Strain Stiffening of Protein Hydrogels by Charge Modification. *Int. J. Mol. Sci.* **23**, 3032 (2022).

18. C. Ollier, R., Xiang, Y., M. Yacovelli, A. & J. Webber, M. Biomimetic strain-stiffening in fully synthetic dynamic-covalent hydrogel networks. *Chem. Sci.* **14**, 4796–4805 (2023).

19. Jaspers, M. *et al.* Ultra-responsive soft matter from strain-stiffening hydrogels. *Nat. Commun.* **5**, 5808 (2014).

20. Luo, J. *et al.* Biomimetic Strain-Stiffening Hydrogel with Crimped Structure. *Adv. Funct. Mater.* **31**, 2104139 (2021).

21. Nia, H. T., Han, L., Li, Y., Ortiz, C. & Grodzinsky, A. Poroelasticity of Cartilage at the Nanoscale. *Biophys. J.* **101**, 2304–2313 (2011).

22. Weir Weiss, M.-J., Shrestha, P., Basak, R. & Stoeber, B. Poroelastic behavior of skin tissue in response to pressure driven flow. *Phys. Fluids* **35**, 081902 (2023).

23. Lee, R. C., Frank, E. H., Grodzinsky, A. J. & Roylance, D. K. Oscillatory Compressional Behavior of Articular Cartilage and Its Associated Electromechanical Properties. *J. Biomech. Eng.* **103**, 280–292 (1981).

24. Wang, M. *et al.* Characterizing poroelasticity of biological tissues by spherical indentation: an improved theory for large relaxation. *J. Mech. Phys. Solids* **138**, 103920 (2020).

25. Wells, R. G. Tissue Mechanics and Fibrosis. *Biochim. Biophys. Acta* **1832**, 884–890 (2013).

26. Wang, Q.-M., Mohan, A. C., Oyen, M. L. & Zhao, X.-H. Separating viscoelasticity and poroelasticity of gels with different length and time scales. *Acta Mech. Sin.* **30**, 20–27 (2014).

27. Bhattacharjee, T. *et al.* Writing in the granular gel medium. *Sci. Adv.* **1**, e1500655 (2015).

28. Highley, C. B., Song, K. H., Daly, A. C. & Burdick, J. A. Jammed Microgel Inks for 3D Printing Applications. *Adv. Sci.* **6**, 1801076 (2019).

29. Widener, A. E., Duraivel, S., Angelini, T. E. & Phelps, E. A. Injectable Microporous Annealed Particle Hydrogel Based on Guest–Host-Interlinked Polyethylene Glycol Maleimide Microgels. *Adv. NanoBiomed Res.* **2**, 2200030 (2022).

30. Muir, V. G. *et al.* Sticking Together: Injectable Granular Hydrogels with Increased Functionality via Dynamic Covalent Inter-Particle Crosslinking. *Small* **18**, 2201115 (2022).

31. Gramlich, W. M., Kim, I. L. & Burdick, J. A. Synthesis and orthogonal photopatterning of hyaluronic acid hydrogels with thiol-norbornene chemistry. *Biomaterials* **34**, 9803–9811 (2013).

32. K, J., Naskar, D., Kundu, S. C. & James, N. R. Fabrication of cationized gelatin nanofibers by electrospinning for tissue regeneration. *RSC Adv.* **5**, 89521–89530 (2015).

33. Tamura, M. *et al.* Click-crosslinkable and photodegradable gelatin hydrogels for cytocompatible optical cell manipulation in natural environment. *Sci. Rep.* **5**, 15060 (2015).

34. Lunardi, C. N., Gomes, A. J., Rocha, F. S., De Tommaso, J. & Patience, G. S. Experimental methods in chemical engineering: Zeta potential. *Can. J. Chem. Eng.* **99**, 627–639 (2021).

35. Bhattacharjee, T. & Angelini, T. E. 3D T cell motility in jammed microgels. *J. Phys. Appl. Phys.* **52**, 024006 (2018).

36. Otsu, N. A Threshold Selection Method from Gray-Level Histograms. *IEEE Trans. Syst. Man Cybern.* **9**, 62–66 (1979).

37. Domander, R., Felder, A. A. & Doube, M. BoneJ2 - refactoring established research software. *Wellcome Open Res.* **6**, 37 (2021).

38. Ewoldt, R. H., Hosoi, A. E. & McKinley, G. H. Nonlinear viscoelastic biomaterials: meaningful characterization and engineering inspiration. *Integr. Comp. Biol.* **49**, 40–50 (2009).

39. Lopez-Sanchez, P. *et al.* Micromechanics and Poroelasticity of Hydrated Cellulose Networks. *Biomacromolecules* **15**, 2274–2284 (2014).

40. Lopez-Sanchez, P. *et al.* Poroelastic Mechanical Effects of Hemicelluloses on Cellulosic Hydrogels under Compression. *PLOS ONE* **10**, e0122132 (2015).

41. Bertsch, P., Andrée, L., Besheli, N. H. & Leeuwenburgh, S. C. G. Colloidal hydrogels made of gelatin nanoparticles exhibit fast stress relaxation at strains relevant for cell activity. *Acta Biomater.* **138**, 124–132 (2022).

42. New measures for characterizing nonlinear viscoelasticity in large amplitude oscillatory shear | Journal of Rheology | AIP Publishing. https://pubs.aip.org/sor/jor/article/52/6/1427/240149/New-measures-for-characterizing-nonlinear.

43. Trappe, V., Prasad, V., Cipelletti, L., Segre, P. N. & Weitz, D. A. Jamming phase diagram for attractive particles. *Nature* **411**, 772–775 (2001).

44. Koeze, D. J. & Tighe, B. P. Sticky Matters: Jamming and Rigid Cluster Statistics with Attractive Particle Interactions. *Phys. Rev. Lett.* **121**, 188002 (2018).

45. Cai, F.-F., Heid, S. & Boccaccini, A. R. Potential of Laponite® incorporated oxidized alginate–gelatin (ADA-GEL) composite hydrogels for extrusion-based 3D printing. *J. Biomed. Mater. Res. B Appl. Biomater.* **109**, 1090–1104 (2021).

46. Paxton, N. *et al.* Proposal to assess printability of bioinks for extrusion-based bioprinting and evaluation of rheological properties governing bioprintability. *Biofabrication* **9**, 044107 (2017).

47. Park, J. *et al.* Cell-laden 3D bioprinting hydrogel matrix depending on different compositions for soft tissue engineering: Characterization and evaluation. *Mater. Sci. Eng. C* **71**, 678–684 (2017).

48. Bom, S., Ribeiro, R., Ribeiro, H. M., Santos, C. & Marto, J. On the progress of hydrogel-based 3D printing: Correlating rheological properties with printing behaviour. *Int. J. Pharm.* **615**, 121506 (2022).

Supplemental Information

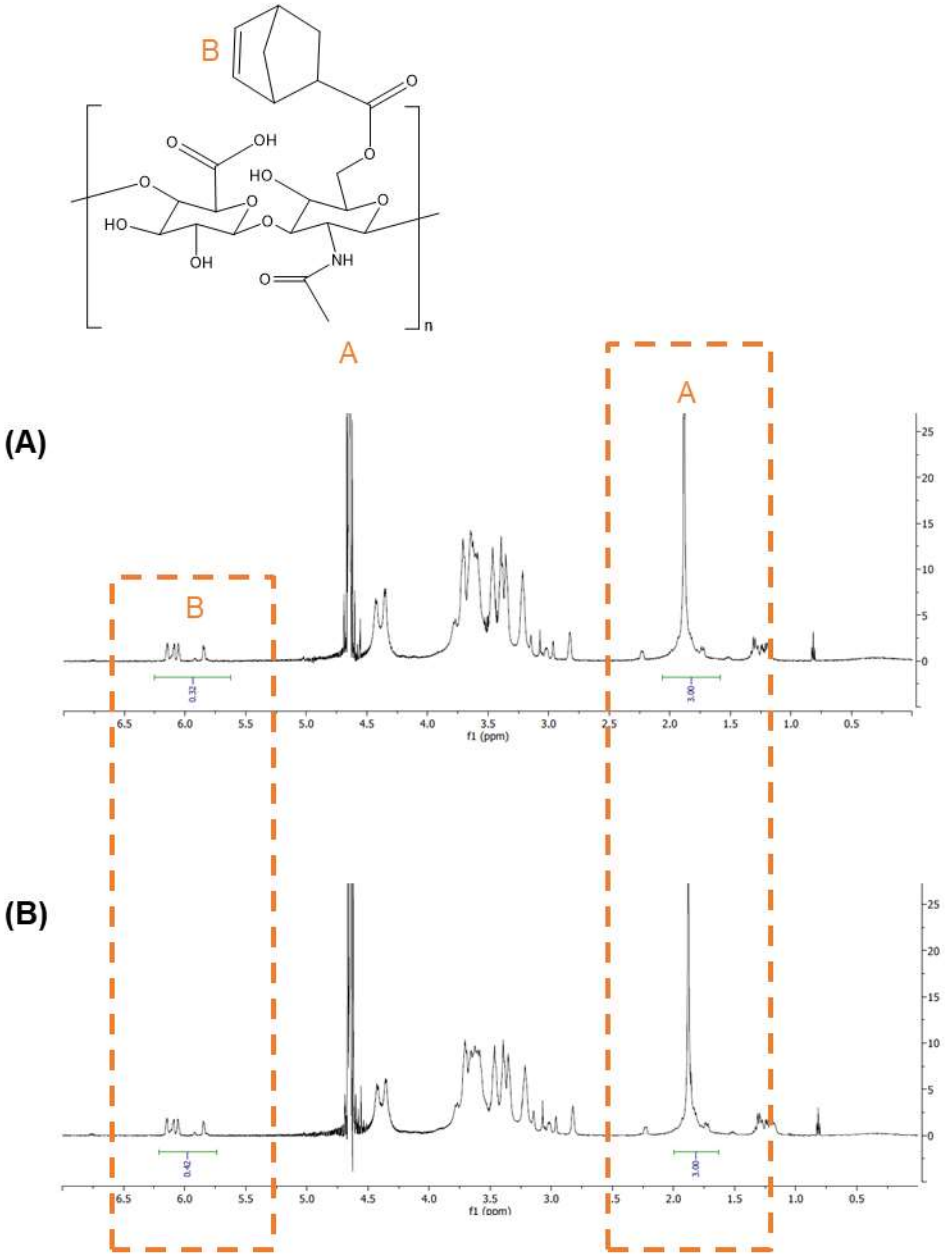

SI Fig. 1: NMR for two batches of NorHA, one modified to (A) 16% and (B) the other to 21%

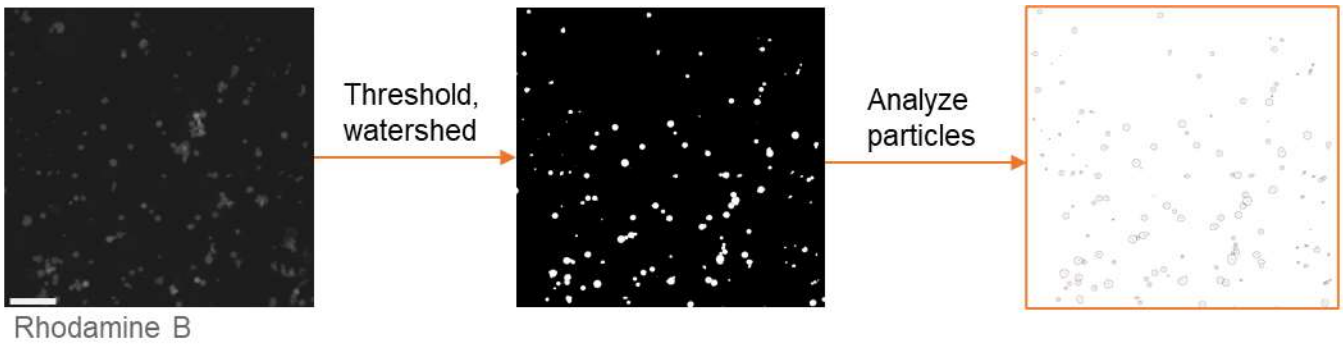

SI Fig. 2: image processing to obtain NorHA microgel diameters, scalebar=100μm

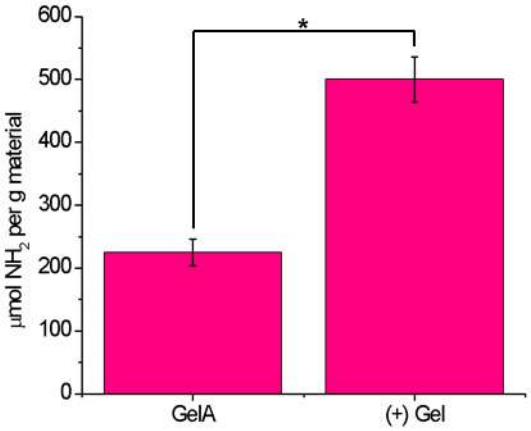

SI Fig. 3: Fluorescamine on neat gelatin and (+) Gel, * denotes $p<0.05$, error bars are standard deviation, n=3

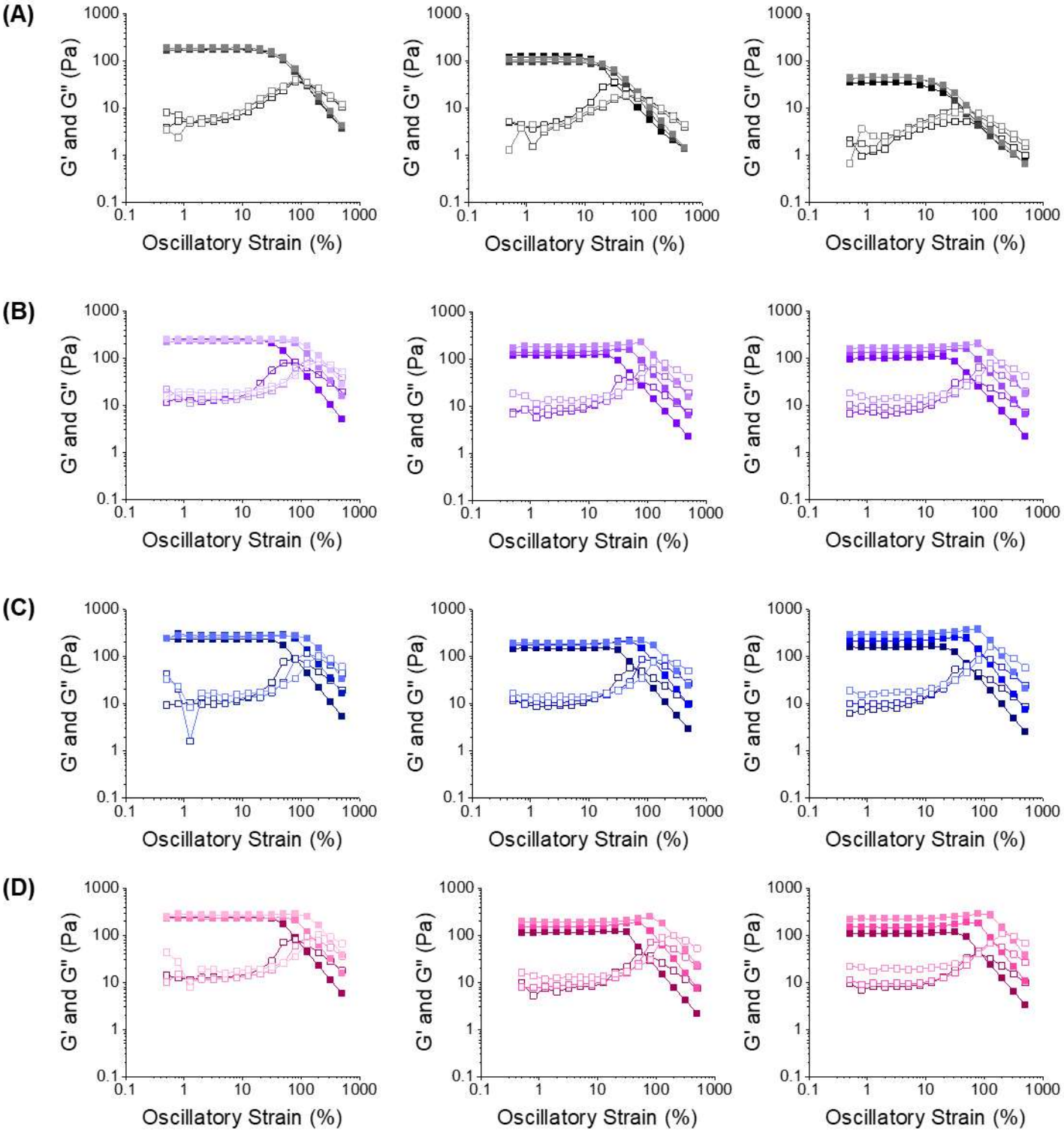

SI Fig. 4: raw rheological data showing that as compression is increased, particles tethered with (+) Gel show increases in several variables, as analyzed in Fig. 3 of the main text

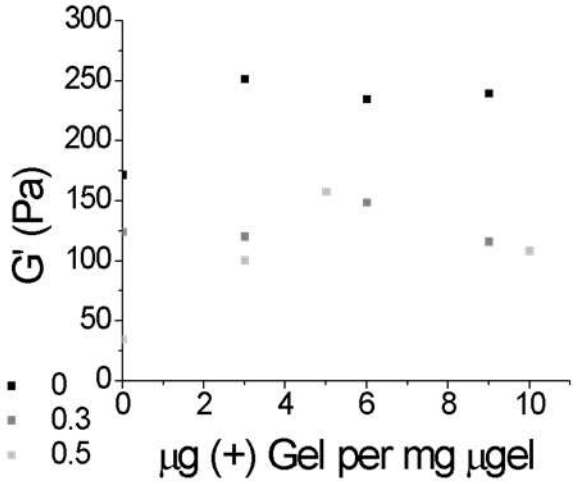

SI Fig. 5: Dependence of G' on (+) Gel concentration under non-compressive conditions

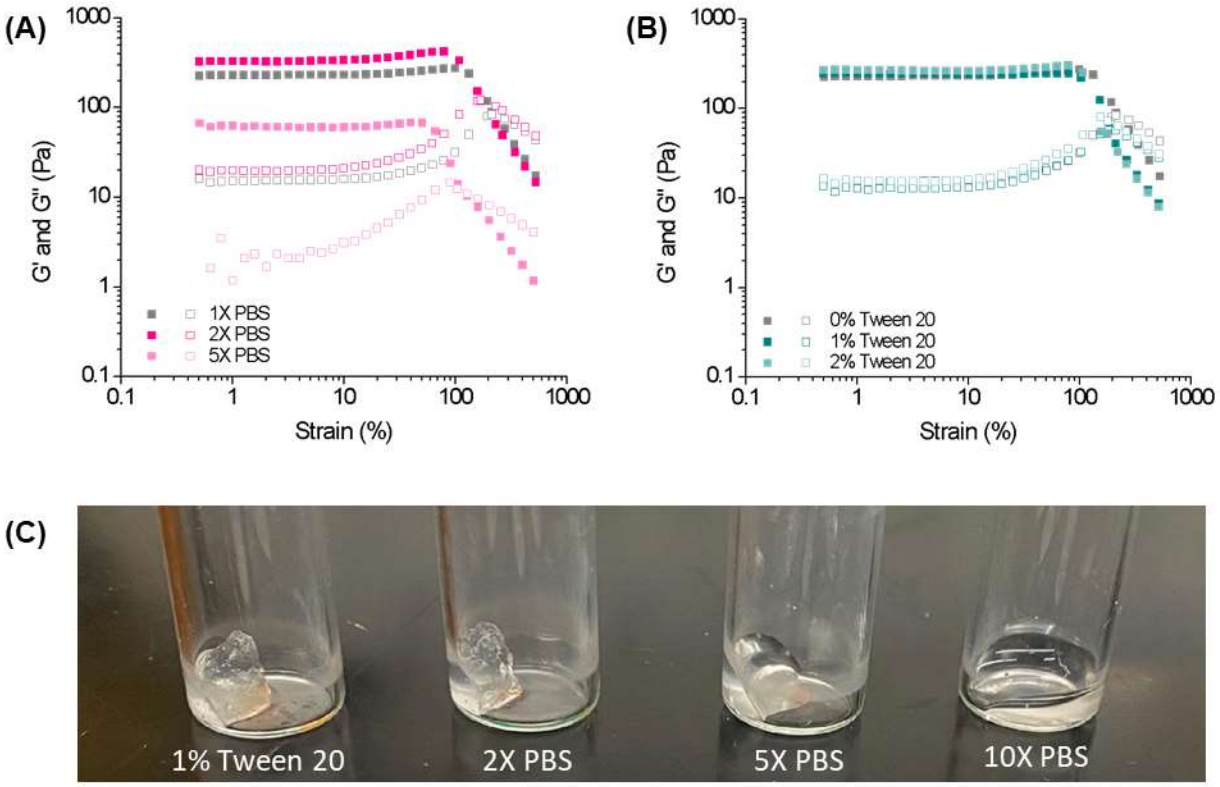

SI Fig. 6 : Assessment of (A) electrostatic and (B) hydrophobic contributions in the (+) Gel with NorHA microgels, with (C) visual confirmation that the interactions are primarily electrostatic

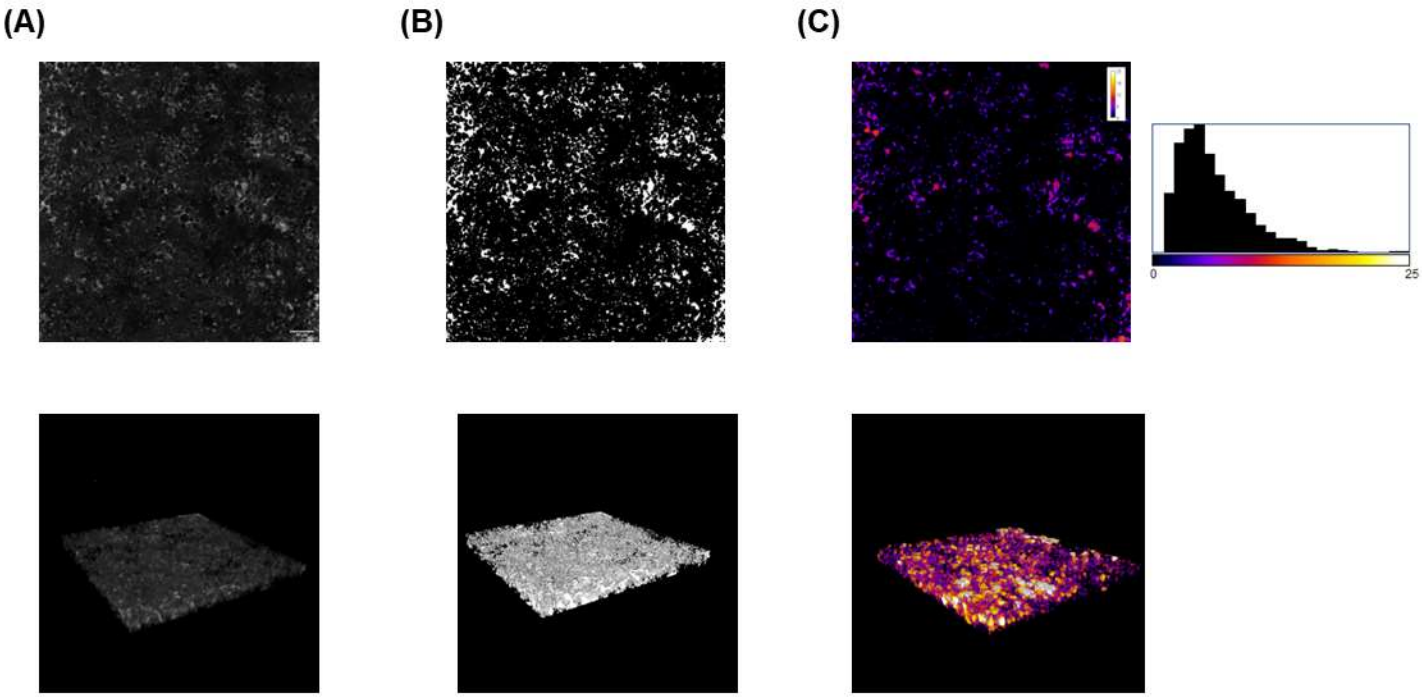

SI Fig. 7: (A) A confocal image of 2% (+) Gel formulation at a jamming fraction of 0, (B) thresholded image of (A) using Otsu's method, and (C) the trabecular thickness map generated from the thresholded z-stack in BoneJ, from which pore size distributions can be extracted. The second row is a 3D view of the z-stacks in the first row.

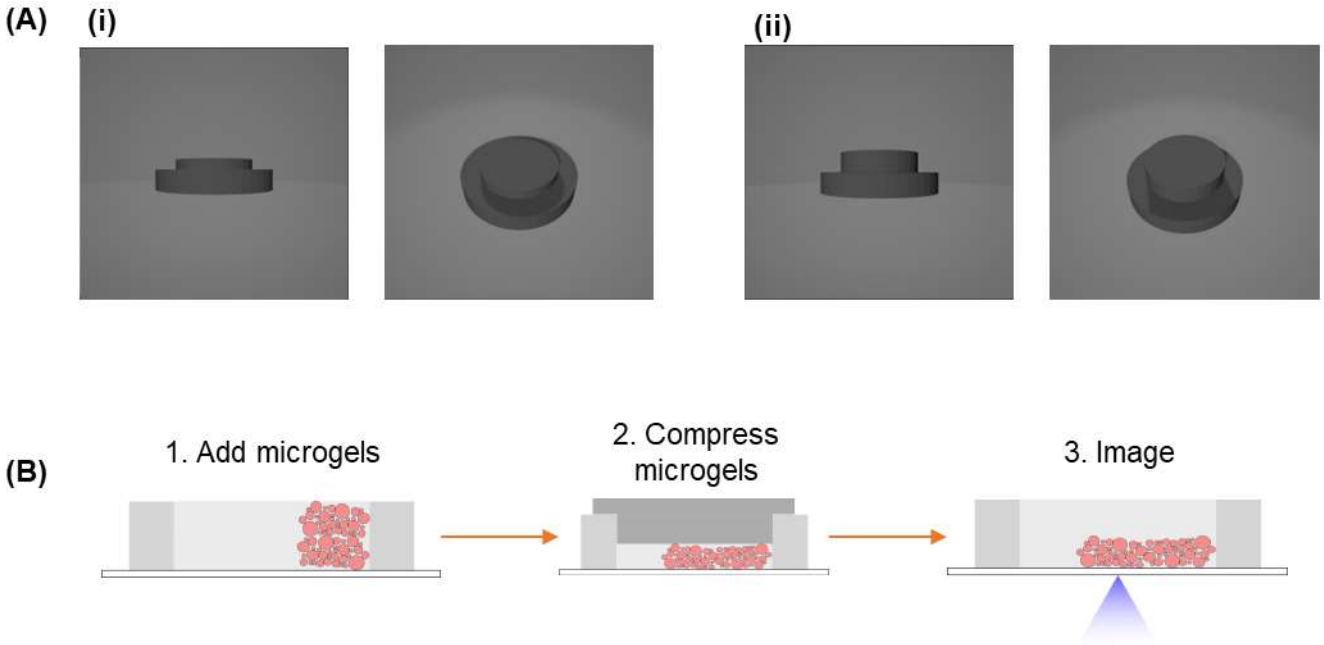

SI Fig. 8: (A) Compression testing devices for (i) 33% and (ii) 67% compressive strains, and (B) testing setup where material added to PDMS holder, then device used to compress material to selected strain, then imaging done

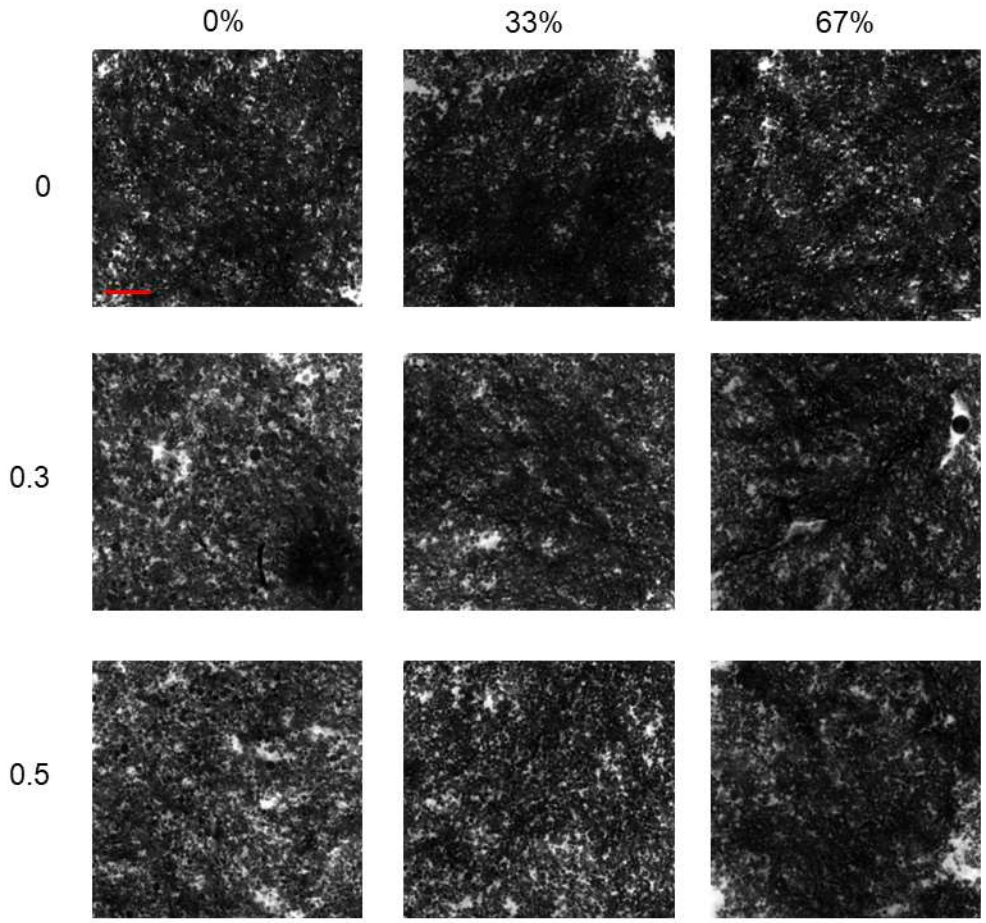

SI Fig. 9: Confocal images of 2% compression at different compressive strains and jamming fractions, scalebar=100μm

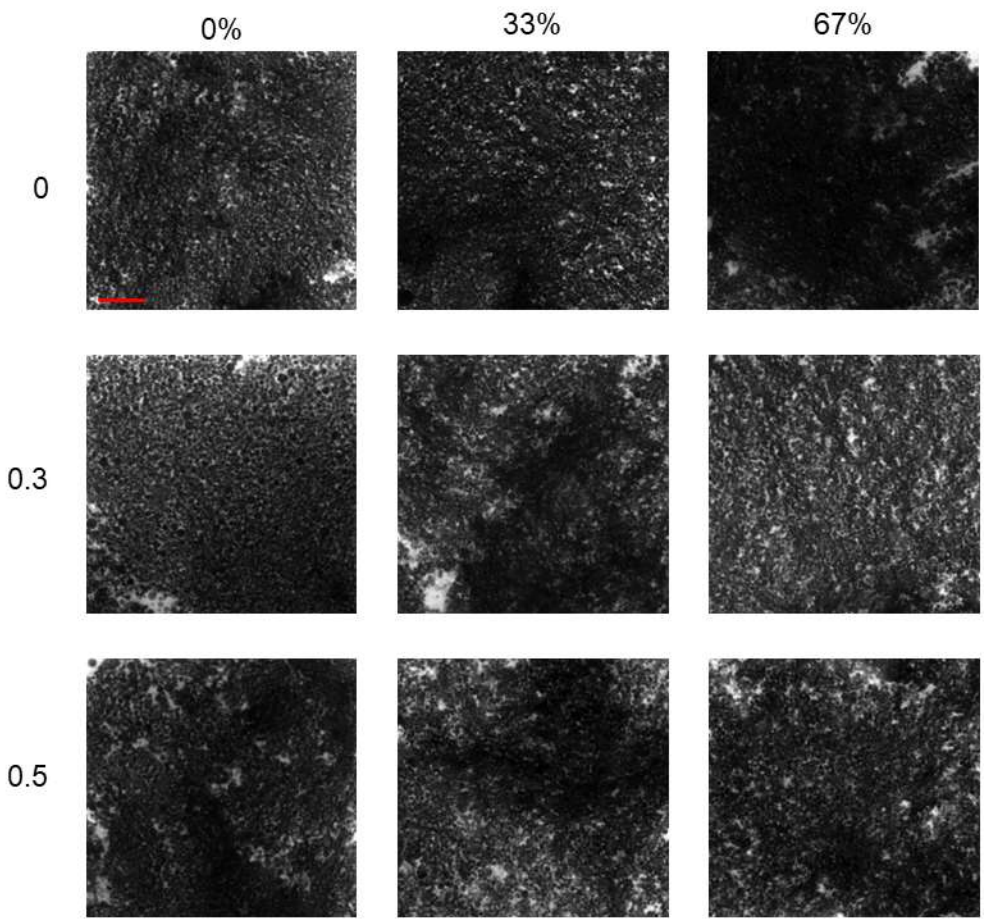

SI Fig. 10: Confocal 1% (+) gel compression at different compressive strains and jamming fractions, scalebar=100μm

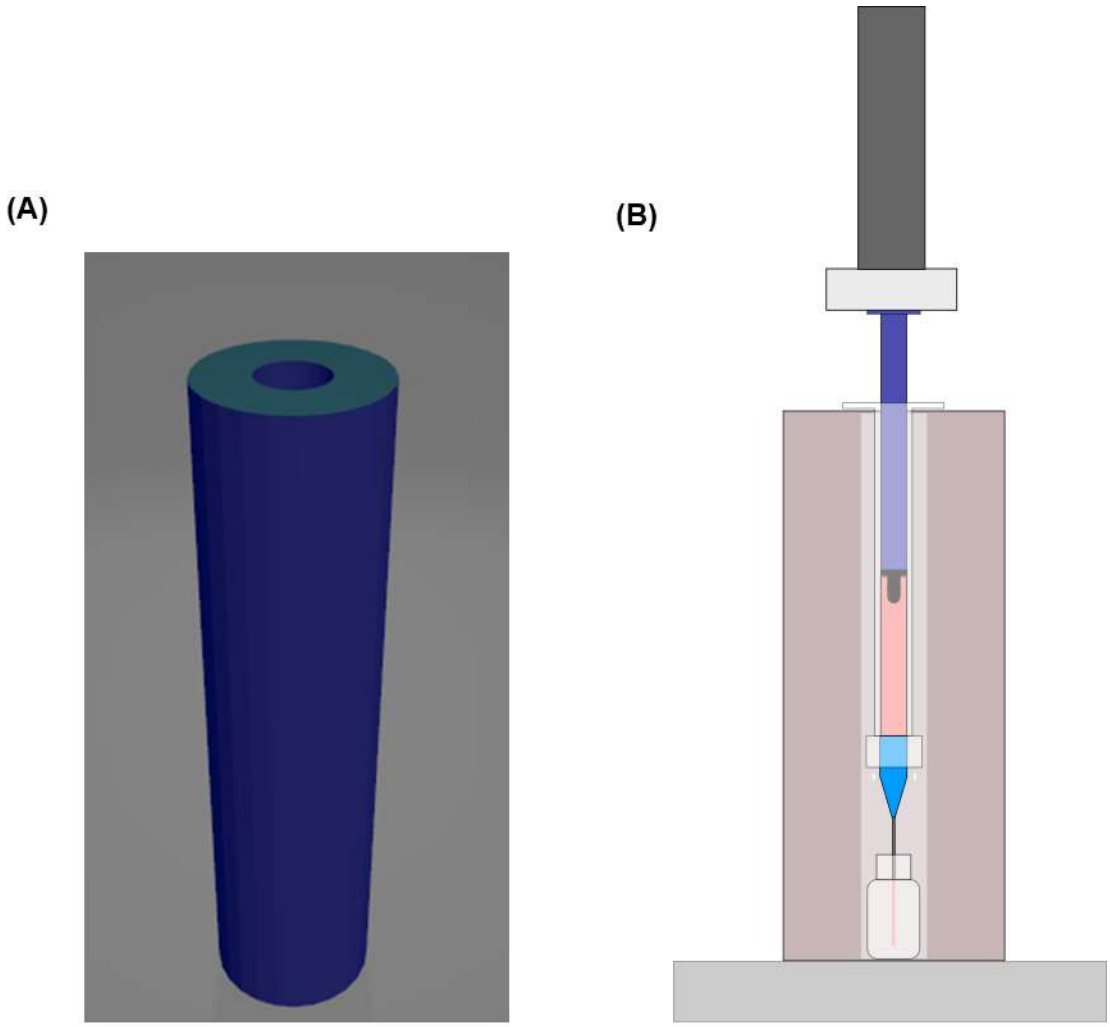

SI Fig. 11: (A) STL file of syringe holder used on instron device, and (B) cross-sectional schematic of setup on instron instrument.

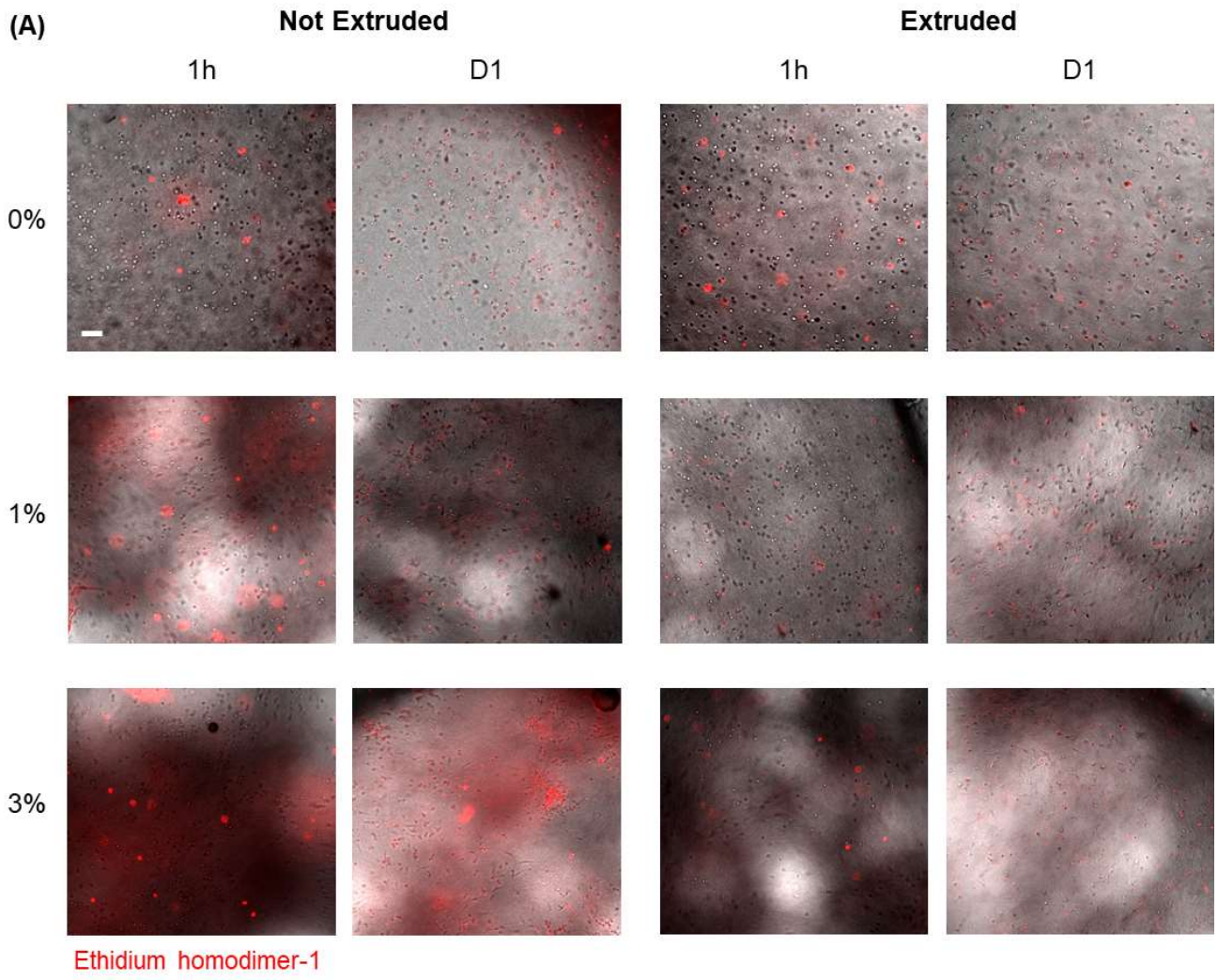

SI Fig. 12: Fibroblasts-no extrusion and extrusion groups at varying (+) Gel concentrations, separate experiment without CellTracker Green, scalebar=100µm

Chapter 4:

Pancreatic cancer: background, migration, and *in vitro* models

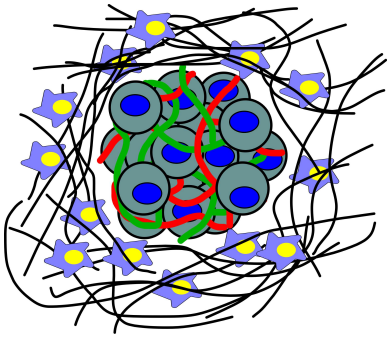

Part 1: Pancreatic ductal adenocarcinoma

PDAC statistics and background information

Pancreatic ductal adenocarcinoma (PDAC) is a devastating disease. Worldwide, there is a crude incidence rate of 6.5 per 100,000 people, and a mortality of 5.9 per 100,000[1]. In the US, this incidence is higher, at 18 per 100,000, and a mortality of 14.8 per 100,000, making it one of the top leading causes of death due to cancer. The incidence in males is typically slightly higher than females, but there is an increasing trend of pancreatic cancer diagnoses in women in the U.S.[2] These numbers are expected to increase over time[3]. The reason for this high mortality is the lack of early detection[4] and lack of noticeable symptoms[5]. Typically, patients are diagnosed at the metastatic stage of the disease, stage IV[6]. This leads to a poor prognosis, typically a 5-year survival rate of 3%[4]. Current treatment options typically include chemotherapy and surgical resection, and while the survival rate increases, it's limited to less than 20%[7,8]. Despite treatment, recurrence is also common[9]. Therefore, more research and new therapies are required to understand and treat this disease.

The pancreas is a major organ in the digestive tract, located behind the stomach. The pancreas is generally split into three parts, the head, body, and tail, and into two primary functions: endocrine and exocrine. The endocrine pancreas consists of the islets of Langerhans, well known for their control over blood sugar levels via glucagon and insulin release, as well as other hormonal functions. The exocrine pancreas is involved in the digestive process, secreting enzymes like trypsin and amylase into the duodenum. These enzymes are produced in glands that connect to a main pancreatic duct that ultimately connects with the bile duct and then into the duodenum[10]. This ductal system is where pancreatic cancer starts.

The glands, located along the ducts, are constructed as follows. The acinar cells, which are the primary cell type found in the pancreas, are polar to function appropriately. One side is associated with

exocytosis of enzymes that are then transported out of the glands into the pancreatic duct then ultimately into the duodenum to aid in digestion. The duct cells secrete bicarbonate, and the secretion of both enzymes and bicarbonate are synergized.

PDAC can be initiated from either duct cells, or acinar cells that de-differentiate into duct-like cells[11,12]. These are termed basal-type and classical-type, respectively[12]. This de-differentiation of acinar cells is known as the acinar-ductal metaplasia. Acinar cells are actively kept in their state, through expression of MIST1, GATA6, and NR5A2 to name a few[13,14]. Loss of a genetic factor causes the acinar cells to de-differentiate into a duct-like phenotype, forming a pancreatic intraepithelial neoplasia (PanIN) lesion[15]. These are separated into two grades, high and low[16]. Low-grade PanINs are normally found in pancreatic tissue and are not necessarily correlated with the development of PDAC, but high-grade PanIns generally are[16,17].

KRAS is a key player in the development of PDAC, found in over 90% of cases. KRAS is a well-studied oncogene that codes for the KRAS protein. Mutations to the genes encoding this molecular switch are commonly found in many cancers, such as PDAC[18], colorectal cancer[19], lung cancers[20], and endometrial cancer[21]. Normally, KRAS cycles between two forms: GTP- and GDP-bound, i.e. active and inactive[22]. This controls signaling pathways such as RAF-MEK-ERK, and the PI3K-AKT-mTOR pathways. These pathways are involved in cell activities such as proliferation, apoptosis, and migration[18,23]. However, once mutations have occurred, this cycling becomes aberrant. Many codons are responsible for these mutations and can lead to differences in the KRAS structure depending on which codon is mutated. The mutations lead to changes in the KRAS GTPase that confer decreased affinity to GDP, as well as a decrease in GDP production[24,25]. This leads to an accumulation of GTP-bound KRAS within the afflicted cells. As a result, the afflicted cells begin to proliferate uncontrollably and not undergo apoptosis, leading to tumor formation[18,23].

KRAS alone, however, may not be sufficient to induce tumor formation[12]. The ECM is heavily implicated in this process, where an inflammatory process leads to the positive feedback loop that confers tumor progression. When the pancreas incurs injury, inflammation occurs. Pancreatic stellate cells (PSCs), located near the acinar cells, transition from a quiescent to active state and produce extracellular matrix (ECM) components such as collagen and hyaluronic acid to combat this inflammation and repair the tissue[26,27]. The acinar cells during this process also undergo a process called acinar-ductal-metaplasia. Under normal circumstances, the inflammation resolves and the acinar cells re-differentiate from duct cells back to acinar cells and PSCs revert to a quiescent state[27,28]. With KRAS mutations, this inflammatory process can then lead to the activation of multiple cell signaling pathways. Changes in the ECM can then cause downstream cell signaling events that alter behaviors such as proliferation and

migration. Tumorigenesis is dependent on the JAK-STAT pathway, where the presence of cytokines like IL-6[29] and IL-17[30] contributes to progression from a PanIN to a tumor. This cycle continues as a positive feedback loop as the JAK/STAT pathway contributes to PSC activation[31].

As a result, the carcinogenesis of PDAC points to the importance of the ECM. The ECM is also implicated in the difficulties of treating PDAC. As collagen, hyaluronic acid, and other biopolymers are produced, a high-pressure environment is created[32,33]. This high-pressure area collapses blood vessels, leading to a hypoperfused tissue compared to the surrounding, healthy tissue[34]. The high-pressure gradient and hypoperfusion lead to issues with diffusion of chemotherapeutics and immunotherapeutics such as engineered T-cells in reaching this tumor site.

Cells in the Tumor Microenvironment

The PDAC TME is highly heterogeneous, consisting of multiple cell types. Cancer-associated fibroblasts (CAFs) are heterogeneous and come from many cell types found within the pancreatic tissue. Most common are pancreatic-stellate cells (PSCs), which are nearly in a constant activated state during tumor progression[26,31]. When TGF-beta is present, CAFs can become myofibroblast-like, and cause a stiffening of the ECM, facilitating metastasis[35]. Blood[36] and lymphatic endothelial cells[37], adipocytes[38], and other mesenchymal stromal cells[39] can also become cancer-associated fibroblasts, thus creating a highly heterogeneous and thus difficult to target group of cells. For the first type, there is a transition known as the endothelial-to-mesenchymal transition, mediated by the presence of cytokines like TNF-alpha[36]. These phenomena further contribute to the heterogeneity of the tumor microenvironment.

Immune cells, along with the cancer cells and CAFs, play a significant role in transforming the tumor area into an immune-suppressive environment. Neutrophils are recruited to the tumor site via cytokine gradients. In a study, neutrophils were able to enhance migratory behavior of PDAC cells when either directly or indirectly co-cultured through the release of TNF-alpha and TGF-beta[40]. Immune cells can also aid in the metastatic cascade. Tumor-associated macrophages (TAMs), recruited via cytokines like ICAM-1[41], contribute to an immunosuppressive environment through release of cytokines like TGF-beta[42]. Regulatory T cells are often an important aspect of the immune system to prevent attack on native tissues, but aid in creating the immunosuppressive PDAC TME. Similar to TAMs, regulatory T cells can help to reinforce the immune-suppressed TME through inhibitory interactions with dendritic cells[43], or via recruitment by myeloid-derived suppressor cells[44]. Higher activities of these cells within

PDAC tumors often indicate poor patient outcomes and are currently being assessed for targeted therapies[45–47].

Extracellular matrix of PDAC tumors

In the PDAC tumor microenvironment (TME), drastic changes to the ECM occur. Some key changes include the production of excess hyaluronic acid (HA) and collagen by PSCs[12]. HA is a polysaccharide that can be found in nearly every tissue. The hydrophilicity of HA leads to increased water retention[32,33] and this elevated pressure constricts the recruited and pre-existing blood vessels, creating a hypoxic environment and a difficult to treat tumor as circulating drugs or other types of therapeutics cannot be perfused through the tumor[34]. In PDAC, HA enhances cell migration through the CD44 receptor. As molecular weight of HA decreases, mobility of PDAC cells increases[48]. It was also found in a recent study that pancreatic tumor cells can use HA as a nutrient source, thus creating a proliferative environment[49]. Because of the impact HA has on the tumor microenvironment, it has been previously examined as a target for treating PDAC[50].

Collagen is a well-known and well-studied protein that is also extremely common in human tissue. It consists of triple-helix structures which can form fibrils, thus forming the fibrous component of native ECM. Collagen typically provides structure to tissues and has strain-stiffening behavior, similar to other ECM proteins[51]. This behavior serves to protect tissue from damage and comes from the alignment of the polymer chains. In the PDAC TME, as well as other tumor stromas like those found in breast cancer, collagen fibers become more aligned in addition to being more abundant and crosslinked. The upregulation of collagen is also due to the pancreatic stellate cells. Collagen fiber alignment, due to CAFs taking on a myofibroblast phenotype and tumor growth[52], causes an increase in stiffness due to the inherent strain-stiffening behavior found in collagen[53]. Crosslinking, a well-known mechanism to stiffen hydrogels, of collagen can occur via release of transglutaminase from PDAC cells[54]. Additionally, the alignment of collagen fibrils facilitates metastasis through a phenomenon known as contact guidance where the aligned collagen fibrils enable cell migration along the alignment direction and has been demonstrated in multiple cancer types including PDAC[55,56]. This further points to the importance of the ECM in tumor progression.

Part 2: Epithelial-Mesenchymal Transition and Cell Migratory Modes

Cell migration is an integral aspect in nearly all physiological functions. Neutrophils and T cells, for example, migrate from the blood stream into sites of infection, squeezing through capillary walls. During wound healing, cells such as fibroblasts migrate towards the wound site to produce new ECM. Cell migration is also a key player when discussing cancer metastasis. For metastasis to occur, cells must migrate out of the tumor and travel through the stroma, a process known as invasion, and finally intravasate into nearby lymphatic and blood vasculature. The cancer cells are then carried via blood vasculature to another tissue site. The metastatic cells must then extravasate into the tissue and begin proliferating and forming a new tumor[47]. The initiation of the initial movement out of the tumor requires the epithelial-mesenchymal transition[42], and has many key aspects, one of which entails ECM mechanics and composition[32,33,53].

As stated above, the ECM of the PDAC microenvironment changes drastically during tumor progression and these changes drive the epithelial-mesenchymal transition (EMT) of the mutated acinar cells. HA and collagen are erroneously upregulated by activated PSCs, and microstructural changes such as collagen fibril alignment[52] and crosslinking[54], and decreased pore size[57] can cause a subsequent increase in tumor ECM stiffness contribute to the transformation from an epithelial phenotype to a migratory mesenchymal phenotype i.e. EMT. This increased stiffness in several cancers causes a shift from epithelial to mesenchymal phenotypes[58–60].

During EMT, key epithelial features become lost, and cells take on a mesenchymal phenotype[61]. Cells lose E-Cadherin expression, responsible for connecting to other epithelial cells, and instead express N-Cadherin[62]. Transcription factors Slug, Snail, and Twist become heavily involved in facilitating the transformation[63], activated via multiple signaling pathways such as JAK-STAT, TGF-beta, Wnt, and Hippo[64–70]. Cytoskeletal changes to increase vimentin and keratin expression to enhance migratory capabilities also take place[71–73]. Polarity that was established in the epithelial phase also becomes lost, as cells detach from neighboring cells due to decreased expression of E-Cadherin[61].

The mesenchymal transition, however, includes three primary modes of migration. In addition to mesenchymal migration, two other migratory modes can be used, and interchanged, to migrate through a tissue's ECM: amoeboid and lobopodial[74]. Described in further detail below, these migratory modes enable the cell to move through a variety of environments, and cells can rapidly switch between modes as needed, a transition known as the mesenchymal-amoeboid transition (MAT) or amoeboid-mesenchymal transition (AMT)[75]. These additional transitions may also be required during the metastatic cascade for cancer cells to successfully invade other tissues and can contribute to complications with cancer treatments such as chemoresistance[76].

Mesenchymal

The mesenchymal mode of migration is defined by long extensions, slow migration speeds, and attachment to the ECM, and can be referred to as 'path-creating'. Slow speeds of this migration type, generally below 1μm/min[77], are due to formation and deformation of integrin attachments to the ECM. Cells using this mode of migration also release proteolytic enzymes to degrade the ECM, facilitating cell migration and hence 'path-creating' behavior. Cells often use filopodia and lamellipodia to move through or on a 3D or 2D substrate, respectively[74].

Mesenchymal migration is generally mediated by the Rac pathway. This pathway allows for actin polymerization to take place and form extensions like lamellipodia and therefore allow the cell to migrate. This pathway is initiated from integrins, where once the cell attaches to the surrounding ECM, Rac activation leads to the formation of lamellipodial and filopodial extension[78]. Downstream, activation of the Rac pathway leads to activation of pathways such as Hippo and Wnt. Integrins can also interact with TGF-beta in cancer cells to enhance downstream effects[79]. If the Rac pathway is inhibited through a Rho activator molecule[75] or treatment with taxol[80], then cells can transition to another mode of migration, amoeboid, which, as described below, is fast and is triggered by factors like confinement and low adhesion environments. This migration mode has been observed in collective cell migration as well[81].

Amoeboid

Amoeboid migration is defined by bleb formation and lack of adhesion to the ECM and is often termed 'path-finding' migration. These blebs allow the cell to 'sense' around its environment and lack of cell-ECM attachments mean that the cell can move quickly within a tissue[74]. This mode of migration is fast, around 10μm/min[77]. Bleb formation is a complex process dependent on actomyosin contractility[82]. The actin cytoskeleton is positioned around the perimeter of the cell, attached to the membrane. Bleb formation is initiated when part of this cytoskeleton detaches from the membrane, allowing cytoplasm to flow towards that region. This region later becomes restabilized[83]. Some evidence suggest that if actomyosin contractility is polarized, this polarization could lead to directed cell movement[84].

The major mechanotransduction pathway involved in amoeboid migration is the RhoA/ROCK pathway. This pathway mediates actin-myosin contractility that is required for amoeboid migration[83]. This pathway can become initiated by pathways such as JAK/STAT[85] and NF-kB[86]. When a ROCK inhibitor

like Y-27632 is used, cells that were undergoing amoeboid migration switch to mesenchymal migration mode[87]. This Rho pathway can also be stimulated by other factors such as interstitial flow[88] or confinement[89,90]. This Rho pathway and resulting contractility has also been observed in collective cell migration and invasion[91].

Lobopodial

Lobopodial migration is a more recent migration mode and is defined as a combination of mesenchymal and amoeboid movements. Cells undergoing this mode of migration are often elongated, but without extensions typically seen in mesenchymally-driven cell locomotion, and cell speeds are moderate[74]. Lobopodial migration can occur in instances where adhesion sites are present, and the cell is confined. Lobopodial migration is not dependent on proteolysis of the ECM, and a recent study showed that this type of migration could be re-established when protease activity was inhibited[92].

This migration type appears to be mediated by the RhoA pathway[92–94], causing a 'nuclear piston' type of migratory behavior that has been shown to propel cells forward[92,93]. To form this pressure, the nucleus is moved forward through coordination of intermediate filaments and a linker protein called nesprin-3. The resulting pull of the nucleus causes an increase in pressure at the front of the cells. This action of building pressure within the leading edge of a cell is also driven by integrin adhesions to the ECM, and actomyosin contractility[93].

Part 3: Cancer migration models

To further study mechanisms and treatment options to prevent cancer metastasis, *in vitro* models have been in development. Hydrogels, described in further detail in chapter 1, have shown great promise in this field due to their biocompatibility and tunability. Hydrogel processing for studying cancer *in vitro* can be broadly separated into three categories: 1) bulk hydrogels, 2) channel-based systems, and 3) porous constructs. Below are examples of studies for each category.

3-1 Bulk hydrogels

Bulk hydrogels are a common choice to measure the effects of distinct properties on cancer cell migration. For example, stress relaxation can be independently tuned from stiffness due to the inherent

crosslinking structure that forms the gel, causing downstream effects on cell behaviors like morphology and differentiation. Systems like these have shown great promise in deciphering the effects of ECM properties on cancer cell behaviors such as growth and migration.

A dynamic environment consisting of polymer synthesized via RAFT polymerization and containing boronate-diol bonds was fabricated and used to study viscoelastic effects on PDAC proliferation and EMT with the presence of cancer-associated fibroblasts. Boronate-diol bonds are well-characterized dynamic bonds, and the use of such bonds in combination with covalent thiol-based bonds leads to a stress-relaxing gel. Compared to completely elastic gels, which have nearly infinite stress relaxation times, PDAC cell proliferation and markers for MMPs and inflammatory cytokines were enhanced in the viscoelastic gel[95].

A sarcoma model was fabricated using collagen of varying stress-relaxation times to study the effects of hypoxia on sarcoma cell migration. Collagen fibrils were controlled to maintain fiber density even when collagen concentration changed. This allowed for control over oxygen gradients. As stress relaxation time decreased, cell migration was found to increase when in a hypoxic environment. This was accompanied by an increase in a marker known as PLOD2, a collagen crosslinker, an increase in collagen size and density, and metastasis[96].

To examine the effects of plasticity on breast cancer, an interpenetrating network of alginate and reconstituted basement membrane was made. To create different levels of matrix plasticity, alginate molecular weight was modified. Data showed that cells do not require proteases to move through the matrix material, but rather can open or deform the local region to migrate. Cells contained in hydrogels with high plasticity generally showed greater probabilities of protrusions and max displacement compared to cells encapsulated in low plasticity hydrogels. It was also found that this movement was mediated via the Rho pathway and actomyosin contractility[97].

Glioblastoma cells were encapsulated either as single cells or as a spheroid in Matrigel. The purpose was to determine if cells coming from a spheroid follow a biased persistent random walk model as opposed to the more popular persistent random walk model. Compared with single cells, cells coming off a spheroid were found to quickly move away from the spheroid, thus showing directionality and higher velocity[98].

Another study using Matrigel and glioblastoma spheroids analyzed the effects of matrix stiffness on glioblastoma cell migration from spheroids. Here, researchers examined motility of individual cells disseminating from a spheroid. Lower matrix stiffness led to an increase in spheroid area, which indicated a decrease in invasiveness of the cells in high stiffness matrices. No effect on migration

speeds were observed. For this line of tumor cells, migration was done in a primarily independent manner, and were found to migrate with directionality and persistence. The researchers were also able to identify super-spreading cells by examining cell trajectories[99].

As stated earlier, motile cancer cells can switch from mesenchymal to amoeboid migration modes in response to the local environment. In one study, this behavior was captured in a silk-collagen composite hydrogel. By keeping collagen concentration the same to keep cell-attachment points constant, silk fibroin, a protein derived from *B. mori* cocoons, was included at varying concentrations to alter mechanical and microarchitectural properties as it does not have inherent cell-attachment moieties. When pore size decreased, cells that were migrating in a primarily mesenchymal mode switched to a more amoeboid mode. Additionally, cells in gels without collagen also exhibited amoeboid migration, due to the lack of cell attachment moieties. The cells could also be made to adopt other migration modes by including excipients like Taxol for inducing amoeboid migration, or EGF to induce mesenchymal migration[80].

3-2 Channel-based systems

The origin of PDAC comes from a topographically-defined region of the pancreas: the ductal system. This is a tubular network with glands along and branching off of these structures. To make a more physiologically-relevant model, open channels can be fabricated into hydrogels in a number of ways. For example, casting and molding around a needle provides a facile and reproducible method. Microfluidics are another option to create channels with tunable sizes that can then be lined with cells or proteins and then used to study cell migration through the channel or invading into the surrounding hydrogel.

A collagen gel was casted around two 300 μm needles then removed to form open channels after the collagen polymerized. These channels were separated at an approximately 500μm distance. In one channel, mouse PDAC cells were seeded to form the PDAC-lined channel, while the other channel contained HUVECs to form an endothelialized channel. An FBS gradient was established coming from the endothelial channel to stimulate PDAC migration towards that channel. PDAC cells were found to collectively migrate through the collagen towards then invade the endothelial channel. This ablation was found to occur through TGF-beta and activin-ALK7 signaling pathways. This ablation is thought to be a path for PDAC metastasis[100].

Another study used this casting and molding technique on collagen to create a ductal-tumor-microenvironment-on-chip (dT-MOC) to study heterogeneous populations of PDAC cells. PDAC, as stated earlier, is known to be a heterogeneous tumor. The researchers examined cells from different mutated mouse models and seeded them into these perfused channels. Channels formed here ranged from 500-800μm in diameter. The mesenchymal subtype for one of the two cell lines harvested exhibited EMT markers like SNAIL. On days 3 and 4 post-seeding, the mesenchymal subtype showed greater invasion scores and average sprout lengths compared to the epithelial subtype of the same line and the other cell line. For the non-migratory cells, the presence of TGF-beta enhanced both invasion scores and sprout lengths. Multiple cell lines could be seeded into the perfused channels, illustrating the adaptability of this system to studying heterogeneous tumors[101].

Microtracks are a common feature found in the ECM of tissues like mammary tissue and can be used by migratory cancer cells to exit the TME and metastasize. Using a PDMS stamp, microtracks within a collagen hydrogel were created. Compared to collagen hydrogels without microtracks, a greater fraction of breast cancer cells were migratory independent of collagen concentration. Collagen concentration played a greater role in samples without microtracks, causing a decrease in cell motility. Contraction of the actin cytoskeletal was important to cell migration through these microtracks. This study illustrated how cells can migrate through a 'path of least resistance' mechanism that is independent of ECM mechanics[102].

Microchannels to study the effect of pore size on migration have been fabricated using lithographic techniques to create devices similar to microfluidic devices. To establish a link between confinement, as defined by channel width, and the mesenchymal-amoeboid transition (MAT), channels of 150μm in length and either 3μm or 10μm in diameter were fabricated using photolithography. The devices were comprised of PDMS bonded to a glass substrate. This study evaluated the switch in migration modes of eight cell lines. For three of four cell lines, migration through the 3μm channels was faster compared to the 10μm channel. For cells that traversed the length of the 3μm channels, amoeboid-like morphology was observed upon the cell exiting the microchannel. Cancer cells also had lower levels of integrins in the 3μm channels compared to unconfined cells and cells within the 10μm channels, further confirming the potential of a MAT controlled via confinement[89].

Patterned microchannels have been used to separate a heterogeneous cell population via chemotaxis. Also using PDMS and photolithography, a device with serpentine channels was fabricated. Migration of breast cancer cells was studied. Upon separation of chemotactic and non-chemotactic cells, further analyses were done to compare the two groups. The chemotactic cells showed greater aspect ratio

compared to non-chemotactic, as well as greater migration distance. Chemotactic cells also showed upregulation in RhoC compared to non-chemotactic cells[103].

3-3 Granular and microporous systems

Porosity can be introduced in a number of ways. One way is to add porogens to a hydrogel precursor solution, and upon stabilization of the hydrogel solution, porogens can then be leached. Another method is through freeze-drying processes. 3D printing can be utilized to form pore structures. Granular materials, as explained in chapter 1, have an inherent porosity that can be exploited and easily tuned in cell migration studies. Because cancer cell migration work within these material types is limited, the work summarized here includes other cell types.

T cells were placed into a jammed microgel system composed of Carbopol (poly(acrylic acid)) particles. To modulate the yield stress of the material, global polymer concentration was changed. T cell migration was monitored over time, and it was shown that migration was dependent on yield stress. As yield stress increased from 2.1 Pa to 6.2 Pa, cell movement transitioned from subdiffusive behavior to superdiffusive behavior i.e. from stationary to on par with active motility. This however was dependent on timescale and cells could, for example, become trapped at longer timescales in the highest yield stress material tested. It was also found that T cells would migrate through available pore spaces rather than yielding the material to migrate[104].

Chitosan and alginate were combined to form highly porous constructs to study breast cancer cell migration. These scaffolds were easily tunable to enable studies into effects of ECM stiffness, and the pores were interconnected. Results demonstrated that in porous materials, material stiffness significantly impacts cell migratory behaviors, as the highest polymer concentration tested, 6wt%. Because chitosan and alginate do not have cell-binding moieties, this indicates that cells can sense ECM stiffness in the absence of integrin adhesion[59].

The effect of pore anisotropy on breast cancer cell migration was studied using collagen scaffolds. This was achieved by modulating a freeze-drying process when processing the collagen material. The researchers observed that cells directionally migrated in scaffolds with anisotropic pores. Migratory behavior was also greater in these constructs compared to the isotropic scaffolds[105].

3D printing techniques have been used to control scaffold architectures[106–108], and has been used to decouple pore size from material modulus. Poly(ethylene glycol)-diacrylate (PEGDA) scaffolds were printed using digital micromirror-based projection printing and designed to have pore spaces between

250 and 300um. To modify stiffness, PEGDA concentration was tuned. Mammary epithelial and TWIST-modified mammary epithelial cell migration was tested on these porous constructs and compared with 2D migration on hydrogels with stiffnesses matched. It was found that displacement was greater in 3D compared to 2D. A greater difference attributed to stiffness was seen in the TWIST-modified cells[109].

Molecular weight (MW) of hyaluronic acid (HA) can impact cell behaviors and has been found to aid in cancer cell migration. To test this on breast cancer cells in a 3D environment, HA of varying molecular weights were made into hydrogels with collagen to mimic the fibrous ECM. The addition of high MW HA produced scaffolds with larger pore sizes. The higher MW HAs tested showed that cell migration was inhibited compared to the lowest MW tested and to collagen-only gels[110].

Pore features as well as size can contribute to changes in cell migratory behavior. In one study, pores of varying aspect ratios were created using nanolithography techniques. Normal and metastatic breast epithelial cells were studied. It was found that, even though pore size remained constant, aspect ratio played a significant role in cell migration, and that metastatic cells tend to travel in a ‘path of least resistance’ manner whereas the normal epithelial cells maintained directionality[111].

Granular or porous media can also impact prokaryotic cell migration. E. coli motility in a Carbopol-based granular medium was monitored over time. Similar to mammalian cells, bacteria would show ‘trapped’ behavior within the granular medium, and also exhibit ‘hopping’ motions. Effects from pore sizes were also studied and showed that as pore size increased, the mean-squared displacement became larger and appeared to show more persistent migratory paths[112].

References

1. Cancer Today. https://gco.iarc.who.int/today/.
2. Abboud, Y. *et al.* Increasing Pancreatic Cancer Incidence in Young Women in the United States: A Population-Based Time-Trend Analysis, 2001–2018. *Gastroenterology* **164**, 978-989.e6 (2023).
3. SEER*Explorer Application. https://seer.cancer.gov/statistics-network/explorer/application.html?site=40&data_type=1&graph_type=2&compareBy=sex&chk_sex_3=3&chk_sex_2=2&rate_type=2&race=1&age_range=1&stage=101&advopt_precision=1&advopt_show_ci=on&hdn_view=0&advopt_show_apc=on&advopt_display=2#resultsRegion0.
4. Pancreatic Cancer - Statistics. *Cancer.Net* https://www.cancer.net/cancer-types/pancreatic-cancer/statistics (2012).
5. Siegel, R. L., Miller, K. D. & Jemal, A. Cancer statistics, 2018. *CA. Cancer J. Clin.* **68**, 7–30 (2018).
6. Rawla, P., Sunkara, T. & Gaduputi, V. Epidemiology of Pancreatic Cancer: Global Trends, Etiology and Risk Factors. *World J. Oncol.* **10**, 10–27 (2019).
7. Ruess, D. A. *et al.* The prognostic influence of intrapancreatic tumor location on survival after resection of pancreatic ductal adenocarcinoma. *BMC Surg.* **15**, 123 (2015).
8. van Erning, F. N. *et al.* Association of the location of pancreatic ductal adenocarcinoma (head, body, tail) with tumor stage, treatment, and survival: a population-based analysis. *Acta Oncol.* **57**, 1655–1662 (2018).
9. Fischer, R. *et al.* Early Recurrence of Pancreatic Cancer after Resection and During Adjuvant Chemotherapy. *Saudi J. Gastroenterol. Off. J. Saudi Gastroenterol. Assoc.* **18**, 118–121 (2012).
10. Longnecker, D. S. & Thompson, E. D. Anatomy, Histology, and Fine Structure of the Pancreas. in *The Pancreas* 9–22 (John Wiley & Sons, Ltd, 2023). doi:10.1002/9781119876007.ch2.
11. Xu, Y., Liu, J., Nipper, M. & Wang, P. Ductal vs . acinar? Recent insights into identifying cell lineage of pancreatic ductal adenocarcinoma. *Ann. Pancreat. Cancer* **2**, (2019).
12. Storz, P. & Crawford, H. C. Carcinogenesis of Pancreatic Ductal Adenocarcinoma. *Gastroenterology* **158**, 2072–2081 (2020).

13. Storz, P. Acinar cell plasticity and development of pancreatic ductal adenocarcinoma. *Nat. Rev. Gastroenterol. Hepatol.* **14**, 296–304 (2017).

14. Grimont, A., Leach, S. D. & Chandwani, R. Uncertain Beginnings: Acinar and Ductal Cell Plasticity in the Development of Pancreatic Cancer. *Cell. Mol. Gastroenterol. Hepatol.* **13**, 369–382 (2021).

15. Figura, G. von, Morris, J. P., Wright, C. V. E. & Hebrok, M. Nr5a2 maintains acinar cell differentiation and constrains oncogenic Kras-mediated pancreatic neoplastic initiation. *Gut* **63**, 656–664 (2014).

16. Basturk, O. *et al.* A Revised Classification System and Recommendations From the Baltimore Consensus Meeting for Neoplastic Precursor Lesions in the Pancreas. *Am. J. Surg. Pathol.* **39**, 1730 (2015).

17. Andea, A., Sarkar, F. & Adsay, V. N. Clinicopathological Correlates of Pancreatic Intraepithelial Neoplasia: A Comparative Analysis of 82 Cases With and 152 Cases Without Pancreatic Ductal Adenocarcinoma. *Mod. Pathol.* **16**, 996–1006 (2003).

18. Luo, J. KRAS mutation in Pancreatic Cancer. *Semin. Oncol.* **48**, 10–18 (2021).

19. Zhu, G., Pei, L., Xia, H., Tang, Q. & Bi, F. Role of oncogenic KRAS in the prognosis, diagnosis and treatment of colorectal cancer. *Mol. Cancer* **20**, 143 (2021).

20. Westcott, P. M. K. & To, M. D. The genetics and biology of KRAS in lung cancer. *Chin. J. Cancer* **32**, 63–70 (2013).

21. Sideris, M. *et al.* The Role of KRAS in Endometrial Cancer: A Mini-Review. *Anticancer Res.* **39**, 533–539 (2019).

22. Bos, J. L., Rehmann, H. & Wittinghofer, A. GEFs and GAPs: Critical Elements in the Control of Small G Proteins. *Cell* **129**, 865–877 (2007).

23. Huang, L., Guo, Z., Wang, F. & Fu, L. KRAS mutation: from undruggable to druggable in cancer. *Signal Transduct. Target. Ther.* **6**, 1–20 (2021).

24. Smith, M. J., Neel, B. G. & Ikura, M. NMR-based functional profiling of RASopathies and oncogenic RAS mutations. *Proc. Natl. Acad. Sci. U. S. A.* **110**, 4574–4579 (2013).

25. Hunter, J. C. *et al.* Biochemical and Structural Analysis of Common Cancer-Associated KRAS Mutations. *Mol. Cancer Res.* **13**, 1325–1335 (2015).

26. Masamune, A., Watanabe, T., Kikuta, K. & Shimosegawa, T. Roles of Pancreatic Stellate Cells in Pancreatic Inflammation and Fibrosis. *Clin. Gastroenterol. Hepatol.* **7**, S48–S54 (2009).

27. Yokota, T. *et al.* Pancreatic Stellate Cell Activation and MMP Production in Experimental Pancreatic Fibrosis. *J. Surg. Res.* **104**, 106–111 (2002).

28. Wang, L., Xie, D. & Wei, D. Pancreatic Acinar-to-Ductal Metaplasia and Pancreatic Cancer. in *Pancreatic Cancer: Methods and Protocols* (ed. Su, G. H.) 299–308 (Springer, New York, NY, 2019). doi:10.1007/978-1-4939-8879-2_26.

29. Corcoran, R. B. *et al.* STAT3 Plays a Critical Role in KRAS-Induced Pancreatic Tumorigenesis. *Cancer Res.* **71**, 5020–5029 (2011).

30. Loncle, C. *et al.* IL17 Functions through the Novel REG3β–JAK2–STAT3 Inflammatory Pathway to Promote the Transition from Chronic Pancreatitis to Pancreatic Cancer. *Cancer Res.* **75**, 4852–4862 (2015).

31. Komar, H. M. *et al.* Inhibition of Jak/STAT signaling reduces the activation of pancreatic stellate cells in vitro and limits caerulein-induced chronic pancreatitis in vivo. *Sci. Rep.* **7**, 1787 (2017).

32. DuFort, C. C. *et al.* Interstitial Pressure in Pancreatic Ductal Adenocarcinoma Is Dominated by a Gel-Fluid Phase. *Biophys. J.* **110**, 2106–2119 (2016).

33. Provenzano, P. P. & Hingorani, S. R. Hyaluronan, fluid pressure, and stromal resistance in pancreas cancer. *Br. J. Cancer* **108**, 1–8 (2013).

34. Park, M.-S. *et al.* Perfusion CT: Noninvasive Surrogate Marker for Stratification of Pancreatic Cancer Response to Concurrent Chemo- and Radiation Therapy. *Radiology* **250**, 110–117 (2009).

35. Tomasek, J. J., Gabbiani, G., Hinz, B., Chaponnier, C. & Brown, R. A. Myofibroblasts and mechano-regulation of connective tissue remodelling. *Nat. Rev. Mol. Cell Biol.* **3**, 349–363 (2002).

36. Adjuto-Saccone, M. *et al.* TNF-α induces endothelial–mesenchymal transition promoting stromal development of pancreatic adenocarcinoma. *Cell Death Dis.* **12**, 649 (2021).

37. Wei, W.-F. *et al.* Cancer-associated fibroblast-derived PAI-1 promotes lymphatic metastasis via the induction of EndoMT in lymphatic endothelial cells. *J. Exp. Clin. Cancer Res.* **42**, 160 (2023).

38. Bochet, L. *et al.* Adipocyte-Derived Fibroblasts Promote Tumor Progression and Contribute to the Desmoplastic Reaction in Breast Cancer. *Cancer Res.* **73**, 5657–5668 (2013).

39. Helms, E. J. *et al.* Mesenchymal Lineage Heterogeneity Underlies Nonredundant Functions of Pancreatic Cancer–Associated Fibroblasts. *Cancer Discov.* **12**, 484–501 (2022).

40. Lianyuan, T. *et al.* Tumor associated neutrophils promote the metastasis of pancreatic ductal adenocarcinoma. *Cancer Biol. Ther.* **21**, 937–945 (2020).

41. Liou, G.-Y. *et al.* Mutant KRAS–Induced Expression of ICAM-1 in Pancreatic Acinar Cells Causes Attraction of Macrophages to Expedite the Formation of Precancerous Lesions. *Cancer Discov.* **5**, 52–63 (2015).

42. Bonde, A.-K., Tischler, V., Kumar, S., Soltermann, A. & Schwendener, R. A. Intratumoral macrophages contribute to epithelial-mesenchymal transition in solid tumors. *BMC Cancer* **12**, 35 (2012).

43. Jang, J.-E. *et al.* Crosstalk between Regulatory T Cells and Tumor-Associated Dendritic Cells Negates Anti-tumor Immunity in Pancreatic Cancer. *Cell Rep.* **20**, 558–571 (2017).

44. Pan, P.-Y. *et al.* Immune Stimulatory Receptor CD40 Is Required for T-Cell Suppression and T Regulatory Cell Activation Mediated by Myeloid-Derived Suppressor Cells in Cancer. *Cancer Res.* **70**, 99–108 (2010).

45. Gulhati, P. *et al.* Targeting T cell checkpoints 41BB and LAG3 and myeloid cell CXCR1/CXCR2 results in antitumor immunity and durable response in pancreatic cancer. *Nat. Cancer* **4**, 62–80 (2023).

46. Penny, H. L. *et al.* Targeting Glycolysis in Macrophages Confers Protection Against Pancreatic Ductal Adenocarcinoma. *Int. J. Mol. Sci.* **22**, 6350 (2021).

47. Jiang, W., Li, X., Xiang, C. & Zhou, W. Neutrophils in pancreatic cancer: Potential therapeutic targets. *Front. Oncol.* **12**, 1025805 (2022).

48. Cheng, X.-B., Kohi, S., Koga, A., Hirata, K. & Sato, N. Hyaluronan stimulates pancreatic cancer cell motility. *Oncotarget* **7**, 4829 (2016).

49. Kim, P. K. *et al.* Hyaluronic acid fuels pancreatic cancer cell growth. *eLife* **10**, e62645 (2021).

50. Sato, N., Cheng, X.-B., Kohi, S., Koga, A. & Hirata, K. Targeting hyaluronan for the treatment of pancreatic ductal adenocarcinoma. *Acta Pharm. Sin. B* **6**, 101–105 (2016).

51. Storm, C., Pastore, J. J., MacKintosh, F. C., Lubensky, T. C. & Janmey, P. A. Nonlinear elasticity in biological gels. *Nature* **435**, 191–194 (2005).

52. Seo, B. R. *et al.* Collagen microarchitecture mechanically controls myofibroblast differentiation. *Proc. Natl. Acad. Sci.* **117**, 11387–11398 (2020).

53. Seager, R. J., Hajal, C., Spill, F., Kamm, R. D. & Zaman, M. H. Dynamic interplay between tumour, stroma and immune system can drive or prevent tumour progression. *Converg. Sci. Phys. Oncol.* **3**, 034002 (2017).

54. Lee, J. *et al.* Tissue Transglutaminase Mediated Tumor–Stroma Interaction Promotes Pancreatic Cancer Progression. *Clin. Cancer Res.* **21**, 4482–4493 (2015).

55. Ramirez-San Juan, G. R., Oakes, P. W. & Gardel, M. L. Contact guidance requires spatial control of leading-edge protrusion. *Mol. Biol. Cell* **28**, 1043–1053 (2017).

56. Modeling the two-way feedback between contractility and matrix realignment reveals a nonlinear mode of cancer cell invasion | PNAS. https://www.pnas.org/doi/full/10.1073/pnas.1617037114.

57. García-Gareta, E. *et al.* Physico-chemical characterization of the tumour microenvironment of pancreatic ductal adenocarcinoma. *Eur. J. Cell Biol.* **103**, 151396 (2024).

58. Rice, A. J. *et al.* Matrix stiffness induces epithelial–mesenchymal transition and promotes chemoresistance in pancreatic cancer cells. *Oncogenesis* **6**, e352–e352 (2017).

59. Le, M.-C. N. *et al.* Evaluation of the effect of 3D porous Chitosan-alginate scaffold stiffness on breast cancer proliferation and migration. *J. Biomed. Mater. Res. A* **109**, 1990–2000 (2021).

60. Dong, Y. *et al.* Higher matrix stiffness as an independent initiator triggers epithelial-mesenchymal transition and facilitates HCC metastasis. *J. Hematol. Oncol.J Hematol Oncol* **12**, 112 (2019).

61. Yang, J. *et al.* Guidelines and definitions for research on epithelial–mesenchymal transition. *Nat. Rev. Mol. Cell Biol.* **21**, 341–352 (2020).

62. Mrozik, K. M., Blaschuk, O. W., Cheong, C. M., Zannettino, A. C. W. & Vandyke, K. N-cadherin in cancer metastasis, its emerging role in haematological malignancies and potential as a therapeutic target in cancer. *BMC Cancer* **18**, 939 (2018).

63. Debnath, P., Huirem, R. S., Dutta, P. & Palchaudhuri, S. Epithelial–mesenchymal transition and its transcription factors. *Biosci. Rep.* **42**, BSR20211754 (2021).

64. Liu, X. *et al.* Roles of Signaling Pathways in the Epithelial-Mesenchymal Transition in Cancer. *Asian Pac. J. Cancer Prev.* **16**, 6201–6206 (2015).

65. Deshmukh, A. P. *et al.* Identification of EMT signaling cross-talk and gene regulatory networks by single-cell RNA sequencing. *Proc. Natl. Acad. Sci.* **118**, e2102050118 (2021).

66. Kong, F. *et al.* Regulation of epithelial-mesenchymal transition by protein lysine acetylation. *Cell Commun. Signal.* **20**, 57 (2022).

67. Cho, K. H. *et al.* STAT3 mediates TGF-β1-induced TWIST1 expression and prostate cancer invasion. *Cancer Lett.* **336**, 167–173 (2013).

68. Akrida, I., Bravou, V. & Papadaki, H. The deadly cross-talk between Hippo pathway and epithelial–mesenchymal transition (EMT) in cancer. *Mol. Biol. Rep.* **49**, 10065–10076 (2022).

69. Yin, L. *et al.* SH3BGRL2 inhibits growth and metastasis in clear cell renal cell carcinoma via activating hippo/TEAD1-Twist1 pathway. *EBioMedicine* **51**, 102596 (2020).

70. The Hippo transducer TAZ promotes epithelial to mesenchymal transition and cancer stem cell maintenance in oral cancer - Li - 2015 - Molecular Oncology - Wiley Online Library. https://febs.onlinelibrary.wiley.com/doi/10.1016/j.molonc.2015.01.007.

71. Wu, H. *et al.* Vimentin intermediate filaments and filamentous actin form unexpected interpenetrating networks that redefine the cell cortex. *Proc. Natl. Acad. Sci. U. S. A.* **119**, e2115217119 (2022).

72. Alisafaei, F. *et al.* Vimentin Intermediate Filaments Can Enhance or Abate Active Cellular Forces in a Microenvironmental Stiffness-Dependent Manner. 2022.04.02.486829 Preprint at https://doi.org/10.1101/2022.04.02.486829 (2022).

73. Battaglia, R. A., Delic, S., Herrmann, H. & Snider, N. T. Vimentin on the move: new developments in cell migration. Preprint at https://doi.org/10.12688/f1000research.15967.1 (2018).

74. Yamada, K. M. & Sixt, M. Mechanisms of 3D cell migration. *Nat. Rev. Mol. Cell Biol.* **20**, 738–752 (2019).

75. Taddei, M. L. *et al.* Mesenchymal to amoeboid transition is associated with stem-like features of melanoma cells. *Cell Commun. Signal.* **12**, 24 (2014).

76. Ketchen, S. E. *et al.* Drug Resistance in Glioma Cells Induced by a Mesenchymal–Amoeboid Migratory Switch. *Biomedicines* **10**, 9 (2022).

77. Bear, J. E. & Haugh, J. M. Directed migration of mesenchymal cells: where signaling and the cytoskeleton meet. *Curr. Opin. Cell Biol.* **30**, 74–82 (2014).

78. Price, L. S., Leng, J., Schwartz, M. A. & Bokoch, G. M. Activation of Rac and Cdc42 by Integrins Mediates Cell Spreading. *Mol. Biol. Cell* **9**, 1863–1871 (1998).

79. Li, S., Sampson, C., Liu, C., Piao, H. & Liu, H.-X. Integrin signaling in cancer: bidirectional mechanisms and therapeutic opportunities. *Cell Commun. Signal.* **21**, 266 (2023).

80. Khoo, A. S. *et al.* Breast Cancer Cells Transition from Mesenchymal to Amoeboid Migration in Tunable Three-Dimensional Silk–Collagen Hydrogels. *ACS Biomater. Sci. Eng.* **5**, 4341–4354 (2019).

81. Yamaguchi, N., Mizutani, T., Kawabata, K. & Haga, H. Leader cells regulate collective cell migration via Rac activation in the downstream signaling of integrin β1 and PI3K. *Sci. Rep.* **5**, 7656 (2015).

82. Wickman, G. R. *et al.* Blebs produced by actin–myosin contraction during apoptosis release damage-associated molecular pattern proteins before secondary necrosis occurs. *Cell Death Differ.* **20**, 1293–1305 (2013).

83. Schick, J. & Raz, E. Blebs—Formation, Regulation, Positioning, and Role in Amoeboid Cell Migration. *Front. Cell Dev. Biol.* **10**, 926394 (2022).

84. Gabbireddy, S. R., Vosatka, K. W., Chung, A. J. & Logue, J. S. Melanoma cells adopt features of both mesenchymal and amoeboid migration within confining channels. *Sci. Rep.* **11**, 17804 (2021).

85. Sanz-Moreno, V. *et al.* ROCK and JAK1 Signaling Cooperate to Control Actomyosin Contractility in Tumor Cells and Stroma. *Cancer Cell* **20**, 229–245 (2011).

86. Georgouli, M. *et al.* Regional Activation of Myosin II in Cancer Cells Drives Tumor Progression via a Secretory Cross-Talk with the Immune Microenvironment. *Cell* **176**, 757-774.e23 (2019).

87. Cui, Y., Cole, S., Pepper, J., Javier Otero, J. & O. Winter, J. Hyaluronic acid induces ROCK-dependent amoeboid migration in glioblastoma cells. *Biomater. Sci.* **8**, 4821–4831 (2020).

88. Huang, Y. L., Tung, C., Zheng, A., Kim, B. J. & Wu, M. Interstitial flows promote amoeboid over mesenchymal motility of breast cancer cells revealed by a three dimensional microfluidic model. *Integr. Biol.* **7**, 1402–1411 (2015).

89. Holle, A. W. *et al.* Cancer Cells Invade Confined Microchannels via a Self-Directed Mesenchymal-to-Amoeboid Transition. *Nano Lett.* **19**, 2280–2290 (2019).

90. Liu, Y.-J. *et al.* Confinement and Low Adhesion Induce Fast Amoeboid Migration of Slow Mesenchymal Cells. *Cell* **160**, 659–672 (2015).

91. Rodriguez-Hernandez, I., Cantelli, G., Bruce, F. & Sanz-Moreno, V. Rho, ROCK and actomyosin contractility in metastasis as drug targets. *F1000Research* **5**, F1000 Faculty Rev-783 (2016).

92. Petrie, R. J., Harlin, H. M., Korsak, L. I. T. & Yamada, K. M. Activating the nuclear piston mechanism of 3D migration in tumor cells. *J. Cell Biol.* **216**, 93–100 (2016).

93. Petrie, R. J., Koo, H. & Yamada, K. M. Generation of compartmentalized pressure by a nuclear piston governs cell motility in a 3D matrix. *Science* **345**, 1062–1065 (2014).

94. Petrie, R. J., Gavara, N., Chadwick, R. S. & Yamada, K. M. Nonpolarized signaling reveals two distinct modes of 3D cell migration. *J. Cell Biol.* **197**, 439–455 (2012).

95. Nguyen, H. D. & Lin, C.-C. Viscoelastic stiffening of gelatin hydrogels for dynamic culture of pancreatic cancer spheroids. *Acta Biomater.* (2024) doi:10.1016/j.actbio.2024.02.010.

96. Lewis, D. M. *et al.* Collagen Fiber Architecture Regulates Hypoxic Sarcoma Cell Migration. *ACS Biomater. Sci. Eng.* **4**, 400–409 (2018).

97. Wisdom, K. M. *et al.* Matrix mechanical plasticity regulates cancer cell migration through confining microenvironments. *Nat. Commun.* **9**, 4144 (2018).

98. Audoin, M., Søgaard, M. T. & Jauffred, L. Tumor spheroids accelerate persistently invading cancer cells. *Sci. Rep.* **12**, 14713 (2022).

99. Nousi, A., Søgaard, M. T., Audoin, M. & Jauffred, L. Single-cell tracking reveals super-spreading brain cancer cells with high persistence. *Biochem. Biophys. Rep.* **28**, 101120 (2021).

100. Nguyen, D.-H. T. *et al.* A biomimetic pancreatic cancer on-chip reveals endothelial ablation via ALK7 signaling. *Sci. Adv.* **5**, eaav6789 (2019).

101. Bradney, M. J., Venis, S. M., Yang, Y., Konieczny, S. F. & Han, B. A Biomimetic Tumor Model of Heterogeneous Invasion in Pancreatic Ductal Adenocarcinoma. *Small* **16**, 1905500 (2020).

102. Carey, S. P. *et al.* Comparative mechanisms of cancer cell migration through 3D matrix and physiological microtracks. *Am. J. Physiol.-Cell Physiol.* **308**, C436–C447 (2015).

103. Chen, Y.-C. *et al.* Single-cell Migration Chip for Chemotaxis-based Microfluidic Selection of Heterogeneous Cell Populations. *Sci. Rep.* **5**, 9980 (2015).

104. Bhattacharjee, T. & Angelini, T. E. 3D T cell motility in jammed microgels. *J. Phys. Appl. Phys.* **52**, 024006 (2018).

105. Campbell, J. J., Husmann, A., Hume, R. D., Watson, C. J. & Cameron, R. E. Development of three-dimensional collagen scaffolds with controlled architecture for cell migration studies using breast cancer cell lines. *Biomaterials* **114**, 34–43 (2017).

106. Kim, W. & Kim, G. H. An intestinal model with a finger-like villus structure fabricated using a bioprinting process and collagen/SIS-based cell-laden bioink. *Theranostics* **10**, 2495–2508 (2020).

107. Wu, W., DeConinck, A. & Lewis, J. A. Omnidirectional Printing of 3D Microvascular Networks. *Adv. Mater.* **23**, H178–H183 (2011).

108. Yan, Y. *et al.* Vascularized 3D printed scaffolds for promoting bone regeneration. *Biomaterials* **190–191**, 97–110 (2019).

109. Soman, P. *et al.* Cancer cell migration within 3D layer-by-layer microfabricated photocrosslinked PEG scaffolds with tunable stiffness. *Biomaterials* **33**, 7064–7070 (2012).

110. Unnikandam Veettil, S. R., Hwang, D., Correia, J., Bartlett, M. D. & Schneider, I. C. Cancer cell migration in collagen-hyaluronan composite extracellular matrices. *Acta Biomater.* **130**, 183–198 (2021).

111. Green, B. J. *et al.* Pore Shape Defines Paths of Metastatic Cell Migration. *Nano Lett.* **18**, 2140–2147 (2018).

112. Bhattacharjee, T. & Datta, S. S. Bacterial hopping and trapping in porous media. *Nat. Commun.* **10**, 2075 (2019).

Chapter 5:

PDAC migration: what's charge got to do with it?

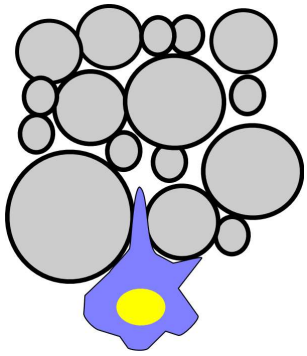

Introduction

Pancreatic ductal adenocarcinoma (PDAC) is an aggressive, devastating disease. The prognosis at the time of diagnosis is typically a 3% five-year survival rate[1]. The reasons for this include late-stage diagnosis[2], lack of early detection[1], and the tumor microenvironment (TME)[3,4]. The development of PDAC generally starts with chronic inflammation[5,6], forming of a lesion that gradually goes from a low-grade to high-grade lesion, and finally, tumor formation. PDAC typically starts from acinar cells located within the glands of the exocrine pancreas that then undergo irreversible acinar-to-ductal metaplasia due to KRAS mutations[6–8]. To further study this devastating disease, accurate in vitro models using human cell lines must be developed.

The PDAC TME is primarily composed of a dense stroma of collagen[9,10] and hyaluronic acid (HA)[11,12] produced in excess by pancreatic stellate cells due to the chronic inflammatory environment[13]. Both polymers contribute to an increase in tumor stiffness and hydrostatic pressure[14,15]. The elevated hydrostatic pressure leads to tumor hypoperfusion relative to healthy pancreatic tissue as blood vessels collapse[16], preventing chemotherapeutics, immunotherapeutics, and cell-therapies from reaching the tumor site. Additionally, the TME can promote the epithelial-mesenchymal transition (EMT)[17], a well-studied and required transition that cancer cells must undergo to metastasize. Several methods have been used to mimic this stroma and use these models to study cell behaviors like cell migration, and to potentially test therapeutics. For example, viscoelastic and stiffening gelatin-based hydrogels with dynamic boronate-acid bonds and elastic thiol crosslinking have been formulated to test PDAC spheroid migration, showing that matrix stiffness plays an important role in malignancy[18]. Matrix stiffness has also been shown to play a role in PDAC proliferation and metastasis[17,19]. Thus, the

development of physiologically-relevant in vitro PDAC models is crucial to the understanding and treatment of PDAC.

In addition to increasing stiffness and hydrostatic pressure, collagen fibrils become aligned within the PDAC TME, thus producing a strain-stiffening effect. This strain-stiffening can come from contractile forces from the myofibroblast characteristics of cancer-associated fibroblasts[20] and from the increased intra-tumoral pressure leading to stiffening towards the outside of the tumor[21]. This strain-stiffening behavior can contribute to cell migration outside of the TME. Because strain-stiffening comes from collagen fiber alignment, the aligned fibers can be used to migrate onto and out of the tumor microenvironment, a phenomenon known as contact guidance[22,23]. These drastic changes in tumor mechanics, creating a pro-migration environment, point to the importance of the ECM in the metastatic cascade.

Granular materials are a promising platform for in vitro cell studies. Granular materials, comprised of packed microparticles, are inherently porous, preventing issues with nutrient and oxygen diffusion. This porosity can be modified by simply adjusting the packing density, achievable through means such as centrifugation speed[24]. Granular material mechanics are also tunable. Interparticle interactions, which dominate bulk mechanical properties[25], can be altered to create a more fluid or solid environment, such as through interparticle guest-host linkages[26]. These changes have implications for cell behaviors such as migration. Lastly, granular materials can mimic native human tissue microarchitecture, as tissues are densely packed with cells through which other cells cannot travel and must instead travel between cells. Granular materials have had many applications in the biomaterials field, from biofabrication with 3D printing[27–29], to wound healing with MAP particles[30], and to studying cell behaviors as a function of particle size and shape[24,31]. Thus, a granular system provides a potential platform from which to create a relevant PDAC model.

The goal of this work was to create granular systems with tunable interparticle interactions based on the biopolymers HA and gelatin to study PDAC cell migration. HA was modified to become UV-crosslinkable via coupling of a norbornene group to the n-acetylglucosamine group of the HA backbone, termed NorHA. This NorHA was then used to formulate microparticles on the lengthscale of cells. Because HA is an anionic biopolymer, we aimed to tune interparticle interactions via dynamic electrostatic interactions. To do so, gelatin was modified to contain additional amine or carboxylic acid groups to create a cationic or anionic interstitial material, respectively. Intermediate charges of gelatin were also tested by using gelatin types A and B to alter the extent of gelatin adsorption to the NorHA particles. To test this system for use as an *in vitro* PDAC model, three primary goals were outlined. First, the change in variables, namely jamming fraction, (+) Gel concentration, and gelatin zeta

potential, were correlated to changes in porosity, microstructure, and rheological properties. Second, cell migration behaviors were studied over time as a function of jamming fraction, (+) Gel concentration, and gelatin zeta potential. These behaviors included mean squared displacements, and instantaneous and average cell speeds. Third, we examined changes in vimentin concentration over time as a function of jamming fraction and gelatin zeta potential. Vimentin is a well-known EMT marker, and it was expected that cells would increase vimentin expression when in an environment conducive to cell motility.

Methods

NorHA and gelatin syntheses and characterization

NorHA was synthesized using a previously described method[32]. Briefly, sodium hyaluronate was mixed with Dowex resin for 2-3h, followed by filtration and pH correction to roughly 7 to fabricate HA-TBA. Post-lyophilization, HA-TBA modification was measured using H^1 NMR. Based on this modification, HA-TBA was then reacted with 5-norbornene-2-carboxylic acid to form NorHA through an esterification reaction with di-tert-butyl dicarbonate and 4-dimethylaminopyridine. The degree of modification was calculated based on H^1 NMR spectra to be 16-21% (SI Fig. 1).

Positively-charged gelatin ((+) Gel) was prepared as described in Chapter 3 and modified based on a previously reported method[33]. Briefly, cationic gelatin ((+) Gel) was prepared by reacting gelatin Type A (300 bloom) at 2wt% in PBS with 1-ethyl-3-(3-dimethylaminopropyl)carbodiimide (EDC HCl, Sigma), N-hydroxyl succinimide (NHS), and ethylene diamine (EDA) (Fig. 1B). Per gram of gelatin, the weight ratios of reactants were 1:0.6:3.6 of EDC:NHS:EDA. The gelatin was first dissolved in PBS, then NHS and EDA were added to the solution. The pH was adjusted to 5.5 to 6, after which EDC was added. The pH was then further adjusted to 4.5 to 5 and allowed to react for approximately 24h. The (+) Gel was then dialyzed against DI water for 2-3 days at room temperature. A fluorescamine assay was used to determine the change in amine groups using a calibration curve with glycine and compared with unmodified gelatin.

Anionic gelatin ((-) Gel) was prepared using succinic anhydride using a method similar to synthesizing norbornene-modified gelatin[34]. Gelatin (type A, 300 bloom, Sigma) was dissolved in PBS at a concentration of 5wt% in a 40°C oil bath. Succinic anhydride was then added to a final concentration of 10wt%. The pH of the solution was adjusted using 10M sodium hydroxide to a pH between 8 and 9. This solution was allowed to react for approximately 24h at 40°C. The solution was then purified via ultrafiltration against DI water. A fluorescamine assay was used to calculate change in amine groups.

Gelatins type A (300 bloom, Sigma) and type B (from bovine skin, Sigma) were also used without further modification to test intermediate zeta potentials on material properties and subsequent cell migration behaviors.

NorHA microgel fabrication and jammed system preparation and characterization

Particle preparation

NorHA particles were fabricated as described in previous chapters. A precursor 3 wt% NorHA solution was prepared in PBS containing 0.313 mg/mL dithiothreitol (DTT, Sigma) and 6.6mM lithium phenyl-2,4,6-trimethylbenzoylphosphinate (LAP, Sigma). This NorHA solution was homogenized in light mineral oil with 2% Span80 for 2 minutes at 3000rpm, followed by UV curing for 5min at approximately 10mW/cm^2. De-emulsification was started by adding isopropanol to the emulsion. After stirring the oil, particles, and isopropanol, the mixture was filtered over a 0.22μm hydrophilic PVDF membrane with vacuum. Microgels were washed an additional two times over the filter with isopropanol. After filtering, the microgels were left to dry then added into a 50mL conical and vortexed with 70% ethanol and placed on a rocker at least overnight. To finish processing, microgels were washed with PBS four times using centrifugation to ensure ethanol removal and equilibration in PBS. Microgels were then filtered over a 40μm cell strainer and stored at 4°C until needed.

Preparation of jammed microgel systems

Particles were jammed in pre-weighed eppendorf tubes at 21130xg for 5 minutes. Excess PBS or media was then removed. Particles were centrifuged again if needed to fully remove excess PBS or media. Once particles were packed, the particles were weighed out. Based on this weight, gelatin solutions were added to achieve a 0.3 jamming fraction. To achieve a 0 jamming fraction, the particles were centrifuged again and excess solution was removed. To achieve a 0.5 jamming fraction, additional PBS was added to the particles.

Characterizations

Rheology

Rheological characterizations were carried out on a stress-controlled rheometer (DHR-3, TA instruments). Materials were freshly prepared prior to testing. A sandblasted 8mm parallel plate system was used due to microgel size. Sandpaper was used on the bottom of the Peltier plate system to help prevent slip. Frequency and strain sweeps were conducted at 37°C with a 1%, and oil was placed around the sample edges to prevent dehydration during testing.

Zeta potential

All materials were prepared in filtered 0.1X PBS. For the gelatin samples, all samples were prepared at 5mg/mL. NorHA microgels were tested at 3mg/mL due to their size. Zeta potentials were measured using a zetasizer (Zetasizer Ultra, Malvern) and calculated using the Smoluchowski equation. Each sample was run three times with independently-prepared samples.

Confocal microscopy, and area fraction and pore size calculations

NorHA microgels were prepared at different jamming fractions, (+) Gel concentrations, and gelatin of varying charge. The interstitial gelatin contained high molecular weight FITC-dextran (2MDa, Sigma) to aid in visualization during image acquisition. Images were acquired using a confocal microscope (Stellaris 5, Leica). Z-stacks were taken with slices set to 2μm for a total depth of 25-40μm. Area fraction was calculated from three independently-prepared samples for each jamming fraction, gelatin charge, and gelatin concentration using FIJI.

To calculate pore size, the FIJI plugin BoneJ was used[35]. Z-stacks from confocal imaging were thresholded using Otsu's method[36,37]. Trabecular thickness was selected, as this corresponds to the pore space being measured. Pore sizes were extracted from the resulting thickness map and used to create pore size distributions (SI Fig. 3).

PDAC culture

366-PDACs with GFP luciferase were kindly provided by the Bauer lab at UVA. These cells are derived from a PDAC tumor located in the pancreas and are considered non-metastatic. PDACs were cultured in TCP-treated flasks using RPMI 1640 with l-glutamine, 10% FBS, and 1% antibiotic-antimycotic. Once

~70-80% confluence was achieved, PDACs were harvested using 0.05% trypsin in EDTA for 15 min, followed by neutralization with complete media and centrifugation at 130xg for 5min. After cell counting, single-cell experiments were initiated.

Cell migration experiment setup and measurements

Support preparation and PDAC cell addition

To hold microgels in place during experiments, 4-5mm holes were punched into a roughly 3mm thick PDMS (Sylgard 184) slab using a biopsy punch. The PDMS slabs and a 6-well glass-bottom well plate were plasma treated with air for two minutes to allow the PDMS holders to bond to the glass. The well plate was then sterilized via UV exposure for 60 minutes.

NorHA microgels were prepared aseptically after hydration in 70% EtOH, with other steps described above occurring in a biosafety cabinet. Particles were washed with DPBS followed by washing with excess complete media. All gelatin solutions were prepared using PBS and were sterilized via UV exposure for 60min. Jammed microgels with different gelatin solutions were prepared aseptically according to the description above.

For single cell migration tests, PDACs were harvested using 0.05% trypsin for 15min. After counting, PDACs were resuspended to 50 million cells/mL. Per 50µL of support, 2µL of cell suspension was added and gently mixed using a wide-bore pipet tip, giving an approximate cell density of 2 million cells per mL of support. This cell-laden support was then added to the PDMS holders. Samples were prepared separately in triplicate. Using an Okolab on-stage microscope incubator with medical gas flow, z-stacks were taken every 15min for 15-16h. Cells used in these experiments were used at passages 17-20.

Single cell migration analysis

Widefield z-stacks obtained from the overnight experiments described above were analyzed using FIJI, adapted from a previously published method[38]. Z-stacks were converted into z-projections using maximum intensity then converted into 8-bit. From here, the background was subtracted and contrast enhanced by 0.1%. TrackMate[39] was used to obtain tracks over time. Object diameter was set to 25µm

with a quality threshold of 0.1-0.2, and this was visually inspected prior to calculating cell tracks to ensure that only cells were detected. The LoG detector and LAP algorithms were selected. If drift occurred in a sample area, those tracks were removed using the 'trim non-visible data' function. Once tracks were calculated, a MotilityLab table was created and imported into MotilityLab[40]. MotilityLab was used to calculate mean squared displacements and mean track speeds. If consistent drift was observed, the 'correct drift' function in MotilityLab was used for correction. Significant differences in mean track speeds amongst tested groups were found using a one-way ANOVA test with post-hoc Tukey test. A p-value less than 0.05 was considered significant.

Instantaneous speed was calculated using the following formula:

$$v_{inst} = \frac{|x_i - x_{i-1}|}{t_i - t_{i-1}}$$

Where the value of x_i-x_{i-1} is the distance travelled by the cell, divided by the time[41]. To compare instantaneous speeds amongst tested groups, a one-way ANOVA with a post-hoc Tukey test was used, and a p-value of less than 0.05 was considered significant.

Mean-squared displacements can be described by the following anomalous diffusion power law:

$$MSD = K\tau^{\alpha}$$

Where K is a transport coefficient, tau is lag time, and alpha describes cell movement[36,41]. Subdiffusive behavior occurs when α<1, diffusive when α=1, superdiffusive when α>1, and ballistic when α=2[36,41,42]. Linear regression was used after transforming the data to be on a log scale to obtain alpha for all materials tested. Tau below 25% of total tau was used to calculate α, as suggested by a previous study[41] due to decreased sampling at longer timescales.

Yielding of granular support

Fluorescent beads (Fluospheres, 10μm, Invitrogen) were added to cell-laden and acellular supports, with a final concentration of 36,000-60,000 beads per mL of support. Supports were monitored over a 16h time period as described above. Images were processed using the same method for tracking cell movements as described above. If drift was observed, these were corrected in MotilityLab prior to displacement calculations. Displacement was calculated by first calculating the displacements in x- and y-directions, then calculating the total displacement. A two-sample t-test was used to compare cell-laden supports and the corresponding acellular supports.

Vimentin staining

A live vimentin stain (BioTracker TiY Vimentin Live Cell Dye, Sigma) was used to evaluate vimentin expression over time. Cell suspensions and supports were set up as described before. The vimentin live stain was first prepared according to manufacturer's directions by dissolving the dye in DMSO to create a 5mM stock solution. This solution was then diluted with PBS, then added to the interstitial gelatin solutions for a final gelatin concentration of roughly 2.94% and final vimentin concentration of 1μM. Live imaging was then carried out as described earlier, with images being taken over a 15-16h period on a widefield microscope. Controls were cell-laden PBS-based supports. Images were processed in FIJI to create a z-stack using average intensity followed by background subtraction using a rolling ball algorithm. Mean gray values over a set ROI were then measured at hourly timepoints.

Results and Discussion

Materials characterization

The goal of this study was to formulate a particle-based system with tunable interparticle interactions. We also sought to understand the effects of interstitial material concentration and porosity on cell migrations within these developed granular systems. Hyaluronic acid is a well-characterized anionic polymer found upregulated in PDAC tumors that has been shown in the previous chapters to be easily modified via addition of the UV-crosslinkable moiety norbornene to formulate microgels. Thus, to modulate interparticle interactions with the above goal in mind, we aimed to alter zeta potentials of added interstitial gelatin solutions. To make cationic gelatin ((+) Gel), gelatin type A was reacted with EDA via EDC-coupling to modify the carboxylic acid groups, responsible for negative charges at physiological pH, to an amine-ending moiety, thus producing a positively-charged polymer (Fig. 1A). To form a negatively-charged polymer, succinic anhydride can instead be added to a gelatin solution, replacing amine groups with carboxylic acid-containing moieties (Fig. 1B). Fluorescamine assays show an increase in amine groups with the amine-coupling reaction, from 224.65 ± 21.54 μmol of amine per g of gelatin to roughly 500.08 ± 35.76 μmol of amine per g of gelatin. There was a large decrease in the amine groups for the negatively-charged gelatin, as expected. The amine group amount decreased to 9.87 ± 1.34 μmol of amine per g of gelatin. The amine content for neat GelA and GelB, used in this study as intermediately-charged interstitial gelatin, were roughly similar, at 224.65 ± 21.54 and 234.55 ± 12.99 μmol per g material, respectively.

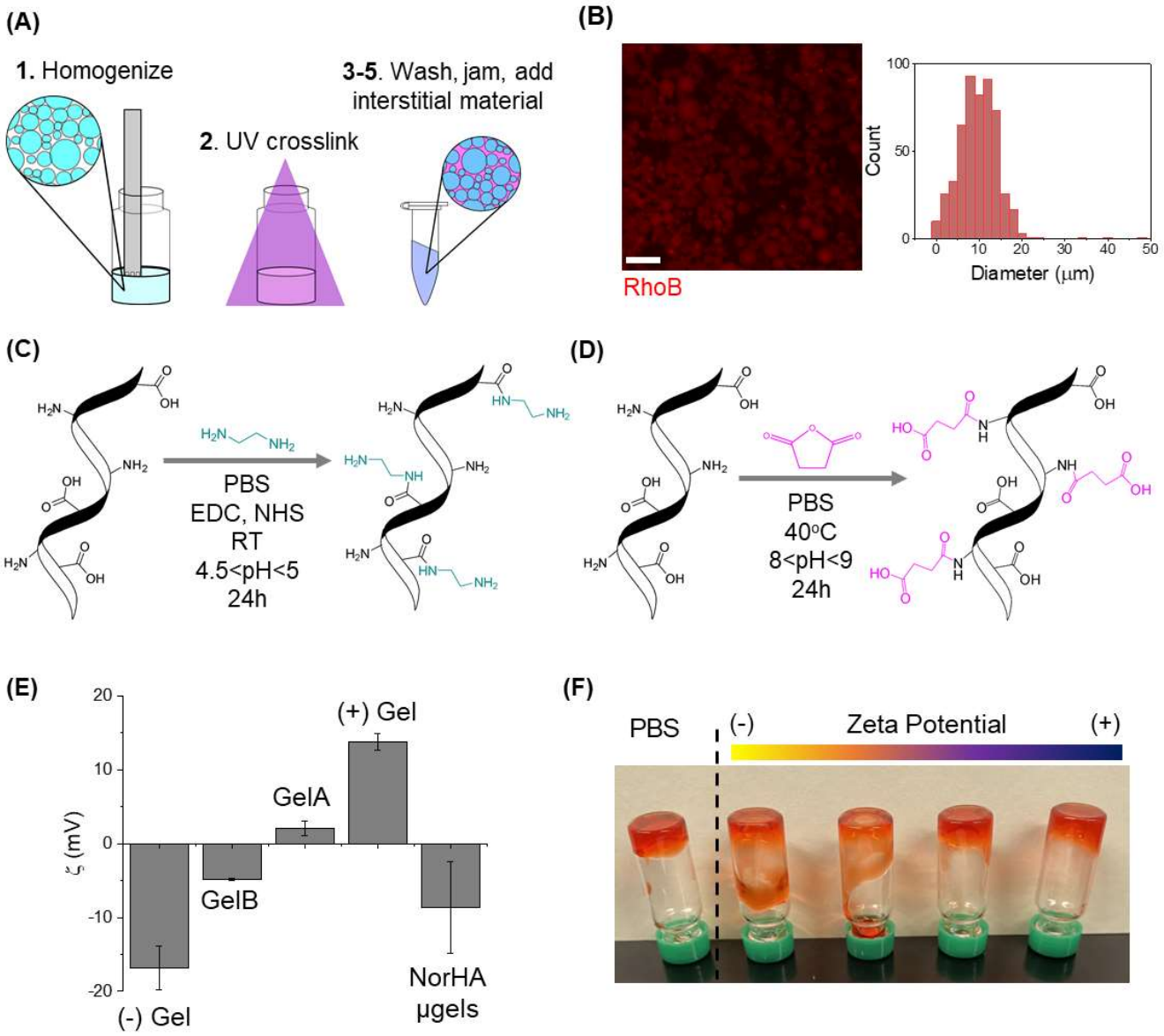

Fig. 1: (A) schematic of NorHA microgel processing, (B) widefield image of fluorescently tagged NorHA microgels with particle size distribution, (C) synthesis route of (+) Gel, (D) synthesis route of (-) Gel, (E) zeta potentials of all materials used in this study (error bars represent standard deviation), (F) photo of NorHA microgels with 1% gelatin solutions of varying zeta potentials with comparison to PBS.

Zeta potentials were measured for each material (Fig. 1E). For the anionic materials, zeta potentials were predictably negative, with a lower zeta potential for (-) Gel at -16.81 ± 2.97 mV, while GelB had a small negative charge of -4.80 ± 0.14 mV. As amine groups on the gelatin backbone increased, the charges predictably increased. GelA had a measured zeta potential of 2.08 ± 0.97 mV, and this increased to 13.76 ± 1.11 mV for the (+) Gel. This data, in combination with the fluorescamine assay, shows successful modifications of the gelatin backbones.

NorHA microgels were characterized similarly. NorHA was first synthesized using a previously established method that couples a norbornene group to the n-acetylglucosamine sugar group on the HA backbone. Particles were made via batch emulsification. Particles were measured to be 9.91 ± 4.85 μm in diameter. Because a batch emulsification method was used, particle sizes were polydisperse, as seen in Fig. 1B. The coefficient of variation was calculated to be 48.99%, also indicating high polydispersity. Zeta potential of the particles was measured to be -8.64 ± 6.23 mV. When NorHA particles were mixed with interstitial gelatin of varying charges, a visual change in material behavior can be seen. As the gelatin becomes more negatively charged, and thus the jammed particle system more repulsion-dominated, the jammed particle systems become more fluid-like, visualized using an inversion test. When 1% gelatin solutions were introduced to particles, clear differences due to gelatin zeta potential were observed, where increasingly negative gelatin solutions produced more liquid-like supports (Fig. 1F).

Jamming fraction alters confinement and influences cell migratory behavior

Rheological characterization and microstructural analyses were conducted to determine effects due to jamming fraction (Fig. 2A and B). As described in the methods section, jamming fraction refers to the extent to which NorHA microgels are packed based on particle weight, and higher jamming fractions correspond to lower packing densities. To rheologically characterize jammed supports containing 3% (+) Gel at different jamming fractions, frequency and strain sweeps were carried out. Frequency sweeps in Fig. 2A show primarily gel-like behavior for all tested jamming fractions, as seen by the constant storage and loss moduli values across the testing range. Frequency sweeps showed a decrease in G' with jamming fraction. Strain sweeps for supports at all jamming fractions show a key rheological signature typically found in jammed microgel systems, where a peak in the loss modulus occurs at the moduli crossover point. Strain-stiffening behavior is seen in all tested samples, which could be attributed to the adsorption of (+) Gel chains onto the anionic NorHA microgels that are then being pulled at increasing applied strains. In comparison, PBS-based supports showed no strain-stiffening behavior, as expected, and a clearer change in rheological properties as a function of jamming fraction. Additionally, the onset of strain-stiffening appears to be within a physiologically-relevant range. It has been stated in previous studies that in 3D, cells can exert a strain between 20-30% on the surrounding ECM[43,44]. Onset of strain-stiffening for these supports occurs at roughly 10% strain, marked by a departure in the linear regime of the storage modulus curve.

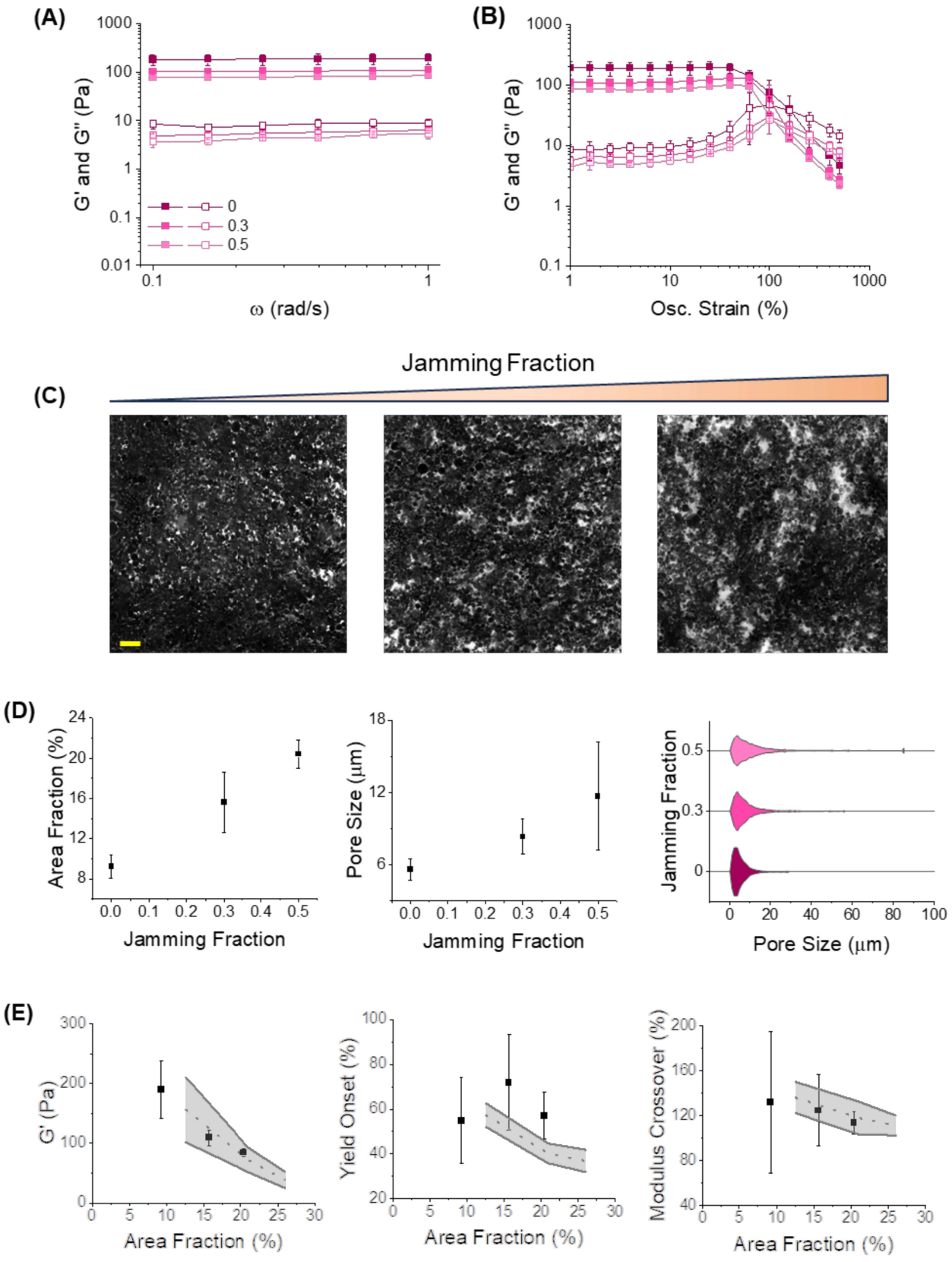

Fig. 2: (A) Frequency and (B) strain sweeps of (+) Gel-based supports at varying jamming fractions, (C) confocal images of (+) Gel-based supports at varying jamming fractions (scalebar=50μm), (D) trend in area fraction, average pore size, and pore size distributions as a function of jamming fraction, and (E) trends in G', yield onset, and modulus crossover as a function of porosity. Error bars represent standard deviation.

Microstructural analysis using confocal microscopy (Fig. 2C) was used to examine the changes in area fraction, average pore size, and pore size distributions as a function of jamming fraction (Fig. 2D). With jamming fraction increase, area fraction increased, as expected. This indicates a successful alteration in porosity of the supports. Average pore size similarly increases with jamming fraction, from about 6μm in the highest packed supports to roughly 12μm in the lowest packing density group. This can be explained by examining the pore size distributions, which show an increase in the polydispersity of the pore sizes with jamming fraction. A lower packing density produces a larger distribution of pore sizes. In the PBS-based supports, broader distributions were achieved as a function of jamming fraction but this change was smaller in comparison. PBS-based supports prepared at a jamming fraction of 0.5 attained a maximum pore size of 13μm, whereas supports prepared at the same jamming fraction but with 3% (+) Gel achieved a maximum pore size of 85μm. This difference in pore size distributions can be attributed to the presence of aggregate-like clusters in the (+) Gel-based supports. Additionally, the (+) Gel chains present on the NorHA microgels are likely contributing to attractive interparticle interactions, which has been previously shown to form similar microstructures[45,46].Trends in the rheological properties of these supports were then correlated to area fraction and compared to PBS. As seen in Fig. 2E, a similar trend is observed for storage modulus and area fraction for both (+) Gel-based and PBS-based supports. Onset of yielding did not show any clear trend in the (+) Gel-based supports. Modulus crossover values tended to decrease with increasing area fraction and were similar between both types of supports tested. This data shows that packing density alters bulk stiffness values, likely due to the presence of larger pores, and interestingly the presence of (+) Gel seems to only alter yielding onset when compared to PBS-based supports.

Jamming fraction effects on PDAC migration were assessed. Porosity is a well-studied variable in cell migratory studies, as pore size can influence migration speeds and migration modes. Cells generally move through pores provided that the pores are larger than the nucleus to prevent nuclear damage. Thus, jamming fraction was studied to assess changes to PDAC cell migratory behavior. Representative cell tracks are shown in Fig. 3A, where greater displacement can be seen as jamming fraction is increased, signifying a lower packing density.

A key metric for cell migration is the mean-squared displacement (MSD) which describes average area covered by migrating cells. MSD is calculated as follows:

$$MSD = <\left(r\left(t+\tau\right)-r\left(t\right)\right)^2>$$

Where r is the distance travelled at time t, and tau is lag time[36,41]. Cells had similar MSD values over the course of the experiment regardless of jamming fraction. This would indicate that cells migrated over roughly the same area regardless of jamming fraction.

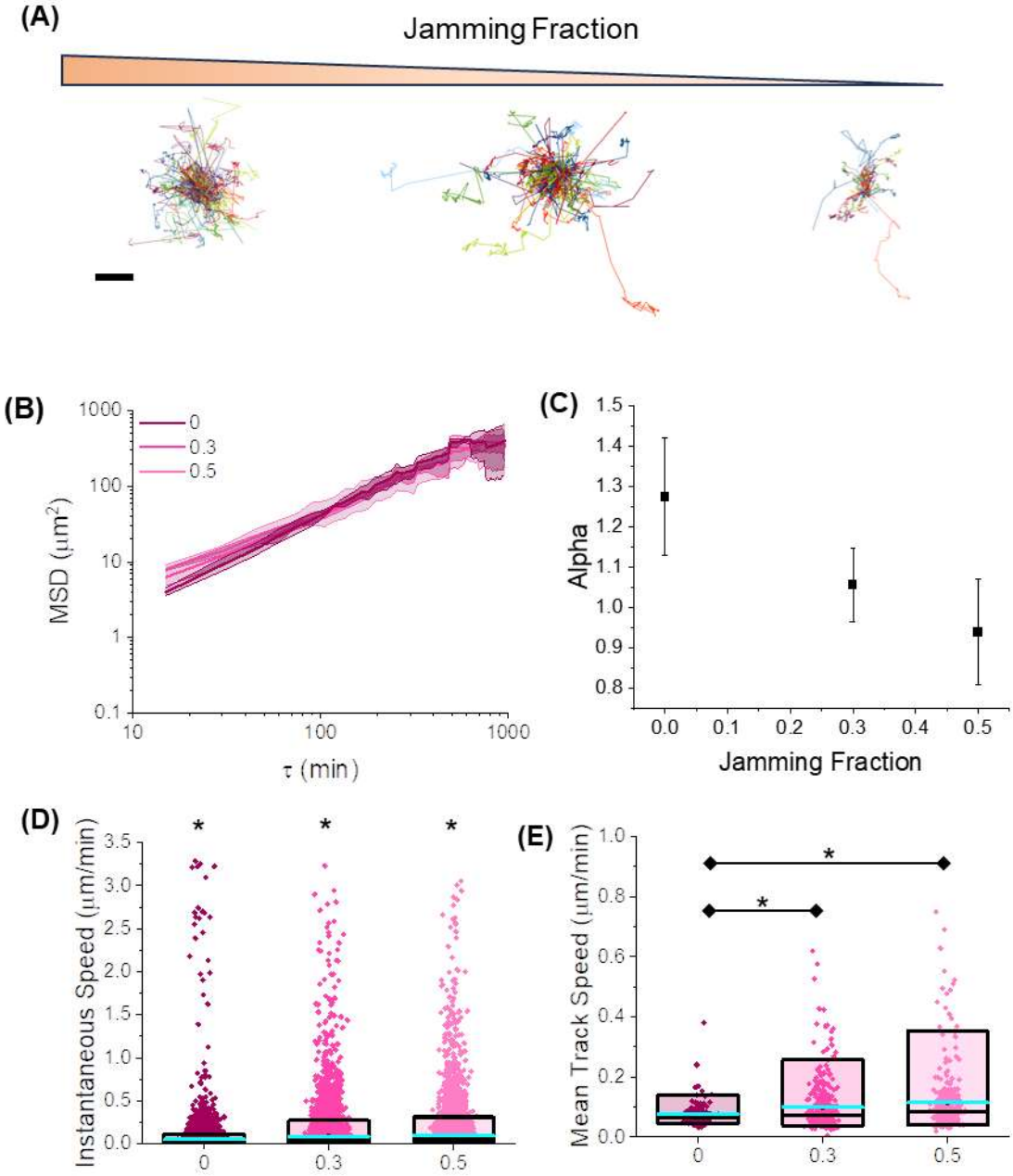

Fig. 3: (A) cell tracks from representative supports with varying jamming fractions (scalebar=50μm), and measuring the effects of jamming fraction on (B) mean-squared displacement, (C) alpha values calculated from the MSD data, (D) instantaneous cell speeds (* denotes $p<0.05$), and (E) mean track speeds (* denotes $p<0.05$). For (D) and (E), the boxes represent 95% confidence intervals, the cyan line refers to the mean and the black line is the median.

As described in the methods section, a power-law model, termed the anomalous diffusion model, can be fit to the data for MSD, and is as follows:

$$MSD = K\tau^{\alpha}$$

Where K is a transport coefficient, tau is lag time, and α is a constant that describes cell migratory behavior. At an α value below one, cells are considered sub-diffusive and would indicate primarily stationary cells or migration within a small region. A value equal to one represents diffusive motion, and cells tend to move using a random walk pattern. An α value greater than one suggests super-diffusive behavior and cells migrate in a more persistent random-walk fashion. And an alpha value equivalent to two is considered ballistic motion[36,41,42]. Pore sizes for supports with 0 and 0.3 jamming fractions allowed for superdiffusive behavior, with the 0 jamming fraction condition having a higher value, while the 0.5 jamming fraction condition had an alpha value of less than one, indicating subdiffusive behavior. This trend corresponds to results in a previous study monitoring T cell migration in a granular system comprised of Carbopol[36]. There, yield stress was modified by adjusting total polymer concentration, and this in turn altered porosity. Similar findings were observed, where high yield stress and thus less porous supports enabled superdiffusive cell behavior, but this became subdiffusive as yield stress was decreased and pore size increased. Thus, as pore size increases, cell migration becomes increasingly subdiffusive and cells are generally not migrating outward from their original positions.

Instantaneous and mean track speeds were calculated as well (Fig. 2D and 2E). The speed at which a cell is migrating can help to indicate the mode of migration being used, being mesenchymal, lobopodial, or amoeboid. In this study, mean track speed increased, but only significantly between the 0 jamming fraction and the 0.3 and 0.5 jamming fraction groups. Mean track speeds were found to primarily be within range for a mesenchymal migration mode, which has been considered to be less than 1μm/min[47]. Instantaneous speed, on the other hand, shows greater values compared to mean track speeds and indicate lobopodial migration based on the speed values alone[48]. Because the supports consist of a large range of pore spaces, this difference in mean and instantaneous speeds could be due to this pore size distribution. It has been well-characterized that cells migrate faster through smaller pore spaces[49,50]. Thus, cells may be migrating from small into larger pore spaces and track speeds correspondingly decrease as a result. This was observed in a study where controlled microchannel diameters were used to measure breast cancer migration[49]. As cells migrated through small channels and then large spaces sequentially, cell track speed decreased accordingly[50]. Another study also showed that the shape of the pore also plays a role, with cells opting for the ‘path of least resistance’[51], and this could be a factor in these supports.

(+) Gel concentration leads to greater travelled area and higher migration speeds

Previous studies have shown that quantity of cell-binding moieties, namely RGD, affect cell behaviors such as migration. In cancer research, amoeboid and mesenchymal migration modes have been extensively studied as a function of ECM and shown that low adhesion environments are conducive to amoeboid-based migration, while mesenchymal migration tends to occur in environments with high cell adhesion capabilities. Thus, we aimed to study (+) Gel concentration on cell migration behaviors within supports of varying (+) Gel concentrations. Similar to the above experiment, rheological and microstructural characterizations were carried out to test effects of (+) Gel concentration. For all tested (+) Gel concentrations, frequency sweeps showed primarily elastic-like behavior (Fig. 4A), in line with previous research. Strain sweeps showed that (+) Gel increased storage modulus compared to PBS-based supports. Strain-stiffening also seemed to become more apparent with (+) Gel concentration (Fig. 2B). From this data, trends in storage moduli, yielding onset, and moduli crossover values were examined as a function of (+) Gel concentration (Fig. 2C). Increase of (+) Gel concentration produced supports with decreasing storage moduli values. This could be the result of increased electrostatic repulsions from the (+) Gel chains. Increasing (+) Gel concentration also caused an increase in yield onset as well as modulus crossover.

Area fraction, average pore size and pore size distributions were also analyzed using confocal microscopy. Confocal images show an increase in aggregate-like clusters with increasing (+) Gel concentration (Fig. 4D). Area fraction was higher in the PBS-based supports and were roughly similar for all (+) Gel-containing supports (Fig. 4E, left), which could be attributed to the (+) Gel chains pulling particles together via electrostatic interactions[45]. Average pore size also increased with (+) Gel concentration, but with 2% and 3% (+) Gel having similar average pore sizes (Fig. 4E, middle). Examination of pore size distributions shows an increasingly broad size distribution with (+) Gel concentration (Fig. 4E, right). Both 2% and 3% (+) Gel-based supports had nearly identical distributions. Due to similarities in rheological and microstructural properties of the 3% and 2% (+) Gel-based supports, 0%, 1%, and 3% (+) Gel concentrations were used for cell migration studies.

Representative cell tracks show greater displacement as (+) Gel concentration increases (Fig. 5A). In Fig. 5B, MSD for supports with 3% (+) Gel were greater compared to the 0% and 1% cases, further showing that (+) Gel concentration, at least within the range tested here, promotes cancer cell migration. Alpha values calculated from the MSD data show no effect on cell migration pattern, as all tested (+) Gel concentrations had alpha values in the superdiffusive range (Fig. 5C). This indicates that (+) Gel concentration does not affect the migratory path used by the cells during migration.

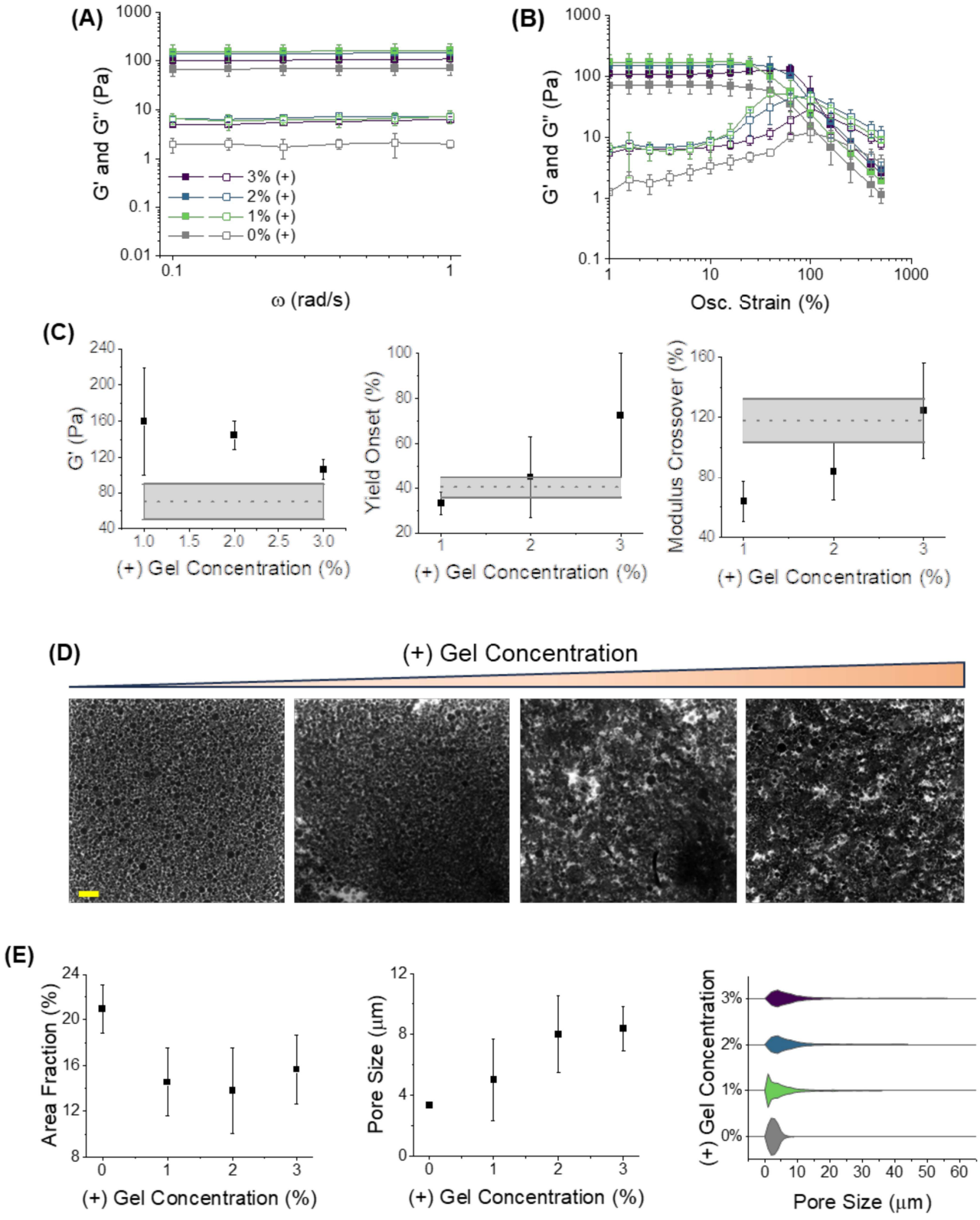

Fig. 4: Effects of (+) Gel concentration on (A) frequency and (B) strain sweep behaviors, (C) trends in storage modulus, yield onset, and modulus crossover values (gray regions represent PBS-based controls with standard deviation), (D) microstructure via confocal imaging (scalebar=50μm), and (E) on area fraction, average pore size, and pore size distributions. Error bars denote standard deviation.

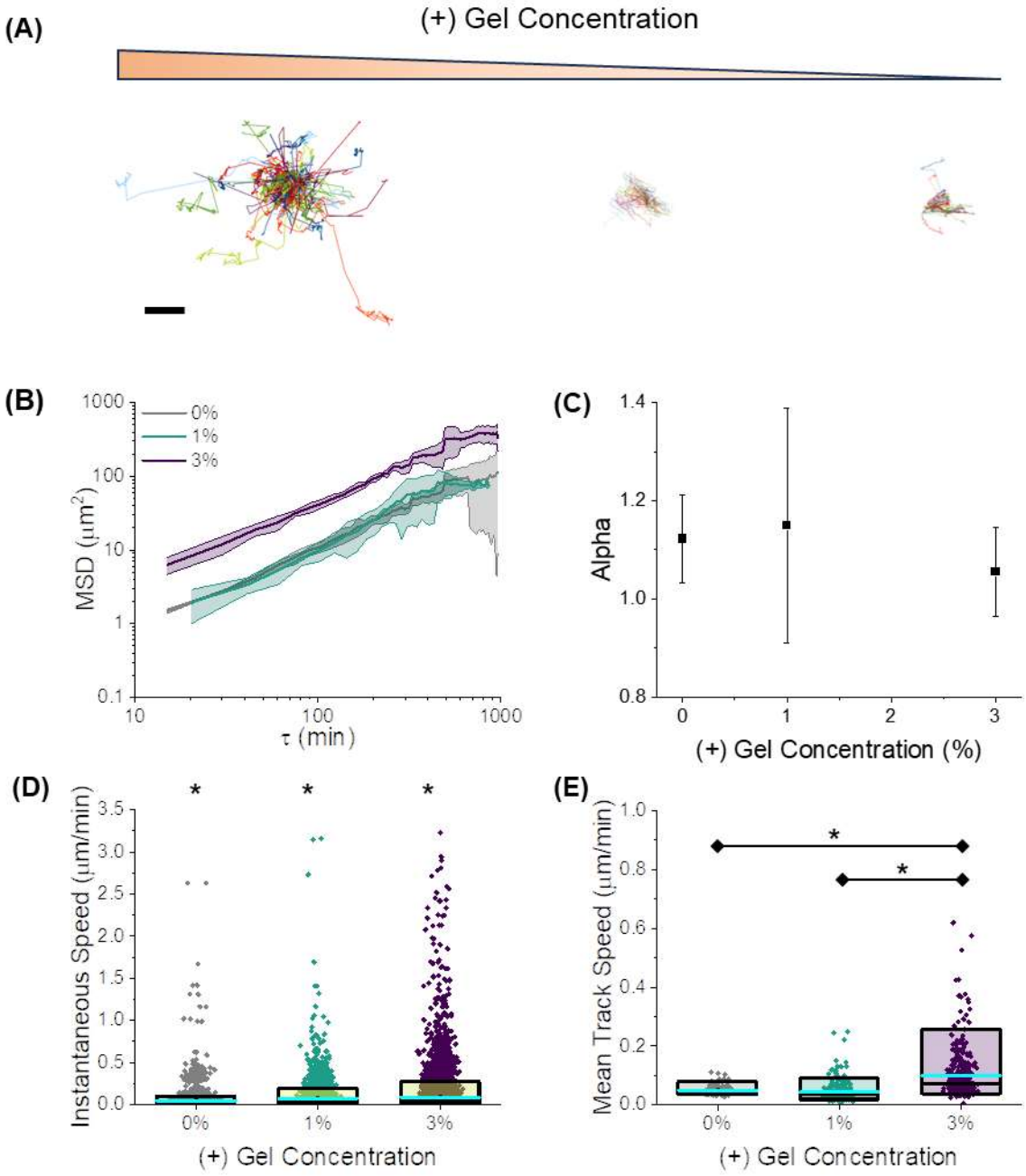

Fig. 5: (A) cell tracks of representative samples of supports with varying (+) Gel concentration (scalebar=50μm), and analysis on (B) MSD, (C) alpha values from MSD data (error bars represent standard deviation), (D) instantaneous cell speeds, and (E) mean track speeds (* denotes $p<0.05$)

Mean and instantaneous migration speeds increased due to increased (+) Gel concentration (Fig. 5D and 5E). Instantaneous speed values show a greater proportion of cells are migrating lobopodially as (+) Gel concentration increases, and this change was found to be statistically significant. Mean track speeds, similar to the experiment above, showed primarily mesenchymal migration, but the average speed was higher in the 3% (+) Gel supports and decreased with decreasing (+) Gel concentration.

Again, the instantaneous speeds are significantly higher than mean track speeds and could be attributed to the broad pore size distributions present in the supports prompting speed adjustments and possible ‘trapping’ of cells within a pore space[36,49,50,52].

Gelatin with different zeta potentials tune interparticle interactions and cell migratory behaviors

As described earlier, gelatin with varying zeta potentials were used to modify interparticle interactions due to the changes in electrostatic interactions between the anionic NorHA microgels and interstitial gelatin. As seen in Fig. 6A and B, modulation of the zeta potential of gelatin produced obvious changes in the rheological properties of the supports. Again, NorHA microgels with (+) Gel had higher storage moduli values and strain-stiffening behavior within a physiologically-relevant range. As the zeta potential of added gelatin became increasingly negative, storage moduli decreased and a more strain-softening effect can be seen. Supports comprised of GelA and GelB were nearly identical, which can be attributed to the nearly neutral zeta potential of those gelatin types. Storage moduli values showed a clear dependence on zeta potential (Fig. 6C), where (-) Gel increased electrostatic repulsion, and thus produced a ‘softer’ material as particles are not adhered to neighboring particles. Supports with GelA and GelB had storage moduli values near those of PBS-based supports. Supports with (+) Gel had higher storage moduli than the equivalent PBS-based support. Onset of yielding was found to have an interesting trend as a function of zeta potential, where the highest yielding onsets were found for the (+) Gel- and (-) Gel-based supports, and those consisting of GelA and GelB had the lowest yielding onsets (Fig. 6C, middle). A similar trend was found for moduli crossover values (Fig. 6C, right). This could be due to gelatin-particle interactions, where, for example, (+) Gel leads to higher yielding onset and moduli crossover due to enhanced interparticle interactions keeping the bulk material in a gel-like configuration, whereas increased electrostatic repulsions could be attributed to the higher yielding onset and moduli crossover values in the (-) Gel-based supports.

Confocal microscopy showed clear differences in pore spaces (Fig. 6D). First, area fraction remained roughly consistent with zeta potential, showing that porosity is not heavily impacted by zeta potential of the interstitial gelatin (Fig. 6E, left). Second, average pore size remains roughly equivalent for supports with (-) Gel, GelB, and GelA. An increase is observed for (+) Gel-based supports (Fig. 6C, middle). This can be explained by the pore size distributions (Fig. 6C, right) and confocal images. As seen earlier, (+) Gel-based supports contain aggregate-like clusters, contributing to a broad pore size distribution. Upon decreasing the zeta potential, pore spaces look to be more evenly distributed and the pore size distributions show more narrow distributions compared to the (+) Gel-based supports. This change in

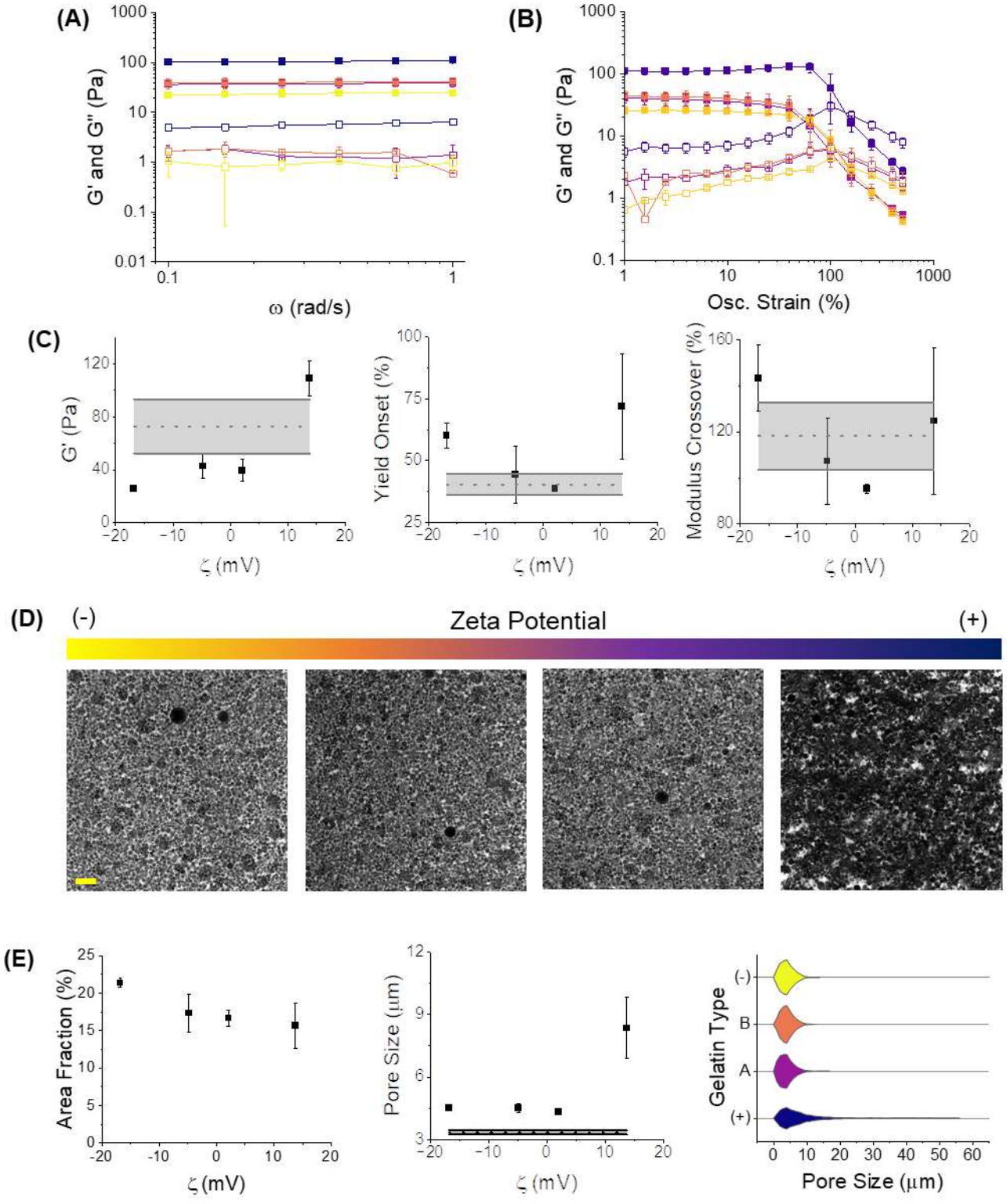

Fig. 6: Effect of gelatin zeta potential on rheological behaviors shown in (A) frequency and (B) strain sweeps, (C) trends in storage modulus, yield onset, and modulus crossover values, (D) microstructure via confocal imaging (scalebar=50μm), and (E) changes in area fraction, average pore size, and pore size distributions (error bars denote standard deviation). Error bars represent standard deviation.

distributions is due to the gelatin zeta potential, where increased electrostatic repulsions can cause particles to become repelled from neighboring particles.

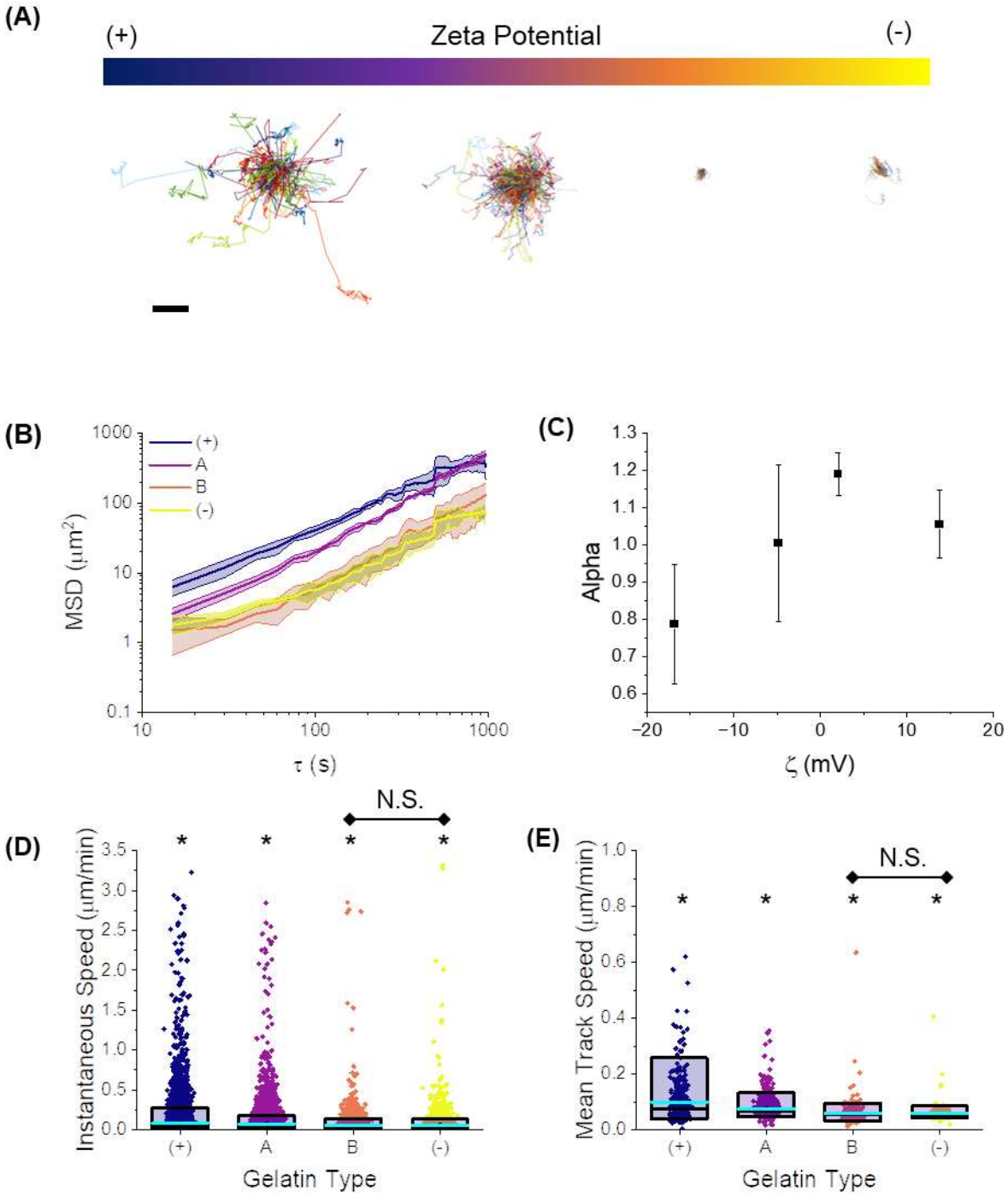

Fig. 7: (A) representative cell tracks showing change in displacement as a function of gelatin zeta potential (scalebar=50μm), and effects of gelatin zeta potential on (B) MSD, (C) alphas calculated from MSD data (error bars denote standard deviation), and (D) instantaneous and (E) mean track speeds (* denotes $p<0.05$). Boxes in (D) and (E) represent 95% confidence intervals, the cyan line refers to the mean and the black line is the median.

To examine the effect of interparticle interactions on cell migration, the same analyses as earlier were conducted. Representative cell tracks shown in Fig. 7A show a clear difference in displacements over the testing period with gelatin zeta potential. Mean squared displacement was measured as a function of zeta potential (Fig. 7B). Supports with (+) Gel had higher MSDs, followed by those comprised of GelA, then GelB and (-) Gel. The latter two had nearly identical MSD curves. Along with the cell tracks, this data indicates that (+) Gel allows for greater cell displacement. This greater displacement could be attributed to (+) Gel adsorption which may promote cell migration via cell traction. There could also be contributions due to the strain-stiffening behavior of the (+) Gel-based supports. It has been shown in previous studies that cells can locally strain-stiffen fibrils in the ECM to create a positive feedback loop that enhances migration[53].

Alpha values calculated from the MSD data increased with zeta potential (Fig. 7C). Cells migrating within supports containing (-) Gel were subdiffusive, as alpha was below a value of one. GelB supports had a diffusive alpha, and both GelA and (+) Gel were conducive to superdiffusive migration, as α values were greater than one for both types of supports. GelA had a higher α value, which may be indicative of a greater persistent random walk behavior. The difference in behavior could also be attributed to the microstructural differences, as shown in Fig. 6D, where (+) Gel supports contain aggregate-like clusters not seen in the GelA supports. GelA-based supports instead appear to have more evenly distributed pore sizes, again shown in Fig. 6D. Thus, the paths available for cells to migrate through can differ, which may cause a ‘contact guidance’ type of phenomenon and therefore alter cell migratory paths[22].

Mean and instantaneous speeds were measured as a function of zeta potential (Fig. 7D and E). Mean track speeds decreased with decreasing zeta potential, with significant differences occurring as the gelatin zeta potential transition from positively-charged to negatively-charged. Values were generally below 0.6μm/min, indicating primarily mesenchymal motion. A similar trend was observed in the instantaneous speeds but at higher values, with cell speeds being smaller than 3.5μm/min in general This thus indicates, like in the previous two sections, that cells can migrate in the lobopodial range, likely due to the presence of adhesive surfaces. The proportion of cells within this lobopodial regime decreases with increasingly negative zeta potential, as illustrated by the cell tracks were increasingly negative gelatin zeta potential leads to cells almost being at a standstill. As stated earlier, the difference in mean and instantaneous speed values could be a result of microstructural differences along with changing pore sizes during migration leading to corresponding changes in migration speeds. Again, confocal microscopy shows that for GelA, GelB, and (-) Gel-based supports, a more even pore size distribution is observed, whereas (+) Gel-containing supports have much larger pore size distributions.

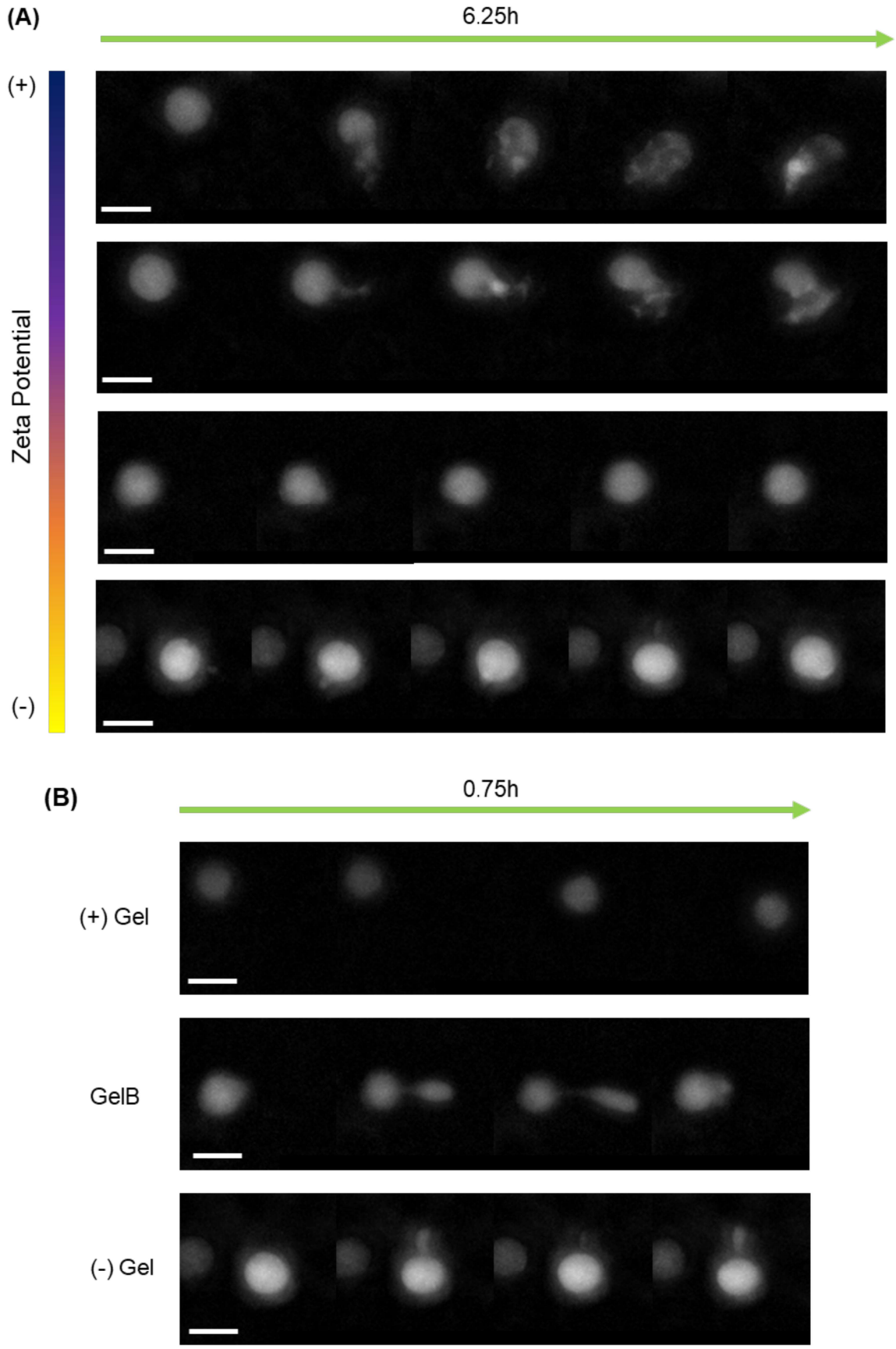

Fig. 8: (A) cell migration through supports of varying gelatin zeta potentials over a 6.25h period, (B) snapshots of cells in (+) Gel 'hopping', and cells in GelB and (-) Gel-support extending then retracting extensions into the surrounding material. Scalebars represent 20µm.

This can influence cell migratory paths and lead to cells becoming 'trapped'[36,52], adjusting speeds due to entering and exiting pore spaces of different sizes[50], or selecting pore spaces that are more conducive to migration[51].

Cells movements change with zeta potential

Cells were examined more closely in supports with gelatin of different zeta potentials. In the last section, zeta potential of the gelatin solutions appeared to have the greatest impact on cell migratory behavior, and thus were investigated more closely. In supports containing (+) Gel, two migration types are seen. For one, migrating cells showed a more adhesion-based phenotype where extensions were used for the cell to move through, as shown in Fig. 8A where over the course of 6.25h, the cell has migrated downwards about 20μm and appears to move around microgels, forming what appear to be lamellipodial-like extensions. For two, motile cells within these supports would instead show rapid movements in the form of 'hops', as illustrated in Fig. 8B, where the cell migrates about 20μm but no extensions are observed. This could be simply due to sampling interval and this cell moving at a faster speed compared to the one shown in Fig. 8A, thus limiting chances for observing cellular extensions. For GelA-based supports, migratory cells also show a similar pattern to that of the cell in the (+) Gel-based support, but slower. In the GelA-based support, a migrating cell is shown to create lamellipodial-like extensions that can bind to another region to allow the cell to move, albeit at a smaller displacement compared to cell in the (+) Gel-based support. For GelB and (-) Gel-based supports, an interesting phenomenon takes place where cells will create extensions, but possibly due to the lack or decrease of gelatin adsorption to NorHA particles, cells are less likely to migrate through pores and the extensions retract back towards the cell. Thus, it is likely that the (+) Gel chains adsorbing onto the NorHA microgels may be providing a source of traction to allow cells to migrate in the (+) Gel-based supports that may be lost as gelatin becomes increasingly negative.

Cells likely utilize pore space to migrate

Analysis of bead displacements within cell-laden and acellular constructs was conducted to assess if cells were modifying or yielding the material to migrate through the supports (Fig. 9). We anticipated that, based on a previous study with Carbopol[36] and controlled pore aspect ratios[51], that cells would adopt a 'path of least resistance' motion and move primarily through the available pore spaces. Effects from zeta potential and jamming fraction were studied. Controls with PBS were examined as well. If

cells yield the material, a significant difference in bead displacements would be noted, while no change in displacement would be observed if cells are instead using the available pore space. A similar analysis was completed in a previous study on T cell migration in Carbopol-based granular supports[36]. In this study, bead displacement in cell-laden granular supports were compared via two-sample t tests to bead displacements in corresponding acellular granular supports. In short, this analysis revealed that no significant differences between cell-laden bead displacements and the corresponding acellular bead displacements were found, thus indicating that PDAC cells are likely migrating via available pore spaces rather than yielding the local region.

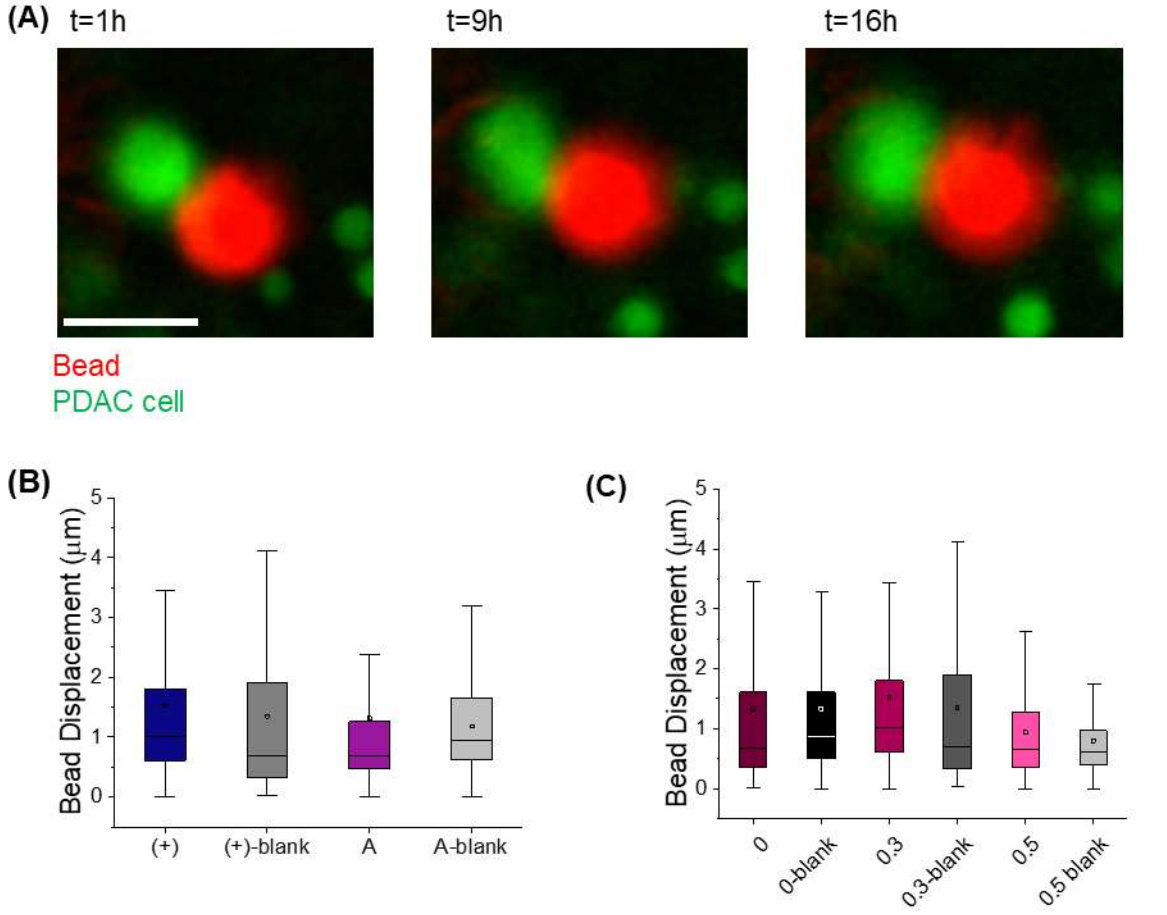

Fig. 9: (A) image of cells near a bead in a support comprised of 3% (+) Gel at a jamming fraction of 0.5, illustrating how the bead does not move significantly even as cells nearby are moving around (scalebar=50μm), and (B) bead displacements in cell-laden gels with different gelatin zeta potentials compared with acellular constructs, and (B) bead yielding as a function of jamming fraction. No statistical significance was found between corresponding groups. Error bars in (B) and (C) represent standard deviation.

Vimentin expression is greater in (+) Gel-based supports

Vimentin is an intermediate filament and biomarker found in cancer cells that have undergone EMT[54]. Because of this, it is being examined as a therapeutic target[55]. During migration, vimentin acts to protect nuclei from damage as cells migrate through porous materials using any cell migration mode. Additionally, cells utilized vimentin when migrating mesenchymally to help establish focal adhesions with the ECM[56]. Vimentin expression via a live fluorescence stain was monitored over a 16h period. When examining the effect of gelatin zeta potential, there is a clear difference between the (+) Gel-based support and the rest of the gelatin-based supports. Vimentin expression was higher over the entire testing time on average for supports with (+) Gel. This corroborates the quantified migration data, where higher cell speeds and MSD values were found, and thus can indicate that the environment provided by the (+) Gel-based support is conducive to cell motility. This could be a result of the likely adsorption of (+) Gel chains onto the anionic NorHA microgels, providing an anchor for the cells to use to move through the pore spaces of the support, especially since vimentin is also part of focal adhesions that are likely forming in this support. Interestingly, nearly identical vimentin expressions were calculated for GelA, GelB, and (-) Gel supports, despite the enhanced migratory behavior of cells within the GelA-based support. The effect of jamming fraction on vimentin expression was also tested. Vimentin had the highest expression in the 0.3 jamming fraction support compared to 0 and 0.5. The 0 jamming fraction case had the lowest vimentin expression and was comparable to supports without any gelatin (Fig. 10B and C). This could be attributed to other signaling pathways like the Hippo pathway or cytoskeletal changes that can be involved in the cell migration process, and further studies into measuring these variables would help provide insight and pinpoint specific mechanisms being used by cells in this study.

Conclusions and Future Work

A tunable, dynamic system was created by simply adjusting zeta potential of added interstitial gelatin solutions to packed NorHA microparticles. This tunable system introduces granularity, similar to in vivo microarchitectures, maintains constant total polymer concentration and is inherently porous. This produced particle-based supports with varying interparticle-interactions, and strain-stiffening behavior in the (+) Gel-based supports, similar to native tumor ECM characteristics. By increasing zeta potential, PDAC cells became increasingly motile, with the fastest migration speeds achieved in the (+) Gel-

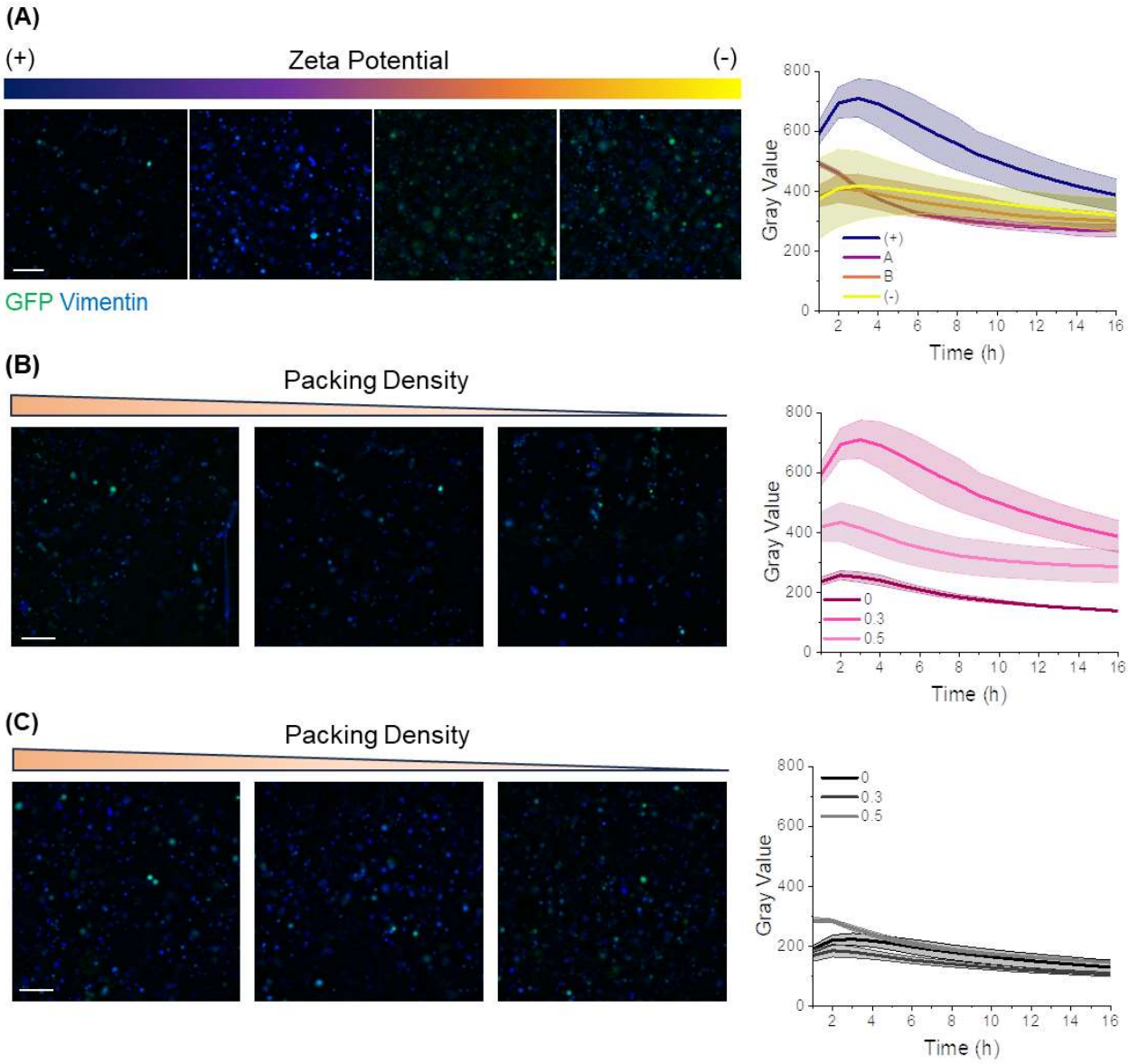

Fig. 10: vimentin expression over time as a function of (A) gelatin zeta potential, and (B) packing density, and compared with (C) PBS-based controls .Scalebars represent 200μm. Images of cells taken at t=1h. Shaded regions in graphs represent standard deviation.

based supports within the lobopodial migration range. This is also seen in the MSD and calculated α values, where PDAC cells migrated more over the testing period and had superdiffusive α values in the positively-charged gelatin samples compared to the negatively-charged gelatin-based supports.

Future experiments for this chapter include measurements of other EMT biomarkers through techniques like RT-PCR and Western blots. These experiments would provide more insight into how granular support properties affect cell migratory behavior. YAP/TAZ nuclear localization is also known to play a role in EMT as well as mechanosensing in general. This could be done via staining after fixing

cells at specified time points. Staining of actin networks with phalloidin could also be done to help further understand the effect of support mechanics on cytoskeletal rearrangements during migration. Further examination into the current vimentin experiments may need to be done to ensure that all parameters are equivalent or to re-process to correct for any discrepancies. Other future experiments would aim to further dissect cell-material interactions during migration. For instance, traction force microscopy could be employed that would provide additional insight into material yielding behaviors as well as calculate forces put onto the material as a cell is migrating. This can be combined with further analysis correlating cell shape and pore shape, as well as examining any differences in rescaled pore size and step size distributions[36].

References

1. Pancreatic Cancer - Statistics. *Cancer.Net* https://www.cancer.net/cancer-types/pancreatic-cancer/statistics (2012).
2. Rawla, P., Sunkara, T. & Gaduputi, V. Epidemiology of Pancreatic Cancer: Global Trends, Etiology and Risk Factors. *World J. Oncol.* **10**, 10–27 (2019).
3. Perez, V. M. & Kearney, J. F. The PDAC Extracellular Matrix: A Review of the ECM Protein Composition, Tumor Cell Interaction, and Therapeutic Strategies. *Front. Oncol.* **11**, (2021).
4. Erkan, M. *et al.* The Activated Stroma Index Is a Novel and Independent Prognostic Marker in Pancreatic Ductal Adenocarcinoma. *Clin. Gastroenterol. Hepatol.* **6**, 1155–1161 (2008).
5. Guerra, C. *et al.* Pancreatitis-Induced Inflammation Contributes to Pancreatic Cancer by Inhibiting Oncogene-Induced Senescence. *Cancer Cell* **19**, 728–739 (2011).
6. Storz, P. & Crawford, H. C. Carcinogenesis of Pancreatic Ductal Adenocarcinoma. *Gastroenterology* **158**, 2072–2081 (2020).
7. Ji, B. *et al.* Ras Activity Levels Control the Development of Pancreatic Diseases. *Gastroenterology* **137**, 1072-1082.e6 (2009).
8. Xu, Y., Liu, J., Nipper, M. & Wang, P. Ductal vs . acinar? Recent insights into identifying cell lineage of pancreatic ductal adenocarcinoma. *Ann. Pancreat. Cancer* **2**, (2019).
9. Whatcott, C. J. *et al.* Desmoplasia in Primary Tumors and Metastatic Lesions of Pancreatic Cancer. *Clin. Cancer Res.* **21**, 3561–3568 (2015).
10. Hamada, S. & Masamune, A. Elucidating the link between collagen and pancreatic cancer: what's next? *Expert Rev. Gastroenterol. Hepatol.* **12**, 315–317 (2018).
11. Ho, W. J., Jaffee, E. M. & Zheng, L. The tumour microenvironment in pancreatic cancer — clinical challenges and opportunities. *Nat. Rev. Clin. Oncol.* **17**, 527–540 (2020).
12. Provenzano, P. P. *et al.* Enzymatic Targeting of the Stroma Ablates Physical Barriers to Treatment of Pancreatic Ductal Adenocarcinoma. *Cancer Cell* **21**, 418–429 (2012).
13. Bynigeri, R. R. *et al.* Pancreatic stellate cell: Pandora's box for pancreatic disease biology. *World J. Gastroenterol.* **23**, 382–405 (2017).

14. DuFort, C. C. *et al.* Interstitial Pressure in Pancreatic Ductal Adenocarcinoma Is Dominated by a Gel-Fluid Phase. *Biophys. J.* **110**, 2106–2119 (2016).

15. Provenzano, P. P. & Hingorani, S. R. Hyaluronan, fluid pressure, and stromal resistance in pancreas cancer. *Br. J. Cancer* **108**, 1–8 (2013).

16. Park, M.-S. *et al.* Perfusion CT: Noninvasive Surrogate Marker for Stratification of Pancreatic Cancer Response to Concurrent Chemo- and Radiation Therapy. *Radiology* **250**, 110–117 (2009).

17. Rice, A. J. *et al.* Matrix stiffness induces epithelial–mesenchymal transition and promotes chemoresistance in pancreatic cancer cells. *Oncogenesis* **6**, e352–e352 (2017).

18. Nguyen, H. D. & Lin, C.-C. Viscoelastic stiffening of gelatin hydrogels for dynamic culture of pancreatic cancer spheroids. *Acta Biomater.* (2024) doi:10.1016/j.actbio.2024.02.010.

19. Tilghman, R. W. *et al.* Matrix Rigidity Regulates Cancer Cell Growth by Modulating Cellular Metabolism and Protein Synthesis. *PLOS ONE* **7**, e37231 (2012).

20. Seo, B. R. *et al.* Collagen microarchitecture mechanically controls myofibroblast differentiation. *Proc. Natl. Acad. Sci.* **117**, 11387–11398 (2020).

21. Seager, R. J., Hajal, C., Spill, F., Kamm, R. D. & Zaman, M. H. Dynamic interplay between tumour, stroma and immune system can drive or prevent tumour progression. *Converg. Sci. Phys. Oncol.* **3**, 034002 (2017).

22. Ramirez-San Juan, G. R., Oakes, P. W. & Gardel, M. L. Contact guidance requires spatial control of leading-edge protrusion. *Mol. Biol. Cell* **28**, 1043–1053 (2017).

23. Modeling the two-way feedback between contractility and matrix realignment reveals a nonlinear mode of cancer cell invasion | PNAS. https://www.pnas.org/doi/full/10.1073/pnas.1617037114.

24. Qazi, T. H. *et al.* Anisotropic Rod-Shaped Particles Influence Injectable Granular Hydrogel Properties and Cell Invasion. *Adv. Mater.* **34**, 2109194 (2022).

25. Emiroglu, D. B. *et al.* Building block properties govern granular hydrogel mechanics through contact deformations. *Sci. Adv.* **8**, eadd8570 (2022).

26. Widener, A. E., Duraivel, S., Angelini, T. E. & Phelps, E. A. Injectable Microporous Annealed Particle Hydrogel Based on Guest–Host-Interlinked Polyethylene Glycol Maleimide Microgels. *Adv. NanoBiomed Res.* **2**, 2200030 (2022).

27. Hinton, T. J. *et al.* Three-dimensional printing of complex biological structures by freeform reversible embedding of suspended hydrogels. *Sci. Adv.* **1**, e1500758 (2015).

28. Bhattacharjee, T. *et al.* Writing in the granular gel medium. *Sci. Adv.* **1**, e1500655 (2015).

29. Highley, C. B., Song, K. H., Daly, A. C. & Burdick, J. A. Jammed Microgel Inks for 3D Printing Applications. *Adv. Sci.* **6**, 1801076 (2019).

30. Griffin, D. R., Weaver, W. M., Scumpia, P., Di Carlo, D. & Segura, T. Accelerated wound healing by injectable microporous gel scaffolds assembled from annealed building blocks. *Nat. Mater.* **14**, 737–744 (2015).

31. Cunha, A. F. *et al.* Cell Response in Free-Packed Granular Systems. *ACS Appl. Mater. Interfaces* **14**, 40469–40480 (2022).

32. Gramlich, W. M., Kim, I. L. & Burdick, J. A. Synthesis and orthogonal photopatterning of hyaluronic acid hydrogels with thiol-norbornene chemistry. *Biomaterials* **34**, 9803–9811 (2013).

33. K, J., Naskar, D., Kundu, S. C. & James, N. R. Fabrication of cationized gelatin nanofibers by electrospinning for tissue regeneration. *RSC Adv.* **5**, 89521–89530 (2015).

34. Madl, A. C., Madl, C. M. & Myung, D. Injectable Cucurbit[8]uril-Based Supramolecular Gelatin Hydrogels for Cell Encapsulation. *ACS Macro Lett.* **9**, 619–626 (2020).

35. Domander, R., Felder, A. A. & Doube, M. BoneJ2 - refactoring established research software. *Wellcome Open Res.* **6**, 37 (2021).

36. Bhattacharjee, T. & Angelini, T. E. 3D T cell motility in jammed microgels. *J. Phys. Appl. Phys.* **52**, 024006 (2018).

37. Otsu, N. A Threshold Selection Method from Gray-Level Histograms. *IEEE Trans. Syst. Man Cybern.* **9**, 62–66 (1979).

38. Visweshwaran, S. P. & Maritzen, T. A simple 3D cellular chemotaxis assay and analysis workflow suitable for a wide range of migrating cells. *MethodsX* **6**, 2807–2821 (2019).

39. Ershov, D. *et al.* TrackMate 7: integrating state-of-the-art segmentation algorithms into tracking pipelines. *Nat. Methods* **19**, 829–832 (2022).

40. Wortel, I. M. N. *et al.* CelltrackR: An R package for fast and flexible analysis of immune cell migration data. *ImmunoInformatics* **1–2**, 100003 (2021).

41. Nousi, A., Søgaard, M. T., Audoin, M. & Jauffred, L. Single-cell tracking reveals super-spreading brain cancer cells with high persistence. *Biochem. Biophys. Rep.* **28**, 101120 (2021).

42. Passucci, G., Brasch, M. E., Henderson, J. H., Zaburdaev, V. & Manning, M. L. Identifying the mechanism for superdiffusivity in mouse fibroblast motility. *PLOS Comput. Biol.* **15**, e1006732 (2019).

43. Legant, W. R. *et al.* Measurement of mechanical tractions exerted by cells in three-dimensional matrices. *Nat. Methods* **7**, 969–971 (2010).

44. Chaudhuri, O. *et al.* Hydrogels with tunable stress relaxation regulate stem cell fate and activity. *Nat. Mater.* **15**, 326–334 (2016).

45. Trappe, V., Prasad, V., Cipelletti, L., Segre, P. N. & Weitz, D. A. Jamming phase diagram for attractive particles. *Nature* **411**, 772–775 (2001).

46. Koeze, D. J. & Tighe, B. P. Sticky Matters: Jamming and Rigid Cluster Statistics with Attractive Particle Interactions. *Phys. Rev. Lett.* **121**, 188002 (2018).

47. Bear, J. E. & Haugh, J. M. Directed migration of mesenchymal cells: where signaling and the cytoskeleton meet. *Curr. Opin. Cell Biol.* **30**, 74–82 (2014).

48. Yamada, K. M. & Sixt, M. Mechanisms of 3D cell migration. *Nat. Rev. Mol. Cell Biol.* **20**, 738–752 (2019).

49. Holle, A. W. *et al.* Cancer Cells Invade Confined Microchannels via a Self-Directed Mesenchymal-to-Amoeboid Transition. *Nano Lett.* **19**, 2280–2290 (2019).

50. Lautscham, L. A. *et al.* Migration in Confined 3D Environments Is Determined by a Combination of Adhesiveness, Nuclear Volume, Contractility, and Cell Stiffness. *Biophys. J.* **109**, 900–913 (2015).

51. Green, B. J. *et al.* Pore Shape Defines Paths of Metastatic Cell Migration. *Nano Lett.* **18**, 2140–2147 (2018).

52. Bhattacharjee, T. & Datta, S. S. Bacterial hopping and trapping in porous media. *Nat. Commun.* **10**, 2075 (2019).

53. Fibrous nonlinear elasticity enables positive mechanical feedback between cells and ECMs | PNAS. https://www.pnas.org/doi/10.1073/pnas.1613058113.

54. Battaglia, R. A., Delic, S., Herrmann, H. & Snider, N. T. Vimentin on the move: new developments in cell migration. Preprint at https://doi.org/10.12688/f1000research.15967.1 (2018).

55. Tabatabaee, A. *et al.* Targeting vimentin: a multifaceted approach to combatting cancer metastasis and drug resistance. *Cancer Metastasis Rev.* (2023) doi:10.1007/s10555-023-10154-7.

56. Wu, H. *et al.* Vimentin intermediate filaments and filamentous actin form unexpected interpenetrating networks that redefine the cell cortex. *Proc. Natl. Acad. Sci. U. S. A.* **119**, e2115217119 (2022).

Supplemental Information

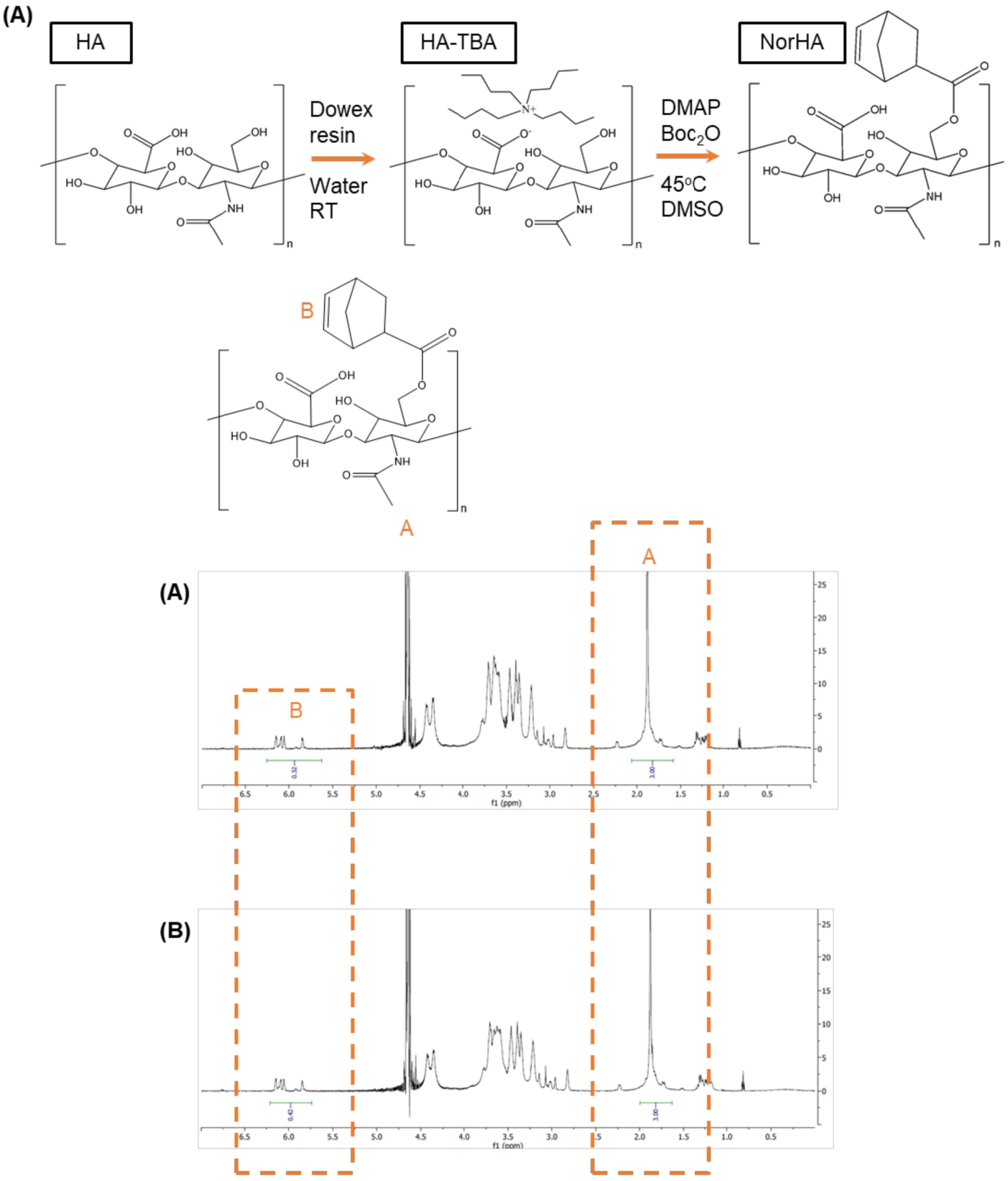

SI Fig. 1: (A) NorHA synthesis route and (B) NMR for two batches used in this study, one with 16% modification and another with 21% modification

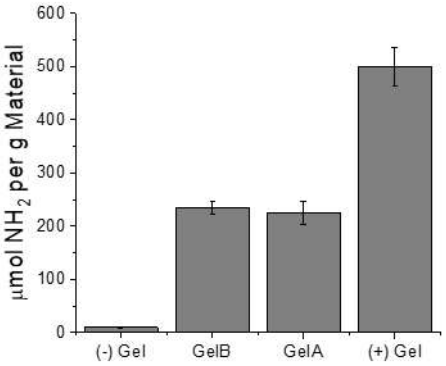

SI Fig. 2: Fluorescamine assay for all gelatin materials used in this study (n=3)

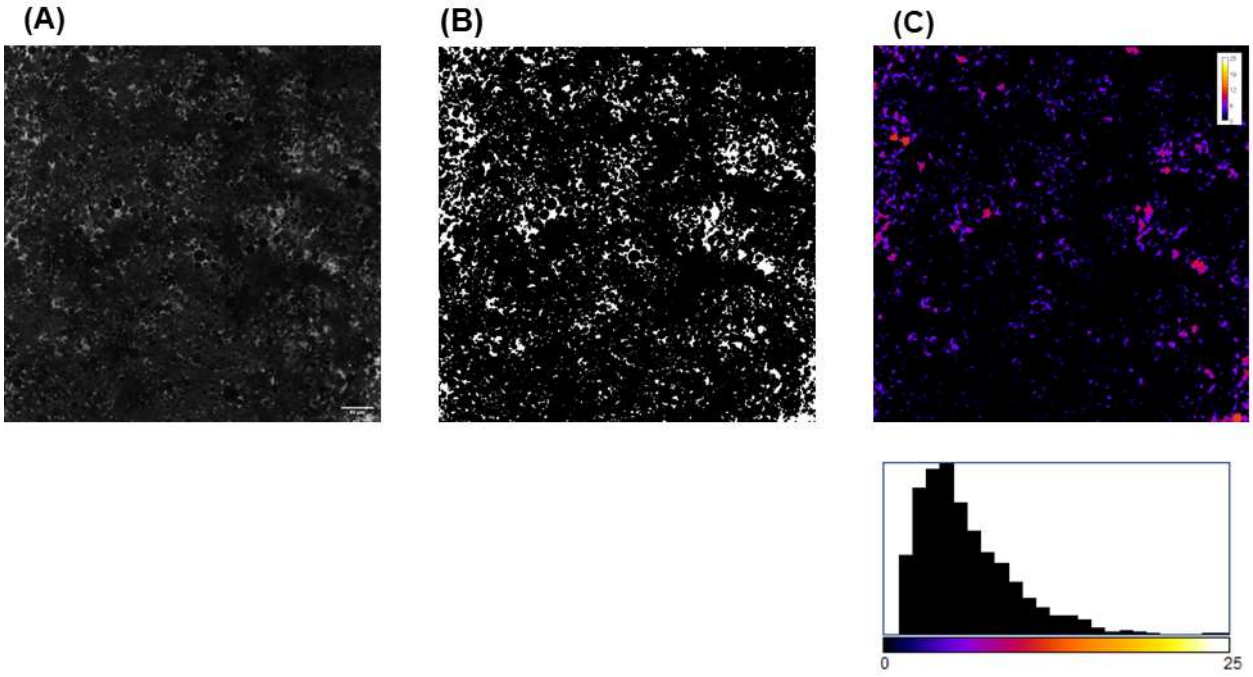

SI Fig. 3: Example of image processing used to obtain pore sizes from BoneJ, (A) confocal image of a support with 2% (+) Gel, (B) thresholded z-stack using Otsu's method, and (C) resulting thickness map from which pore sizes can be obtained.

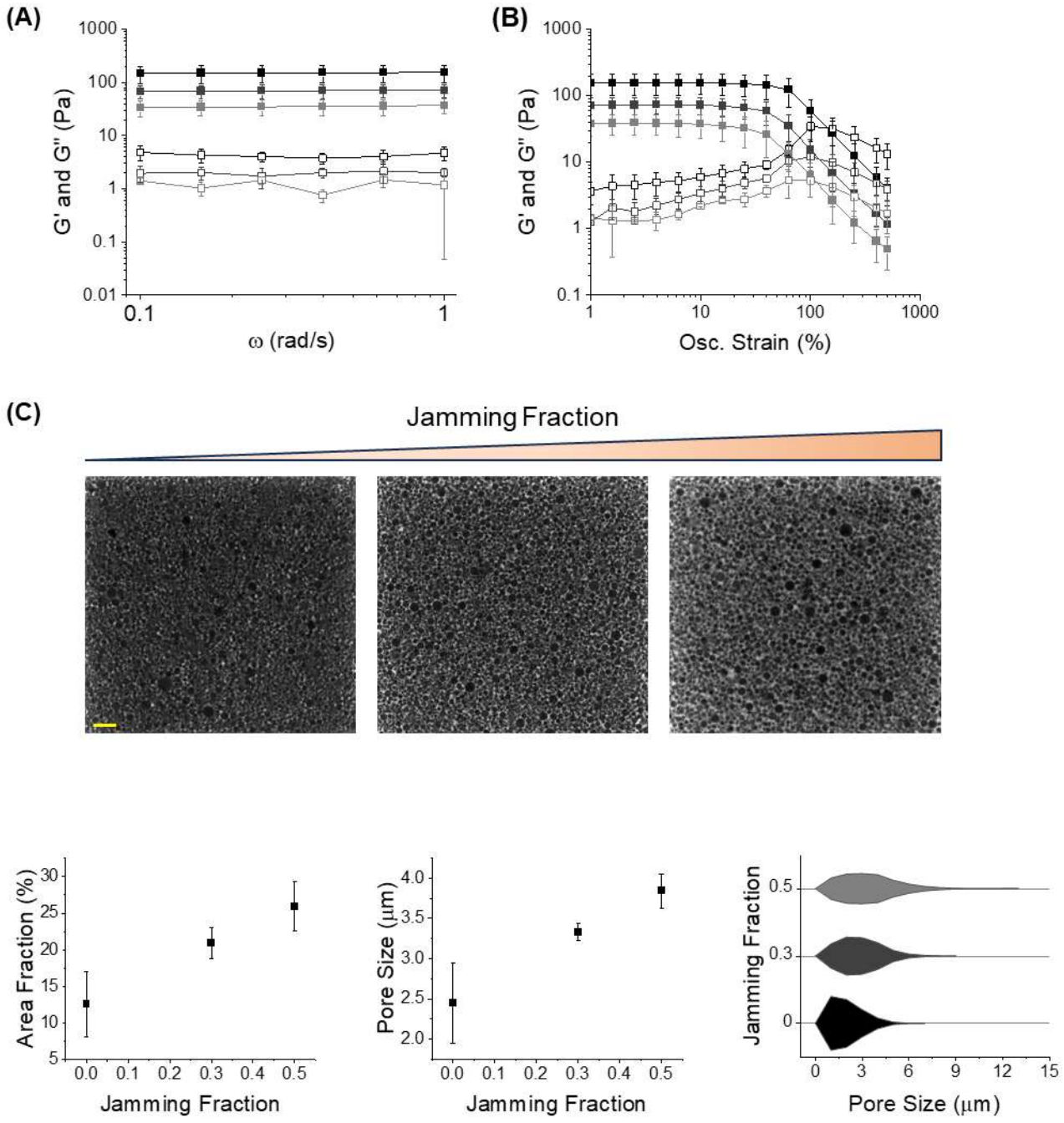

SI Fig. 4: (A) Frequency and (B) strain sweeps of PBS-based supports at different jamming fractions, (C) confocal images of PBS-based supports at different jamming fractions, and (D) effects of jamming fraction on trends in area fraction, average pore size, and pore size distributions.

Chapter 6:

Conclusions and Future Work

Conclusions

In Chapter 2, 3D printing of tunable perfusable channels was achieved using a microgel-based ink and support. By using a microgel-based ink and formulating both the ink and support with single-digit particle diameters, smaller filaments were able to be printed. However, this may have been limited due to the 3D printing motor, as the turning of this motor ultimately can dictate the extruded volume. Channels could be perfused and we showed HUVEC linings could be obtained as well as enhanced fibroblast viability when embedded in the surrounding support. This work paves the path towards future endeavors in complex, vascularized *in vitro* models.

In Chapter 3, NorHA microgel supports could be tuned through the inclusion of (+) Gel, forming a dynamically-crosslinked, porous system. The dynamic electrostatic interactions tethered particles together as the (+) Gel adsorbs onto the anionic NorHA microgels. Rheological studies showed that strain-stiffening behavior occurs in the presence of (+) Gel, and (+) Gel-containing formulations displayed poroelastic-like behavior, with the caveat that the interaction system being used here is dynamic so particle rearrangements can still occur under compressive loading. These two characteristics provide a more physiologically-relevant model, as native tissues exhibit strain-stiffening and poroelastic behaviors. The dynamic nature of electrostatic interactions also allows for the use of this material system in injectable applications such as 3D printing and cell delivery. However, additional work is needed to enhance cell viability within these granular formulations. This work, however, still remains promising.

In Chapter 5, the tunability of the electrostatic granular system was further developed by modifying the zeta potential of gelatin. The concentration of (+) Gel and jamming fraction were also assessed for effects on single cell migratory behaviors. It was found that by altering the interparticle interactions via modulation of gelatin zeta potential, cell migratory behaviors could be altered. This work sets the stage for a variety of applications in cancer research as well as cell migratory work in general, as nearly all

cell types are affected by ECM mechanics. The work provides an easily tunable platform in which granularity is introduced and total polymer concentration can be kept consistent between groups.

Future Work and Applications

Future Work for Chapter 2: Biofabrication strategies and applications

Extravasation studies of cancer cells and pathogenic infections and vasculature-pathogen interactions

Cancer cell extravasation is a required step in the metastatic cascade. Once a cancer cell is in the blood vasculature, the cell attaches to the vessel wall, and enters into another tissue[1]. However, extravasation is a difficult process to monitor *in vivo* due to limited imaging techniques[1,2] and time[1,3,4]. Thus, a printed channel, or a network of printed channels, could be formed, processed, endothelialized, and then used to flow cancer cells through and continuously monitor extravasation and test variables that enhance this capability such as tissue mechanics, or therapeutics that could potentially inhibit this process. A recent study showed promise in this area by creating a vascular network with organ-like chambers[5]. The system developed in Chapter 2 could thus be used in this capacity.

Similar to cancer cells, parasites are known to undergo an analogous process called parasitic tropism[6]. For parasitic diseases like malaria, part of the parasite life cycle involves the parasite exiting the blood vasculature and entering the liver, where the parasite can fully mature prior to exiting and traveling into the next mosquito[7]. However, the determination of where a parasite may extravasate into to begin this step in a lifecycle can be difficult to test[6]. Thus, to further understand this step in a parasite lifecycle and be able to test therapeutics that target this aspect, relevant *in vitro* models may be required. By being able to print endothelialized channels using the materials and techniques developed in Chapter 2, an endothelial channel could be established, then a chemotactic gradient can be formed using a parallel reservoir. A parasite-laden solution can be perfused through the channel and the effect of chemotactic gradients and local mechanics can be tested to help pinpoint to which variables the parasite in question is responsive. This would provide further understanding into this phenomenon and establish technology that can be used to test therapeutic efficacy.

Pathogenic diseases can often interact with blood vasculature. For example, during the COVID-19 pandemic, it was observed that the virus, while primarily causing respiratory illness, can affect blood endothelial cells and cause serious complications such as thromboses[8,9]. Other infectious diseases like Ebola and other hemorrhagic fevers[10], HIV[11], and complications from cancer like sepsis[12] also heavily affect vasculature. As a result, an *in vitro* model that can accurately mimic a native blood vessel would

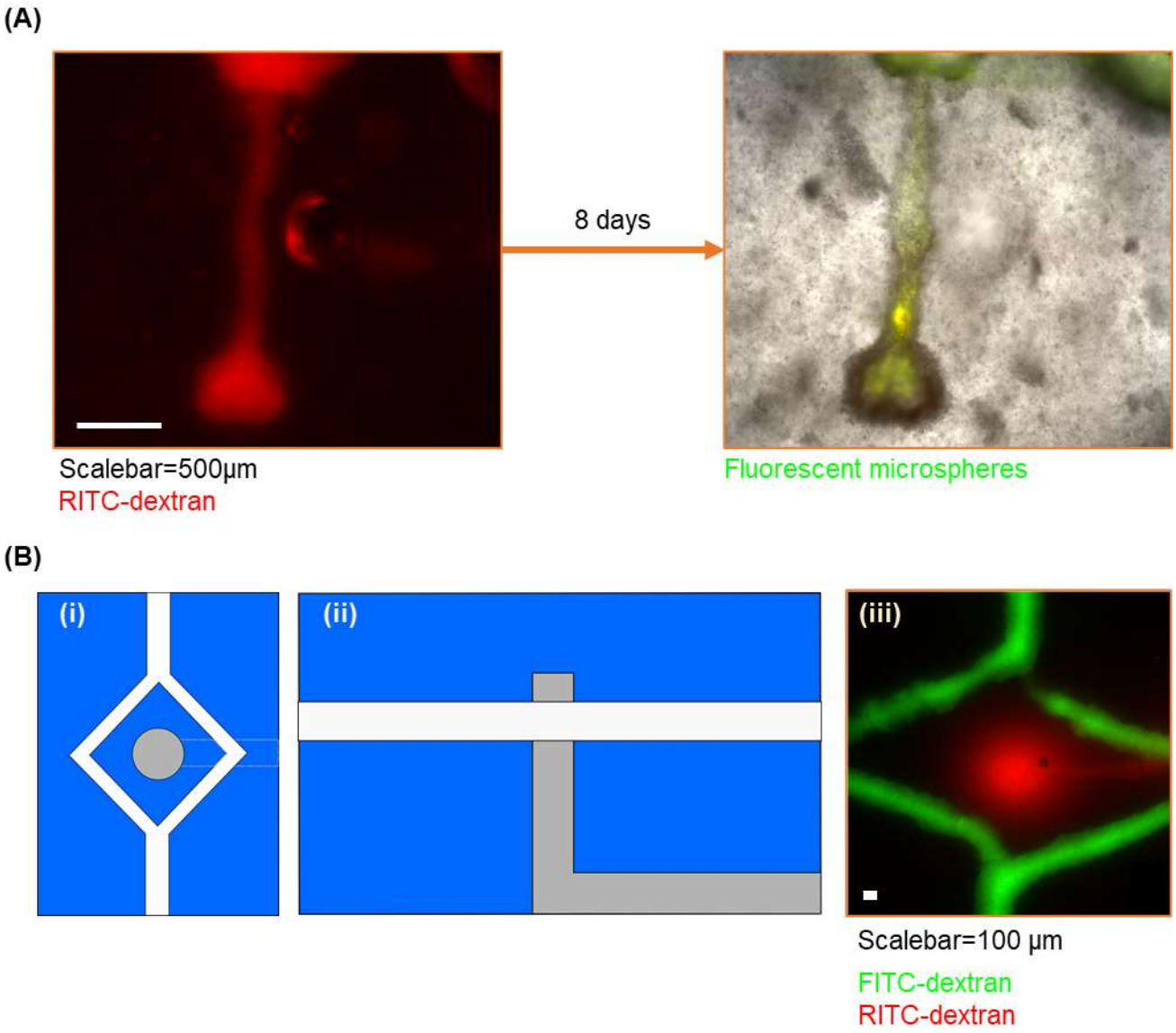

Fig. 1: (A) printing of a blind-ended channel using the ink and support system developed in Chapter 1, with a widefield image of an as-printed filament on the left, and 8 days later the open blind-ended channel retains shape fidelity (left), (B) another example of lymphatic printing using the materials developed in Chapter 1, showing a blueprint ((i) top and (ii) side) of a branching design to mimic vasculature with a blind-ended channel printed between the branching structures, and (iii) a widefield image showing the resulting printed filaments

be of great importance for immediately identifying any other possible routes that an infection might use and how to therapeutically target these routes.

Lymphatic vessel engineering

Lymphatic capillaries are a crucial yet often overlooked aspect in tissue engineering. Like blood vasculature, lymphatic vasculature is found in nearly all human tissues and plays a significant role in normal functions like immune cell trafficking[13], but also in aberrant functions like cancer metastasis[13,14]. These capillaries are located near the blood vasculature and exist as blind-ended channels. Tissues have interstitial flow that travels from the vasculature to these blind-ended channels and this interstitial fluid is comprised of tissue waste products and proteins. These blind-ended channels conglomerate into larger lymphatic vessels that eventually enter a lymph node, from which immune cell trafficking can be coordinated if needed. From the lymph node, the filtered material travels into the main blood stream. Lymphatic capillaries differ from blood capillaries in structure[13]. Blood capillaries are often referred to as having a ‘zipper’ configuration due to the structure of the tight junctions, whereas the lymphatic capillaries have a ‘button’ configuration, as there are less tight junctions in comparison[15]. Previous work has shown that the inclusion of lymphatic channels within an *in vitro* system can be crucial to aspects like endothelial channel stability in an engineered construct[16]. Thus, inclusion of lymphatic vasculature must be considered when designing *in vitro* systems.

Preliminary work has shown that the printing technique outlined in Chapter 2 can be used for printing and evacuation of blind-ended channels. A printed blind-ended filament is shown in Fig. 1A. The gelatin ink can be evacuated, leaving behind an open blind-ended channel that remains open over an 8-day period. Mediated by the receptor LYVE-1, lymphatic endothelial cells would be expected to readily attach to the NorHA support, as this receptor mediates binding to HA in native tissues[17]. Printing can be used to establish a blood-lymphatic network, as seen in Fig. 1B, where a blind-ended channel, shown in red and representing lymphatic vasculature, can be printed between two branching then unifying channels, shown in green and representing a branching blood vascular network. Thus, the technique and materials developed in Chapter 2 provide a platform in which complex vascular networks could be created.

Addition of unidirectional flow to endothelialized network

It is well established that blood flows unidirectionally from the heart to the tissues, then back. In the devices and endothelialized channels shown in Chapter 2, bidirectional flow was used. Bidirectional flow, however, has been shown to give blood endothelial cells a diseased morphology and barrier

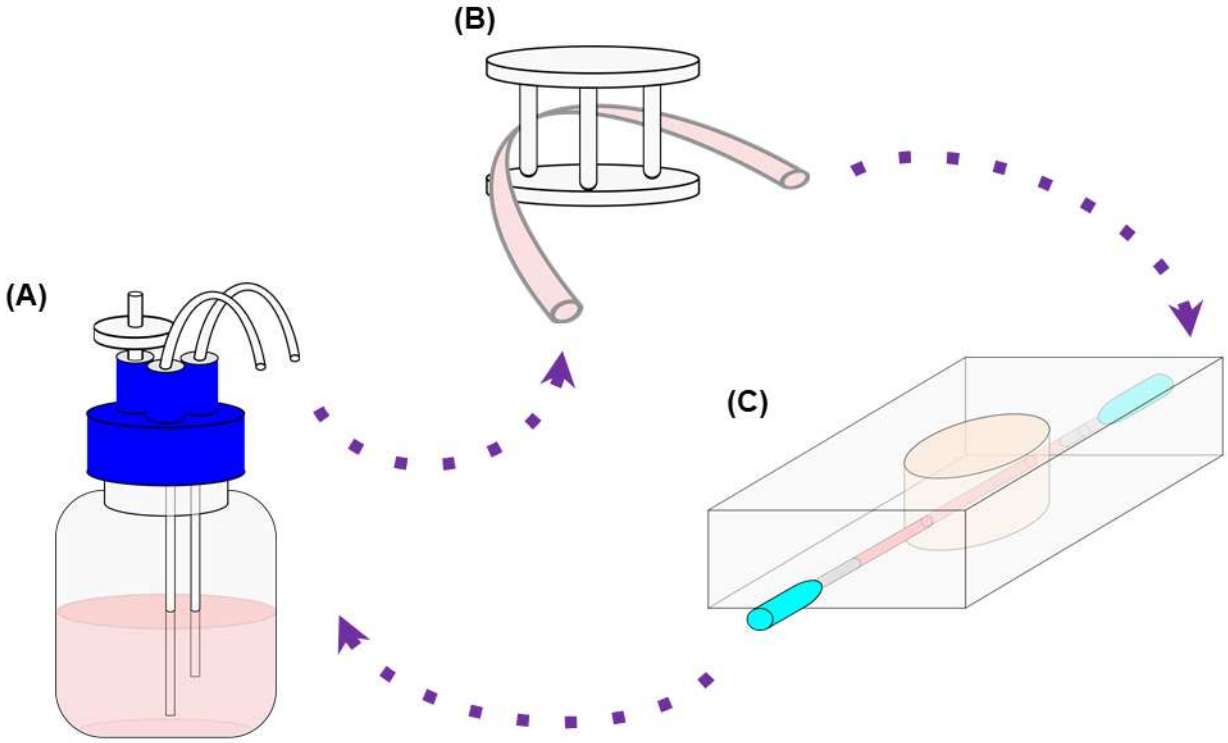

Fig. 2: Design of a unidirectional flow system for future endothelialized-channel work. (A) media can be placed in a media bottle fed with two tubes, one of which would go around a (B) peristaltic pump, from which then tubing can branch or new tubing with smaller diameters can be attached via connectors to adjust flow rate to reach a physiologically-relevant value, which can then lead into a (C) device housing the endothelialized channel, after which the media would be pumped back into the media bottle.

properties compared to unidirectional flow[18]. As a result, the device in chapter 2 would need improvements. To do this, a peristaltic pump can be used to flow media in a unidirectional manner (Fig. 2). This would require modifications to the device, where needles can be used to create channels within the PDMS that can attach to tubing that then connects to the pump. The flow within this system can be adjusted to reach physiologically-relevant flow rates. This system can also be adjusted to perfused multiple devices. Additionally, it is known in some diseases can produce aberrant flows and thus this could be easily adjusted in this system.

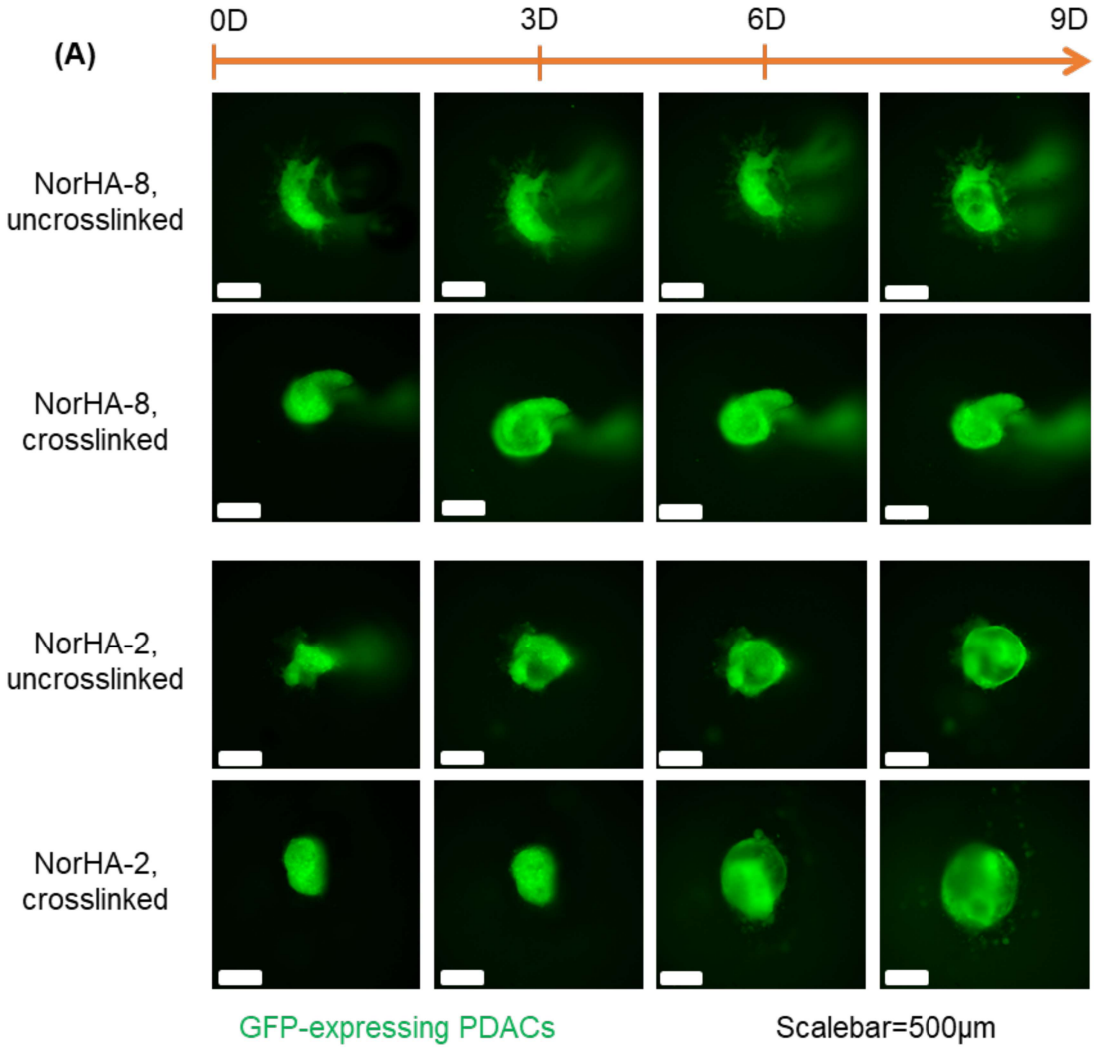

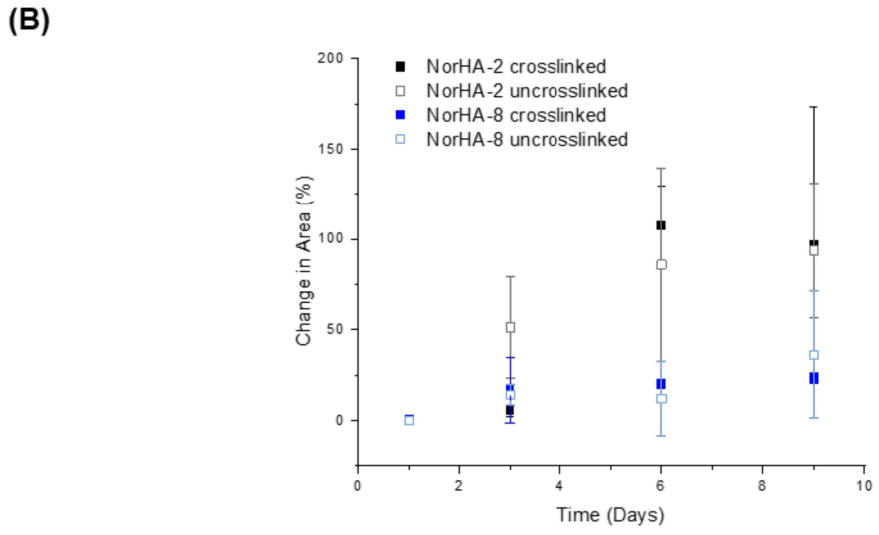

Fig. 3: (A) growth of PDAC cells in materials developed in Chapter 2, both crosslinked and non-crosslinked groups with high and low stiffness particles over a 9 day period, (B) quantification of images from (A) over time, showing how bulk yielding properties and particle stiffness can affect proliferation of cancer cells

Growth of spheroids as function of support properties

Granular supports have been previously used to examine spheroid or collective cell growth over time[19]. From Chapter 2, NorHA-based microgel supports can be tuned by simply adjusting the local microgel mechanics via crosslinking density. As crosslinking density decreased, bulk mechanical properties changed accordingly, as illustrated in the yield stress values. Yield stress can have an influence in spheroid behaviors. Additionally, the ability to inject a cell-dense or cell-only ink is advantageous in the biofabrication field. Preliminary work in Fig. 3 shows that cells, when injected into NorHA-2 and -8 supports with or without post-injection crosslinking via brief UV exposure, tended to grow more rapidly in the NorHA-2 supports compared to the NorHA-8 supports, and this was independent of crosslinking of the interstitial NorHA solution. This paves the path to creating more complex microenvironments, such as those of PDAC, with the inclusion of an endothelialized channel to more accurately mimic native tissue environments.

Future Work for Chapter 3: Injectable granular hydrogel applications

Wound healing applications

A primary application for injectable materials is wound healing. This is a complex cascade that produces the self-healing behavior found in native tissues. However, pre-existing conditions such as diabetes can prevent full functioning of this cascade due to inadequate immune response[20]. Thus, materials conducive to wound healing, through cell or therapeutic delivery, must be developed. The work described in Chapter 3 shows great promise in this type of application. The electrostatically-driven granular gel was shown to be injectable and possess characteristics found in native human tissue such as granularity, strain-stiffening behavior, and poroelasticity. However, the viability data from Chapter 3 showed low shear-protecting capabilities of the granular system. Thus, further work to achieve this must be accomplished. Previously, shear-protection of cells has been accomplished through careful design of hydrogels to enhance shear-thinning behavior to relieve mechanical stresses that cells can experience during extrusion. In the system described in Chapter 3, this could include the addition of another polymer, such as hyaluronic acid, to help create a shear-thinning environment between the particles that can improve cell viabilities. By enhancing cell viabilities within the granular hydrogel, further applications into delivery fibroblasts to aid in wound healing can be developed.

3D printing

3D printing remains a key technique in the development of customized *in vitro* models. Similar to injectable hydrogels, 3D printing has the same requirements in addition to other necessary features such as filament formation and shape fidelity upon deposition onto a substrate. The system developed in Chapter 3 showed these requirements, where the granular system required low pressures for extrusion and exhibited self-healing behavior. Good filament formation was also observed when testing the effects of (+) Gel concentration on microgel formulations. Thus, the microgel-based formulations developed in Chapter 3 provide a good platform for future applications in creating 3D printed, cell-laden constructs.

Creating injectable cell delivery system with endothelial cells

Other cell types, such as endothelial cells, have been used in previous studies to demonstrate therapeutic effects for wound healing applications[21–23]. Endothelial cells are commonly examined as tissue regeneration requires a blood supply for proper oxygenation and nutrient diffusion to aid in proper tissue regeneration. Thus, once shear-protecting capabilities have been improved, further examination into long-term cell viability and other cellular behaviors can be conducted. This can be done via metabolic testing through repeated alamar blue assays, or repeated live/dead assays. If endothelial cells are to be studied, further work into vascular network formation such as quantification of branching and expression of VE-Cadherin can be conducted.

Future Work for Chapter 5: directed PDAC migration, and vasculature and immune cell inclusion

As shown in Chapter 5, tunable granular material systems can be used to modify an environment in which cancer cells reside and thus examine the environmental effects on single cell cancer migration. To dive further into this project, a few key paths can be taken. One, a chemotactic gradient can be introduced. Two, collective PDAC migration can be studied using the same tunable system developed n Chapter 5. And three, cell types relevant to the PDAC microenvironment can be studied and even included with PDAC cells to determine if migration is modulated as a result. These paths aim to help create a more physiologically-relevant *in vitro* PDAC model.

Cancer cell migration in the presence of a chemotactic gradient

Cancer cells, like many other cells, can migrate directionally in the presence of a chemotactic gradient. Within the tumor microenvironment, several gradients are created that attract cells like macrophages and regulatory T cells to help create an immunosuppressive environment, such as CX3CL1 and CCL19[24]. Gradients are also established that facilitate cancer cell migration outside of the tumor. For example, CCL-2, also known as MCP-1, can facilitate the extravasation of breast cancer cells into bone[25] and lung tissues[26]. Thus, the tunable support system developed in Chapter 5 could be used for such studies to help further understand cancer cell migration in the presence of a chemoattractant gradient.

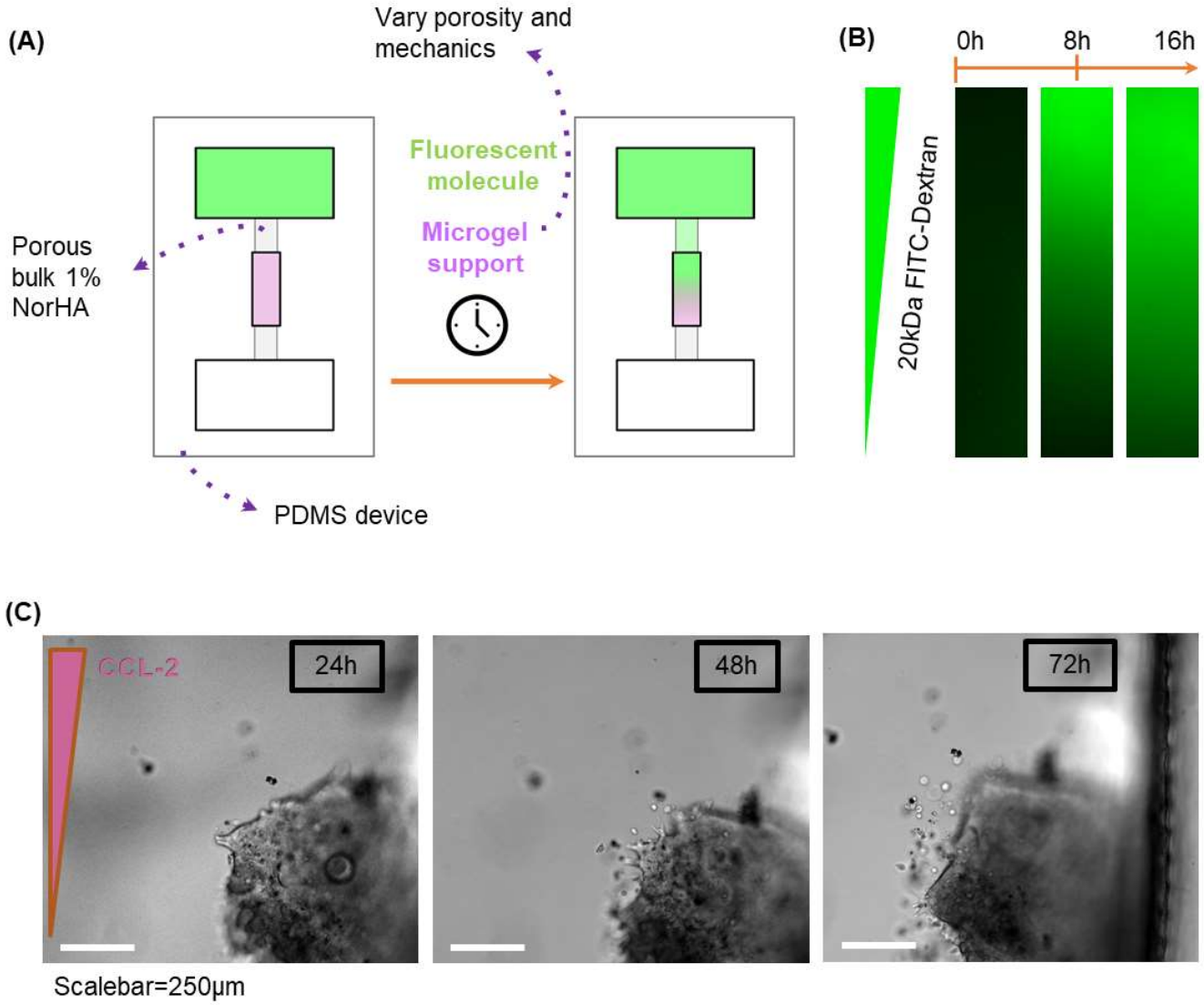

Fig. 4: (A) setup for chemotaxis experiments, done using a PDMS device with two reservoirs housing media with and without a chemoattractant and where cell migration, taking place in the central reservoir in a microgel-based support, can be monitored over time, (B) diffusion of FITC-dextran through a highly packed microgel-based support over a 16h period, illustrating that a chemoattractant gradient can be established in these systems, and (C) dissemination of PDAC cells from a PDAC spheroid over a 72h period using the above setup with a CCL-2 gradient.

In preliminary work, diffusive gradients can be established using a modified device shown in Fig. 4. Three reservoirs are in parallel, with the central reservoir designed to hold the microgels plus cells, while the two flanking reservoirs would hold media. One of these flanking reservoirs would contain a chemoattractant that can then diffuse down into the other media-only reservoir. This device is made by casting PDMS around a mold, then plasma bonding it to a glass slide or glass-bottom well plate. The central reservoir contains the support with dispersed cells or spheroids. In Fig. 4B, diffusion of a 20kDa FITC-dextran solution was measured over a 16h period in a support consisting only of highly packed NorHA microgels, showing that a chemoattractant gradient could be established using this technique. Migration of PDAC spheroids in the presence of a MCP-1 gradient was also assessed over a 72h period, showing dissemination of cells from the spheroid (Fig. 4C). Thus, this system can be used to further understand PDAC as well as other processes such as angiogenesis, lymphangiogenesis, and immune cell migration in the presence of a chemoattractant gradient.

Collective cell migration studies using spheroids

While the tunable electrostatic system characterized in Chapter 5 showed to have an impact on single cell migration when bulk mechanics were modified via tuning gelatin zeta potential, the use of spheroids to study collective cell migration would be more physiologically-relevant. Tumors are generally collections of cells rather than single-cell dispersion throughout a tissue. Collective cell migration is a complex process where cells in a spheroid coordinate with other neighboring cells to invade the local tissue. Typically, there is a ‘leader-follower’ setup where cells from the edge of the spheroid invade into the surrounding material and other cells follow in response[27]. Mechanics of this environment also play a role in how collective cell migration occurs. If resistance is high, more branching may be observed rather than single cells leaving the spheroid environment[27,28]. From Chapters 4 and 5, other cues such as porosity play an important role in cell migration, and thus, the developed tunable granular support system from Chapter 5 can be used to study the effects of mechanics on collective cell behavior.

Preliminary work in Fig. 5 shows that packing density/porosity and (+) Gel concentration play a role in collective cell migration of PDAC spheroids. In samples containing 3% (+) Gel, noticeable invasion of the PDAC spheroids is observed. This was not the case in the 0-2% (+) Gel scenarios. Vimentin expression was also tested as a function of gelatin zeta potential, as seen in Fig. 6, where vimentin expression was greater in (+) Gel-based supports, followed by GelA, then (-) Gel and GelB. Futurework into collective cancer cell migration within these supports would entail measuring the invasive radius over time, rate of invasion, and complexity, described by the following equation[29]:

$$Complexity = \frac{P^2}{4\pi * A}$$

Where P is the perimeter of the spheroid and A is the area. For a perfect sphere, complexity would be measured as a value of one. If sprouting is observed, then we expect that complexity will increase[29].

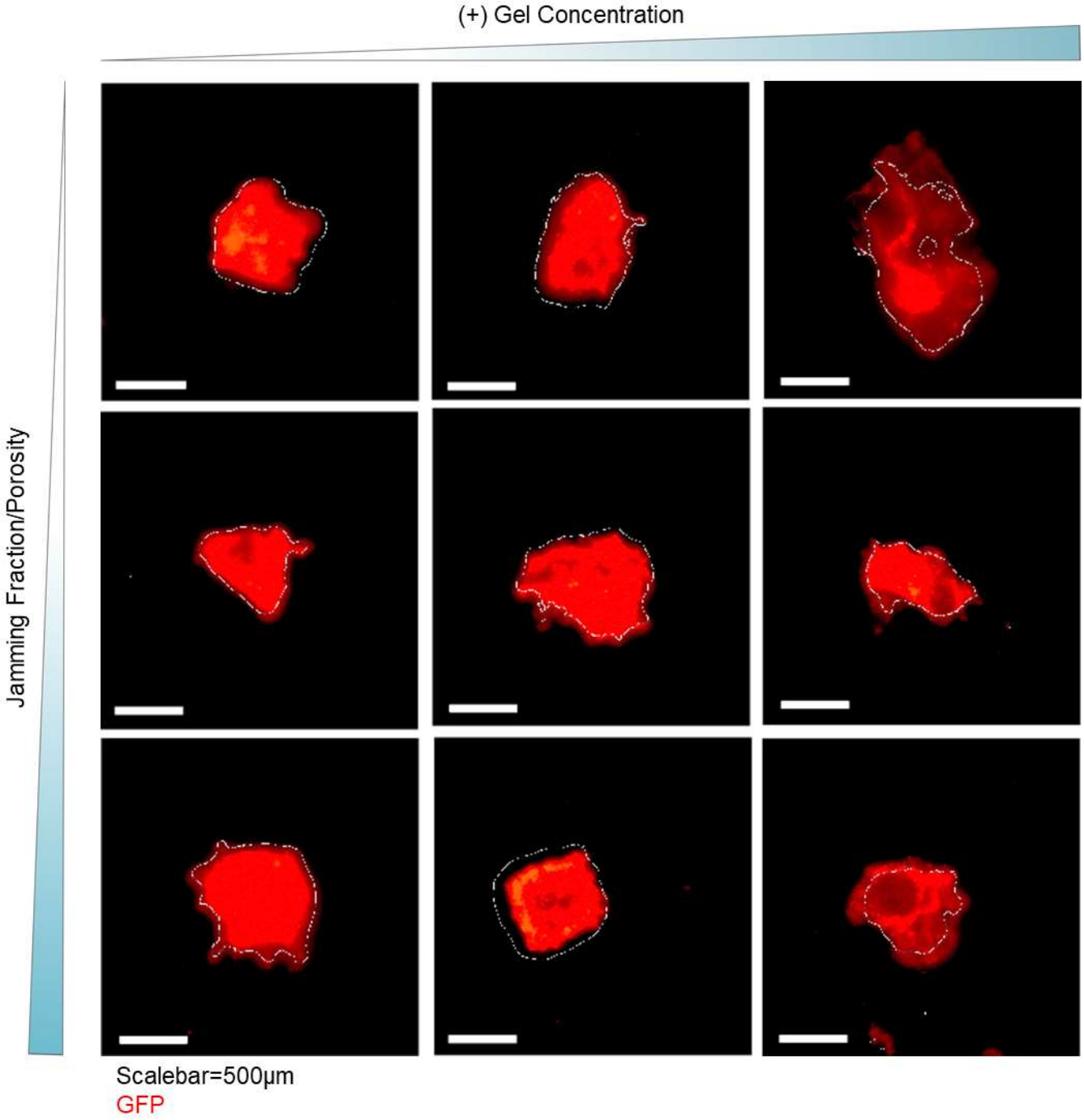

Fig. 5: Effect of porosity and (+) Gel concentration on invasion by PDAC spheroids, illustrating how interparticle interactions, adhesion, and pore spaces can affect cancer cell migratory behaviors. White outlines represent the original spheroid shape.

With the change of interparticle interactions, along with the work shown in Chapter 5 and preliminary spheroid work, we also expect that greater collective cell migration will be observed in the (+) Gel-based supports.

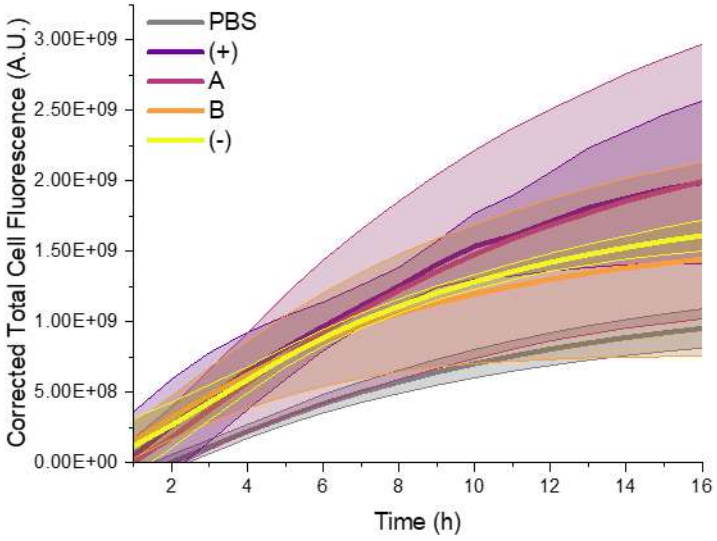

Fig. 6: Vimentin expression over time in PDAC spheroids in supports comprised of gelatin with varying zeta potentials.

Inclusion of other relevant cell types

The PDAC TME is not homogeneous. Other cell types are heavily involved in the progression of this TME (Fig. 7). The pancreatic stellate cells, as described in Chapter 4, overproduce collagen, hyaluronic acid, and other ECM components to form the dense stroma characteristic of the PDAC TME. These cells are also involved in coordinating the metastatic cascade, allowing PDAC cells to migrate out of the TME and towards the lymphatic and/or blood vasculature[30]. Immune cells such as macrophages are very common in the PDAC TME. The immune cells receive signals from chemokines like TGF-beta and MCP-1 that instruct immune cells to maintain an

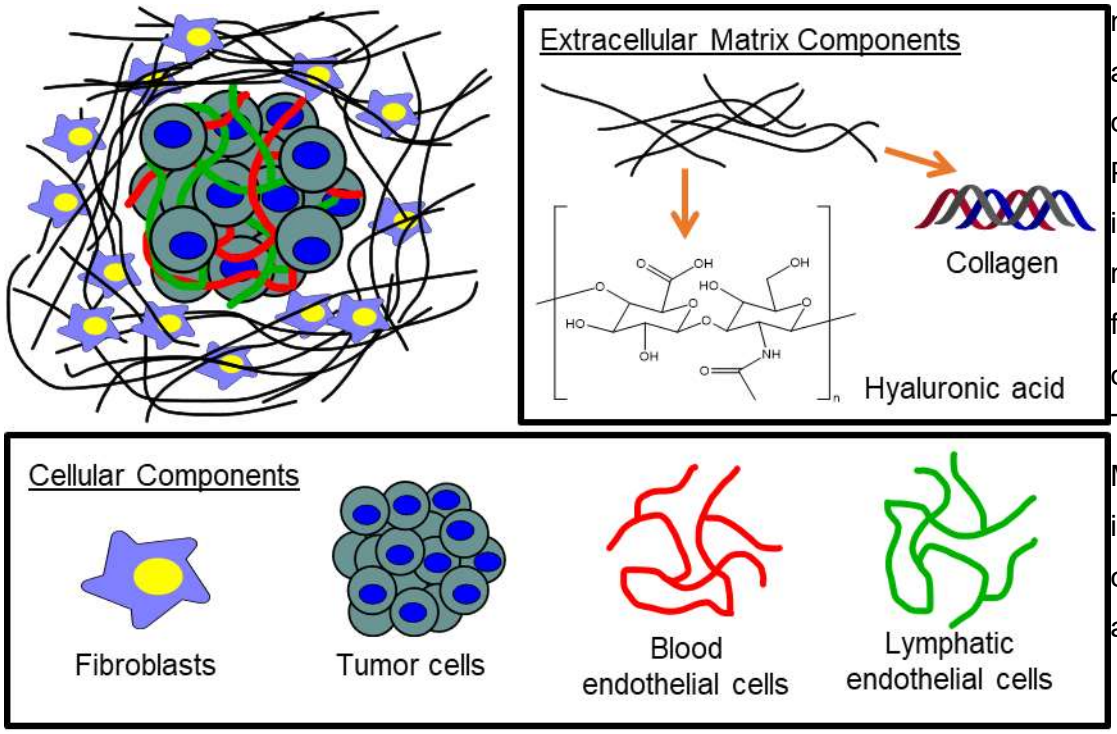

Figure 7: breakdown of the PDAC environment, separated into cellular and ECM components

immunosuppressive environment[24,31]. Thus, a physiologically-relevant *in vitro* PDAC model must include these cells types.

While the PDAC TME is hypoperfused, vasculature can still play a role in progression, namely in the metastatic cascade. Cancer cells can migrate to either blood or lymphatic vasculature, and immune cells such as T-cells are trafficked through the lymphatic system[32]. Blood endothelial cells can also undergo phenotypic changes to become cancer associated fibroblasts[33]. Thus, the inclusion of these other relevant cell types would enhance an *in vitro* model for studies to further understand PDAC metastasis and namely the intravasation process.

Formation of cationic norbornene-modified gelatin ((+) GelNB) and fiber creation

Rather than adsorbing a cationic polymer onto an anionic microgel, multiple synthesis routes can be used to create a crosslinkable cationic gelatin. By reacting gelatin with carbic anhydride[34], we can create gelatin-norbornene (GelNB) (Fig. 8A), already known to undergo crosslinking via exposure to UV light in the presence of a dithiol crosslinker. However, this reaction produces an anionic polymer, as seen by the decrease in amine groups and zeta potential (Fig. 8B and C). To reverse this, GelNB can be reacted using the same EDC chemistry as shown in Chapter 3 to modify the carboxylic acid groups into amine-containing moieties[35]. This reaction is reproducible, where the number of amines across three different syntheses was calculated to be between roughly 550 and 800 μmol of NH_2 per g of material, compared to approximately 240 μmol of NH_2 per g gelatin in gelatin type A, and roughly 13 μmol of NH_2 in GelNB (Fig. 8B). Zeta potentials also predictably changed, going from slightly positive to negative upon addition of the norbornene group, then to a higher positive charge upon addition of the amine moiety (Fig. 8C).

This (+) GelNB is also crosslinkable, as shown in the rheology testing (Fig. 9A and 9B). Predictably, as polymer concentration increases, so does the storage modulus. All polymer concentrations had at least a 1000x increase in storage modulus with exposure to UV light. The final storage moduli tested ranged from roughly 100Pa to over 1000 Pa for both (-) and (+) GelNB, demonstrating its wide range of potential uses in soft tissue engineering.

Because (+) GelNB is crosslinkable, several processing techniques open up. One of these is electrospinning, where an electric field is used to pull a polymer filament from a solution to form nanofibers. Electrospun fibers are typically on the nanoscale in diameter and have been shown in several previous studies to have many uses in biofabrication and tissue engineering. In Fig. 9C, (+)

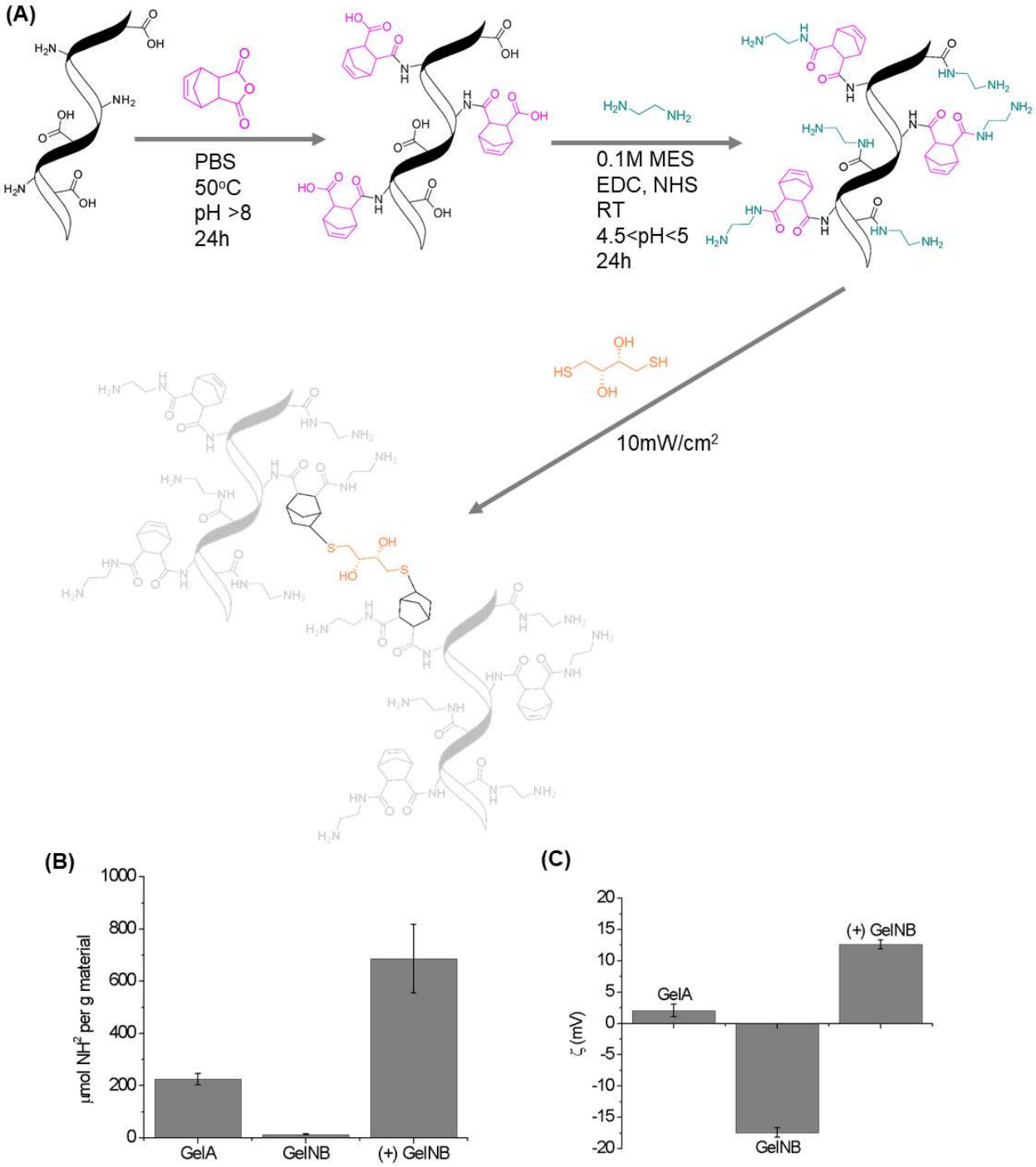

Fig. 8: (A) synthesis route to create (+) GelNB, where gelatin is first modified to couple norbornene groups onto pre-existing amines located on the gelatin backbone, then EDC chemistry is used in a second reaction to couple amines to the carboxylic acid groups located on the norbornene, then the resulting polymer can be crosslinked via UV exposure with DTT and LAP, (B) fluorescamine assay showing successful synthesis routes, where amines are decreased from the first reaction, then increased with the second reaction, and (C) zeta potential measurements also showing successful synthesis reactions, as zeta potential becomes negative from the first reaction, then positive from the second reaction.

GelNB fibers were successfully fabricated using this technique. Voltage and flow rate were altered to qualitatively assess differences in fiber production. Beading was observed under certain conditions, such as high voltage and low flow rate, as expected.

Several potential uses exist for (+) GelNB. Since (+) GelNB can be turned into nanofibers, these nanofibers can be added to NorHA microgels to reinforce the particles to one another, similar to what was achieved in Chapter 5. Altering of the particle:fiber ratio may yield interesting mechanical behaviors

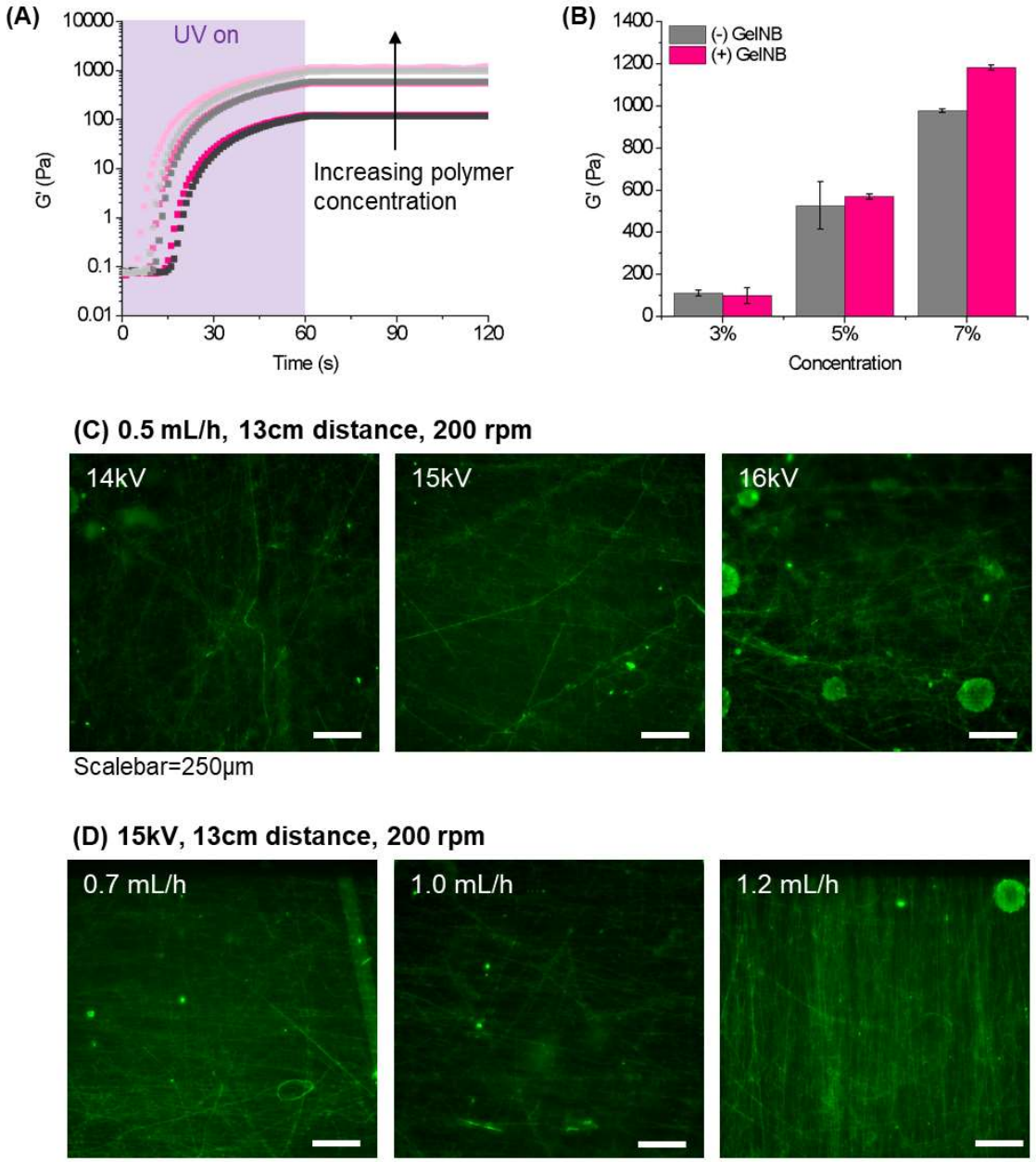

Fig. 9: (A) time sweeps showing UV crosslinking of GelNB (gray) (+) GelNB (pink) hydrogels from 3-7% concentrations, showing an increase in G' indicating that crosslinking can occur, (B) differences in G' for each GelNB and (+) GelNB concentration tested, (C) electrospun (+) GelNB fibers testing flow rates

relevant to biofabrication techniques or injectable materials, as well as cell migration platforms. The ECM in many tissues is not only granular but contains fibrous proteins like collagen as well. Therefore, addition of (+) GelNB fibers can provide a potentially more physiologically-relevant in vitro model that could more closely mimic collagen fibrils.

Due to the charge present on the (+) GelNB, nanofibers of this material can be added to nanofibers of (-) GelNB or NorHA, forming a fibrous gel system that again can be used in applications requiring shear-thinning. A fully fibrous system may also prove useful in studying cell behaviors like cell migration, especially in a cancer or fibrotic setting. A previous study demonstrated the positive feedback loop of breast cancer cells with collagen fibers. As the cancer cells modulated the collagen fibers to where they became more aligned, the local TME changed, becoming stiffer. In turn, this ECM stiffness caused the cancer cells to become stiffer, and again in turn, this resulted in more local alignment of the collagen fibrils[36]. Therefore, it is possible to use a fibrous gel system to create an *in vitro* model to further study this behavior.

References

1. Cheng, X. & Cheng, K. Visualizing cancer extravasation: from mechanistic studies to drug development. *Cancer Metastasis Rev.* **40**, 71–88 (2021).
2. Cao, J. *et al.* Recent Progress in NIR-II Contrast Agent for Biological Imaging. *Front. Bioeng. Biotechnol.* **7**, (2020).
3. Ito, S. *et al.* Real-time observation of micrometastasis formation in the living mouse liver using a green fluorescent protein gene–tagged rat tongue carcinoma cell line. *Int. J. Cancer* **93**, 212–217 (2001).
4. Kedrin, D. *et al.* Intravital imaging of metastatic behavior through a mammary imaging window. *Nat. Methods* **5**, 1019–1021 (2008).
5. Mao, M. *et al.* Human-on-Leaf-Chip: A Biomimetic Vascular System Integrated with Chamber-Specific Organs. *Small* **16**, 2000546 (2020).
6. Silva Pereira, S., Trindade, S., De Niz, M. & Figueiredo, L. M. Tissue tropism in parasitic diseases. *Open Biol.* **9**, 190036 (2019).
7. Prevention, C.-C. for D. C. and. CDC - Malaria - About Malaria - Biology. https://www.cdc.gov/malaria/about/biology/index.html (2020).
8. Martínez-Salazar, B. *et al.* COVID-19 and the Vasculature: Current Aspects and Long-Term Consequences. *Front. Cell Dev. Biol.* **10**, (2022).
9. Iba, T., Levy, J. H., Levi, M., Connors, J. M. & Thachil, J. Coagulopathy of Coronavirus Disease 2019. *Crit. Care Med.* **48**, 1358 (2020).
10. What are VHFs? | Viral Hemorrhagic Fevers (VHFs) | CDC. https://www.cdc.gov/vhf/about.html (2023).
11. Pillay, B., Ramdial, P. K. & Naidoo, D. P. HIV-associated large-vessel vasculopathy: a review of the current and emerging clinicopathological spectrum in vascular surgical practice. *Cardiovasc. J. Afr.* **26**, 70–81 (2015).
12. Matsuda, N. & Hattori, Y. Vascular biology in sepsis: pathophysiological and therapeutic significance of vascular dysfunction. *J. Smooth Muscle Res.* **43**, 117–137 (2007).

13. Jones, D. & Min, W. An overview of lymphatic vessels and their emerging role in cardiovascular disease. *J. Cardiovasc. Dis. Res.* **2**, 141 (2011).

14. Carr, I. Lymphatic metastasis. *Cancer Metastasis Rev.* **2**, 307–317 (1983).

15. Yao, L.-C., Baluk, P., Srinivasan, R. S., Oliver, G. & McDonald, D. M. Plasticity of Button-Like Junctions in the Endothelium of Airway Lymphatics in Development and Inflammation. *Am. J. Pathol.* **180**, 2561–2575 (2012).

16. Wong, K. H. K., Truslow, J. G., Khankhel, A. H., Chan, K. L. S. & Tien, J. Artificial lymphatic drainage systems for vascularized microfluidic scaffolds. *J. Biomed. Mater. Res. A* **101A**, 2181–2190 (2013).

17. Banerji, S. *et al.* LYVE-1, a New Homologue of the CD44 Glycoprotein, Is a Lymph-specific Receptor for Hyaluronan. *J. Cell Biol.* **144**, 789–801 (1999).

18. Yang, Y. *et al.* Pumpless microfluidic devices for generating healthy and diseased endothelia. *Lab. Chip* **19**, 3212–3219 (2019).

19. Bhattacharjee, T. *et al.* Liquid-like Solids Support Cells in 3D. *ACS Biomater. Sci. Eng.* **2**, 1787–1795 (2016).

20. Dasari, N. *et al.* Updates in Diabetic Wound Healing, Inflammation, and Scarring. *Semin. Plast. Surg.* **35**, 153–158 (2021).

21. Bidarra, S. J. *et al.* Injectable *in situ* crosslinkable RGD-modified alginate matrix for endothelial cells delivery. *Biomaterials* **32**, 7897–7904 (2011).

22. Kim, P.-H. *et al.* Injectable multifunctional microgel encapsulating outgrowth endothelial cells and growth factors for enhanced neovascularization. *J. Controlled Release* **187**, 1–13 (2014).

23. Nemati, S. *et al.* Alginate-gelatin encapsulation of human endothelial cells promoted angiogenesis in in vivo and in vitro milieu. *Biotechnol. Bioeng.* **114**, 2920–2930 (2017).

24. Unver, N. Macrophage chemoattractants secreted by cancer cells: Sculptors of the tumor microenvironment and another crucial piece of the cancer secretome as a therapeutic target. *Cytokine Growth Factor Rev.* **50**, 13–18 (2019).

25. Mulholland, B. S., Forwood, M. R. & Morrison, N. A. Monocyte Chemoattractant Protein-1 (MCP-1/CCL2) Drives Activation of Bone Remodelling and Skeletal Metastasis. *Curr. Osteoporos. Rep.* **17**, 538–547 (2019).

26. Qian, B.-Z. *et al.* CCL2 recruits inflammatory monocytes to facilitate breast-tumour metastasis. *Nature* **475**, 222–225 (2011).

27. Yamada, K. M. & Sixt, M. Mechanisms of 3D cell migration. *Nat. Rev. Mol. Cell Biol.* **20**, 738–752 (2019).

28. Trappmann, B. *et al.* Matrix degradability controls multicellularity of 3D cell migration. *Nat. Commun.* **8**, 371 (2017).

29. Hou, Y., Konen, J., Brat, D. J., Marcus, A. I. & Cooper, L. A. D. TASI: A software tool for spatial-temporal quantification of tumor spheroid dynamics. *Sci. Rep.* **8**, 7248 (2018).

30. Jin, G., Hong, W., Guo, Y., Bai, Y. & Chen, B. Molecular Mechanism of Pancreatic Stellate Cells Activation in Chronic Pancreatitis and Pancreatic Cancer. *J. Cancer* **11**, 1505–1515 (2020).

31. Principe, D. R., Timbers, K. E., Atia, L. G., Koch, R. M. & Rana, A. TGFβ Signaling in the Pancreatic Tumor Microenvironment. *Cancers* **13**, 5086 (2021).

32. Shen, C.-N. *et al.* Lymphatic vessel remodeling and invasion in pancreatic cancer progression. *EBioMedicine* **47**, 98–113 (2019).

33. Adjuto-Saccone, M. *et al.* TNF-α induces endothelial–mesenchymal transition promoting stromal development of pancreatic adenocarcinoma. *Cell Death Dis.* **12**, 649 (2021).

34. Madl, A. C., Madl, C. M. & Myung, D. Injectable Cucurbit[8]uril-Based Supramolecular Gelatin Hydrogels for Cell Encapsulation. *ACS Macro Lett.* **9**, 619–626 (2020).

35. K, J., Naskar, D., Kundu, S. C. & James, N. R. Fabrication of cationized gelatin nanofibers by electrospinning for tissue regeneration. *RSC Adv.* **5**, 89521–89530 (2015).

36. Fibrous nonlinear elasticity enables positive mechanical feedback between cells and ECMs | PNAS. https://www.pnas.org/doi/10.1073/pnas.1613058113